Improved Guidance, Navigation, and Control for Autonomous Underwater Vehicles: Theory and Experiment

by

Jan Petrich

Dissertation submitted to the Faculty of
Virginia Polytechnic Institute and State University
in partial fulfillment of the requirements for the degree of

Doctor of Philosophy
in
Electrical Engineering

Dr. Daniel J. Stilwell, Chair
Dr. Douglas K. Lindner
Dr. Wayne L. Neu
Dr. A. Lynn Abbott
Dr. Craig A. Woolsey

Blacksburg, Virginia
April 17th, 2009

Keywords: Autonomous Underwater Vehicles, Equivalent Models, System Identification, Uniform Observability, Persistence of Excitation, $\mathcal{H}_\infty$ Control, Pitch and Yaw Coupling, Gyroscope Calibration, Flow Field Identification

©Copyright by Jan Petrich, 2009
All rights reserved

ABSTRACT

This dissertation addresses attitude control and inertial navigation of autonomous underwater vehicles (AUVs). We present theoretical justification for using simplified models, derive system identification algorithms, and verify our results through extensive field trials. Although this research focuses on small AUVs with limited instrumentation, the results are useful for underwater vehicles of any size.

For attitude control of aircraft systems, second-order equivalent pitch-axis models are common and extensively studied. However, similar analysis has not been performed for the pitch-axis motion of underwater vehicles. In this dissertation, we study the utility and the limitations of second-order approximate models for AUVs. We seek to improve the flight performance and shorten the time required to re-design a control algorithm when the shape, mass-distribution, and/or net buoyancy of an AUV/payload configuration changes.

In comparison to commonly implemented AUV attitude controllers, which neglect roll motion and address pitch and yaw dynamics separately, we derive a novel linear time-varying model that explicitly displays the coupling between pitch and yaw motion due to nonzero roll angle and/or roll rate. The model facilitates an $\mathcal{H}_\infty$ control design approach that explicitly addresses robustness against those coupling terms and significantly reduces the effect of pitch and yaw coupling.

To improve AUV navigation, we investigate algorithms for calibrating a triaxial gyroscope using angular orientation measurements and formally define AUV trajectories that are persistently exciting and for which the calibration coefficients are uniformly observable. To improve AUV guidance, we propose a near real-time ocean current identification method that estimates a non-uniform flow-field using only sparse flow measurements.

Acknowledgement

This dissertation includes years of research at the Autonomous Systems and Controls Laboratory at Virginia Tech. In the course of time, a large number of great people impacted my work and my life here at Virginia Tech, and I would like to thank all of them. My special thanks goes to my family. This journey would not have been possible without their support and encouragement.

My deepest gratitude goes to my advisor Dr. Daniel Stilwell who shaped my academic career by setting an exceptional example of dedication and excellence from which to learn and grow. Under his guidance and endless support, I felt encouraged and privileged to devote myself to research and science. His insight knowledge and his unrivaled ability to always ask the right question stimulated the innovations and ideas of what has become this dissertation.

Special thanks goes to my committee members Dr. Craig Woolsey, Dr. Wayne Neu, Dr. Douglas Lindner and Dr. Lynn Abbott. With their commitment toward teaching and personal advising, they significantly contributed to my education, shared their passion for science and thus gave me the unique opportunity to develop myself as a researcher in an environment of academic excellence.

I would also like to extend my gratitude to my current and past colleagues and friends at the Autonomous Systems and Controls Laboratory. I am grateful for the opportunity to work surrounded by great individuals and for being part of an outstanding team. I wish everybody good luck in their future endeavors.

Finally, I thank you, the reader, for finding this interesting and valuable for whatever it is you are working on.

Over the course of five years, the work leading to this dissertation was supported by the Office of Naval Research and the National Science Foundation.

Contents

Acknowledgements iii

1 Introduction and Contributions **1**

1.1 Assessment of a Second-order Approximate Model 2

1.2 System Identification 4

1.3 Robust $\mathcal{H}_\infty$ Attitude Control Design 5

1.4 Underwater Navigation 6

1.4.1 Gyroscope Calibration 7

1.4.2 Flow Field Identification 7

1.5 Research Platform: Virginia Tech 475 AUV 8

1.6 Organization 10

2 Justification of a Second-Order Approximate Model **12**

2.1 Introduction 14

2.2 Error Model 17

2.3 Identifiability of Model Parameters 22

2.4 Inherent Stability Assessment 24

2.5 Control Design 27

2.6 Experimental Results, System Identification 33

2.7 Experimental Results, Control Design 41
2.8 Conclusions 47

3 Identification Techniques **48**
3.1 Adaptive Identification Algorithm 50
3.2 Linear State Observer 53
3.3 PE Conditions for AUV Trajectory 57
3.4 Standard Least Squares 60
3.5 Experimental Results and Validation 60
3.5.1 Depth and Pitch Control 62
3.5.2 System Identification for Nominal and Perturbed AUV 65
3.5.3 Control Redesign for Perturbed AUV 71
3.5.4 System Identification for Nominal AUV at Different Speeds . . 75
3.6 Conclusion 77

4 Robust Attitude Control **80**
4.1 Introduction 80
4.2 Joint Pitch and Yaw Model 83
4.2.1 Case 1: Zero Roll Motion 85
4.2.2 Case 2: Nonzero Roll Motion 86
4.3 Decoupling and Fin-Mixing 87
4.4 $\mathcal{H}_\infty$ Control Design 91
4.5 Experimental Results 96
4.6 Conclusions 101

5 Gyroscope Calibration **103**
5.1 Introduction 104

5.2 Gyroscope Model . . . 105
5.3 Calibration Model . . . 108
5.4 Experimental Results . . . 110
5.5 Conclusion . . . 116

6 Identification of a Simplified Flow Field Model 118
6.1 Introduction . . . 119
6.2 Problem Statement and Flow Field Model . . . 122
6.3 Identification . . . 125
6.3.1 Uniform Flow . . . 126
6.3.2 Localization of a Flow Singularity . . . 127
6.3.3 Polar Representation of the Flow Field Model . . . 134
6.3.4 Singular Flow Identification . . . 135
6.3.5 Summary of Identification Algorithm . . . 141
6.4 Experimental Results and Numerical Simulations . . . 143
6.4.1 Flow Field Identification . . . 144
6.4.2 Application in AUV Navigation . . . 153
6.4.3 Numerical Simulation . . . 153
6.5 Conclusions . . . 159

7 Conclusions 162

A AUV Model 164
A.1 Rigid Body Kinematics . . . 165
A.2 Equations of Motion . . . 167
A.3 Coordinate Transformation . . . 169
A.4 External Forces and Moments . . . 172

A.5 Pitch-axis Model 174
A.5.1 Steady State Conditions around Pitch-axis 176
A.5.2 Derivation of a Linear Heave and Pitch Model 178

B **182**

B.1 Parameter Convergence,Proof of Proposition 3.1.2 182
B.2 Convergence for Gradient method,Proof of Proposition 6.3.3 185

Bibliography **188**

List of Figures

1.1 Virginia Tech 475 AUV 9

2.1 Linear pitch axis model 13
2.2 System Identification 19
2.3 Signal diagram of error model 21
2.4 Coupling between pure pitch motion and angle of attack 25
2.5 Root Locus example 26
2.6 AUV/FLS configurations 34
2.7 AUV/Ta configurations 35
2.8 Closed Loop Pitch System 35
2.9 AUV Trajectories, 2nd order model 37
2.10 AUV Trajectories, 3rd order model 38
2.11 Bode plots for 2nd and 3rd order models 40
2.12 Bode plots for 2nd and 3rd order models 41
2.13 Bode plots for 2nd and 3rd order models 42
2.14 Bode plots of open-loop transfer function 44
2.15 Sensitivity Transfer Function 46

3.1 Closed loop simulation 61

3.2 AUV modification 63
3.3 Cascaded AUV Depth controller 64
3.4 Parameter identification for the nominal AUV 66
3.5 Parameter identification for the pertubed AUV 67
3.6 Bode plots for nominal and perturbed AUV 70
3.7 Validation of nominal AUV model 72
3.8 Validation of perturbed AUV model 73
3.9 Results of control redesign 76
3.10 Bode plots for nominal AUV at different speeds 78

4.1 Fin-Mixing and Decoupling 88
4.2 Closed loop control 92
4.3 H_∞ approach 96
4.4 Old Flight performance 98
4.5 Singular Value Plots 99
4.6 Open Loop response 101
4.7 New Flight performance 102

5.1 Parameter estimation via Adaptive identifier 112
5.2 Integration of the calibrated gyroscope measurements, quaternion . . 114
5.3 Integration of the calibrated gyroscope measurements, Euler angles . 115

6.1 solenoidal flow field ($\alpha > 0$, $\beta = 0$). 125
6.2 Rotational flow field ($\alpha = 0$, $\beta > 0$). 125
6.3 Evaluation of the singular flow pattern around $\mathbf{r}$ 130
6.4 Singularity detection based on three measured data vectors. 133
6.5 Flow chart of the flow field identification process. 142

6.6 Extraction of local flow field measurements 145
6.7 Nonzero uniform flow and residual data vectors 147
6.8 Flow field identification using nonzero uniform flow 148
6.9 Flow field identification (vortex) using zero uniform flow 150
6.10 Flow field identification (source) using zero uniform flow 151
6.11 Constrained flow field identification (vortex) using zero uniform flow . 152
6.12 Dead reckoning trajectory 154
6.13 Numerical example 155
6.14 Numerical example, flow field identification 157
6.15 Numerical example, comparison 158
6.16 Normalized magnitude of relative flow field error 159
6.17 Numerical example, dead reckoning trajectories 160

A.1 Rigid body motion of an AUV 166
A.2 Wind and Body frame 170
A.3 Pitch-axis model 177

List of Tables

2.1 System identification RMS errors (2.32) for θ, q and δ. 39

2.2 Following Figure 2.14: phase margins φ_m and actuator bandwidths f_a. 45

3.1 Identified system parameters for nominal and perturbed AUV 69

3.2 Identified AUV system parameters for selected propeller rotation rates 77

5.1 Estimated calibration parameters for different identification techniques 111

5.2 Estimated calibration parameters for different model representation . 111

5.3 RMS estimation error 116

6.1 Several identification options and their impact on the modeled flow. . 146

Chapter 1

Introduction and Contributions

In this dissertation, we develop methods improving guidance, navigation, and control of autonomous underwater vehicles (AUVs). The principal contributions of this dissertation are

(1) the formal assessment and the rigorous justification for using linear second-order approximate models for AUV pitch-axis motion, including conclusions on the utility and limitations of model-based feedback control design based on second-order models,

(2a) the development of in-flight system identification methods that enable quick re-design of an attitude controller when the overall shape, mass-distribution, and/or net buoyancy of an AUV/payload configuration changes,

(2b) the formal characterization of AUV trajectory excitation that guarantees uniform observability and thus enables successful online parameter identification,

(3) the derivation of a novel time-varying linear model that incorporates coupling terms due to roll motion and thus allows for a theoretically justified $\mathcal{H}_\infty$ control

design approach, which provides robustness explicitly against those coupling terms,

(4a) the online identification of scale factors and bias errors of an onboard triaxial gyroscope in order to improve inertial navigation of AUVs, and

(4b) a near real-time ocean current identification method for a simplified ambient flow field model that requires only a sparse set of sample vectors but improves the performance of AUV guidance and navigation noticeably.

In all cases, we present formal analysis of our results *and* experimental verification from extensive field trials.

1.1 Assessment of a Second-order Approximate Model

In steady-state flight at zero angle of attack, the linearized pitch-axis motion of a streamlined AUV, as derived from first principles, is a third-order system. Linear third-order AUV pitch-axis models can be found in [1], [2], [3] and [4]. However, system identification and control design for streamlined AUVs often assume a second-order model for pitch-axis motion, see for example [1], [4], [5], [6], [7] and [8]. The use of second-order models is also common in the aircraft community, where reduced-order equivalent models have been extensively studied for evaluating flight performance, see for example [9] and [10]. However, the utility of second-order approximate models for AUVs has not been previously addressed. For this reason, we attempt to establish theoretical justification for using a second-order pitch-axis model for parameter identification and attitude control design. We discuss fundamental differences in the linearized pitch dynamics between aircraft and neutrally buoyant AUVs, investigate

identifiability of AUV system parameters, and address the ability to deduce stabilizing output feedback gains from a second-order approximation.

Within the scope of linear dynamic model identification, we address identifiability of the underlying physical parameters of the AUV systems, such as lift and drag coefficients. We formally prove that the physical AUV parameters that define the third-oder model cannot be identified without instrumenting linear velocities. Thus for small AUVs with limited instrumentation, a third-order model does not provide any advantages over a second-order approximation for the purpose of parameter identification. Without model parameters, a state observer that estimates linear velocities and enables state feedback control cannot be directly implemented.

In order to analyze why a second-order approximation seems to work well in practice, we introduce an error model that defines a useful relationship between the third-order model and a second-order approximation. The error model quantifies neglected system dynamics in terms of vehicle parameters and enables us to assess stability and performance of the closed-loop third-order model when using a controller that is designed based on a second-order approximation. By formally quantifying the relationship between size of the error model and stability of the closed-loop system, we deduce output-feedback gains from a second-order approximation that stabilize the underlying third-order plant.

An important contribution of our work is to apply our results in practice. Using three drastically different AUV/payload configurations for a case study, we identify both a canonical third-order linear pitch-axis model and an approximated second-order linear pitch-axis model. We compare the resulting models and draw conclusions about the performance and robustness of a control system that is designed based on a second-order approximation. Through our analysis and field trials, we conclude

that a linear second-order pitch-axis model often suffices for system identification and attitude control design of a streamlined AUV of any size.

1.2 System Identification

In general, the parameters of a linear AUV pitch-axis model are obtained through tow-tank experiments as described in [4], [11], [12] and [13], or by employing computational fluid dynamics (CFD) tools as described in [14], [15], [16] and [17]. However, conducting time-consuming and expensive tow-tank experiments or CFD simulations is prohibitive for experimental AUVs whose payload configuration and hydrodynamic characteristics change frequently depending on mission requirements. Thus, the ability to perform in-flight system identification from available input and output signals is of particular importance for revising the control system when the overall shape, mass-distribution, and/or net buoyancy of an AUV changes.

In this dissertation, we present parameter estimation for a linear second-order pitch-axis model utilizing only instrumented variables onboard the AUV. Similar work has been presented in [18], in which the authors identify the parameters of a canonical third-order AUV pitch-axis model using post-flight numerical minimization tools.

For parameter estimation, we reveal a meaningful equivalence between an adaptive identifier and a linear state observer. Formal observability analysis shows equivalence between persistence of excitation and uniform observability for the given system.

We validate our theoretical results by conducting field experiments using multiple AUV configurations. For each AUV configuration, we are able to identify a simplified pitch-axis model that accurately predicts the AUV's motion, and we successfully

demonstrate model-based control re-design.

1.3 Robust $\mathcal{H}_\infty$ Attitude Control Design

Attitude control systems for AUVs are often implemented with separate controllers for pitch motion in the vertical plane and yaw motion in the horizontal plane, neglecting coupling between pitch and yaw motion, see [19], [20] and [21]. In this work, we derive a novel linear time-varying model that explicitly displays the coupled pitch and yaw dynamics of a streamlined AUV that are due to nonzero roll angle and/or roll rate. Our model facilitates the design of a multi-input multi-output $\mathcal{H}_\infty$ controller that provides robustness specifically against roll-induced coupling terms.

Robust attitude control for AUV systems has been addressed using a variety of approaches, see [8] and [20] for sliding mode control, and [22] and [23] for μ-synthesis design. For our purposes, we use $\mathcal{H}_\infty$ tools (e.g., from Section 17 in [24]) for two reasons. First, we address roll-induced coupling as structured uncertainties within the linear plant and thus choose a control design approach that provides robustness specifically against these uncertainties. Second, we formulate fundamental control design criteria such as robustness against parameter uncertainties, overall tracking performance and required actuator bandwidth. Similar $\mathcal{H}_\infty$ approaches for AUV attitude control are presented in [2], [20] and [23], in which the authors focus on providing robustness against model uncertainties for separate pitch and yaw channels. In comparison to existing work, the novelty of our approach lies in formally deriving coupling effects between pitch and yaw motion and in explicitly addressing pitch/yaw coupling for robust feedback control design.

Adopting an $\mathcal{H}_\infty$ control design approach, we are able to compromise between per-

formance, robustness and actuator bandwidth via standard loop shaping techniques, see [19] and [25]. In addition to fully instrumented AUVs, our final control design is applicable to miniature AUVs whose limited instrumentation allows for angular rate and angular orientation feedback only.

Borrowing control strategies used for guided missile systems, see [26] and [27], we allocate sensor measurements and actuator commands in order to minimize kinematic coupling within the linear model. A time-varying, roll-dependent state-space transformation is proposed which allows us to address attitude control assuming an upright AUV body with zero roll angle. We formally show that coupling is reduced by transforming the linear equations of motion into such a zero roll body-axis frame.

The efficacy of our approach is demonstrated with field trials. We obtain an AUV model in situ using flight data and design a model-based multi-input multi-output $\mathcal{H}_\infty$-attitude controller that provides robustness against roll-induced coupling. The flight performance of the AUV is evaluated and a significant reduction in pitch and yaw coupling is verified.

1.4 Underwater Navigation

Providing a reliable position estimate underwater is a crucial requirement when operating AUVs. GPS signals attenuate in water, and thus GPS is not available as position reference for a submerged vehicle. Alternative methods such as long-base-line (LBL) navigation [28] are commonly utilized to triangulate the AUVs position via acoustic pings against a set of transponders prepositioned at the sea floor. Although some miniature AUVs are capable of acoustic underwater navigation [29], LBL navigation is not assumed in this work. Therefore, the AUV must rely on inertial navigation

using accelerometers and gyroscopes.

To improve the navigation capabilities of an AUV, we derive an error model for a triaxial gyroscope as well as a low-complexity representation of an ambient flow field. We utilize flight data to parameterize both models and show the benefits of incorporating them into underwater navigation and vehicle guidance.

1.4.1 Gyroscope Calibration

Gyroscopes are commonly used to stabilize attitude measurements provided by onboard orientation sensors such as an inclinometer or a magnetic compass. The method of combining vehicle orientation and kinematics to deduce the AUV's position underwater is referred to as inertial navigation, or dead reckoning. Since the accuracy of dead reckoned trajectories is directly related to the precision and accuracy of the inertial sensor, online calibration of inertial sensors is of particular importance. For this reason, we attempt to calibrate a triaxial gyroscope, commonly used in miniature AUVs, utilizing angular orientation measurements. A gyroscope error model is proposed containing scaling and bias terms that are subject to parameter identification. We derive sufficient conditions under which successful parameter identification is guaranteed simultaneously for all three gyroscopes and infer preferable AUV trajectories. Bench tests show the ability to acquire a set of calibration parameters that generate a reliable attitude estimate by integrating the calibrated body-fixed angular rates over short periods of time.

1.4.2 Flow Field Identification

Underwater navigation is affected by environmental disturbances such as fluid flow surrounding the vehicle. AUVs of small size are commonly not equipped with a

Doppler Velocity Log (DVL) and therefore underwater currents that alter the AUV trajectory are unknown. To compensate for the influence of currents on underwater navigation, we propose an algorithm to identify a simplified, two-dimensional flow field model for the immediate vicinity of the vehicle's operating area.

As compared to the identification of large-scale ocean currents [30] or particle movements [31], which are commonly based on image sequence processing [32], [33] and rely on a dense set of sample vectors, we develop an identification algorithm that uses only a small, sparse data set collected by a platoon of vehicles. After each dive, the navigation error is evaluated by comparing the dead reckoned underwater trajectory to GPS start and end points. Flow field sample vectors are obtained by attributing the navigation error to fluid flow. Our basic approach involves estimating the uniform flow component, localizing an assumed flow singularity, and identifying the parameters which characterize the singular flow. A convergence proof for the proposed singularity localization algorithm is presented.

A numerical example illustrates the application of the algorithm to a realistic flow data set and provides ground truth to evaluate the performance of the algorithm. Preliminary experimental field trials show the advantage of merging vehicle kinematics and a model of underwater currents for vehicle navigation.

1.5 Research Platform: Virginia Tech 475 AUV

The Virginia Tech 475 AUV, shown in Figure 1.1, was developed by the author and colleagues in the Autonomous Systems and Controls Laboratory at Virginia Tech and is used for most of the experimental activities presented in this dissertation.

The Virginia Tech 475 AUV is 1 meter long, weighs 8.5 kilograms and travels at a

Figure 1.1: Virginia Tech 475 AUV, named after its hull diameter of 4.75 inches or 0.12 meters.

nominal speed of $1.5\,ms^{-1}$ (3 knots). It is of streamlined design with a hull diameter of 0.12 meters, nearly neutrally buoyant, and propelled by a single propeller at the stern. The Virginia Tech 475 AUV is capable of carrying or towing various payload sensors necessary for environmental and acoustic surveys. The instrumentation relevant to this research includes a pressure transducer that measures depth and an onboard attitude and heading reference system that measures the vehicle's attitude and angular rates around all three body axes. The vehicle is controlled by movable control surfaces, elevator and rudder, at the stern.

Our work is motivated by the goals of improving the flight performance of experimental AUVs, whose payload configuration and hydrodynamic characteristics change frequently depending on mission requirements. Thus, we derive model simplifications, system identification and control design strategies that facilitate the frequent changes

in shape, mass-distribution, and/or net buoyancy of an experimental AUV/payload configuration while accounting for the limited onboard instrumentation typical for small AUVs.

1.6 Organization

This dissertation is organized as follows. In Chapter 2, we recall the linearized third-order dynamics for the pitch-axis motion of a streamlined, neutrally buoyant AUV. For system identification and control design, we motivate the use of second-order approximate models. Through our analysis and a series of case studies, we justify the use of a second-order approximation for AUV pitch-axis motion. Identification techniques for the second-order system are discussed in Chapter 3 where we introduce the concepts of an adaptive identifier and a Kalman filter. Parameter convergence is investigated in terms of persistence of excitation and uniform observability. We validate parameter identification using experimental data. We provide a comparison between identification techniques and demonstrate the utility of a second-order approximation for attitude control design. In Chapter 4, we derive a novel linear time-varying AUV model that captures pitch and yaw motion. We show that pitch and yaw coupling is induced by nonzero roll angle and/or roll rate, and we design an $\mathcal{H}_\infty$ controller that addresses roll-induced coupling as structured uncertainties within the linear plant. In Chapter 5, we utilize system identification techniques from Chapter 4 to calibrate a triaxial gyroscope. We propose a measurement error model which contains calibration parameters accounting for offset and scaling terms. The calibration is validated during field trials. This work closes by presenting an algorithm to identify a simplified flow field model in Chapter 6. Using a platoon of AUVs, we describe the process of

obtaining a set of flow field sample vectors, which we utilize to parameterize a uniform and singular flow component. Experimental data shows that the AUV's position estimate benefits significantly from incorporating such an ambient flow field model.

Chapter 2

Justification of a Second-Order Approximate Model

In steady-state flight at zero angle of attack, the linearized pitch-axis motion of a streamlined, neutrally buoyant AUV, as derived from first principles, is a third-order system, see (A.23). A complete derivation of the model is presented in Appendix A. We recall

$$\begin{aligned}\begin{bmatrix}\dot{\alpha}\\ \dot{q}\\ \dot{\theta}\end{bmatrix} &= \begin{bmatrix}a_{22} & a_{23} & 0\\ a_{32} & a_{33} & a_{34}\\ 0 & 1 & 0\end{bmatrix}\begin{bmatrix}\alpha\\ q\\ \theta\end{bmatrix} + \begin{bmatrix}b_{21}\\ b_{31}\\ 0\end{bmatrix}\delta\\ \begin{bmatrix}y_1\\ y_2\end{bmatrix} &= \begin{bmatrix}0 & 1 & 0\\ 0 & 0 & 1\end{bmatrix}\begin{bmatrix}\alpha\\ q\\ \theta\end{bmatrix}\end{aligned} \tag{2.1}$$

Here, the angle of attack is α, the pitch rate is q, the pitch angle is θ, and the elevator fin deflection is δ. As illustrated in Figure 2.1, the angle of attack α is defined between

the body's x-axis and the velocity vector V, and the pitch angle is defined between the body's x-axis and the XY-plane of the inertial frame. Only pitch rate q and pitch angle θ are assumed to be instrumented, and thus the output signals are $y_1 = q$ and $y_2 = \theta$. The parameters of (2.1) are defined in (A.22).

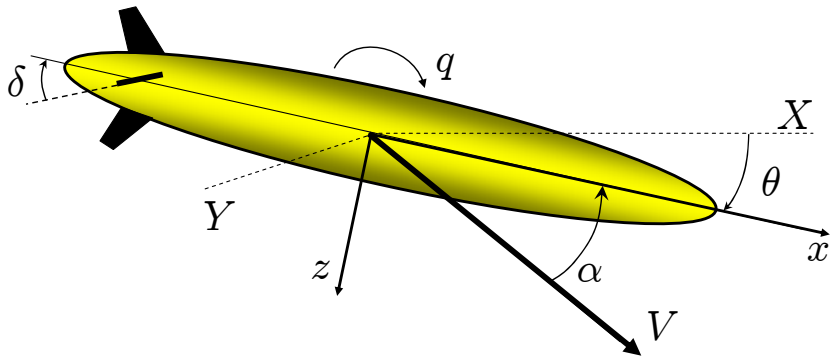

Figure 2.1: A linear pitch-axis model describes the AUV motion in the body's xz plane. Assuming constant velocity V, the states are angle of attack α, pitch rate q, and pitch angle θ. The input is the elevator fin deflection δ.

Although not fully justified, second-order pitch-models are found adequate for AUV system identification and control design in practice, see for example [1], [4], [5], [6], [7] and [8]. A typical second-order approximation is

$$\begin{bmatrix} \dot{q} \\ \dot{\theta} \end{bmatrix} = \begin{bmatrix} A_{33} & A_{34} \\ 1 & 0 \end{bmatrix} \begin{bmatrix} q \\ \theta \end{bmatrix} + \begin{bmatrix} B_{31} \\ 0 \end{bmatrix} \delta \tag{2.2}$$

In [1], [4] and [8], such a second-order model is derived by deleting the state α in the third-order model (2.1), while in [5], [6] and [7] it is proposed without justification.

Although the use of low-order equivalent models is common and extensively studied for control of aircraft systems, similar analysis has not been performed for submersible systems. Toward an improved understanding of the utility of low-order ap-

proximate models for submersible systems, we examine control design for pitch-axis motion of an AUV. In this chapter, we provide theoretical justification for both the use of and limitations of a second-order model, and we verify our results in practice via a series of case studies. We conclude that a second-order pitch-axis model should often be sufficient for system identification and control design.

2.1 Introduction

Complete nonlinear AUV models are introduced in [1], [34] and [35]. In general, the parameters of those models are obtained through tow-tank experiments as described in [4], [11], [12] and [13], or by employing computational fluid dynamics (CFD) tools as described in [14], [15], [16] and [17]. However, conducting time-consuming and expensive tow-tank experiments or CFD simulations is prohibitive for AUVs whose payload configuration and hydrodynamic characteristics change frequently depending on mission requirements. Examples of such modular AUVs that easily accommodate payload sensors are the *Ocean Explorer* [36], the *Mares AUV* [37], and the *Remus AUV* [38]. In our work, we justify simplifying assumptions regarding the highly nonlinear AUV dynamics in theory and practice, and we investigate the utility of a low-order pitch-axis model for in-flight system identification as proposed in [39] and subsequent model-based attitude control design.

The use of second-order models is common in the aircraft community, where reduced-order equivalent models have been extensively studied for evaluating flight performance, see for example [9] and [10]. It is widely accepted that the fourth-order pitch dynamics are governed by two modes, namely *short period* and *phugoid* mode. Due to the time scale separation of both modes, it suffices to examine the

second-order *short period* mode for attitude control, see [40] and [41]. No equivalent work has been done to investigate the utility of low-order approximate models for submersed vehicles, and a rigorous justification for second-order approximate models has not been previously addressed. For this reason, this work attempts to establish theoretical justification for using a second-order pitch-axis model for parameter identification and attitude control design of streamlined AUVs. In order to analyze why a second-order approximation seems to work well in practice, we introduce an error model that defines a useful relationship between the third-order model and a second-order approximation. We use the error model to quantify neglected system dynamics and discuss stability and performance of the closed-loop third-order model when using a controller that is designed based on a second-order approximation. Our analysis and field trials show that a second-order pitch-axis model often suffices in practice for control design.

Limited sensing ability poses fundamental challenges for obtaining reliable model parameters from flight data. In particular, smaller AUVs are often not instrumented to measure linear velocities, and thus the angle of attack α is unknown. With the limited instrumentation in mind, we address identifiability of the underlying physical parameters of AUV systems, such as lift and drag coefficients, within the scope of linear dynamic model identification. We prove that physical AUV parameters are not uniquely identifiable using in-flight system identification techniques, as presented in [39] for linear models and in [42] for nonlinear models, and therefore the parameters of the identified model do not determine the physical parameters of the actual system. Thus, for the purpose of identifying physical AUV parameters, a third-order model does not provide any advantages over a second-order approximation. Without model parameters, a state observer that estimates α and thus enables state feedback

cannot be directly implemented. We deduce output-feedback gains from an identifiable, second-order approximation of the plant, and we show that those feedback gains stabilize the underlying third-order plant if the error model is sufficiently small. We formally quantify the relationship between size of the error model and stability margins of the control system.

When designing AUV controllers, model parameters are commonly assumed to be known. For example, linear third-order model parameters, determined experimentally through tow-tank experiments and CFD simulations, are presented for the *Remus AUV* in [4] or the *MARIUS* vehicle in [43]. In contrast, we identify linear pitch models in situ utilizing only instrumented variables onboard the AUV. Our work is motivated by vehicle systems that change their external shape and/or mass distribution (e.g., new external payload) frequently, and for which a revised control system is required. In this case, control design is expedited if a dynamic model can be identified rapidly from AUV flight data. Thus we address control design in the context of system identification and corresponding parameter estimation errors. Ad-hoc system identification has been presented in [18], in which the authors identify the parameters of a canonical third-order AUV pitch-axis model using numerical minimization tools.

Experimental verification of our analysis is conducted using the Virginia Tech 475 AUV, introduced in Section 1.5. Using three drastically different configurations of the Virginia Tech 475 AUV, we identify both second-order and third-order linear pitch-axis models. We compare the resulting models and draw conclusions about the performance and robustness of a control system that is designed based on a second-order approximation. Comparing the full third-order dynamics to the second-order approximation, we find a modest decrease in phase margin. We conclude that a linear second-order pitch-axis model suffices for attitude control design of a slender

and streamlined AUV.

This chapter is organized as follows. In Section 2.2, we introduce a model for the approximation error due to using a second-order approximation for the third-order model. In Section 2.3, we investigate identifiability of the underlying physical parameters (e.g., lift and drag) in the context of system identification. In Section 2.4, we discuss inherent stability of the pitch-axis motion of a streamlined AUV, and in Section 2.5 we investigate control design. In Sections 5.4 and Section 2.7, we apply our results to the problems of system identification and control design, respectively, for three configurations of the Virginia Tech 475 AUV.

2.2 Error Model

In this section, we address the approximation of the third-order plant (2.1) with the transfer function

$$\begin{aligned} \begin{bmatrix} q(s) \\ \theta(s) \end{bmatrix} &= \begin{bmatrix} s \\ 1 \end{bmatrix} \frac{\beta_1 s + \beta_0}{s^3 + \alpha_2 s^2 + \alpha_1 s + \alpha_0} \delta(s) \\ &= \begin{bmatrix} s \\ 1 \end{bmatrix} G_3(s)\, \delta(s) \end{aligned} \tag{2.3}$$

where

$$\begin{aligned} \beta_1 &= b_{31} \\ \beta_0 &= a_{32} b_{21} - b_{31} a_{22} \\ \alpha_2 &= -a_{22} - a_{33} \\ \alpha_1 &= a_{22} a_{33} - a_{34} - a_{23} a_{32} \\ \alpha_0 &= a_{22} a_{34} \end{aligned} \tag{2.4}$$

using a second-order model (2.2) and the corresponding transfer function

$$\begin{aligned}\begin{bmatrix} q(s) \\ \theta(s) \end{bmatrix} &= \begin{bmatrix} s \\ 1 \end{bmatrix} \frac{B_{31}}{s^2 - A_{33}s - A_{34}} \, \delta(s) \\ &= \begin{bmatrix} s \\ 1 \end{bmatrix} G_0(s) \, \delta(s) \end{aligned} \tag{2.5}$$

In the sequel, we assume the existence of lumped parameters A_{33}, A_{34}, and B_{31} defining a second-order model (2.2) that captures the dominating modes and approximates the input-output behavior of (2.1). In Section 2.6, we verify this assumption in practice.

Applying standard system identification techniques, e.g. [44] and [45], the parameters of $G_0(s)$ in (2.5) are determined by matching the input-output behavior of model and plant. Due to the model approximation and truncation of system modes, we generally find $A_{33} \neq a_{33}$, $A_{34} \neq a_{34}$ and $B_{31} \neq b_{31}$, see [46]. Thus, the physical significance of the parameters A_{33}, A_{34}, and B_{31} is not apparent.

We investigate the relationship between second-order approximation and third-order representation of the plant through an error model. To derive an error model, we decompose the third-order transfer function (2.3) as

$$\begin{bmatrix} q(s) \\ \theta(s) \end{bmatrix} = \begin{bmatrix} s \\ 1 \end{bmatrix} G_2(s) \, G_e(s) \, \delta(s) \tag{2.6}$$

The transfer function $G_2(s)$ contains the second-order approximation (2.5) augmented with the system identification errors ΔA_{33}, ΔA_{34} and ΔB_{31}

$$G_2(s) = \frac{B_{31} + \Delta B_{31}}{s^2 - (A_{33} + \Delta A_{33}) \, s - (A_{34} + \Delta A_{34})}$$

and $G_e(s)$ represents an error model due to the truncation of a zero and a pole located at z_e and p_e, respectively. That is

$$G_e(s) = \frac{s - z_e}{s - p_e}$$

A qualitative pole-zero-plot of a third-order plant (black) and a second-order approximation (gray) is shown in Figure 2.2.

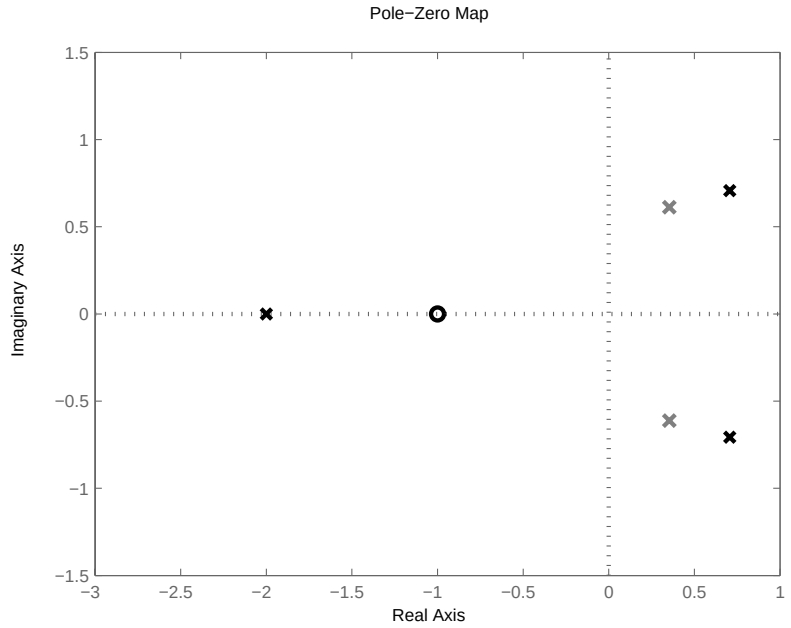

Figure 2.2: System Identification process: A linear second-order model (gray) is identified for an underlying third-order plant (black).

The parameters A_{33}, A_{34} and B_{31} from the second-order model (2.5) relate to the third-order model (2.6) through the selection of a specific state space realization of (2.6). Such a state space realization contains the states and parameters of the

second-order approximation (2.5) as well as a generic, augmented third state x_α

$$\begin{bmatrix} \dot{x}_\alpha \\ \dot{q} \\ \dot{\theta} \end{bmatrix} = \begin{bmatrix} p_\alpha & a_q & a_\theta \\ c_\alpha & A_{33} & A_{34} \\ 0 & 1 & 0 \end{bmatrix} \begin{bmatrix} x_\alpha \\ q \\ \theta \end{bmatrix} + \begin{bmatrix} b_\alpha \\ B_{31} + b_q \\ 0 \end{bmatrix} \delta$$
$$\begin{bmatrix} y_1 \\ y_2 \end{bmatrix} = \begin{bmatrix} 0 & 1 & 0 \\ 0 & 0 & 1 \end{bmatrix} \begin{bmatrix} x_\alpha \\ q \\ \theta \end{bmatrix} \tag{2.7}$$

For any $c_\alpha \neq 0$, the coefficients in (2.7) and (2.6) satisfy the equalities

$$\begin{aligned} p_\alpha &= p_e + \Delta A_{33} \\ b_q &= \Delta B_{31} \\ c_\alpha\, b_\alpha &= (B_{31} + \Delta B_{31})\ (p_e - z_e + \Delta A_{33}) \\ c_\alpha\, a_q &= (A_{33} - p_e)\ \Delta A_{33} + \Delta A_{34} \\ c_\alpha\, a_\theta &= \Delta A_{33}\, A_{34} - p_e\, \Delta A_{34} \end{aligned} \tag{2.8}$$

Using the realization (2.7), the coefficients of the third-order transfer function $G_3(s)$ from (2.3) can be expressed

$$\begin{aligned} \beta_1 &= B_{31} + b_q \\ \beta_0 &= c_\alpha b_\alpha - p_\alpha\,(B_{31} + b_q) \\ \alpha_2 &= -A_{33} - p_\alpha \\ \alpha_1 &= p_\alpha A_{33} - A_{34} - c_\alpha a_q \\ \alpha_0 &= p_\alpha A_{34} - c_\alpha a_\theta \end{aligned} \tag{2.9}$$

Figure 2.3 contains a signal diagram of (2.7) showing the second-order approximation and peripheral, structured uncertainties that define the error system.

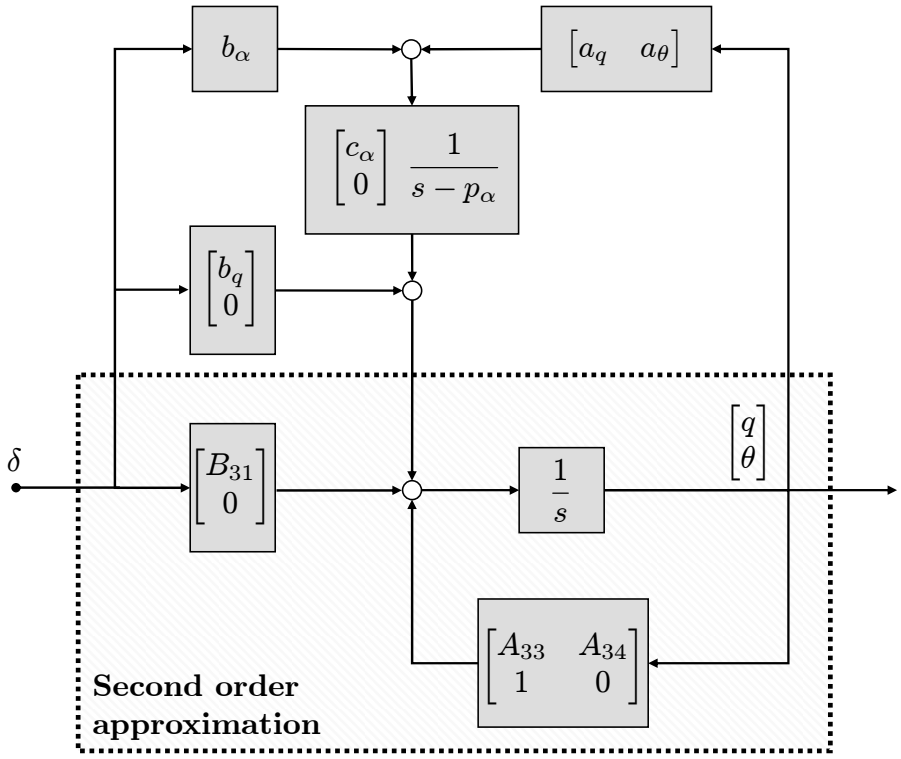

Figure 2.3: Signal diagram of the second-order approximation and the peripheral error model.

Both state space models (2.1) and (2.7) are a realization of $G_3(s)$ in (2.3) and describe the same input-output behavior. They are therefore equivalent under a state space transformation, but contain different parameter sets. In general, we find $x_\alpha \neq \alpha$. Thus, we conclude that the parameters of the third-order state space models (2.1) and (2.7) cannot be determined uniquely from the input-output behavior of the plant. A rigorous analysis addressing the identifiability of the physical AUV parameters (A.22) is presented in the next section.

2.3 Identifiability of Model Parameters

In this section, we investigate *identifiability* of the physical AUV parameters (A.22) given the available input and output signals. Although, a canonical third-order model can always be identified, it cannot be used to infer physical parameters of the underlying plant. Thus, we show that the state space representation (2.1) is not uniquely identifiable from input-output data.

For the identifiability analysis, we rewrite (2.1)

$$\begin{aligned} \dot{\mathbf{x}} &= \mathbf{A}(\mathbf{p})\,\mathbf{x} + \mathbf{B}(\mathbf{p})\,\delta \\ \mathbf{y} &= \mathbf{C}\,\mathbf{x} + \mathbf{D}\,\delta \end{aligned} \tag{2.10}$$

where the state vector is $\mathbf{x} = \begin{bmatrix} \alpha & q & \theta \end{bmatrix}^T$, the output vector is $\mathbf{y} = \begin{bmatrix} q & \theta \end{bmatrix}^T$ and $\mathbf{p}$ is

$$\mathbf{p} = \begin{bmatrix} a_{22} & a_{23} & a_{32} & a_{33} & a_{34} & b_{21} & b_{31} \end{bmatrix}^T \in \mathbb{R}^7 \tag{2.11}$$

a vector of parameters that contains the coefficients of (2.1). The parameterization of $\mathbf{A}(\mathbf{p})$ and $\mathbf{B}(\mathbf{p})$ follows immediately from (2.1) with the matrix components defined in (A.22).

Identifiability is discussed in [47] for a variety of systems. For our purposes, we recall that the input-output behavior of a linear, time-invariant system is uniquely determined by the Markov parameters g_i. For the state space representation (2.10), the Markov parameters are given by

$$g_0 = \mathbf{D} \qquad \text{and} \qquad g_i = \mathbf{C}\,\mathbf{A}^{i-1}(\mathbf{p})\,\mathbf{B}(\mathbf{p}) \qquad i = 1, 2 \ldots \tag{2.12}$$

and the Markov parameter matrix defined in [47] is

$$\mathbf{G}(\mathbf{p}) = \begin{bmatrix} \mathbf{D} \\ \mathbf{C}\,\mathbf{B}(\mathbf{p}) \\ \mathbf{C}\,\mathbf{A}(\mathbf{p})\,\mathbf{B}(\mathbf{p}) \\ \mathbf{C}\,\mathbf{A}^2(\mathbf{p})\,\mathbf{B}(\mathbf{p}) \\ \vdots \\ \mathbf{C}\,\mathbf{A}^{2n-1}(\mathbf{p})\,\mathbf{B}(\mathbf{p}) \end{bmatrix} \in \mathbb{R}^{2(2n+1)} \tag{2.13}$$

where n is the order of the system. For (2.10), $n = 3$. For the single-input system (2.10), the Markov parameter matrix $\mathbf{G}(\mathbf{p})$ is a vector. The following theorem from [47] states a sufficient condition for local identifiability.

Theorem 2.3.1. *The parameter vector* $\mathbf{p} \in \mathbb{R}^q$ *is said to be* locally identifiable *at* $\hat{\mathbf{p}} \in \mathbb{R}^q$ *if*

$$\text{rank} \left[\frac{\partial}{\partial \mathbf{p}} \mathbf{G}(\mathbf{p})\right] = q \qquad at \qquad \mathbf{p} = \hat{\mathbf{p}} \tag{2.14}$$

In other words, the Markov parameter matrix $\mathbf{G}(\mathbf{p})$ provides a local *one-to-one* map between system parameters $\mathbf{p}$ and Markov parameters g_i at $\hat{\mathbf{p}}$. Specifying Theorem 2.3.1 to the system at hand, we deduce the following corollaries.

Corollary 2.3.2. *Given the output signals* $\mathbf{y} = \begin{bmatrix} q & \theta \end{bmatrix}^T$ *for system (2.1), the parameter vector* $\mathbf{p}$ *from (2.11) is not identifiable.*

Corollary 2.3.3. *Suppose an augmented output signal* $\mathbf{y} = \begin{bmatrix} \alpha & q & \theta \end{bmatrix}^T$*, that is the output matrix of system (2.1) satisfies* $\mathbf{C} = \mathbf{I}$*. Then, the parameter vector* $\mathbf{p}$ *from (2.11) is locally identifiable at every* $\hat{\mathbf{p}}$*, for which poles and zeros of (2.1) do not coincide.*

To prove Corollaries 2.3.2 and 2.3.3, we construct the Markov parameter matrix $\mathbf{G}(\mathbf{p})$ from (2.13) for each case of $\mathbf{C}$, and check the rank condition of the Jacobian matrix (2.14).

Corollaries 2.3.2 and 2.3.3 imply that identifying the parameter vector $\mathbf{p}$ requires that α is instrumented. Therefore, deducing the physical AUV parameters (A.22) uniquely from the input-output behavior (2.1) is not possible given the limited instrumentation of typical small AUV systems.

As compared to the seven parameters of (2.1), one can show that the five coefficients of transfer function $G_3(s)$ in (2.3)

$$\mathbf{p}_c = \begin{bmatrix} \alpha_0 & \alpha_1 & \alpha_2 & \beta_0 & \beta_1 \end{bmatrix}^T \in \mathbb{R}^5 \tag{2.15}$$

are identifiable if the numerator and denominator polynomials in (2.3) do not share roots. In Section 2.6, we estimate the coefficients $\mathbf{p}_c$ and obtain a canonical third-order model $\hat{G}_3(s)$ for the Virginia Tech 475 AUV.

2.4 Inherent Stability Assessment

In practice, linear second-order pitch-axis models are widely used for system identification and attitude control design for AUVs. A common way to derive such a second-order model is to simply truncate α in (2.1), see [1], [4] or [8]. For conventional vehicles, for which the center of gravity is located below the center of buoyancy (z_{cg} is positive), truncating α seems poorly justified, because it always yields a stable system. In this section we show that fundamental system properties such as stability need to be addressed more formally in the context of system simplification. In particular, we examine the role of vehicle parameters in assessing stability of the third-order model (2.1), and we demonstrate that stability assumptions about the second-order approximation do not imply stability of the underlying third-order dynamics. For this reason, assuming a stable linear second-order AUV pitch-axis model may not be feasible for system identification and control design.

We assess internal stability of the AUV's pitch-axis model (2.1) by analyzing the coupling between α and the remaining states q and θ. To expose these coupling terms, we propose a different representation of the plant. We set $\delta = 0$ and decompose the system (2.1) into two coupled subsystems

$$\alpha(s) = G_\alpha(s)\, q(s) \qquad \text{and} \qquad q(s) = G_q(s)\, a_{32}\, \alpha(s)$$

with

$$G_\alpha(s) = \frac{a_{23}}{s - a_{22}} \qquad \text{and} \qquad G_q(s) = \frac{s}{s^2 - a_{33}s - a_{34}} \tag{2.16}$$

Recalling $q(s) = s\,\theta(s)$, the transfer functions $G_\alpha(s)$ and $G_q(s)$ originate from the first and second row in (2.1), respectively. The overall internal system dynamics (2.1) are represented by the feedback system shown in Figure 2.4.

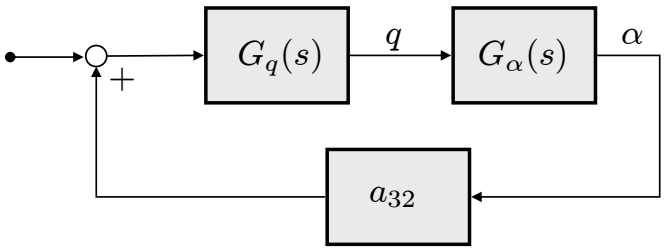

Figure 2.4: Coupling between $G_q(s)$ and $G_\alpha(s)$ through the parameter a_{32}.

For a small horizontal separation x_{cg} between center of gravity and center of buoyancy, we verify that the poles of $G_q(s)$ and $G_\alpha(s)$ remain in the open left half plane indicating stability of both subsystems. In fact, the system parameters a_{33} and a_{34} in (A.22) suggest that $G_q(s)$ resembles the motion of a physical pendulum around the center of buoyancy. This motion is stable assuming both the existence of viscous damping, modeled by a_{33} through the vehicle parameter $C_{m_q} < 0$, and the location of the center of gravity satisfying $z_{cg} > 0$. Note that simply truncating α

in (2.1) yields this stable pendular motion

$$q(s) \;=\; G_q(s)\, b_{31}\, \delta(s)$$

The pole location of $G_\alpha(s)$ at $a_{22} < 0$ is characterized by the drag coefficient $C_{D_0} < 0$ and the slope $C_{L_\alpha} < 0$ of the body's lift coefficient, see (A.22).

We evaluate internal stability of (2.1) using the *root locus* of the series connection $G_\alpha(s)\, G_q(s)$ with respect to the system parameter a_{32}. Figure 2.5 shows a comparable numerical example of a root locus as function of a_{32}.

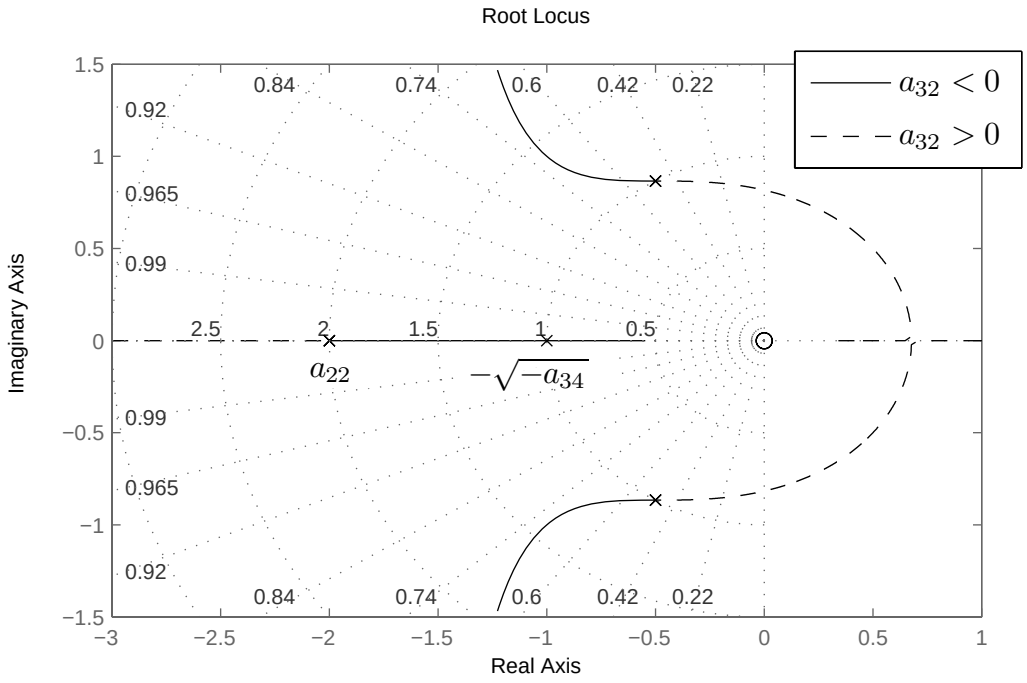

Figure 2.5: Root Locus representation of system poles as function of a_{32}.

For $a_{32} = 0$, one recognizes the two complex poles of $G_q(s)$ close to the imaginary axis and the single pole of $G_\alpha(s)$ at a_{22}. The parameter a_{32} is given in (A.22) and contains a destabilizing *centripetal* or *munk* moment $(m_z - m_x)\, V_0^2 > 0$ and a restoring

moment $\frac{1}{2}\rho V_0^2 A_b L C_{m_\alpha} < 0$ provided by the vehicle's body. Increasing a_{32} destabilizes the overall system by pushing two poles to the right half plane, while the pole originally located at a_{22} moves further left. As illustrated in Figure 2.4, the parameter a_{32} acts as positive feedback gain for the stable series connection $G_\alpha(s)\, G_q(s)$. Due to the proportionality between a_{32} and V_0^2, higher speeds are expected to increase the coupling.

We conclude that stability of both subsystems $G_\alpha(s)$ and $G_q(s)$ does not imply stability of (2.1), and simply truncating α may not preserve stability properties of the linear pitch-axis model. Thus, second-order approximations, which are derived by deleting α, may not be reliable for system identification and control design.

2.5 Control Design

In this section, we combine the results from previous sections to illustrate a control design approach that utilizes the second-order approximation (2.5). We derive conditions under which output-feedback gains derived from the second-order approximation ensure that the underlying third-order dynamics are stabilized.

Referring to the state space representation (2.1), we distinguish between the AUV's *pitch* motion defined by the outputs q and θ and the AUV's *heave* motion defined by the output α. It is well known that AUV heave motion is *non-minimum phase*, see [48] and [49], and thus the corresponding transfer function contains a pole and/or a zero in the right half plane. However, a similar statement about the pitch motion is not true in general.

Our control design strategy focuses on the case of stabilizing an unstable plant (2.6). The stability analysis in Section 2.4, in particular the root locus approach in Fig-

ure 2.5, concludes that an unstable plant (2.6) satisfies $a_{32} > 0$. With this assumption, it follows from (2.4) that

$$z_e \;=\; -\frac{\beta_0}{\beta_1} \;=\; a_{22} - a_{32}\frac{b_{21}}{b_{31}} \;<\; 0$$

for a conventional vehicle with $b_{31} < 0$, $b_{21} < 0$ and $a_{22} < 0$. Thus, the zero z_e of the transfer functions (2.3) and (2.6) is located in the open left half plane.

For the control design process, we address output-feedback for the AUV pitch-axis models (2.5) and (2.6) and select output-feedback gains K_p and K_d similar as in [4]. However, for stability analysis, we find it useful to suppose a single output $\theta(s)$. Then, the feedback gains K_p and K_d define a PD-controller transfer function

$$G_c(s) = K_p + sK_d \tag{2.17}$$

recalling $q(s) = s\,\theta(s)$. We choose the feedback law (2.17) over a more general PID-framework that is commonly used for AUV attitude control, see [1], [18] or [39], because PD-control suffices to stabilize the second-order system. Integral control may be added to meet performance criteria, e.g. zero steady-state error and overshoot.

When selecting feedback gains for the second-order model $G_0(s)$ from (2.5), one commonly specifies the natural frequency $\omega_0 > 0$ and the damping coefficient $D > 0$ for the closed-loop system

$$H_2(s) \;=\; \frac{G_c(s)\,G_0(s)}{1 \;+\; G_c(s)\,G_0(s)} \;=\; \frac{n_2(s)}{d_2(s)}$$

Then, the denominator polynomial satisfies

$$\begin{aligned} d_2(s) \;&=\; s^2 + (B_{31}K_d - A_{33})\,s + B_{31}K_p - A_{34} \\ &=\; s^2 + 2D\omega_0 s + \omega_0^2 \end{aligned}$$

and the nominal feedback gains are

$$K_p \;=\; \frac{1}{B_{31}}\left(A_{34} + \omega_0^2\right) \qquad \text{and} \qquad K_d \;=\; \frac{1}{B_{31}}\left(A_{33} + 2D\omega_0\right) \tag{2.18}$$

Since K_p and K_d are chosen exclusively based on a second-order approximation, nothing can be said about whether or not the feedback law $\delta(s) = -G_c(s)\theta(s)$ suffices to stabilize the third-order dynamics. In the following, we augment the nominal feedback gains (2.18) such that closed-loop stability is guaranteed for the underlying third-order plant (2.6). The third-order closed-loop system is

$$H_3(s) \;=\; \frac{G_c(s)\,G_2(s)\,G_e(s)}{1 \;+\; G_c(s)\,G_2(s)\,G_e(s)} \;=\; \frac{n_3(s)}{d_3(s)} \tag{2.19}$$

The following proposition addresses the selection of such feedback gains.

Proposition 2.5.1. *Suppose the second-order approximation satisfies* $|\Delta B_{31}| < |B_{31}|$, *and assume that the truncated mode is stable implying* $p_e < 0$. *For the controller (2.17), let the feedback gains be*

$$K_p \;=\; \frac{1}{B_{31}}\left(A_{34} + \omega_0^2 + \gamma_p\right) \qquad \textit{and} \qquad K_d = \frac{1}{B_{31}}\left(A_{33} + 2D\omega_0 + \gamma_d\right) \tag{2.20}$$

with $\gamma_p > 0$, $\gamma_d > 0$ *and suppose* ω_0 *and* D *are selected to satisfy*

$$D^2 \;>\; \frac{1}{4K_e}\left(1 \;+\; \frac{2\gamma_p}{\omega_0^2}\right) \tag{2.21}$$

where

$$K_e = 1 + \frac{\Delta B_{31}}{B_{31}} \;\in\; (0, 2)$$

Then, the closed-loop system (2.19) consisting of the third-order plant (2.6) and the controller (2.17) is asymptotically stable if

$$\begin{aligned} -z_e K_e \gamma_p \;&>\; |p_e + 2z_e|\,|A_{34}| + |p_e + z_e|\,|\Delta A_{34}| \\ -z_e K_e \gamma_d \;&>\; |p_e + 2z_e|\,|A_{33}| + |p_e + z_e|\,|\Delta A_{33}| \end{aligned} \tag{2.22}$$

In other words, we increase robustness against parameter estimation errors and truncated pitch dynamics by augmenting the nominal feedback gains (2.18) with sufficiently large, positive constants γ_p and γ_d.

Proof of Proposition 2.5.1: Using the assumptions $z_e < 0$ and $p_e < 0$, we divide the inequalities (2.22) by $-z_e > 0$ and note that

$$K_e\,\gamma_p \;>\; 2\,|A_{34}| + |\Delta A_{34}| \qquad \text{and} \qquad K_e\,\gamma_d \;>\; 2\,|A_{33}| + |\Delta A_{33}|$$

Using $\left|\dfrac{\Delta B_{31}}{B_{31}}\right| < 1$, we conclude

$$K_e\,\gamma_p \;>\; \left|\frac{\Delta B_{31}}{B_{31}}\right| |A_{34}| + |\Delta A_{34}| \quad \text{and} \quad K_e\,\gamma_d \;>\; \left|\frac{\Delta B_{31}}{B_{31}}\right| |A_{33}| + |\Delta A_{33}| \tag{2.23}$$

Similarly, we invoke $0 < K_e < 2$ in (2.22), and find that

$$\begin{aligned} -z_e K_e \gamma_p &> |p_e + z_e K_e|\,|A_{34}| + |p_e|\,|\Delta A_{34}| \\ &> |p_e - z_e K_e|\,|A_{34}| + |p_e|\,|\Delta A_{34}| \\ -z_e K_e \gamma_d &> |p_e + z_e K_e|\,|A_{33}| + |p_e|\,|\Delta A_{33}| \\ &> |p_e - z_e K_e|\,|A_{33}| + |p_e|\,|\Delta A_{33}| \end{aligned} \tag{2.24}$$

The denominator polynomial of the closed-loop transfer function $H_3(s)$ from (2.19) is

$$d_3(s) = s^3 + \kappa_2 s^2 + \kappa_1 s + \kappa_0$$

The coefficients $\kappa_i,\ i = 0, 1, 2$ are

$$\begin{aligned} \kappa_2 &= -p_e - (A_{33} + \Delta A_{33}) + (B_{31} + \Delta B_{31})\,K_d \\ \kappa_1 &= p_e\,(A_{33} + \Delta A_{33}) - (A_{34} + \Delta A_{34}) + (B_{31} + \Delta B_{31})\,K_p - z_e\,(B_{31} + \Delta B_{31})\,K_d \\ \kappa_0 &= p_e\,(A_{34} + \Delta A_{34}) - z_e\,(B_{31} + \Delta B_{31})\,K_p \end{aligned} \tag{2.25}$$

Referring to Routh's Stability Criterion [50], all roots of the polynomial $g(s)$ have negative real part if and only if

$$\kappa_i > 0,\ i = 0, 1, 2 \qquad \text{and} \qquad \kappa_2 \kappa_1 > \kappa_0$$

Thus, we substitute K_p and K_d from (2.20) into (2.25) and check the signs of each coefficient κ_i individually. For κ_2, we find

$$\begin{aligned} \kappa_2 &= -p_e - (A_{33} + \Delta A_{33}) + K_e (A_{33} + 2D\omega_0 + \gamma_d) \\ &= -p_e - \Delta A_{33} + \frac{\Delta B_{31}}{B_{31}} A_{33} + K_e (2D\omega_0 + \gamma_d) \end{aligned}$$

Recalling the lower bound for $K_e \gamma_d$ from (2.23), we conclude

$$\kappa_2 > -p_e + K_e 2D\omega_0 > 0 \tag{2.26}$$

For κ_1, we find

$$\begin{aligned} \kappa_1 &= p_e (A_{33} + \Delta A_{33}) - (A_{34} + \Delta A_{34}) + K_e (A_{34} + \omega_0^2 + \gamma_p) \ldots \\ &\qquad -z_e K_e (A_{33} + 2D\omega_0 + \gamma_d) \\ &= (p_e - z_e K_e) A_{33} + p_e \Delta A_{33} - z_e K_e (2D\omega_0 + \gamma_d) + \frac{\Delta B_{31}}{B_{31}} A_{34} \ldots \\ &\qquad -\Delta A_{34} + K_e (\omega_0^2 + \gamma_p) \end{aligned}$$

With the lower bound for $K_e \gamma_p$ from (2.23), we simplify

$$\kappa_1 > (p_e - z_e K_e) A_{33} + p_e \Delta A_{33} - z_e K_e (2D\omega_0 + \gamma_d) + K_e \omega_0^2$$

Invoking the lower bound for $-z_e K_e \gamma_d$ from (2.24), we find

$$\kappa_1 > -z_e K_e 2D\omega_0 + \omega_0^2 > 0 \tag{2.27}$$

For κ_0, we find

$$\begin{aligned} \kappa_0 &= p_e\left(A_{34}+\Delta A_{34}\right) - z_e K_e\left(A_{34}+\omega_0^2+\gamma_p\right) \\ &= \left(p_e - z_e\right)A_{34} + p_e\Delta A_{34} - z_e K_e\left(\omega_0^2+\gamma_p\right) \end{aligned} \tag{2.28}$$

Again, invoking the lower bound for $-z_e K_e \gamma_p$ from (2.24), we conclude

$$\kappa_0 > -z_e K_e \omega_0^2 > 0$$

Finally, it remains to show that $\kappa_2\kappa_1 > \kappa_0$. A lower bound for $\kappa_2\kappa_1$ is found by multiplying (2.26) and (2.27), that is

$$\kappa_2\kappa_1 \;>\; \left(-p_e + K_e 2D\omega_0\right)\left(-z_e K_e 2D\omega_0 + \omega_0^2\right) \;>\; -z_e K_e^2\left(2D\omega_0\right)^2$$

Using the control design requirement (2.21), we rewrite the previous inequality as

$$\kappa_2\kappa_1 > -z_e K_e\left(\omega_0^2 + 2\gamma_p\right) \tag{2.29}$$

We find an upper bound of κ_0 by applying (2.24) to (2.28), that is

$$\begin{aligned} \kappa_0 &= \left(p_e - z_e\right)A_{34} + p_e\Delta A_{34} - z_e\omega_0^2 - z_e\gamma_p \\ &< -z_e K_e\omega_0^2 - z_e K_e 2\gamma_p \end{aligned} \tag{2.30}$$

Combining (2.29) and (2.30), we conclude

$$\kappa_2\kappa_1 > -z_e K_e\left(\omega_0^2 + 2\gamma_p\right) > \kappa_0$$

Thus, all stability criteria are met.

□

For control design purposes, Proposition 2.5.1 can be used to derive stabilizing output-feedback gains based a second-order approximation (2.2). The assumptions in Proposition 2.5.1 include bounds on modeling errors parameterized as coefficient errors ΔA_{33}, ΔA_{34} and ΔB_{31}, as well as signs of real-valued, truncated zero z_e and pole p_e. Using an experimentally identified linear pitch-axis model for the Virginia Tech 475 AUV, we provide insight into the selection of γ_p and γ_d in Section 2.7.

2.6 Experimental Results, System Identification

In this section, we estimate the parameters of a linear second-order and third-order AUV pitch-axis model using real data collected during field trials. The detailed parameter estimation process is presented for the nominal configuration of the Virginia Tech 475 AUV shown in Figure 1.1. Comparing the identified pitch-axis models for the Virginia Tech 475 AUV, we find that the difference between third-order model and second-order approximation is marginal. In addition, we identify and compare third-order and second-order models for two dramatically different payload configurations: the Virginia Tech 475 AUV equipped with a forward-looking sonar, shown in Figure 2.6, and the Virginia Tech 475 AUV equipped with a towed-hydrophone array, shown in Figure 2.7. All field trials are conducted at a constant propeller rate of 2400 rpm which corresponds to a speed of approximately 1.5 ms^{-1}.

We presume the closed loop system illustrated in Figure 2.8 in order to identify the parameters of a generic pitch model Σ. The controller transfer function $\mathbf{K}(s)$ and the commanded pitch angle $\theta_{\text{r}}(t)$ are known, and the collected data set contains the AUV's trajectory $\theta(t)$, $q(t)$ and $\delta(t)$. We simulate the trajectories for pitch angle $\hat{\theta}(t)$, pitch rate $\hat{q}(t)$, and elevator fin deflection $\hat{\delta}(t)$ using the closed loop system from

Figure 2.6: Virginia Tech 475 AUV with an attached Forward Looking Sonar (AUV/FLS configuration).

Figure 2.8. The notation $\hat{\theta}, \hat{q}, \hat{\delta}$ distinguishes the simulated trajectories from the real trajectories θ, q, δ.

Applying a Nelder-Mead Simplex Method [51], we estimate the parameters of the linear pitch model Σ (second or third order) by numerically minimizing the cost function

$$J \;=\; \theta_{\text{rms}} \;+\; \tau\, q_{\text{rms}} \;+\; \delta_{\text{rms}} \tag{2.31}$$

The root-mean-square error q_{rms} is multiplied by $\tau = 1$ second to obtain compatible units. The individual root-mean-square errors are

$$\eta_{\text{rms}} = \sqrt{\frac{1}{T}\int_0^T \|\eta(t) - \hat{\eta}(t)\|^2\, dt}\;, \quad \eta = \theta, q, \delta \tag{2.32}$$

For the data set in Figure 2.9, $T = 180$ seconds.

Case 1: Using a second-order model (2.2) for Σ. The numerical minimization

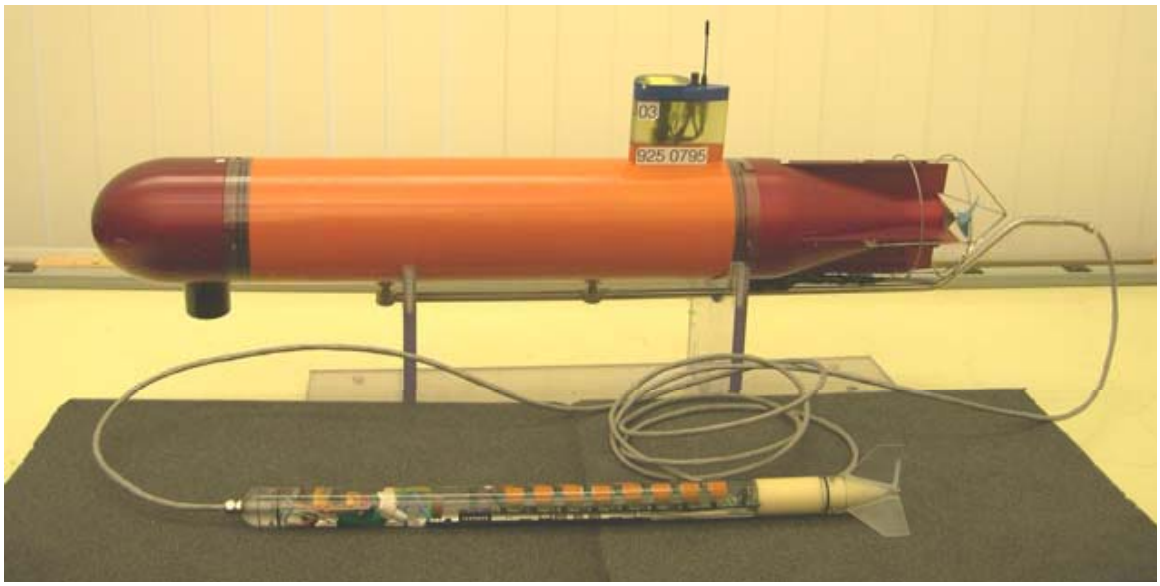

Figure 2.7: Virginia Tech 475 AUV with an attached towed sensor array (AUV/TSA configuration).

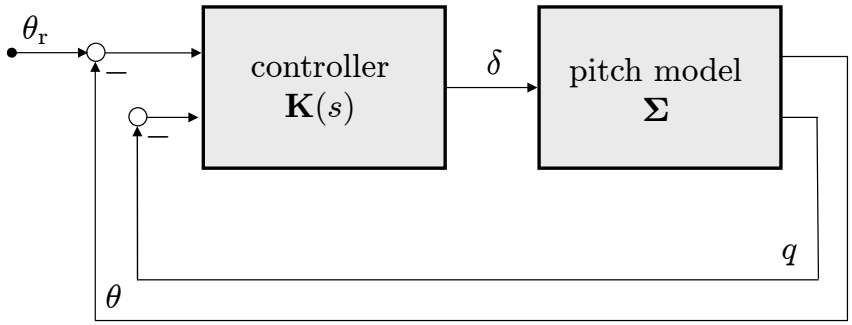

Figure 2.8: Closed loop system consisting of pitch model $\mathbf{\Sigma}$ that is second or third order, a controller transfer function $\mathbf{K}(s)$ and a known commanded pitch angle θ_r.

yields $J = 3.70\,deg$, and the parameter estimates are

$$A_{34} = -0.27, \quad A_{33} = -0.91 \quad \text{and} \quad B_{31} = -1.84 \tag{2.33}$$

Thus, the second-order model (2.2) is

$$\begin{bmatrix} \dot{\hat{q}} \\ \dot{\hat{\theta}} \end{bmatrix} = \begin{bmatrix} -0.91 & -0.27 \\ 1 & 0 \end{bmatrix} \begin{bmatrix} \hat{q} \\ \hat{\theta} \end{bmatrix} + \begin{bmatrix} -1.84 \\ 0 \end{bmatrix} \hat{\delta} \tag{2.34}$$

The associated transfer function $\hat{G}_0(s)$ from (2.5) is

$$\hat{G}_0(s) = \frac{\hat{\theta}(s)}{\hat{\delta}(s)} = \frac{-1.84}{s^2 + 0.91s + 0.27} \tag{2.35}$$

Using the second-order model (2.34), the real and simulated trajectories are plotted in Figure 2.9 in gray and black, respectively. Figure 2.9 shows pitch angle $\theta(t), \hat{\theta}(t)$ in the top plot and elevator fin deflection $\delta(t), \hat{\delta}(t)$ in the bottom plot.

Case 2: Using a third-order model (2.7) for Σ. For a canonical third-order realization, the numerical minimization yields $J = 2.97\,deg$. The associated transfer function $\hat{G}_3(s)$ from (2.3), containing the coefficients $\mathbf{p}_c$, is

$$\hat{G}_3(s) = \frac{\hat{\theta}(s)}{\hat{\delta}(s)} = \frac{-1.35s - 2.77}{s^3 + 2.30s^2 + 1.74s + 0.35} \tag{2.36}$$

The parameters in model (2.7) are deduced by fixing the parameters A_{33}, A_{34} and B_{31} from (2.33) and by incorporating the canonical coefficients $\mathbf{p}_c$ into the parameter identities (2.9). Setting $c_\alpha = 1$, the parameter estimates are

$$p_\alpha = -1.39, \quad a_q = -0.21, \quad a_\theta = 0.03, \quad b_\alpha = -0.89 \quad \text{and} \quad b_\delta = 0.49 \tag{2.37}$$

Thus, the state space model (2.7) is given by

$$\begin{bmatrix} \dot{\hat{x}}_\alpha \\ \dot{\hat{q}} \\ \dot{\hat{\theta}} \end{bmatrix} = \begin{bmatrix} -1.39 & -0.21 & 0.03 \\ 1 & -0.91 & -0.27 \\ 0 & 1 & 0 \end{bmatrix} \begin{bmatrix} \hat{x}_\alpha \\ \hat{q} \\ \hat{\theta} \end{bmatrix} + \begin{bmatrix} -0.89 \\ -1.35 \\ 0 \end{bmatrix} \hat{\delta} \tag{2.38}$$

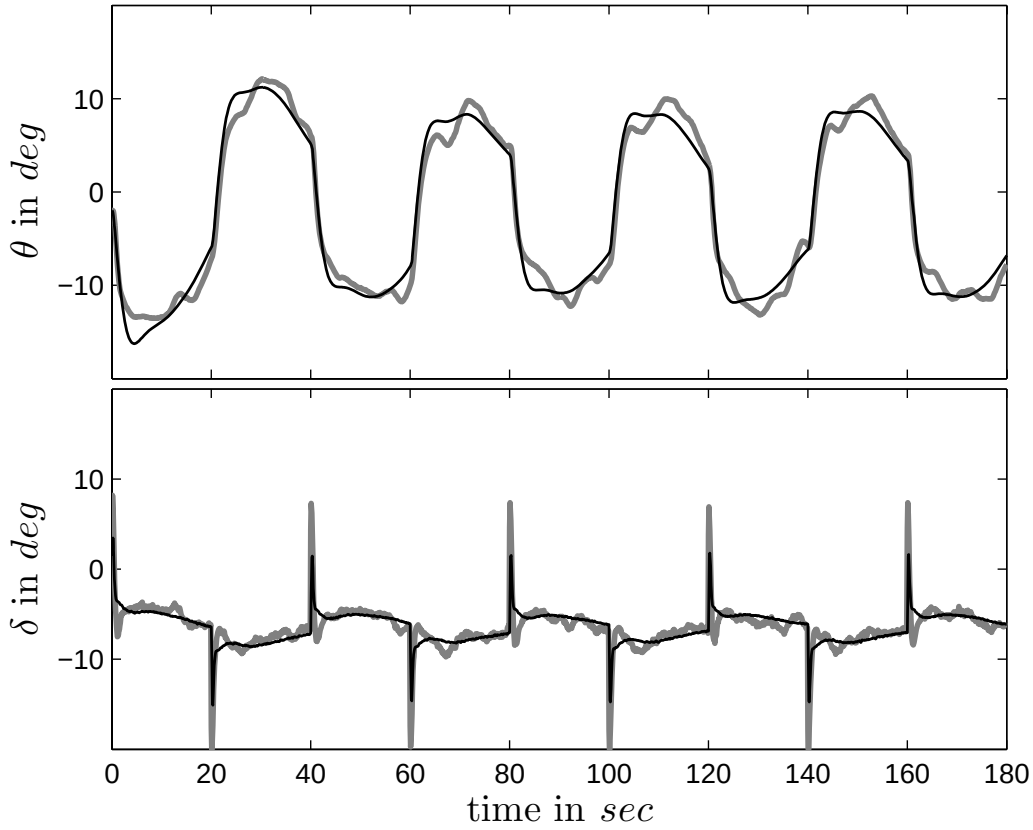

Figure 2.9: Real (gray) versus simulated (black) AUV trajectories using a second-order model. Top: pitch angle $\theta(t), \hat{\theta}(t)$, and bottom: elevator fin deflection $\delta(t), \hat{\delta}(t)$.

Using the third-order model (2.38), the real and simulated trajectories are plotted in Figure 2.10 in gray and black, respectively. Figure 2.10 shows pitch angle $\theta(t), \hat{\theta}(t)$ in the top plot and elevator fin deflection $\delta(t), \hat{\delta}(t)$ in the bottom plot.

Figure 2.9 and Figure 2.10 show that the simulated AUV trajectories are hardly distinguishable between using the second-order model (2.34) and using the third-order model (2.38). For reasons of comparison, we summarize the individual root-mean-square errors (2.32) in Table 2.1. We infer that the numerical fit in the time domain

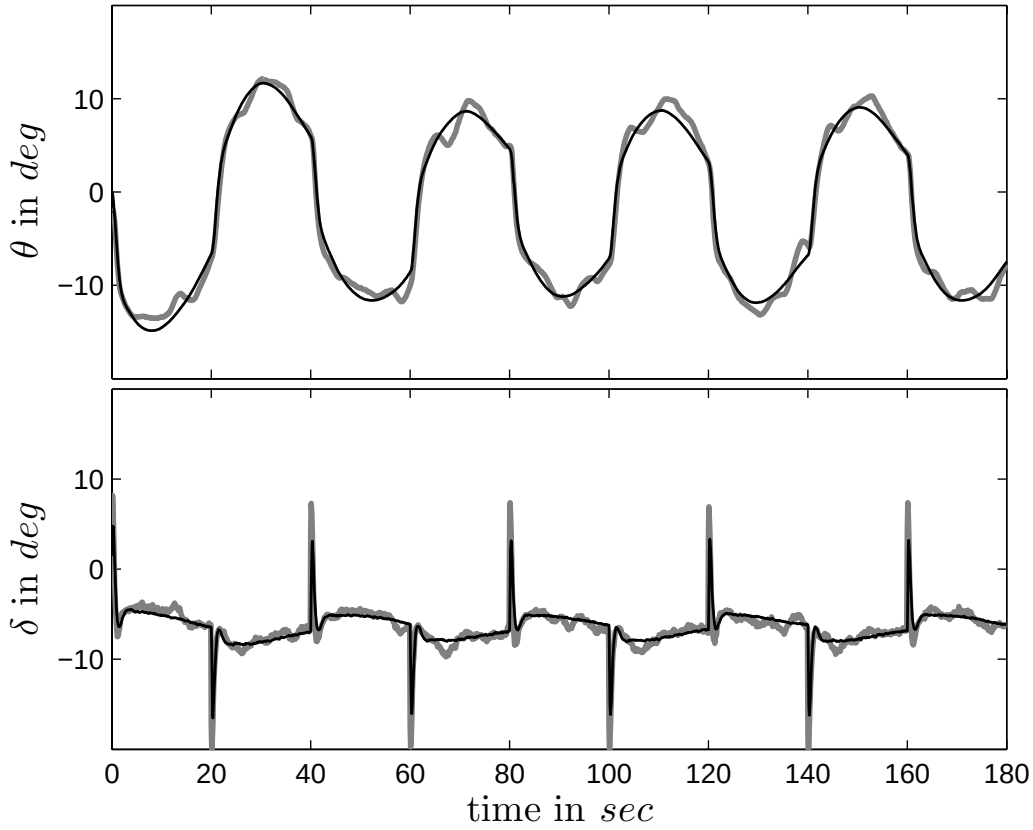

Figure 2.10: Real (gray) versus simulated (black) AUV trajectories using a third-order model. Top: pitch angle $\theta(t), \hat{\theta}(t)$, and bottom: elevator fin deflection $\delta(t), \hat{\delta}(t)$.

barely improves when using a third-order model.

The bode plots and pole-zero plots for the second-order transfer function (2.35) and the third-order transfer function (2.36) are shown in Figure 2.11 in gray and black, respectively.

In the frequency domain, we find in a qualitative sense that a second-order approximation captures the dominating system dynamics with sufficient accuracy, see Figure 2.11. Although, the third-order model contains an additional pole-zero

Table 2.1: System identification RMS errors (2.32) for θ, q and δ.

	second-order model	third-order model
θ_{rms} in deg	1.4172	0.9268
q_{rms} in $deg\ s^{-1}$	0.8977	0.8029
δ_{rms} in deg	1.3857	1.2404
J in deg	3.7006	2.9701

pair (p_e, z_e), the additional mode does not have a significant impact on the input-output behavior of the plant.

In order to quantify the difference between any two transfer functions $P_1(j\omega)$ and $P_2(j\omega)$, we adopt an $\mathcal{L}_2$-error metric

$$\Delta\left(P_1, P_2\right) \;=\; \|P_1 - P_2\|_{\mathcal{L}_2} \;=\; \frac{1}{\pi}\int_0^\infty |P_1(j\omega) - P_2(j\omega)|^2\, d\omega \tag{2.39}$$

For the linear AUV pitch-axis models (2.35) and (2.36), we find $\|\hat{G}_0(s)\|_{\mathcal{L}_2} = 2.62$, $\|\hat{G}_3(s)\|_{\mathcal{L}_2} = 2.68$ and $\Delta(\hat{G}_0, \hat{G}_3) = 0.4244$.

In addition to the nominal AUV configuration, we conduct system identification trials using the AUV/FLS configuration from Figure 2.6 and the AUV/TSA configuration from Figure 2.7. For the AUV/FLS configuration, the cost function J from (2.31) decreases from $4.90\,deg$ when using a second-order model to $4.83\,deg$ when using a third-order model. For the AUV/TSA configuration, the cost function J from (2.31) decreases from $2.50\,deg$ when using a second-order model to $2.37\,deg$ when using a third-order model. Thus, for both AUV/payload configurations the improvement in predicting the AUV's trajectory using a third-order model instead of a second-order model is marginal in the time domain. To evaluate the results in the frequency

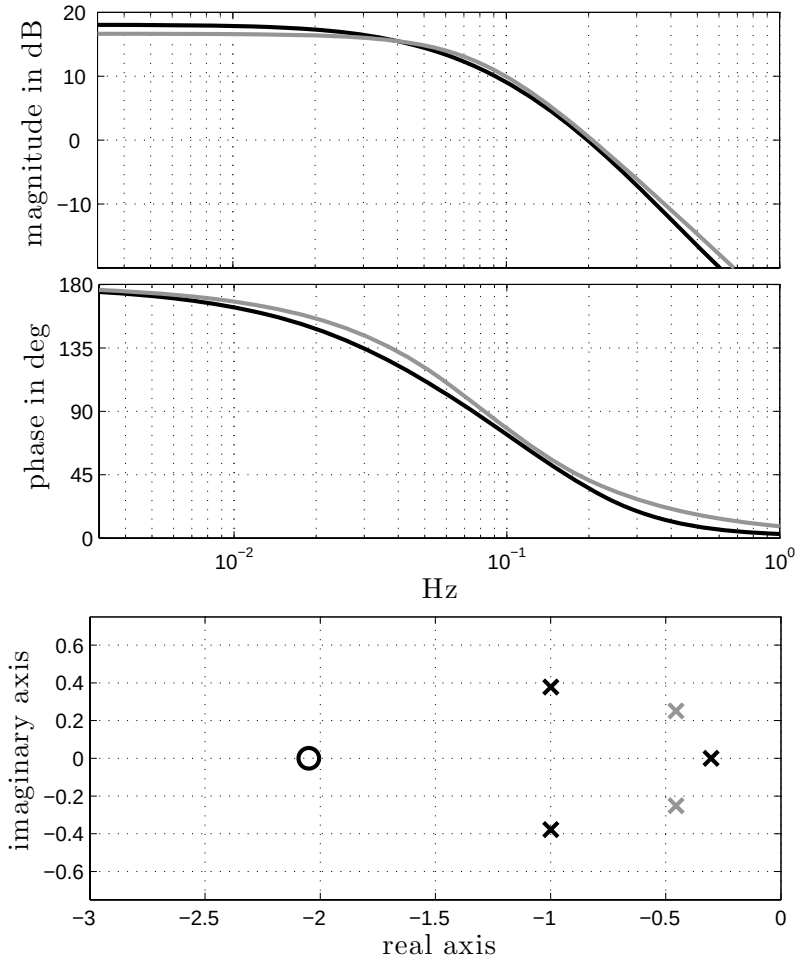

Figure 2.11: Nominal vehicle configuration: Bode plots (upper plots) and pole/zero locations (lower plot) of the second-order pitch model (2.34) in gray and the third-order pitch model (2.38) in black. $\Delta = 0.42$.

domain, we show the bode plots of estimated second-order and third-order models including the associated $\mathcal{L}_2$ error metric Δ in Figure 2.12 for the AUV/FLS configuration and in Figure 2.13 for the AUV/TSA configuration.

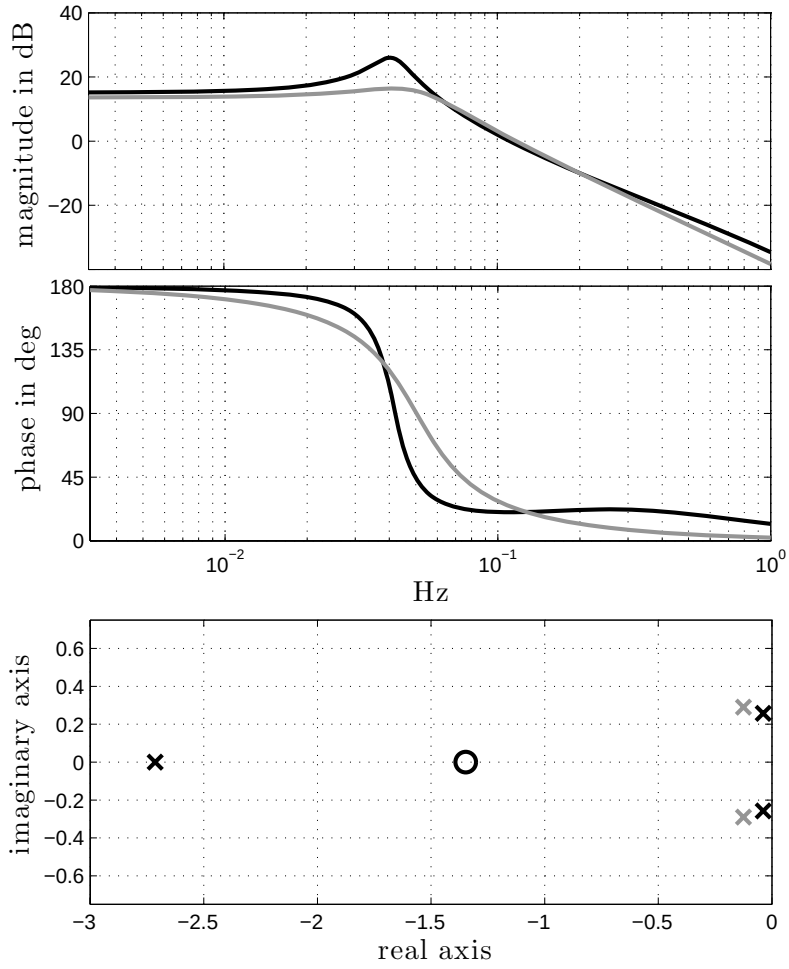

Figure 2.12: Forward Looking Sonar (FLS) vehicle configuration: Bode plots (upper plots) and pole/zero locations (lower plot) of the second-order pitch model (2.34) in gray and the third-order pitch model (2.38) in black. $\Delta = 2.34$.

2.7 Experimental Results, Control Design

In this section, we investigate whether the second-order model (2.34) suffices for designing a controller that guarantees stability for the underlying third-order dynam-

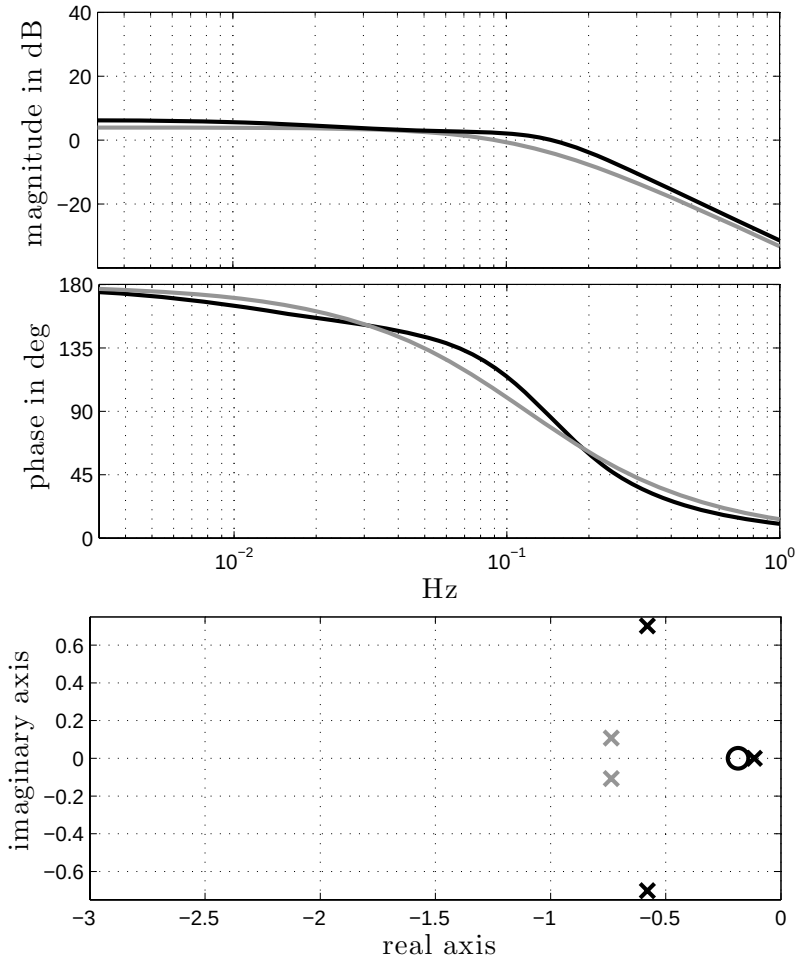

Figure 2.13: Towed sensor array (AUV/TSA) vehicle configuration: Bode plots (upper plots) and pole/zero locations (lower plot) of the second-order pitch model (2.34) in gray and the third-order pitch model (2.38) in black. $\Delta = 0.23$.

ics (2.38). For this reason, we first design a nominal feedback controller (2.18) based on the second-order model. Using the parameter estimates obtained in Section 2.6, we explicitly compute an error model between (2.7) and (2.2), and design a second feedback controller (2.20) using Proposition 2.5.1. Tracking performance and overall

robustness are evaluated for both cases.

For the nominal control design (2.18), we choose

$$\omega_0 = 2\pi f_0, \;\; f_0 = 0.5Hz \qquad \text{and} \qquad D = \frac{1}{\sqrt{2}}$$

and obtain the nominal feedback gains

$$K_p^{(1)} = -5.22 \qquad \text{and} \qquad K_d^{(1)} = -1.91 \tag{2.40}$$

In addition to the nominal controller, we invoke Proposition 2.5.1 and compute additive feedback gains γ_p and γ_d from (2.20), which provides robustness against model uncertainties caused by truncated system dynamics and system identification errors. For this reason, the third-order model (2.6) is populated using the estimated parameters of (2.38) and the parameter equalities (2.8). The parameters of the error model (2.41) are

$$\Delta A_{34} = -0.88, \;\; \Delta A_{33} = -1.09, \;\; \Delta B_{31} = 0.49, \quad p_e = -0.30 \text{ and } z_e = -2.05 \tag{2.41}$$

Invoking Proposition 2.5.1, we find $\gamma_p = 2.17$ and $\gamma_d = 4.37$, and the feedback gains (2.20) become

$$K_p^{(2)} = -6.40 \qquad \text{and} \qquad K_d^{(2)} = -4.28 \tag{2.42}$$

The superscripts $^{(1)}$ and $^{(2)}$ denote the nominal control design approach (2.18) and the robust control design approach (2.20), respectively.

Recalling the controller's transfer function $G_c(s)$ from (2.17), we plot the open-loop transfer functions in Figure 2.14. We use the second-order model $\hat{G}_0(s)$ from (2.35) and show the bode plots of $G_c(s)\hat{G}_0(s)$ in gray, solid for the nominal feedback gains (2.40) and dashed for the robust feedback gains (2.42). Similarly, we use the third-order model $\hat{G}_3(s)$ from (2.36) and show the bode plots of $G_c(s)\hat{G}_3(s)$ in black, solid for the

nominal feedback gains (2.40) and dashed for the robust feedback gains (2.42). For all four cases, phase margins φ_m and required actuator bandwidth f_a are summarized in Table 2.2. The gain margins are infinite.

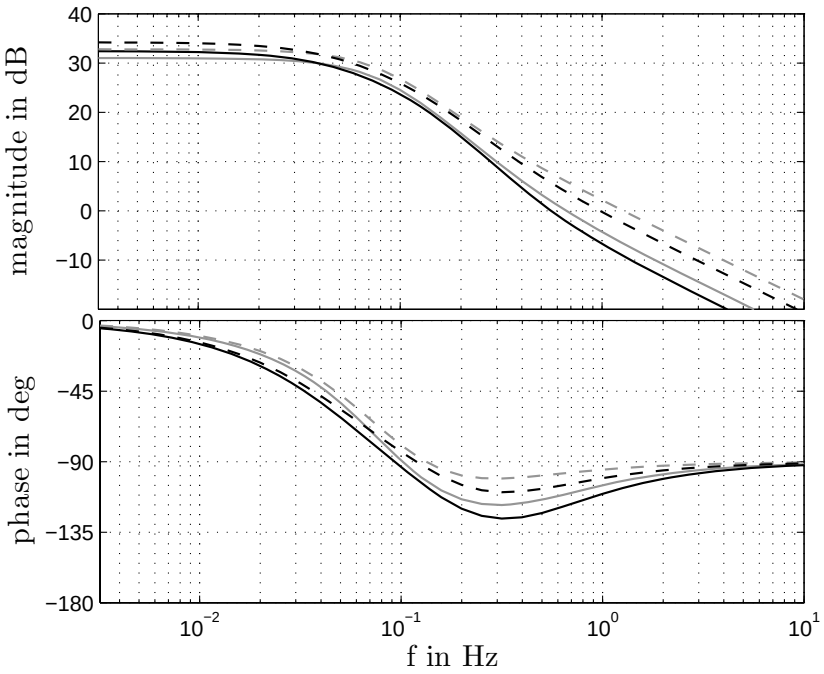

Figure 2.14: Open-loop transfer functions using second-order model (gray) and third order model (black). The bode plots are shown for using nominal feedback gains (2.40) (solid) and robust feedback gains (2.42) (dashed).

For the Virginia Tech 475 AUV, the parameter estimation in Section 2.6 reveals only a small difference between the linear third-order pitch-axis model and the second-order approximation, see Figure 2.11. For this reason, the respective open-loop transfer functions coincide well. In fact, the nominal feedback gains (2.40), chosen based on a second-order model (2.34), already stabilize the underlying third-order dynamics for the particular error model parameters (2.41). Only the phase margin reduces

Table 2.2: Following Figure 2.14: phase margins φ_m and actuator bandwidths f_a.

	second-order model	third-order model
nominal gains (2.40)	(solid gray) $\varphi_m = 69.3\,deg$ $f_a = 0.66\,Hz$	(solid black) $\varphi_m = 58.9\,deg$ $f_a = 0.56\,Hz$
robust gains (2.42)	(dashed gray) $\varphi_m = 85.9\,deg$ $f_a = 1.27\,Hz$	(dashed black) $\varphi_m = 79.2\,deg$ $f_a = 0.97\,Hz$

by $10\,deg$.

From Proposition 2.5.1 follows that the feedback gains (2.42) stabilize the underlying third-order system (2.6) for all $|\Delta A_{34}| \leq 0.88$, $|\Delta A_{33}| \leq 1.09$ and $|\Delta B_{31}| \leq 0.49$. Thus, the feedback gains (2.42) increase robustness as compared to the nominal feedback gains (2.42). We find increased phase margins φ_m visible in Figure 2.14 and listed in Table 2.2. However, the required actuator bandwidth f_a increases as a trade-off between robustness and actuator effort is inevitable.

In order to evaluate the tracking performance, we plot the sensitivity transfer function for all four cases in Figure 2.15. We show the bode plots of $(1+G_c(s)\hat{G}_0(s))^{-1}$ in gray, solid for the nominal feedback gains (2.40) and dashed for the robust feedback gains (2.42). Similarly, we plot $(1+G_c(s)\hat{G}_3(s))^{-1}$ in black, solid for the nominal feedback gains (2.40) and dashed for the robust feedback gains (2.42). Good tracking performance is indicated by small sensitivity magnitude. In Figure 2.15, no significant difference is visible between using a third-order model (black) and a second-

order approximation (gray). However, we find better tracking when using the robust controller (dashed) from (2.42) as compared to using the nominal controller (solid) from (2.40). This is expected since we have increased actuator bandwidth in order to attain increased robustness.

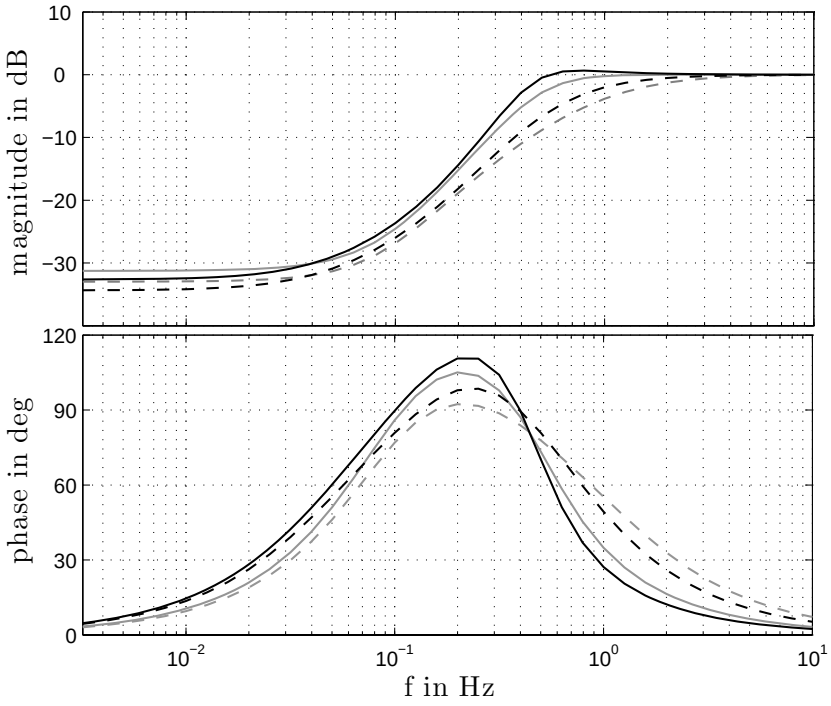

Figure 2.15: Sensitivity transfer function using second-order model (gray) and third order model (black). The bode plots are shown for using nominal feedback gains (2.40) (solid) and robust feedback gains (2.42) (dashed).

2.8 Conclusions

In this chapter, we establish theoretical and practical justification for using linear second-order AUV pitch-axis models for system identification and attitude control design. Our analysis rests on deriving an error model which defines parameter correlations between the true third-order model and the second-order approximation. We are motivated by severe size and weight constraints of miniature AUVs that only allow for limited onboard instrumentation. In particular, we assume that the angle of attack α is not known.

We prove that the physical parameters of a linear third-order model are not identifiable without measuring α. Thus, we show that vehicle parameters such as hydrodynamic coefficients or added mass terms cannot be obtained using online system identification.

We investigate stability of a streamlined AUV and show that truncating the state α always yields a stable second-order model. However, rigorous stability analysis shows that the underlying third-order dynamics may very well be unstable. Thus naive truncation of a state may yield incorrect results.

Field trials are an important component of our work. We use standard system identification techniques to identify the parameters of a second-order pitch-axis model as well as the coefficients of a canonical third-order realization for three different AUV configurations, and we show that a third-order model yields negligible improvement over a second-order approximation in predicting pitch-axis motion.

With our analysis and field trials, we show that second-order models are often adequate for modeling the pitch-axis motion of streamlined AUVs. In Chapter 3, we present online system identification techniques for such a second-order approximate pitch-axis model.

Chapter 3

Identification Techniques

In this chapter, we present the theoretical framework for parameter identification and conduct field experiments to validate our results. We derive algorithms that rely on available sensor and control signals in order to estimate the parameters of the vehicle's linear heave model (A.20)

$$\dot{Z} = -V_0 \left[\theta - \alpha_0\right] = -V_0 \Delta\theta \tag{3.1}$$

and the linear pitch model (A.23)

$$\begin{bmatrix} \dot{q} \\ \Delta\dot{\theta} \end{bmatrix} = \begin{bmatrix} A_{33} & A_{34} \\ 1 & 0 \end{bmatrix} \begin{bmatrix} q \\ \Delta\theta \end{bmatrix} + \begin{bmatrix} B_{31} \\ 0 \end{bmatrix} (\delta - \delta_0) \tag{3.2}$$

Note, as compared to (A.23), the state $\Delta\theta = \theta - \theta_0$ is defined to accommodate for a small nonzero steady state angle of attack during steady state flight.

For both models, the input signals θ and δ are known and all states are measured. Several techniques for identifying the system parameters of (3.1) and (3.2) are introduced: an adaptive identifier, a Kalman filter, and a standard least squares approach. Sufficient conditions for parameter convergence are deduced in terms of

excitation properties for the measured signals. For the remainder of this chapter, we resume the notation (t) to emphasize time dependencies.

By defining a regressor matrix $\mathbf{W}_Z^T(t) = [\theta(t)\ 1] \in \mathbb{R}^{1\times 2}$, we can express the heave kinematics (3.1) as

$$\begin{aligned} \dot{\mathbf{x}}_Z(t) &= \mathbf{A}_Z\mathbf{x}_Z(t) + \mathbf{W}_Z^T(t)\mathbf{p}_Z \\ \mathbf{y}_Z(t) &= \mathbf{x}_Z(t) \end{aligned} \tag{3.3}$$

where the state is $\mathbf{x}_Z(t) = Z(t) \in \mathbb{R}$, the system matrix is $\mathbf{A}_Z = 0 \in \mathbb{R}$, and the parameter vector is $\mathbf{p}_z = [-V_0,\ \gamma_Z]^T \in \mathbb{R}^2$ with $\gamma_Z = V_0\alpha_0$. Similarly, the linear pitch model (3.2) can be expressed

$$\begin{aligned} \dot{\mathbf{x}}_\theta(t) &= \mathbf{A}_\theta\mathbf{x}_\theta(t) + \mathbf{W}_\theta^T(t)\mathbf{p}_\theta \\ \mathbf{y}_\theta(t) &= \mathbf{x}_\theta(t) \end{aligned} \tag{3.4}$$

where the state vector is $\mathbf{x}_\theta(t) = [q(t)\ \Delta\theta(t)]^T \in \mathbb{R}^2$, and the vector of lumped parameters is $\mathbf{p}_\theta = [A_{33},\ A_{34},\ B_{31},\ \gamma_\theta]^T \in \mathbb{R}^4$ with $\gamma_\theta = -B_{31}\delta_0$. The regressor matrix $\mathbf{W}_\theta^T(t) \in \mathbb{R}^{2\times 4}$ and the system matrix $\mathbf{A}_\theta \in \mathbb{R}^{2\times 2}$ are

$$\mathbf{W}_\theta^T(t) = \begin{bmatrix} q(t) & \Delta\theta(t) & \delta(t) & 1 \\ 0 & 0 & 0 & 0 \end{bmatrix} \qquad \text{and} \qquad \mathbf{A}_\theta = \begin{bmatrix} 0 & 0 \\ 1 & 0 \end{bmatrix}$$

Due to the structural similarity between pitch and heave model, we introduce the basic concepts of parameter identification by addressing the pitch dynamics (3.4) containing the parameter vector $\mathbf{p}_\theta$. Identification schemes derived for an adaptive identifier or a linear state observer can easily be adapted to the kinematic heave model (3.3) and the identification of the parameter vector $\mathbf{p}_Z$.

Given the nature of the plant, we assume continuity and boundedness of $q(t)$ and $\theta(t)$. That is

$$|q(t)| \leq q_{max} \qquad \text{and} \qquad |\theta(t)| \leq \theta_{max} \tag{3.5}$$

for all t. The bounds in (3.5) imply that $|\Delta\theta(t)| \leq \theta_{max} + |\alpha_0|$ for all t. The elevator fin deflection is mechanically limited to $|\delta(t)| \leq \delta_{max}$ for all t. Although data collection and attitude control is implemented digitally in discrete time, our analysis assumes continuous-time, which is justified by the relatively high sampling frequency.

3.1 Adaptive Identification Algorithm

We present a Lyapunov-based approach to derive an adaptive identification algorithm intended to estimate the system parameters of the linear pitch model (3.4). Under the assumption that a true, constant parameter vector $\mathbf{p}_\theta$ exists, we define the state and parameter estimation errors $\tilde{\mathbf{x}}_\theta(t)$ and $\tilde{\mathbf{p}}_\theta(t)$ with their respective time derivatives $\dot{\tilde{\mathbf{x}}}_\theta(t)$ and $\dot{\tilde{\mathbf{p}}}_\theta(t)$

$$\begin{aligned} \tilde{\mathbf{x}}_\theta(t) &= \hat{\mathbf{x}}_\theta(t) - \mathbf{x}_\theta(t), \quad \tilde{\mathbf{p}}_\theta(t) &= \hat{\mathbf{p}}_\theta(t) - \mathbf{p}_\theta \\ \dot{\tilde{\mathbf{x}}}_\theta(t) &= \dot{\hat{\mathbf{x}}}_\theta(t) - \dot{\mathbf{x}}_\theta(t), \quad \dot{\tilde{\mathbf{p}}}_\theta(t) &= \dot{\hat{\mathbf{p}}}_\theta(t) \end{aligned} \tag{3.6}$$

The vectors $\hat{\mathbf{x}}_\theta(t)$ and $\hat{\mathbf{p}}_\theta(t)$ denote the estimates of $\mathbf{x}_\theta(t)$ and $\mathbf{p}_\theta$, respectively. In order to track the plant's measured trajectory $\mathbf{x}_\theta(t)$, the state estimate $\hat{\mathbf{x}}_\theta(t)$ is propagated as suggested in [42]

$$\dot{\hat{\mathbf{x}}}_\theta(t) = \mathbf{A}_\theta \hat{\mathbf{x}}_\theta(t) + \mathbf{W}_\theta^T(t)\hat{\mathbf{p}}_\theta(t) + \mathbf{K}_\theta \tilde{\mathbf{x}}_\theta(t) \tag{3.7}$$

The state equation for the state estimation error $\tilde{\mathbf{x}}_\theta(t)$ can be expressed

$$\begin{aligned} \dot{\tilde{\mathbf{x}}}_\theta(t) &= \dot{\hat{\mathbf{x}}}_\theta(t) - \dot{\mathbf{x}}_\theta(t) \\ &= [\mathbf{A}_\theta + \mathbf{K}_\theta]\, \tilde{\mathbf{x}}_\theta(t) + \mathbf{W}_\theta^T(t)\tilde{\mathbf{p}}_\theta(t) \end{aligned} \tag{3.8}$$

The matrix $\mathbf{K}_\theta \in \mathbb{R}^{2\times 2}$ is chosen such that $\mathbf{A}_\theta + \mathbf{K}_\theta$ is Hurwitz, which ensures internal stability

$$\lim_{t\to\infty} \|\tilde{\mathbf{x}}_\theta(t)\| = 0 \tag{3.9}$$

The matrix $\mathbf{A}_\theta + \mathbf{K}_\theta$ is often referred to as reference matrix, and its eigenvalues determine the convergence rate of (3.9). Thus, the matrix $\mathbf{K}_\theta$ can be selected to change the response to initial conditions of (3.8) and the performance of the identifier.

To show convergence of the state estimation error (3.9) using methods from [52], we propose a Lyapunov function candidate

$$\Psi(\tilde{\mathbf{x}}_\theta(t), \tilde{\mathbf{p}}_\theta(t)) \;=\; \tilde{\mathbf{x}}_\theta^T(t)\,\mathbf{P}\,\tilde{\mathbf{x}}_\theta(t) + \tilde{\mathbf{p}}_\theta^T(t)\,\mathbf{\Gamma}^{-1}\,\tilde{\mathbf{p}}_\theta(t) \;\geq\; 0 \tag{3.10}$$

with the symmetric positive-definite matrices $\mathbf{\Gamma} = \mathbf{\Gamma}^T > 0$, $\mathbf{\Gamma} \in \mathbb{R}^{4\times4}$ and $\mathbf{P} = \mathbf{P}^T > 0$, $\mathbf{P} \in \mathbb{R}^{2\times2}$. The matrix $\mathbf{P}$ satisfies the Lyapunov equation [53]

$$\mathbf{P}\;[\mathbf{A}_\theta + \mathbf{K}_\theta] \;+\; [\mathbf{A}_\theta + \mathbf{K}_\theta]^T\;\mathbf{P} \;=\; -\,\mathbf{Q} \tag{3.11}$$

with $\mathbf{Q} = \mathbf{Q}^T > 0$. The time-derivative $\dot{\Psi}(\tilde{\mathbf{x}}_\theta, \tilde{\mathbf{p}}_\theta)$ is computed by substituting $\dot{\tilde{\mathbf{x}}}_\theta(t)$ using the state update equation (3.8)

$$\begin{aligned}
\dot{\Psi}(\tilde{\mathbf{x}}_\theta(t), \tilde{\mathbf{p}}_\theta(t)) \;&=\; \tilde{\mathbf{x}}_\theta^T(t)\,\mathbf{P}\,\dot{\tilde{\mathbf{x}}}_\theta(t) + \dot{\tilde{\mathbf{x}}}_\theta^T(t)\,\mathbf{P}\,\tilde{\mathbf{x}}_\theta(t) + 2\,\tilde{\mathbf{p}}_\theta^T(t)\mathbf{\Gamma}^{-1}\dot{\tilde{\mathbf{p}}}_\theta(t) \\
&=\; \tilde{\mathbf{x}}_\theta^T(t)\,\Big[\mathbf{P}\;(\mathbf{K}_\theta + \mathbf{A}_\theta) \;+\; (\mathbf{K}_\theta + \mathbf{A}_\theta)^T\;\mathbf{P}\Big]\;\tilde{\mathbf{x}}_\theta(t) \\
&\qquad +2\,\tilde{\mathbf{p}}_\theta^T(t)\,\mathbf{W}_\theta(t)\mathbf{P}\,\tilde{\mathbf{x}}_\theta(t) + 2\,\tilde{\mathbf{p}}_\theta^T(t)\mathbf{\Gamma}^{-1}\dot{\tilde{\mathbf{p}}}_\theta(t)
\end{aligned} \tag{3.12}$$

The update law for the parameter estimates is chosen as

$$\dot{\tilde{\mathbf{p}}}_\theta(t) = \dot{\hat{\mathbf{p}}}_\theta(t) = -\mathbf{\Gamma}\,\mathbf{W}_\theta(t)\,\mathbf{P}\,\tilde{\mathbf{x}}_\theta(t) \tag{3.13}$$

which yields a negative semi-definite time derivative (3.12). Combining (3.8) and (3.13), the augmented system containing state estimation error and parameter estimation error becomes

$$\begin{bmatrix} \dot{\tilde{\mathbf{x}}}_\theta(t) \\ \dot{\tilde{\mathbf{p}}}_\theta(t) \end{bmatrix} = \begin{bmatrix} \mathbf{K}_\theta + \mathbf{A}_\theta & \mathbf{W}_\theta^T(t) \\ -\mathbf{\Gamma}\,\mathbf{W}_\theta(t)\mathbf{P} & \mathbf{0}_{4\times4} \end{bmatrix} \begin{bmatrix} \tilde{\mathbf{x}}_\theta(t) \\ \tilde{\mathbf{p}}_\theta(t) \end{bmatrix} \tag{3.14}$$

where $\mathbf{0}$ represents an empty matrix of dimension denoted by the subscript.

Straightforward computation regarding the Lyapunov equation (3.11) and the parameter update law (3.13) verifies negative semi-definiteness of

$$\dot{\Psi}(\tilde{\mathbf{x}}_\theta(t), \tilde{\mathbf{p}}_\theta(t)) = -\,\tilde{\mathbf{x}}_\theta^T(t)\,\mathbf{Q}\,\tilde{\mathbf{x}}_\theta(t)$$

For all $\tilde{\mathbf{x}}_\theta(t) \neq \mathbf{0}$, strict inequality $\dot{\Psi}(\tilde{\mathbf{x}}_\theta(t), \tilde{\mathbf{p}}_\theta(t)) < 0$ holds. Thus, Lyapunov's stability Theorem [54] guarantees both asymptotic stability of the state estimation error $\tilde{\mathbf{x}}_\theta(t)$ as stated in (3.9) and boundedness of the parameter estimation error $\tilde{\mathbf{p}}_\theta(t)$. From (3.14) follows boundedness of $\dot{\tilde{\mathbf{x}}}_\theta(t)$ implying boundedness of $\ddot{\Psi}$ where

$$\ddot{\Psi}(\tilde{\mathbf{x}}_\theta(t), \tilde{\mathbf{p}}_\theta(t)) = -2\,\tilde{\mathbf{x}}_\theta^T(t)\,\mathbf{Q}\,\dot{\tilde{\mathbf{x}}}_\theta(t)$$

Hence, we find uniform continuity for the time derivative $\dot{\Psi}(\tilde{\mathbf{x}}_\theta(t), \tilde{\mathbf{p}}_\theta(t))$ and conclude

$$\lim_{t\to\infty} \dot{\tilde{\mathbf{x}}}_\theta(t) = \mathbf{0} \tag{3.15}$$

from Barbalat's Lemma [54].

Since the state estimation error $\tilde{\mathbf{x}}_\theta(t)$ converges to zero, the parameter update law (3.13) implies

$$\lim_{t\to\infty} \dot{\tilde{\mathbf{p}}}_\theta(t) = \mathbf{0} \tag{3.16}$$

However, parameter error convergence

$$\lim_{t\to\infty} \tilde{\mathbf{p}}_\theta(t) = \mathbf{0}$$

does not follow immediately. Sufficient conditions for parameter errors convergence are well known and are introduced in [55] referring to the notion of persistence of excitation.

Definition 3.1.1 (Persistence of Excitation)**.** *The signal $\nu(t)$ is said to be persistently exciting (PE) if there exist positive constants η and T such that for any $t > 0$*

$$\int_t^{t+T} \nu^T(s)\nu(s)ds \geq \eta\mathbf{I} \tag{3.17}$$

where $\mathbf{I}$ *is the identity matrix.*

For adaptive control and parameter identification of single-input single-output systems, persistence of excitation resembles a sufficient condition for parameter error convergence [52]. To guarantee parameter convergence addressing the multi-output system (3.4), the PE condition extends to the matrix valued regressor function $\mathbf{W}_\theta^T(t)$, as stated in the following proposition.

Proposition 3.1.2. *The adaptive identifier, given by the update laws (3.7) and (3.13) for state and parameter estimates, guarantees parameter error convergence*

$$\lim_{t\to\infty} \tilde{\mathbf{p}}_\theta(t) = 0 \tag{3.18}$$

for the system (3.4) if

$$\mathbf{W}_\theta^T(t) = \begin{bmatrix} q(t) & \Delta\theta(t) & \delta(t) & 1 \\ 0 & 0 & 0 & 0 \end{bmatrix}$$

is persistently exciting.

A proof of Proposition 3.1.2 is presented in Appendix B.1.

From the observation in this section, an adaptive identification algorithm is expected to track the states of the system (3.4). Moreover, if the vehicle's attitude $q(t)$, $\Delta\theta(t)$ and the commanded fin deflection $\delta(t)$ span a persistently exciting regressor matrix $\mathbf{W}_\theta^T(t)$, then the parameter estimation error converges to zero as t approaches infinity.

3.2 Linear State Observer

In this section, we emphasize structural similarities between the adaptive identifier from Section 3.1 and a classical, linear state observer [56]. We show equivalence of ex-

citation conditions for parameter error convergence for either identification technique and present parameter identification using a Kalman filter.

A common way to apply linear state observers for parameter identification is to augment the state vector merging system states and parameters. For the model representation (3.4), this method yields a linear time-varying system

$$\begin{aligned} \dot{\xi}(t) &= \mathbf{A}(t)\,\xi(t) \\ \mathbf{y}(t) &= \mathbf{C}\,\xi(t) \end{aligned} \tag{3.19}$$

with the augmented state vector $\xi(t) = [\mathbf{x}_\theta^T(t),\, \mathbf{p}_\theta^T]^T$, $\xi(t) \in \mathbb{R}^6$ and

$$\mathbf{A}(t) = \begin{bmatrix} \mathbf{A}_\theta & \mathbf{W}_\theta^T(t) \\ \mathbf{0}_{4\times 2} & \mathbf{0}_{4\times 4} \end{bmatrix} \qquad \text{and} \qquad \mathbf{C} = \begin{bmatrix} \mathbf{I}_{2\times 2} & \mathbf{0}_{2\times 4} \end{bmatrix}$$

where $\mathbf{I}$ and $\mathbf{0}$ indicate identity and empty matrices with dimension denoted by the subscripts. Note, we treat the measured vehicle trajectory $q(t)$, $\Delta\theta(t)$ and the commanded elevator fin deflection $\delta(t)$ contained in the regressor matrix $\mathbf{W}_\theta^T(t)$ as known time-varying elements in the system matrix $\mathbf{A}(t)$.

We introduce the state estimate $\hat{\xi}(t)$ satisfying the update equation

$$\dot{\hat{\xi}}(t) = \mathbf{A}(t)\,\hat{\xi}(t) - \mathbf{H}(t)\,\mathbf{C}\,\tilde{\xi}(t) \tag{3.20}$$

containing the time-varying observer gain matrix $\mathbf{H}(t)$ and the state estimation error $\tilde{\xi}(t)$ defined by $\tilde{\xi}(t) = \hat{\xi}(t) - \xi(t)$. By choosing an observer gain matrix

$$\mathbf{H}(t) = \begin{bmatrix} -\mathbf{K}_\theta \\ \mathbf{\Gamma}\,\mathbf{W}_\theta(t)\mathbf{P} \end{bmatrix} \qquad \in \mathbb{R}^{6\times 2} \tag{3.21}$$

we can verified that the estimation error system

$$\dot{\tilde{\xi}}(t) = [\mathbf{A}(t) - \mathbf{H}(t)\,\mathbf{C}]\,\tilde{\xi}(t)$$

equals the system (3.14) resulting from an adaptive identification approach. Therefore, given the observer gain (3.21), the time-varying linear state observer can be interpreted as adaptive identifier and vice versa.

Convergence of the estimation error of the parameter vector $\mathbf{p}_\theta$ using a linear observer requires uniform observability of the system (3.19), see [57]. Due to the similarity between the adaptive identifier from Section 3.1 and a linear state observer (3.21), the PE property of the regressor matrix $\mathbf{W}_\theta^T(t)$ is expected to determine uniform observability of (3.19). The definition for uniform observability is taken from [56], and the observability analysis for the linear system (3.19) is summarized in the sequel.

Definition 3.2.1 (Uniform Observability)**.** *The linear system* $[\mathbf{A}(t), \mathbf{C}(t)]$ *is uniformly observable if and only if there exist positive constants* T, α_1 *and* α_2 *such that*

$$\mathbf{0} < \alpha_1 \mathbf{I} \leq \mathbf{M}(t, t+T) \leq \alpha_2 \mathbf{I}$$

for all t, *where* $\mathbf{I}$ *is the identity matrix and* $\mathbf{M}(t, t+T)$ *denotes the observability gramian*

$$\mathbf{M}(t, t+T) = \int_t^{t+T} \mathbf{\Phi}^T(\sigma, t)\mathbf{C}^T(\sigma)\mathbf{C}(\sigma)\mathbf{\Phi}(\sigma, t)d\sigma \tag{3.22}$$

containing the transition matrix $\mathbf{\Phi}(t, t_0)$ *associated with* $\mathbf{A}(t)$.

The following proposition refers to the PE condition in order to guarantee uniform observability of (3.19).

Proposition 3.2.2. *The system (3.19) is uniformly observable if and only if the regressor matrix*

$$\mathbf{W}_\theta^T(t) = \begin{bmatrix} q(t) & \Delta\theta(t) & \delta(t) & 1 \\ 0 & 0 & 0 & 0 \end{bmatrix}$$

is persistently exciting.

Proof: We first note that a set of states, the vehicle's dive trajectory $\mathbf{x}_\theta(t)$, is directly measured, and therefore observable. For this reason, we truncate $\mathbf{x}_\theta(t)$ and assess observability of (3.19) through a reduced order system as presented in [29]. The reduced order system is

$$\begin{aligned} \dot{\xi}_r(t) &= \mathbf{A}_r(t)\,\xi_r(t) \\ \mathbf{y}_r(t) &= \mathbf{C}_r(t)\,\xi_r(t) \end{aligned}$$

containing the state vector $\xi_r(t) = \mathbf{p}_\theta$ with $\dot{\xi}_r(t) = \mathbf{0}$. The reduced order system matrix becomes $\mathbf{A}_r(t) = \mathbf{0}_{4\times4}$, and the output matrix is $\mathbf{C}_r(t) = \mathbf{W}_\theta^T(t)$.

By Theorems 2.1 and 2.2 in [56], the reduced order, linear time-varying system $[\mathbf{A}_r(t),\ \mathbf{C}_r(t)]$ suffices to investigate uniform observability of the pair $[\mathbf{A}(t),\ \mathbf{C}]$. The transition matrix associated with $\mathbf{A}_r(t)$ is $\mathbf{\Phi}_r(t, t_0) = \mathbf{I}_{4\times4}$ and the observability gramian (3.22) for the pair $[\mathbf{A}_r(t),\ \mathbf{C}_r(t)]$ becomes

$$\mathbf{M}_r(t, t+T) = \int_t^{t+T} \mathbf{W}_\theta(\sigma)\,\mathbf{W}_\theta^T(\sigma)d\sigma$$

It is evident that $\mathbf{M}_r(t, t+T) \in \mathbb{R}^{4\times4}$ is full rank for all t if and only if the matrix $\mathbf{W}_\theta^T(t)$ satisfies the PE condition from Definition 3.1.1 for some $T > 0$. In other words, a persistently exciting signal $\mathbf{W}_\theta^T(t)$ is necessary and sufficient to span a full rank observability gramian $\mathbf{M}_r(t, t+T)$ for every sliding time interval $[t, t+T]$.

An upper bound α_2 for $\mathbf{M}_r(t, t+T)$ follows immediately from the boundedness of the elements in the regressor matrix as stated in (3.5).

□

Propositions 3.1.2 and 3.2.2 illustrate the importance of the PE condition for successful parameter identification using either an adaptive identifier or a linear state

observer. A Kalman filter [58], most commonly used among all state observers, is implemented for the update equation (3.19) in discrete time

$$\begin{aligned} \xi(k+1) &= \mathbf{A}(k)\xi(k) + \mathbf{w}(k) \\ \mathbf{y}_\theta(k) &= \mathbf{C}\xi(k) + \mathbf{v}(k) \end{aligned} \tag{3.23}$$

where

$$\mathbf{A}(k) = \begin{bmatrix} \mathbf{I}_{2\times 2} + h\mathbf{A}_\theta & \mathbf{W}_\theta^T(k)h \\ \mathbf{0}_{4\times 2} & \mathbf{I}_{4\times 4} \end{bmatrix}$$

The sample period is denoted by h. The process and measurement noise $\mathbf{w}(k) \in \mathbb{R}^6$ and $\mathbf{v}(k) \in \mathbb{R}^2$ are assumed to be white Gaussian with the respective known covariance matrices $\mathbf{U} \in \mathbb{R}^{6\times 6}$ and $\mathbf{V} \in \mathbb{R}^{2\times 2}$.

3.3 PE Conditions for AUV Trajectory

Having established a sufficient condition for parameter convergence, it is helpful in a practical sense to express persistence of excitation directly in terms of sensor signals. For example, the following proposition states a PE condition for the heave system's regressor matrix $\mathbf{W}_Z^T(t) = [\theta(t)\ 1]$ with respect to the vehicles pitch angle $\theta(t)$.

Proposition 3.3.1. *The signal* $\mathbf{W}_Z^T(t) = [\theta(t)\ 1]$ *is* <u>*not*</u> *persistently exciting if and only if there exists a time* t_c *such that*

$$\dot{\theta}(t) = 0 \qquad \textit{for all} \qquad t > t_c$$

Proof of Proposition 3.3.1 : First, suppose $\mathbf{W}_Z^T(t)$ is not PE. Then, there exists a t such that no finite time interval $[t,\ t+T]$ meets the PE condition (3.17). In other

words, there exist a t_c such that the positive semi-definite matrix

$$\begin{aligned}\boldsymbol{\Xi}(t) &= \lim_{T\to\infty}\int_t^{t+T}\begin{bmatrix}\theta(\sigma)\\ 1\end{bmatrix}\begin{bmatrix}\theta(\sigma) & 1\end{bmatrix}d\sigma \\ &= \int_t^{\infty}\begin{bmatrix}\theta(\sigma)\\ 1\end{bmatrix}\begin{bmatrix}\theta(\sigma) & 1\end{bmatrix}d\sigma\end{aligned}$$

remains rank deficient for all $t > t_c$. Hence, there exist a constant vector $\mathbf{s} \in \mathbb{R}^2$ satisfying $\mathbf{s} \neq \mathbf{0}$ such that

$$\mathbf{s}^T\,\boldsymbol{\Xi}(t)\,\mathbf{s} = 0 \qquad \text{for all} \qquad t > t_c$$

From the positive semi-definiteness of the integrand, it follows that

$$\begin{bmatrix}\theta(t) & 1\end{bmatrix}\mathbf{s} = 0 \qquad \text{for all} \qquad t > t_c$$

Therefore $\theta(t)$ is constant and $\dot{\theta}(t) = 0$ for all $t > t_c$.

Now suppose $\dot{\theta}(t) = 0$ or equivalently $\theta(t) = \theta_c$ for all $t > t_c$. Clearly, computing (3.17) for $t > t_c$ yields a rank deficiency for every finite $T > 0$ and hence a failure of the PE condition.

□

Proposition 3.3.1 suggests that trajectories other than steady state flight should be selected for successful parameter identification of the AUV's heave model (3.1). With the identification of the vehicle's pitch model in mind, it is interesting to show that the PE condition applies equivalently to both the open loop system (3.2) and to a closed loop system. For the closed loop system, we use state feedback

$$\delta(t) \;=\; K_{\theta,P}\,\left[\Delta\theta_{\text{ref}}(t) - \Delta\theta(t)\right] \;-\; K_{\theta,D}\,q(t) \qquad \text{with} \qquad K_{\theta,P} \neq 0 \tag{3.24}$$

Proposition 3.3.2. *Suppose the feedback law (3.24) is applied to the system (3.2) and assume that the reference signal $\Delta\theta_{ref}(t)$ is chosen such that*

$$\tilde{\mathbf{W}}_\theta^T(t) = \begin{bmatrix} q(t) & \Delta\theta(t) & \Delta\theta_{ref}(t) & 1 \\ 0 & 0 & 0 & 0 \end{bmatrix}$$

is persistently exciting, then the regressor matrix

$$\mathbf{W}_\theta^T(t) = \begin{bmatrix} q(t) & \Delta\theta(t) & \delta(t) & 1 \\ 0 & 0 & 0 & 0 \end{bmatrix}$$

is also persistently exciting.

Proof of Proposition 3.3.2 : We note that $\mathbf{W}_\theta(t) = \mathbf{S}\tilde{\mathbf{W}}_\theta(t)$ where

$$\mathbf{S} = \begin{bmatrix} 1 & 0 & 0 & 0 \\ 0 & 1 & 0 & 0 \\ -K_{\theta,D} & -K_{\theta,P} & K_{\theta,P} & 0 \\ 0 & 0 & 0 & 1 \end{bmatrix}$$

and $\det(S) = K_{\theta,P} \neq 0$. Given any T, we conclude that

$$\begin{aligned} \mathbf{M}_r(t, t+T) &= \int_t^{t+T} \mathbf{W}_\theta(\sigma)\mathbf{W}_\theta^T(\sigma)d\sigma \\ &= \mathbf{S}\int_t^{t+T} \tilde{\mathbf{W}}_\theta(\sigma)\tilde{\mathbf{W}}_\theta^T(\sigma)d\sigma\ \mathbf{S}^T \end{aligned}$$

is full rank for all t if and only if

$$\tilde{\mathbf{M}}_r(t, t+T) = \int_t^{t+T} \tilde{\mathbf{W}}_\theta(\sigma)\tilde{\mathbf{W}}_\theta^T(\sigma)d\sigma$$

is full rank for all t. □

Proposition 3.3.2 allows us to conduct system identification during experimental dives, in which an attitude controller is enabled. We achieve persistence of excitation by generating a sufficiently rich reference input $\Delta\theta_{\text{ref}}(t)$.

3.4 Standard Least Squares

In addition to the adaptive identifier and the Kalman filter, a least squares algorithm is utilized for comparison. Given a known initial condition $\mathbf{x}_\theta(0)$, the system (3.4) is propagated iteratively in discrete time

$$\hat{\mathbf{x}}_\theta(k+1) = \hat{\mathbf{x}}_\theta(k) + h\left[\mathbf{A}_\theta \hat{\mathbf{x}}_\theta(k) + \mathbf{W}_\theta^T(k)\,\hat{\mathbf{p}}_\theta\right]$$

where $\hat{\mathbf{x}}_\theta(k)$ and $\hat{\mathbf{p}}_\theta$ denote the state and parameter estimates.

For a data set of m samples, we use standard least squares techniques [59] or numerical algorithms, e.g. the *Nelder-Mead Simplex Method* [51], to find $\hat{\mathbf{p}}_\theta$ such that the cost function

$$J_\theta(\hat{\mathbf{p}}_\theta) = \sum_{k=1}^{m} \|\mathbf{x}_\theta(k) - \hat{\mathbf{x}}_\theta(k)\|^2 \tag{3.25}$$

is minimized.

It is important to note that a numerical minimization of $J_\theta(\hat{\mathbf{p}}_\theta)$ can only be applied after the entire data set is collected. Hence, the ability to perform system identification via (3.25) is limited to off-line parameter estimation.

3.5 Experimental Results and Validation

In this section, we present field experiments carried out at Claytor Lake, Virginia using the Virginia Tech 475 AUV from Figure 1.1. Using identification techniques from this chapter, the goal of our field experiments is to estimate the parameters of simplified pitch and heave models derived in Appendix A and Chapter 2. We obtain system parameters for two AUV configurations and justify the usage of simplified models for control design experimentally.

To evaluate the performance of the system identification, we focus on two indicators. First, we investigate parameter convergence properties and parameter agreement between the three methods, an adaptive identifier, a Kalman filter, and a least squares fit. Second, we simulate the closed-loop AUV's motion in the dive plane and compare the simulated trajectory with the real data. The closed-loop system, shown in Figure 3.1, utilizes the parameter estimates for the heave model Σ_Z from (3.1) and the pitch model Σ_θ from (3.2) as well as the implemented depth and pitch controller, which is presented in detail in the next section. The closed-loop simulation generates trajectories for depth $\check{Z}$, pitch $\check{\theta}$, and elevator fin deflection $\check{\delta}$.

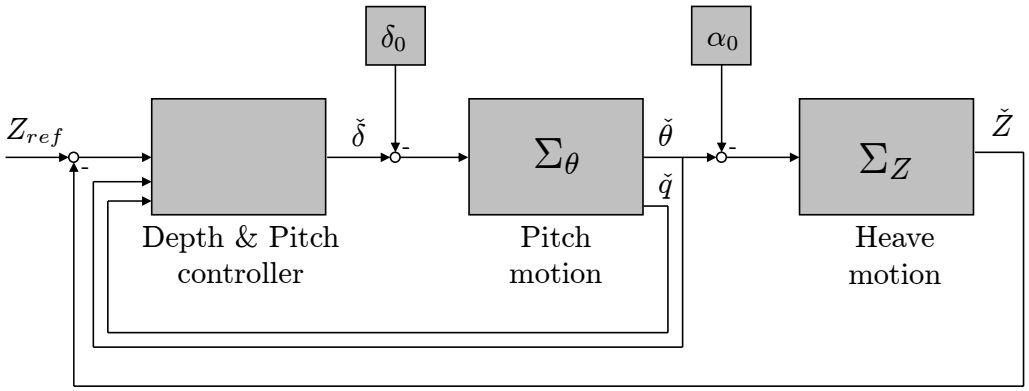

Figure 3.1: Closed loop simulation to validate the parameter estimation for the heave model Σ_Z from (3.1) including the steady state angle of attack α_0 and the pitch model Σ_θ from (3.2) including the steady state elevator fin deflection δ_0.

The field experiments are presented in the following order. First, parameter identification is carried out for the nominal and a perturbed AUV configuration, both are shown in Figure 3.2. For the perturbed AUV configuration, a pair of fixed fins is attached to the body. The fins are deflected -45 deg (trailing edge up) to noticeably

change the hydrodynamic characteristics of the AUV. Parameter estimation for both configurations is presented, and differences between the identified system parameters are discussed. Second, control redesign is performed for the perturbed AUV. We rely on estimated system parameters to select new feedback gains that reestablish nominal dive behavior. Third, parameter identification is addressed for the nominal AUV traveling at different speeds. We conduct dive maneuvers over the achievable range of propeller rotation rates in order to obtain pitch and heave models and to evaluate the vehicle dynamics given different speeds.

3.5.1 Depth and Pitch Control

For the Virginia Tech 475 AUV, depth control is designed based on the heave model (3.2), and attitude control is designed based on the pitch model (3.1). Given parameters A_{33}, A_{34}, and B_{31}, we select PID gains $K_{\theta,I}$, $K_{\theta,P}$ and $K_{\theta,D}$ for the pitch control feedback law

$$\delta(s) = \left[\frac{1}{s}K_{\theta,I} + K_{\theta,P}\right][\Delta\theta_{\text{ref}}(s) - \Delta\theta(s)] - K_{\theta,D}\, s\, \Delta\theta(s)$$

to place the poles of the closed loop pitch model

$$\begin{aligned} G_\theta(s) &= \frac{\Delta\theta(s)}{\Delta\theta_{\text{ref}}(s)} \\ &= \frac{B_{31}\,(K_{\theta,I} + sK_{\theta,P})}{s^3 + (B_{31}K_{\theta,D} - A_{33})\,s^2 + (B_{31}K_{\theta,P} - A_{34})\,s + B_{31}K_{\theta,I}} \end{aligned} \tag{3.26}$$

at

$$\lambda_{\theta_1} = -\omega_\theta \qquad \text{and} \qquad \lambda_{\theta_{2,3}} = -\omega_\theta\left(D_\theta \pm j\sqrt{1 - D_\theta^2}\right)$$

Here, ω_θ determines the bandwidth of $G_\theta(s)$, and the damping coefficient D_θ satisfying $1 \geq D_\theta > 0$ is chosen to meet performance or robustness measures such as overshoot or gain and phase margins. The input signal, the desired pitch angle $\Delta\theta_{\text{ref}}$,

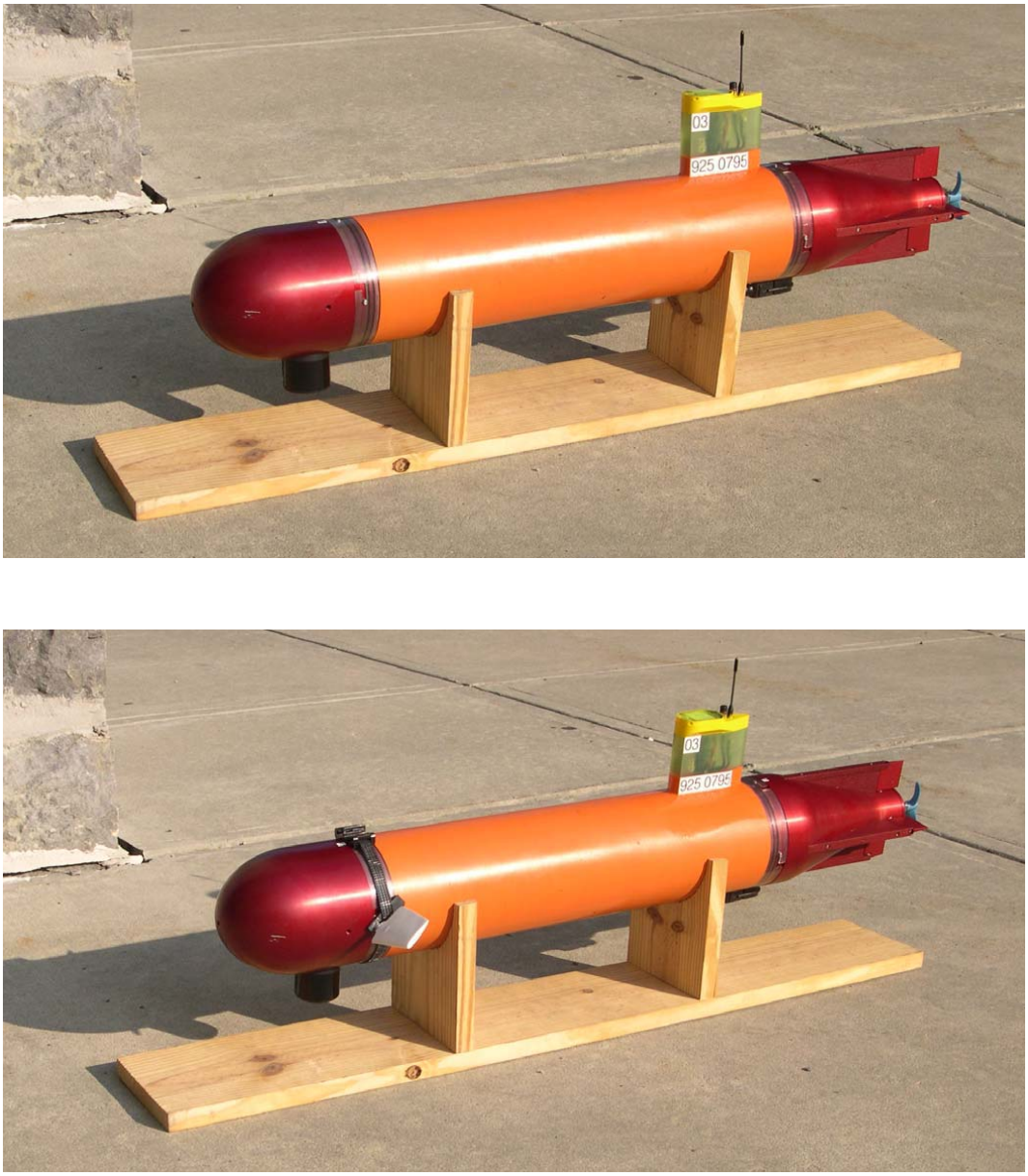

Figure 3.2: Nominal vehicle configuration (upper picture) and modified (perturbed) vehicle configuration with attached fixed fins at the nose (lower picture).

is generated by the depth controller as shown in the overall cascaded control architecture in Figure 3.3.

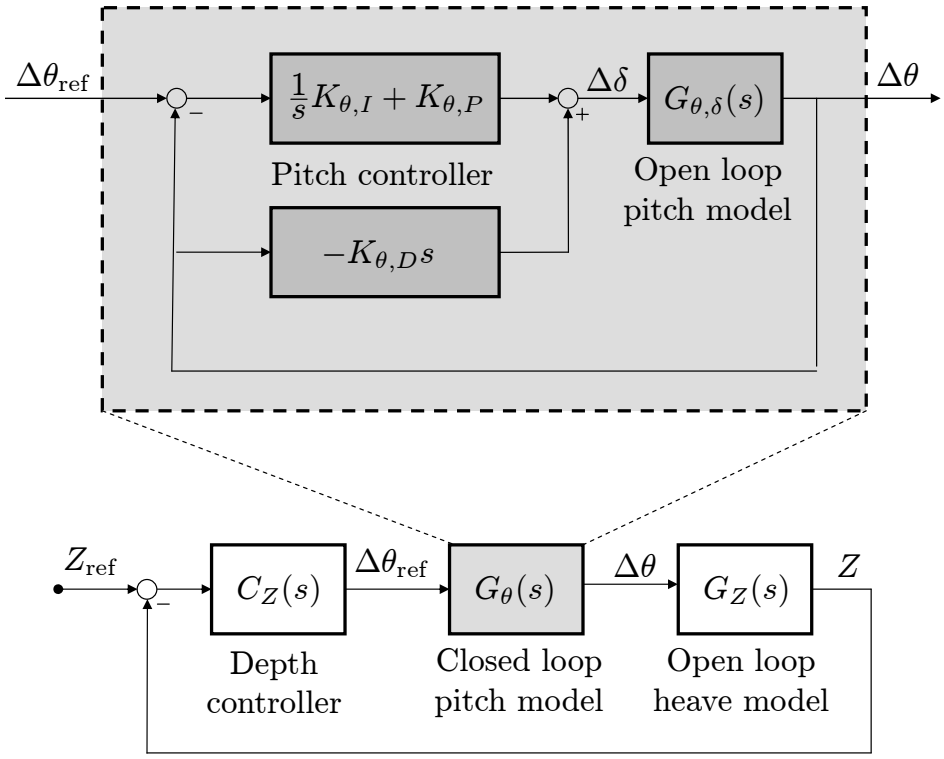

Figure 3.3: Cascaded depth and pitch controller. The AUV depth controller $C_Z(s)$ in the outer loop commands a desired pitch angle $\Delta\theta_{\text{ref}}$. The AUV's attitude $\Delta\theta$ tracks $\Delta\theta_{\text{ref}}$ using an inner loop pitch controller.

For low angular frequencies $\omega << \omega_\theta$, we find that $G_\theta(s) \approx 1$ which is desired for tracking performance, and the closed loop depth transfer function in the outer loop becomes

$$\frac{Z(s)}{Z_{\text{ref}}(s)} = \frac{C_Z(s)G_Z(s)}{1 + C_Z(s)G_Z(s)} \tag{3.27}$$

Here, $C_Z(s)$ denotes the transfer function of the depth controller containing the PI-

feedback gains $K_{Z,I}$ and $K_{Z,P}$

$$C_Z(s) = \frac{1}{s}K_{Z,I} + K_{Z,P} \qquad \text{for} \qquad G_\theta(s) \approx 1$$

We place the poles of (3.27) at

$$\lambda_{Z_{1,2}} = -\omega_Z \left(D_Z \pm j\sqrt{1 - D_Z^2} \right)$$

where $1 \geq D_Z > 0$. To allow for tracking in the inner loop, we separate depth and attitude control in the frequency domain by setting $\omega_Z << \omega_\theta$.

3.5.2 System Identification for Nominal and Perturbed AUV

For both configurations, nominal and perturbed, the AUV is commanded to follow a sequence of depth step inputs to provide sufficient excitation along the pitch axis. The reference depth input Z_{ref} is indicated by the dashed line in the upper graph in Figure 3.7 on page 72. A commanded change in depth between 2 meters and 4 meters occurs every 20 seconds, while the propeller rotation rate is held constant at 3200 rpm. Feedback control is enabled using nominal gains so that the AUV follows attitude and depth commands.

Although the Kalman filter and the adaptive identifier can be implemented online, parameter estimation techniques from Chapter 3 are applied after the data collection. The results are shown in Figure 3.4 for the nominal AUV configuration and in Figure 3.5 for the perturbed AUV configuration.

The upper two plots of Figure 3.4 and Figure 3.5 show the parameters of the kinematic heave model (3.1), namely speed V_0 in ms^{-1} and steady state pitch angle $\theta_0 = \alpha_0$ in deg. The transients are plotted for the Kalman filter (dotted line) and the adaptive identifier (dashed line). Parameter estimates resulting from the

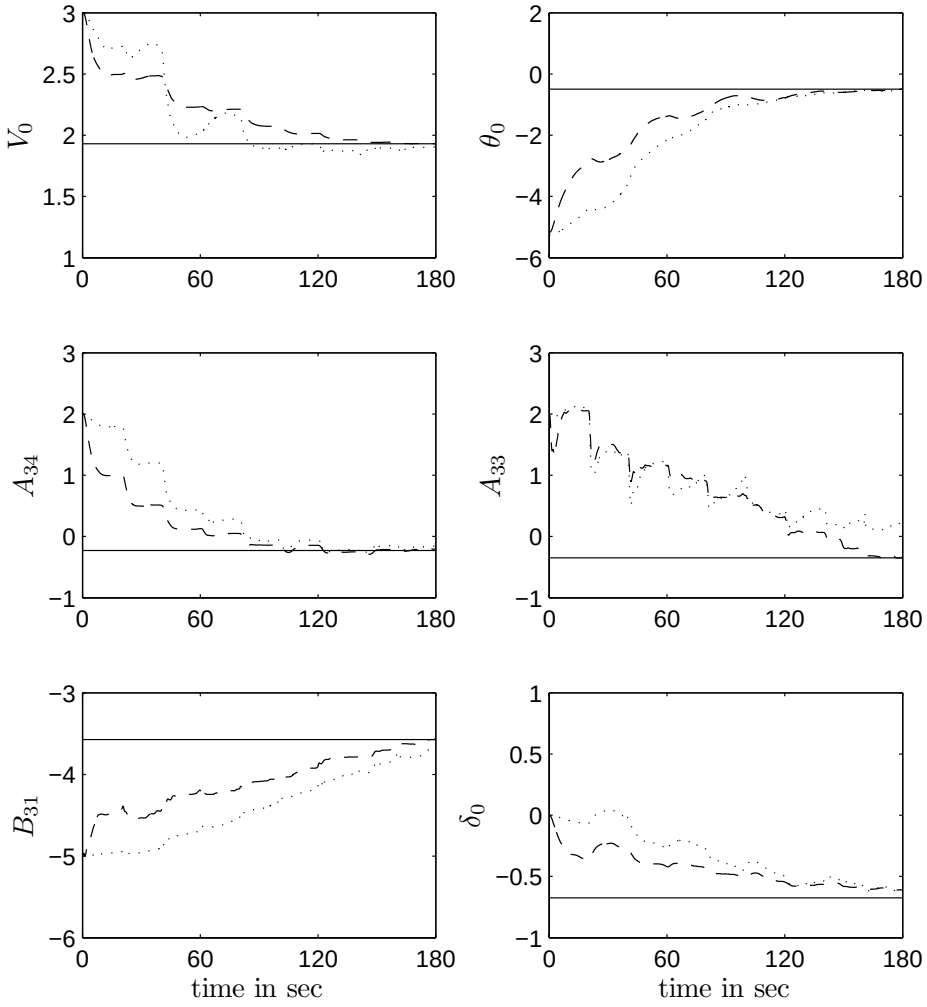

Figure 3.4: Parameter estimation for the nominal vehicle using a Kalman filter (dotted), an adaptive identifier (dashed) and a least squares approach (solid). Speed V_0 in ms^{-1} and θ_0, δ_0 in deg.

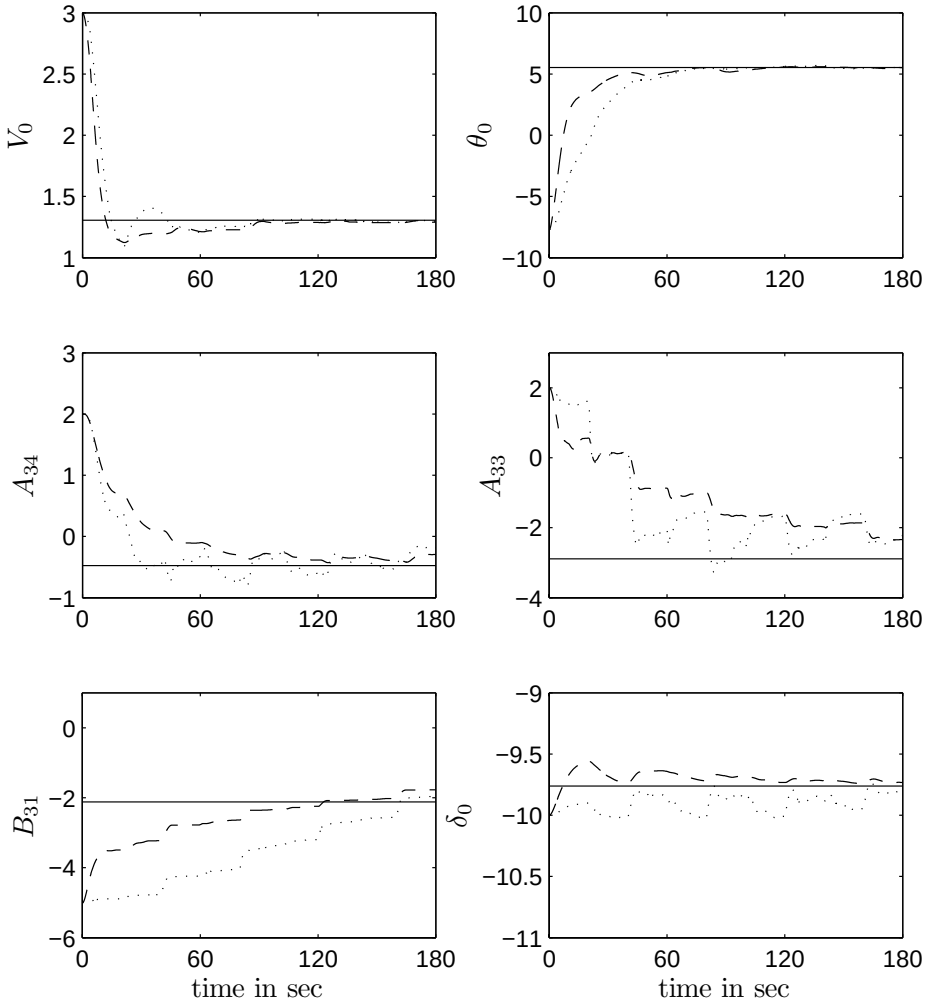

Figure 3.5: Parameter estimation for the perturbed vehicle using a Kalman filter (dotted), an adaptive identifier (dashed) and a least squares approach (solid). Speed V_0 in ms^{-1} and θ_0, δ_0 in deg.

numerical least squares fit (solid) are not a function of time since the numerical optimization from Section 3.4 is a purely offline technique. For the heave model identification, parameter convergence and parameter agreement between all three identification techniques occur for both AUV configurations. Thus, the selected reference depth trajectory appears experimentally to provide persistence of excitation. Note that the initial conditions are intentionally chosen poorly to emphasize the transients of the parameter estimation.

The lower four plots of Figure 3.4 and Figure 3.5 show the parameter estimates of the dynamic pitch model (3.2), containing the elements A_{34} and A_{33} of the system matrix, the element B_{31} of the input matrix and the steady state elevator fin deflection δ_0 in deg. As compared to identifying two parameters for the heave model, we now attempt to estimate four parameters. Increasing the amount of parameters effects the performance of the identification algorithms negatively. The convergence rate decreases and parameter agreement between different identification techniques is not completely reached in 180 seconds for the given data set.

Table 3.1 summarizes the identified system parameters for both AUV configurations. We compromise between parameter estimates resulting from a Kalman filter, an adaptive identifier and a least squares approach by computing the overall average during the last 30 seconds.

Evidently, attaching additional hydrodynamic surfaces to the AUV's body changes drag and lift properties. Thus, the overall vehicle dynamics differ between the two vehicle configurations. The additional drag causes the perturbed vehicle to travel at only 60 percent of the nominal speed, while the AUV's body pitches up significantly (5.5 deg) to compensate for the downward lift forces induced by the attached fins. Also, the parameter A_{33} indicates an increase in pitch damping for the perturbed

Table 3.1: Identified system parameters for nominal and perturbed AUV configuration. V_0 in ms^{-1} and θ_0, δ_0 in deg.

vehicle configuration	V_0 in ms^{-1}	α_0 in deg	A_{34} in s^{-2}	A_{33} in s^{-1}	B_{31} in s^{-2}	δ_0 in deg
nominal	1.9	-0.5	-0.20	-0.17	-3.60	-0.6
perturbed	1.3	$+5.5$	-0.41	-2.90	-2.13	-9.8

vehicle. It is interesting to note that achieving an equilibrium of moments around the pitch axis, see (A.18), requires a steady state elevator fin deflection of $\delta_0 = -10$ deg for the perturbed vehicle configuration, whereas δ_0 is negligible for the well trimmed, nominal AUV.

Figure 3.6 illustrates the difference in the vehicle's pitch dynamics between the nominal and perturbed configuration by showing the bode plot and the pole locations of the open loop pitch model given in (3.2). We recall

$$G_{\theta,\delta}(s) = \frac{\Delta\theta(s)}{\delta(s)} = \frac{B_{31}}{s^2 - A_{33}s - A_{34}} \tag{3.28}$$

The pitch dynamics of the nominal AUV are characterized by a pair of complex conjugate poles. For the perturbed vehicle, this motion is highly damped and the poles move to the real axis.

Using the parameter estimates from Table 3.1 for heave and pitch models, we simulate the closed-loop system as shown in Figure 3.1. Figure 3.7 and Figure 3.8 compare the real trajectories for depth Z, pitch angle θ and elevator fin deflection δ (all gray) to the simulation results $\check{Z}, \check{\theta}$, and $\check{\delta}$ (all black) for the nominal and the

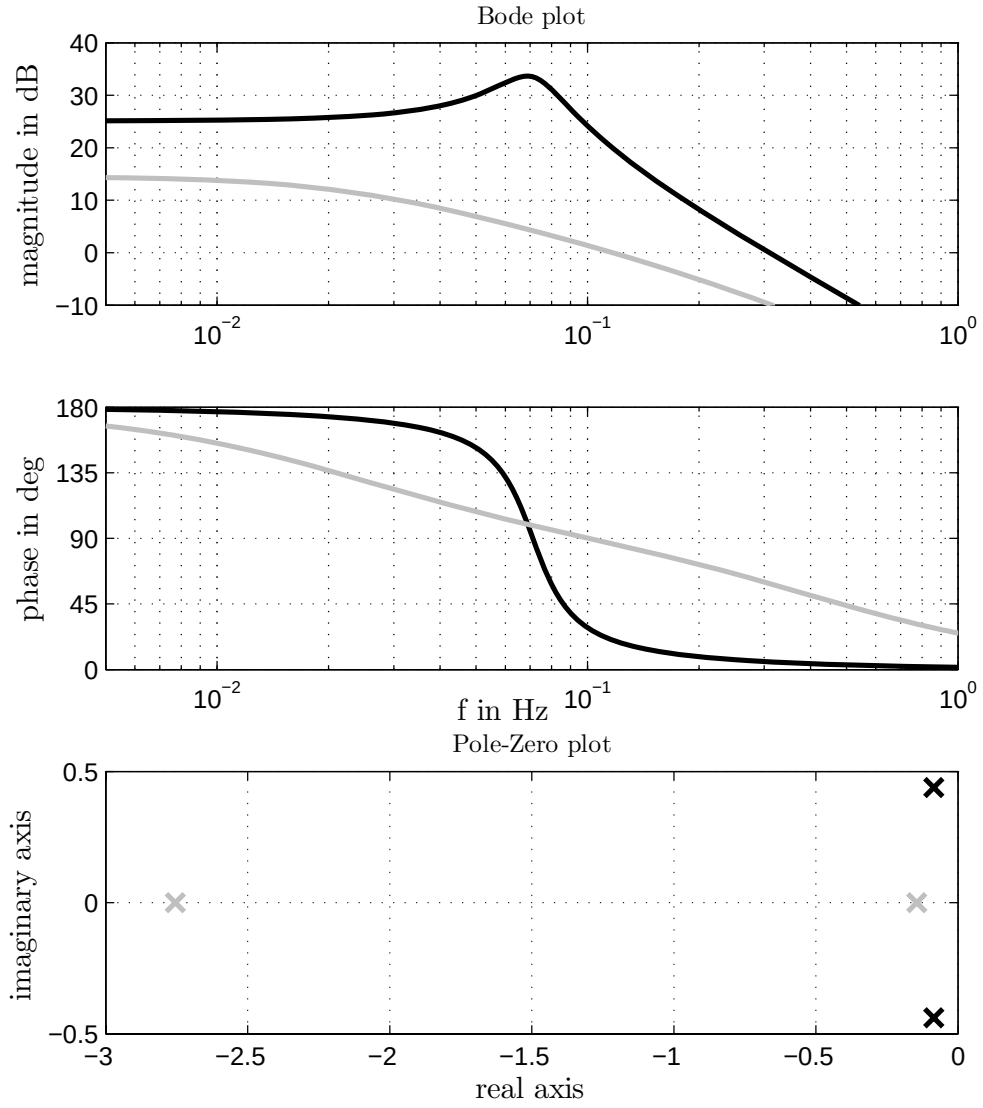

Figure 3.6: Bode plot and pole locations of the open loop pitch model $G_{\theta,\delta}(s)$ for the nominal (black) and perturbed (gray) vehicle.

perturbed AUV, respectively. Noticeable in Figure 3.8, the attitude controller limits the elevator fin deflection to ±15deg to avoid stall.

The nearly perfect matches between the AUV's depth trajectories, shown in the upper plots of Figure 3.7 and Figure 3.8, suggest that the vehicle's heave motion is sufficiently well approximated through pure kinematics (3.1). However, the trajectory comparison for pitch angle and elevator fin deflection reveals oscillatory modes of small amplitude at around $0.2\,Hz$, which are not captured by the model. These modes can be attributed to the model truncation and to neglected coupling between pitch, roll and yaw motion. Overall, simplified models are found to be sufficiently accurate for predicting the AUV's motion during conventional dive maneuvers.

3.5.3 Control Redesign for Perturbed AUV

The ability to quickly redesign a controller and to provide small turnaround times between vehicle deployments with different payloads is a principal contribution of this work. The nominal AUV configuration is modified by attaching a pair of fixed fins to the vehicle's body in order to mimic an external sensor. The differences in the vehicle dynamics between nominal and perturbed AUV are illustrated in Table 3.1 and Figure 3.6. To demonstrate the procedure and the performance of the control redesign, we attempt to reestablish nominal dive behavior for the perturbed vehicle. Feedback control gains for depth and attitude control are adjusted in order to compensate for the changes in the plant.

Suppose the identified vehicle parameters for the nominal and perturbed vehicle are $\{V_0^n,\, A_{33}^n,\, A_{34}^n,\, B_{31}^n\}$ and $\{V_0^p,\, A_{33}^p,\, A_{34}^p,\, B_{31}^p\}$, respectively. The nominal feedback gains $\left\{K_{Z,I}^n,\, K_{Z,P}^n,\, K_{\theta,I}^n,\, K_{\theta,P}^n,\, K_{\theta,D}^n\right\}$ define the nominal, closed-loop depth

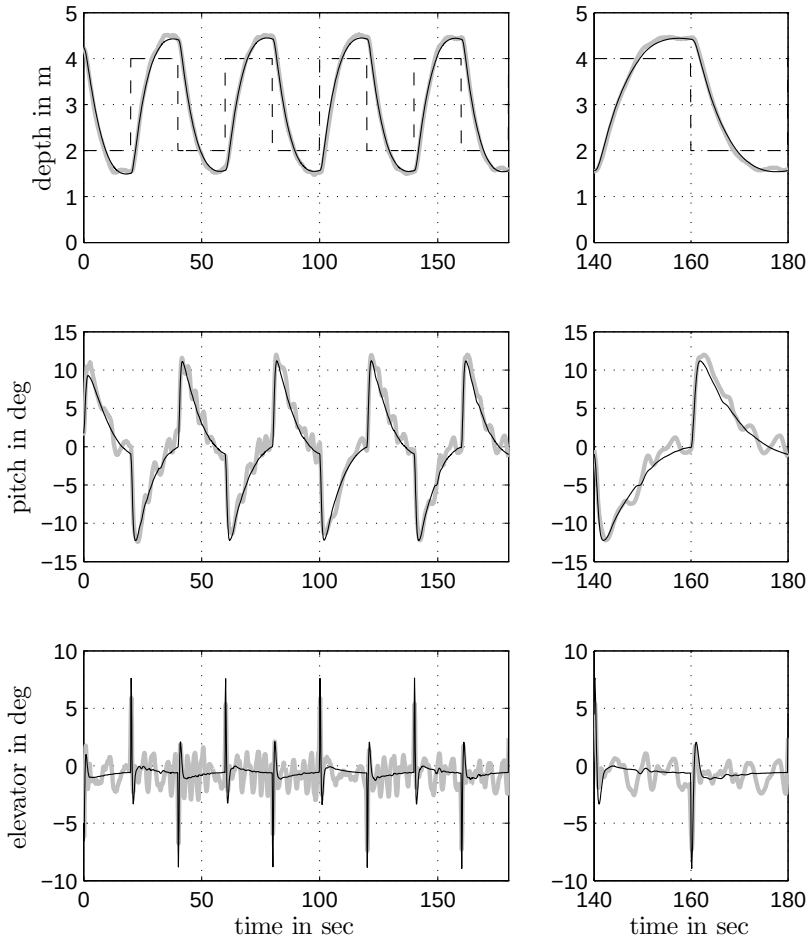

Figure 3.7: Simulated closed loop AUV trajectory for the nominal configuration given the reference depth signal Z_{ref} (dashed). The last 20 seconds are enlarged to show detail. From top to bottom: depth $Z, \check{Z}$, pitch angle $\theta, \check{\theta}$ and elevator fin deflection $\delta, \check{\delta}$ with real data in gray and the simulated plant in black.

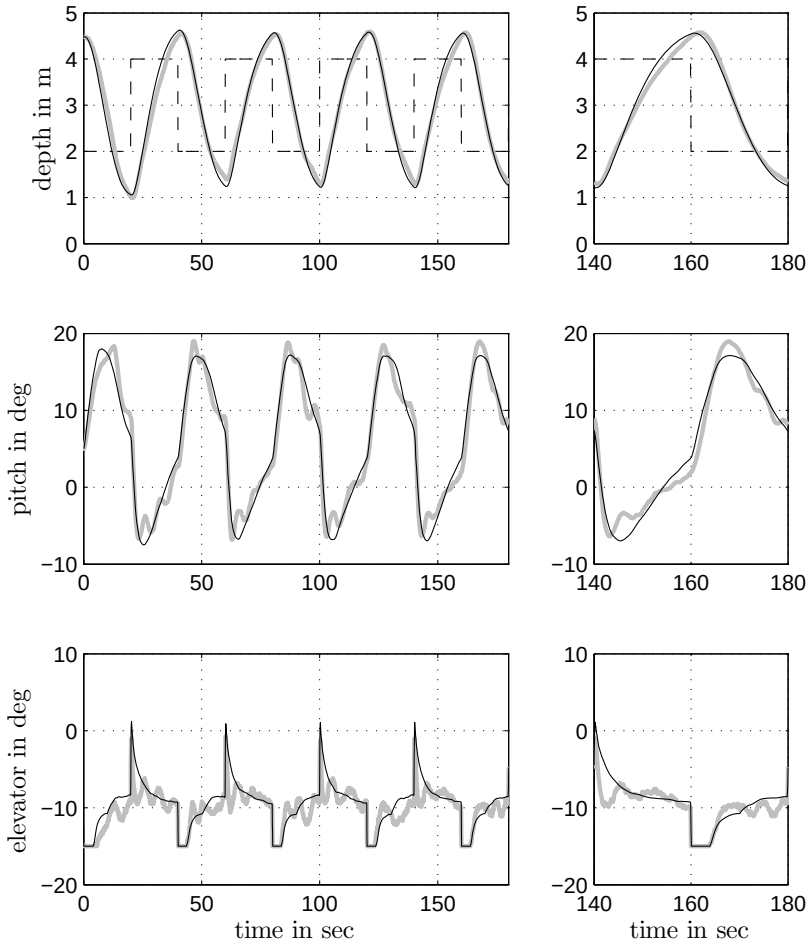

Figure 3.8: Simulated closed loop AUV trajectory for the perturbed configuration given the reference depth signal Z_{ref} (dashed). The last 20 seconds are enlarged to show detail. From top to bottom: depth $Z, \check{Z}$, pitch angle $\theta, \check{\theta}$ and elevator fin deflection $\delta, \check{\delta}$ with real data in gray and the simulated plant in black.

model $G_Z^n(s)$ from (3.27)

$$G_Z^n(s) = \frac{-V_0^n \left(K_{Z,I}^n + sK_{Z,P}^n\right)}{s^2 - sV_0^n K_{Z,P}^n - V_0^n K_{Z,I}^n} \tag{3.29}$$

and the nominal, closed-loop pitch model $G_\theta^n(s)$ from (3.26)

$$G_\theta^n(s) = \frac{B_{31}^n \left(K_{\theta,I}^n + sK_{\theta,P}^n\right)}{s^3 + \left(B_{31}^n K_{\theta,D}^n - A_{33}^n\right) s^2 + \left(B_{31}^n K_{\theta,P}^n - A_{34}^n\right) s + B_{31}^n K_{\theta,I}^n} \tag{3.30}$$

Our goal is to find feedback gains $K_{Z,I}^p$, $K_{Z,P}^p$, $K_{\theta,I}^p$, $K_{\theta,P}^p$ and $K_{\theta,D}^p$ for the perturbed vehicle that yield

$$G_Z^n(s) = G_Z^p(s) \qquad \text{and} \qquad G_\theta^n(s) = G_\theta^p(s) \tag{3.31}$$

where

$$G_Z^p(s) = \frac{-V_0^p \left(K_{Z,I}^p + sK_{Z,P}^p\right)}{s^2 - sV_0^p K_{Z,P}^p - V_0^p K_{Z,I}^p}$$

and

$$G_\theta^p(s) = \frac{B_{31}^p \left(K_{\theta,I}^p + sK_{\theta,P}^p\right)}{s^3 + \left(B_{31}^p K_{\theta,D}^p - A_{33}^p\right) s^2 + \left(B_{31}^p K_{\theta,P}^p - A_{34}^p\right) s + B_{31}^p K_{\theta,I}^p}$$

Clearly, adjusting only five feedback control gains cannot retrieve the nominal closed-loop transfer functions (3.29) and (3.30), which are defined by a total of nine coefficients. Thus, nominal behavior is not achievable for the perturbed vehicle using the control structure from Section 3.5.3. For the results shown in this work, we select feedback gains to simply coincide the closed-loop pole locations of $G_Z^p(s)$ and $G_\theta^p(s)$ with the closed-loop pole locations of $G_Z^n(s)$ and $G_\theta^n(s)$. In other words, we adjust the feedback gains such that the denominators of heave and pitch model given in (3.29) and (3.30) remain unchanged between the two vehicle configurations.

In Figure 3.9, we show a comparison between the nominal vehicle's trajectory (gray) and the perturbed vehicle's trajectory (dashed black) using the nominal controller.

Although, the nominal controller seems to already provide stability for the perturbed AUV, a difference in the depth trajectory is apparent. The perturbed vehicle's trajectory using the redesigned controller is shown in solid black. The upper plot of Figure 3.9 verifies that the perturbed vehicle follows the nominal depth trajectory with acceptable accuracy. Comparing the trajectories of θ and δ between the nominal and perturbed AUV is not feasible as pitch angle and elevator fin deflection differ between both vehicle configurations during steady state flight, see Table 3.1. Nevertheless, it follows from the cascaded control design in Figure 3.3 that achieving a faster depth transient increases the required bandwidth for the closed-loop pitch motion $G_\theta(s)$, which causes unwanted oscillations noticeable in Figure 3.9.

3.5.4 System Identification for Nominal AUV at Different Speeds

From the model derivation in Appendix A, the vehicle dynamics are expected to change dependent on the vehicle's shape and payload configuration. In addition, the equations of motion suggest that the AUV dynamics are significantly affected by the AUV's water relative speed. While the AUV's payload configuration is fixed for single missions, it is desired to operate the AUV throughout the achievable speed range and to maintain nominal dive performance. For this reason, we conduct individual system identification runs for propeller rotation rates ranging from 1600 to 3600 rpm in order to obtain and compare heave and pitch models for the nominal vehicle configuration at different speeds.

Illustrated by the dashed line in the upper graph in Figure 3.7 on page 72, we use the same reference depth input Z_{ref} as for the previous experiments. For all runs, attitude and depth control is enabled using nominal feedback gains. The estimated

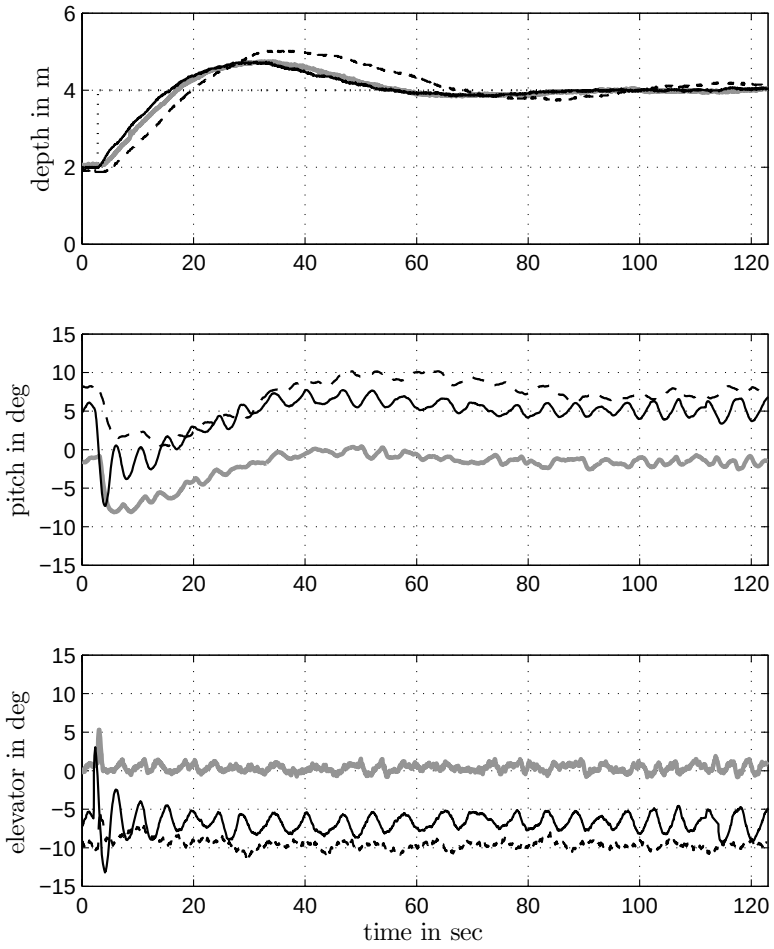

Figure 3.9: Control redesign for the perturbed vehicle. The gray line shows the nominal vehicle trajectory, the dashed black line represents the perturbed vehicle using the nominal controller, and the solid black line shows the perturbed vehicle using the adjusted controller achieving an improved depth trajectory. From top to bottom: depth Z, pitch angle θ and elevator fin deflection δ.

system parameters are listed in Table 3.2.

Table 3.2: Identified system parameters for the nominal AUV configuration for selected propeller rotation rates. V_0 in ms^{-1}, and θ_0, δ_0 in deg.

rpm	V_0	θ_0	A_{34}	A_{33}	B_{31}	δ_0
1600	0.78	−5.30	−0.15	−0.39	−0.79	−0.95
2000	1.10	−2.81	−0.08	−0.31	−1.35	−1.37
2400	1.37	−1.61	−0.11	−0.21	−1.93	−1.16
2800	1.65	−0.83	−0.18	−0.11	−2.59	−0.87
3200	1.93	−0.49	−0.20	−0.17	−3.60	−0.62
3600	2.26	−0.29	−0.15	−0.25	−4.62	−0.48

As expected, the speed V_0 increases and the steady state angle of attack $\alpha_0 = \theta_0$ decreases in magnitude for higher propeller rotation rates. The negative values of A_{33} and A_{34} indicate that the nominal configuration of the Virginia Tech 475 AUV remains inherently stable along the pitch axis over the entire speed range. For higher speeds, we find increased control authority B_{31} due to increased dynamic pressure at the control surfaces. Figure 3.10 shows the Bode plots and the pole locations for the open loop pitch model $G_{\theta,\delta}(s)$ from (3.28) for selected propeller rotation rates, from 1600rpm (black) up to 3600rpm (light gray).

3.6 Conclusion

In this chapter, we present system identification for a linear second-order AUV pitch-axis model and a kinematic AUV heave model while utilizing only instrumented

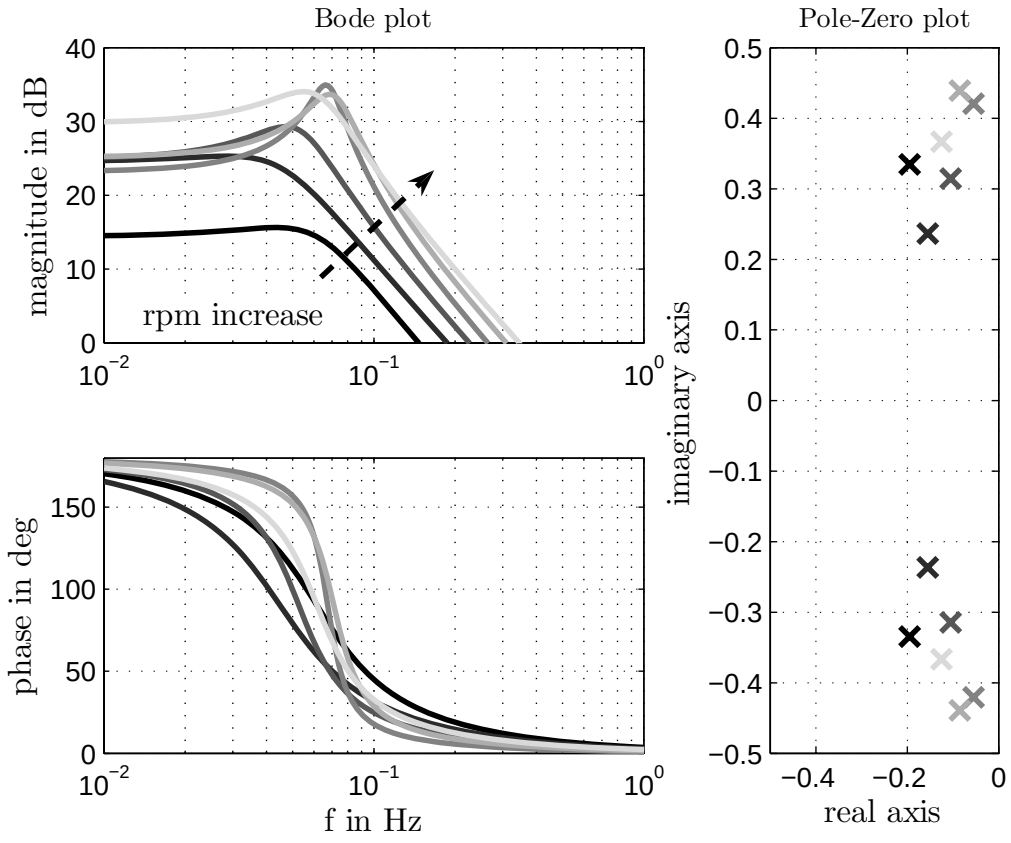

Figure 3.10: Bode plots (left) and pole locations (right) of the open loop pitch model $G_{\theta,\delta}(s)$ for the nominal vehicle configuration at different speeds, from 1600rpm (black) to 3600rpm (light gray).

variables onboard the AUV. By deriving sufficient excitation condition under which successful parameter estimation is guaranteed, we reveal a meaningful equivalence between an adaptive identifier and a linear state observer. In particular, our formal observability analysis shows equivalence between persistence of excitation and uniform observability for the given system. The assessment of AUV excitation allows us to define and select AUV trajectories suitable for successful parameter estimation.

We provide insight into the derivation of an adaptive identifier and a Kalman filter that are used for parameter identification. Both algorithms can potentially be implemented online and onboard the AUV. For reasons of comparison, we utilize a least squares approach to numerically fit a model once input and output signals are collected.

We validate our theoretical results by conducting field experiments using multiple AUV configurations. For each AUV configuration, we are able to parameterize a simplified pitch-axis model and a kinematic heave model that accurately predict the AUV's motion underwater. Differences in the system dynamics between vehicle configurations are analyzed. Using the estimated system parameters, we successfully demonstrate rapid model-based control re-design for a modified AUV.

Chapter 4

Robust Attitude Control

Attitude control systems for AUVs are often implemented with separate controllers for pitch motion in the vertical plane and yaw motion in the horizontal plane. In this chapter, we propose a novel time-varying model for a streamlined AUV that explicitly displays the coupling between yaw and pitch motion due to nonzero roll angle and/or roll rate. The model facilitates the use of a multi-input multi-output $\mathcal{H}_\infty$ control design that is robust to yaw-pitch coupling. The efficacy of our approach is demonstrated with field trials.

4.1 Introduction

For submersed vehicles, roll excursions are inevitable as they are caused by induced propeller torque, wave disturbances and banking motion during turns. Assuming no active roll stabilization, attitude control systems must tolerate nonzero roll motion even though the control system is often designed as two single-axis controllers that separately stabilize pitch and yaw. This is especially true for small AUV systems that

might posses a relatively small righting moment due to limited vertical separation between center of mass and center of buoyancy.

In this chapter, we derive a novel linear time-varying model that explicitly displays the coupled pitch and yaw dynamics of a streamlined AUV that are due to nonzero roll angle and/or roll rate. Our model facilitates the design of a multi-input multi-output $\mathcal{H}_\infty$ controller that provides robustness specifically against roll-induced coupling terms. For our analysis, we presume a streamlined AUV with propulsion and control surfaces at the tail.

In general, feedback controllers are implemented separately for each body axis while coupling between roll, pitch and yaw motion is neglected, see [19], [20] and [21]. Robust attitude control for AUV systems has been addressed using a variety of approaches, see [8] and [20] for *sliding mode* control, and [22] and [23] for μ-synthesis design. For our purposes, we use $\mathcal{H}_\infty$ tools (e.g., from Section 17 in [24]) for two reasons. First, we address roll-induced coupling as structured uncertainties within the linear plant and thus choose a control design approach that provides robustness specifically against these uncertainties. Second, we formulate fundamental control design criteria such as robustness against parameter uncertainties, overall tracking performance and required actuator bandwidth. Similar $\mathcal{H}_\infty$ approaches for AUV attitude control are presented in [2], [20] and [23], in which the authors focus on providing robustness against model uncertainties for separate pitch and yaw channels. In comparison to existing work, the novelty of our approach lies in formally deriving coupling effects between pitch and yaw motion and in explicitly addressing pitch/yaw coupling for robust feedback control design.

Borrowing control strategies used for guided missile systems, see [26] and [27], we allocate sensor measurements and actuator commands in order to minimize kine-

matic coupling within the linear model. A time-varying, roll-dependent state-space transformation is proposed which allows us to address attitude control assuming an upright AUV body with zero roll angle. We formally show that coupling is reduced by transforming the linear equations of motion into such a zero roll body-axis frame.

As compared to fully actuated AUVs capable of station-keeping [25], we present attitude control for under-actuated, tail-controlled AUVs that rely on maintaining forward speed for maneuvering. In addition, we do not assume that linear velocities are instrumented. In [2], [7] and [60] for example, the authors present the design of full state feedback controllers for AUVs that are instrumented with a Doppler velocity log to measure ground-relative velocity. Although our approach can easily be adapted to include linear velocity measurements, we present attitude control using angular rate and orientation feedback exclusively. Adopting an $\mathcal{H}_\infty$ control design approach, we are able to compromise between performance, robustness and actuator bandwidth via standard loop shaping techniques, see [19] and [25].

This chapter is organized as follows. In Section 4.2, we derive a novel linear model that captures the coupled AUV pitch and yaw dynamics. Cross-coupling due to roll motion is discussed in detail. In Section 4.3, we present sensor and actuator allocation techniques that minimize kinematic coupling. We propose a time-varying state-space transformation and rewrite the linear equations of motion with respect to an upright AUV coordinate frame. In Section 4.4, an attitude controller is designed that provides robustness specifically against remaining coupling terms. We introduce fundamental concepts of $\mathcal{H}_\infty$ control design and compromise between design criteria such as robustness, tracking performance and actuator bandwidth. We validate our analysis through field trials presented in Section 4.5.

4.2 Joint Pitch and Yaw Model

In Appendix A, the complete nonlinear AUV dynamics are described by the system (A.6). In this Section, we seek to derive an AUV model that captures coupled pitch and yaw dynamics in order to facilitate our approach to robust control. We identify roll-induced coupling terms and treat them as instrumented exogenous signals within the model. For the model derivation, we use the following assumptions. First, we assume constant speed $V = V_0$ implying $V_0 = u_0$ for small α and β as justified in Section A.5.2. Second, we treat $p(t)$ and $\phi(t)$ as instrumented time-varying parameters instead of states in the equations of motion. This effectively allows us to truncate the first, fourth, and seventh rows in (A.6) and eliminates the states u, p, and ϕ. Thus, the remaining state vector becomes

$$\boldsymbol{\chi} := \begin{bmatrix} \boldsymbol{\chi}_\theta^T & \boldsymbol{\chi}_\psi^T \end{bmatrix}^T \quad \text{where} \quad \boldsymbol{\chi}_\theta := \begin{bmatrix} \alpha & q & \theta \end{bmatrix}^T \quad \text{and} \quad \boldsymbol{\chi}_\psi := \begin{bmatrix} -\beta & r & \psi \end{bmatrix}^T \tag{4.1}$$

It is shown in the following subsections that negating β in (4.1) results in a useful symmetry in the linearized model. The remaining equations of motion are

$$\mathbf{E}\,\dot{\boldsymbol{\chi}} \;=\; \boldsymbol{f}\left(\boldsymbol{\chi}, \boldsymbol{\delta}, t\right) \tag{4.2}$$

The input signal $\boldsymbol{\delta} = \begin{bmatrix} \delta_e & \delta_r \end{bmatrix}^T$ consists of elevator and rudder fin deflection. The time-varying parameters $p(t)$ and $\phi(t)$ introduce time dependencies in the right hand side $\boldsymbol{f}\left(\boldsymbol{\chi}, \boldsymbol{\delta}, t\right)$ with

$$\boldsymbol{f}\left(\boldsymbol{\chi}, \boldsymbol{\delta}, t\right) = \begin{bmatrix} f_1 & f_2 & f_3 & f_4 & f_5 & f_6 \end{bmatrix}^T$$

and

$$
\begin{aligned}
f_1 &= -\left[V_0 m_z \beta - m z_{cg} p + (m x_{cg} + Z_{\dot{q}}) r\right]\ p(t) + \left[V_0 m_x + m z_{cg} q\right]\ q + F_z \\
f_2 &= +\left[(m x_{cg} - Z_{\dot{q}}) V_0 \beta - J_y r\right]\ p(t) - \left[-V_0 m z_{cg} \beta + J_x p(t)\right]\ r \\
&\quad + \left[V_0 m_z \alpha - (m x_{cg} + Z_{\dot{q}})\, q\right]\ V_0 - \left[V_0 m_x + m z_{cg} q\right]\ V_0\, \alpha + M_y \\
f_3 &= \cos\phi(t)\, q\ -\ \sin\phi(t)\, r \\
f_4 &= -\left[V_0 m_z \alpha - (m x_{cg} + Z_{\dot{q}}) q\right]\ p(t) + \left[V_0 m_x + m z_{cg} q\right]\ r - F_y \\
f_5 &= -\left[V_0 m z_{cg} - (m x_{cg} + Z_{\dot{q}}) V_0 \alpha + J_y q\right]\ p(t) + \left[-V_0 m z_{cg} \beta + J_x p(t)\right]\ q \\
&\quad - \left[V_0 m_z \beta - m z_{cg} p + (m x_{cg} + Z_{\dot{q}})\, r\right]\ V_0 + \left[V_0 m_x + m z_{cg} q\right]\ V_0\, \beta + M_z \\
f_6 &= \frac{1}{\cos\theta}\ \left[\sin\phi(t)\, q\ +\ \cos\phi(t)\, r\right]
\end{aligned}
$$

The inertia matrix reduces to

$$
\mathbf{E} = \begin{bmatrix} \mathbf{E}_\theta & \mathbf{0}_{3\times 3} \\ \mathbf{0}_{3\times 3} & \mathbf{E}_\psi \end{bmatrix} \tag{4.3}
$$

with

$$
\mathbf{E}_\theta = \mathbf{E}_\psi = \begin{bmatrix} V_0 m_z & -(m x_{cg} + Z_{\dot{q}}) & 0 \\ -V_0\,(m x_{cg} + Z_{\dot{q}}) & J_y & 0 \\ 0 & 0 & 1 \end{bmatrix}
$$

Note, as compared to the derivation of a linear pitch-axis model in Section A.5.2, we do not assume a diagonal inertia matrix, see Assumption A.5.1.

In order to explicitly show how yaw/pitch coupling arises as a consequence of nonzero roll angle and/or roll rate, we linearize (4.2) for both the case that roll

angle $\phi(t)$ and roll rate $p(t)$ are zero and for the case that roll angle and roll rate are nonzero. Under the assumption of a neutrally buoyant vehicle at zero angle of attack flight, we choose the operating point $\boldsymbol{\chi}_0 = \mathbf{0}$ and $\boldsymbol{\delta}_0 = \mathbf{0}$ for both cases.

4.2.1 Case 1: Zero Roll Motion

For $\phi(t) = 0$ and $p(t) = 0$, linearizing (4.2) around the operating point $\boldsymbol{\chi}_0 = \mathbf{0}$ and $\boldsymbol{\delta}_0 = \mathbf{0}$ yields

$$\mathbf{E}\,\dot{\boldsymbol{\chi}} = \mathcal{A}\,\boldsymbol{\chi} + \mathcal{B}\,\boldsymbol{\delta} \tag{4.4}$$

where

$$\mathcal{A} = \begin{bmatrix} \mathbf{A}_\theta & \mathbf{0}_{3\times3} \\ \mathbf{0}_{3\times3} & \mathbf{A}_\psi \end{bmatrix} \quad \text{and} \quad \mathcal{B} = \begin{bmatrix} \mathbf{B}_\theta & \mathbf{0}_{3\times1} \\ \mathbf{0}_{3\times1} & \mathbf{B}_\psi \end{bmatrix}$$

The system matrices are given by

$$\mathbf{A}_\theta = \begin{bmatrix} \alpha_{22} & \alpha_{23} & 0 \\ \alpha_{32} & \alpha_{33} & \alpha_{34} \\ 0 & 1 & 0 \end{bmatrix} \quad \text{and} \quad \mathbf{A}_\psi = \begin{bmatrix} \alpha_{22} & \alpha_{23} & 0 \\ \alpha_{32} & \alpha_{33} & 0 \\ 0 & 1 & 0 \end{bmatrix}$$

The elements of $\mathbf{A}_\theta$ and $\mathbf{A}_\psi$ are

$$\begin{aligned} \alpha_{22} &= \frac{1}{2}\rho V_0^2 A_b \left(C_{Db_0} + C_{L_\alpha}\right) \\ \alpha_{23} &= m_x V_0 \\ \alpha_{32} &= \left(m_z - m_x\right) V_0^2 + \frac{1}{2}\rho V_0^2\, L A_b C_{m_\alpha} \\ \alpha_{33} &= -V_0 \left(m x_{cg} + Z_{\dot{q}}\right) + \frac{1}{2}\rho V_0^2\, L A_b C_{m_q} \\ \alpha_{34} &= -z_{cg} F_w \end{aligned}$$

The density of water is ρ. The reference length and the reference area of the vehicle are L and A_b, respectively. The weight of the AUV is F_w. Hydrodynamic properties

of the AUV's body are characterized by the lift coefficients C_{L_α} and the drag coefficient C_{Db_0}. The hydrodynamic coefficients $C_{m_\alpha} < 0$ and $C_{m_q} < 0$ account for the body's hydrodynamic moment and viscous damping, respectively. The elements of the input matrix in (4.4) are

$$\mathbf{B}_\theta \;=\; \mathbf{B}_\psi \;=\; \begin{bmatrix} \beta_{21} \\ \beta_{31} \\ 0 \end{bmatrix} \;=\; \frac{1}{2}\rho V_0^2 2 A_f C_{L_\delta} \begin{bmatrix} 1 \\ x_f \\ 0 \end{bmatrix}$$

where the fin location is x_f, the reference fin area is A_f and the fin lift coefficient is C_{L_δ}. A detailed discussion of AUV parameters can be found in Appendix A.

Due to the symmetry of the AUV's body, the input matrices $\mathbf{B}_\theta$ and $\mathbf{B}_\psi$ as well as the system matrices for pitch and yaw motion $\mathbf{A}_\theta$ and $\mathbf{A}_\psi$ are identical, with the exception of a restoring moment $\alpha_{34} = -z_{cg}F_w$ that only appears in the pitch submodel $\mathbf{A}_\theta$. Since the off-diagonal elements of $\mathcal{A}$ and $\mathcal{B}$ are zero, pitch and yaw motion are entirely decoupled.

4.2.2 Case 2: Nonzero Roll Motion

For nonzero roll motion $\phi(t) \neq 0$ and $p(t) \neq 0$, linearizing (4.2) around the operating point $\boldsymbol{\chi}_0 = \mathbf{0}$ and $\boldsymbol{\delta}_0 = \mathbf{0}$ yields

$$\mathbf{E}\,\dot{\boldsymbol{\chi}} \;=\; \mathcal{A}_\phi(t)\,\boldsymbol{\chi} \;+\; \mathcal{B}\,\boldsymbol{\delta} \tag{4.5}$$

where

$$\mathcal{A}_\phi(t) = \begin{bmatrix} \mathbf{A}_\theta(t) & \mathbf{A}_{12}(t) \\ \mathbf{A}_{21}(t) & \mathbf{A}_\psi(t) \end{bmatrix}$$

The diagonal matrices are

$$\mathbf{A}_\theta(t) = \begin{bmatrix} \alpha_{22} & \alpha_{23} & 0 \\ \alpha_{32} & \alpha_{33} & \alpha_{34} \\ 0 & \cos\phi(t) & 0 \end{bmatrix} \quad \text{and} \quad \mathbf{A}_\psi(t) = \begin{bmatrix} \alpha_{22} & \alpha_{23} & 0 \\ \alpha_{32} & \alpha_{33} & 0 \\ 0 & \cos\phi(t) & 0 \end{bmatrix}$$

While the system matrix $\mathcal{A}$ from case 1 contains only zeros on the block off-diagonal entries, the system matrix $\mathcal{A}_\phi(t)$ for case 2 contains nonzero off diagonal coupling terms

$$\mathbf{A}_{12}(t) = -\mathbf{A}_{21}(t) = \begin{bmatrix} p(t)\, V_0 m_y & -p(t)\, (m x_{cg} + Z_{\dot{q}}) & 0 \\ -p(t)\, V_0\, (m x_{cg} + Z_{\dot{q}}) & p(t)\, (J_z - J_x) & 0 \\ 0 & -\sin\phi(t) & 0 \end{bmatrix} \tag{4.6}$$

Kinematic coupling is expressed in the state equations for θ and ψ, which are the third and sixth row of (4.5). For small θ we find

$$\begin{bmatrix} \dot{\theta} \\ \dot{\psi} \end{bmatrix} = \begin{bmatrix} \cos\phi(t) & -\sin\phi(t) \\ \sin\phi(t) & \cos\phi(t) \end{bmatrix} \begin{bmatrix} q \\ r \end{bmatrix} \tag{4.7}$$

Thus, for a nonzero roll angle, pitch rate q and yaw rate r are no longer the time derivatives of Euler angles θ and ψ, that is $\dot{\theta} \neq q$ and $\dot{\psi} \neq r$, see (A.2).

The state equation (4.5) and coefficients (4.6) clearly show that coupling between pitch and yaw is induced by nonzero roll angle $\phi(t)$ and/or roll rate $p(t)$. We address those coupling terms as structured uncertainties within the linear model (4.5) and design an AUV attitude controller that provides robustness specifically against them.

4.3 Decoupling and Fin-Mixing

Although commonly neglected for AUV applications, pitch and yaw coupling has been studied for the design and control of guided missiles that encounter significant roll

motion during flight, see Section 4.3 in [26]. In this section, we adapt the sensor and actuator allocation algorithms presented in [26] and [27] for the purpose of reducing the number of off-diagonal terms in (4.5). Having fewer nonzero entries facilitates the use of standard robust control techniques, because robustness to those fewer entries is expected to be less conservative.

From Section 6.11 in [26], we adopt the notion of a control frame, whose origin and x-axis are coincident with the origin and the x-axis of the AUV body frame. By definition, the control frame's y-axis is in the XY plane of the inertial frame. Thus, the control frame is equivalent to the AUV's body-axis frame for $\phi = 0$, i.e. the AUV's body is upright. For attitude control design, we transform the linear equations of motion (4.5) into the control frame which results in significant model simplifications and in fewer nonzero off-diagonal terms. Figure 4.1 shows the tail view of an AUV and depicts the control frame on the left and the body-axis frame for a nonzero roll angle ϕ on the right.

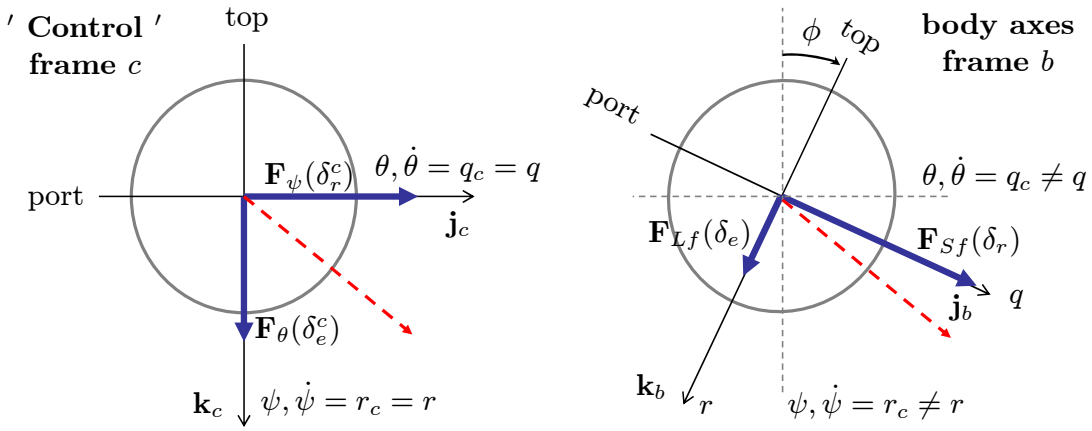

Figure 4.1: Tail view of the AUV showing control frame on the left and body-axis frame on the right.

To describe the vehicle's motion (4.5) in the control frame, we define the state vector

$$\boldsymbol{\chi}^c := \begin{bmatrix} \boldsymbol{\chi}_\theta^{cT} & \boldsymbol{\chi}_\psi^{cT} \end{bmatrix}^T \qquad \text{where} \qquad \boldsymbol{\chi}_\theta^c := \begin{bmatrix} \alpha_c & q_c & \theta \end{bmatrix}^T \quad \text{and} \quad \boldsymbol{\chi}_\psi^c := \begin{bmatrix} -\beta_c & r_c & \psi \end{bmatrix}^T$$

With respect to the control frame, the angle of attack and the sideslip angle are α_c and β_c. The angular rates around the control frame's pitch and yaw axes are q_c and r_c. Euler angles θ and ψ are defined with respect to the inertial frame and are invariant under a change in roll angle ϕ. The transformation of vehicle states between body-axis frame and control frame is

$$\boldsymbol{\chi}^c = \mathbf{T}(t)\, \boldsymbol{\chi} \tag{4.8}$$

with the time-varying transformation matrix

$$\mathbf{T}(t) = \begin{bmatrix} \cos\phi(t) & 0 & 0 & -\sin\phi(t) & 0 & 0 \\ 0 & \cos\phi(t) & 0 & 0 & -\sin\phi(t) & 0 \\ 0 & 0 & 1 & 0 & 0 & 0 \\ \sin\phi(t) & 0 & 0 & \cos\phi(t) & 0 & 0 \\ 0 & \sin\phi(t) & 0 & 0 & \cos\phi(t) & 0 \\ 0 & 0 & 0 & 0 & 0 & 1 \end{bmatrix}$$

For actuator allocation [61] or *fin-mixing*, we assume that all control surfaces work in a linear regime and that fin forces are proportional to fin deflection. We command both actuators such that the total fin force in the body-axis frame, denoted $F_{Sf}(\delta_r) + F_{Lf}(\delta_e)$ on the right-hand side in Figure 4.1, equals the desired fin force in the control frame, denoted $F_\psi(\delta_r^c) + F_\theta(\delta_e^c)$ on the left-hand side in Figure 4.1. The total fin force is shown as dashed arrow on both sides of Figure 4.1. The input

transformation matrix $\mathbf{T}_{\text{fm}}(t)$ satisfies

$$\begin{bmatrix} \delta_e \\ \delta_r \end{bmatrix} = \begin{bmatrix} \cos\phi(t) & \sin\phi(t) \\ -\sin\phi(t) & \cos\phi(t) \end{bmatrix} \begin{bmatrix} \delta_e^c \\ \delta_r^c \end{bmatrix} \tag{4.9}$$

$$\boldsymbol{\delta} = \mathbf{T}_{\text{fm}}(t)\,\boldsymbol{\delta}^c$$

The demanded elevator fin deflection δ_e^c and the demanded rudder fin deflection δ_r^c are defined in the control frame, see also Section 3.5.1 in [27].

Applying the state and input transformations (4.8) and (4.9) to model (4.5), we obtain the linear equations of motion expressed in the control frame. Referring to state variable changes presented in Chapter 4 in [53], we find

$$\mathbf{E}\,\dot{\boldsymbol{\chi}}^c = \mathcal{A}^c(t)\,\boldsymbol{\chi}^c + \mathcal{B}\,\boldsymbol{\delta}^c \tag{4.10}$$

The inertia matrix $\mathbf{E}$ and the input matrix $\mathcal{B}$ remain unchanged, since

$$\mathbf{T}(t)\,\mathcal{B}\,\mathbf{T}_{\text{fm}}(t) = \mathcal{B} \quad \text{and} \quad \mathbf{T}(t)\,\mathbf{E}\,\mathbf{T}(t)^{-1} = \mathbf{E}$$

In the control frame, the system matrix $\mathcal{A}^c(t)$ becomes

$$\begin{aligned} \mathcal{A}^c(t) &= \mathbf{T}(t)\mathcal{A}_\phi(t)\mathbf{T}(t)^{-1} + \mathbf{E}\,\dot{\mathbf{T}}(t)\mathbf{T}(t)^{-1} \\ &= \begin{bmatrix} \mathbf{A}_\theta + \Delta\mathbf{A}_\theta(t) & \mathbf{A}_{12}^c(t) \\ \mathbf{A}_{21}^c(t) & \mathbf{A}_\psi \end{bmatrix} \end{aligned} \tag{4.11}$$

We recover the time-invariant diagonal elements of the decoupled system matrix $\mathcal{A}$ from (4.4) with the exception of an error term

$$\Delta\mathbf{A}_\theta(t) = \begin{bmatrix} 0 & 0 & 0 \\ 0 & 0 & \alpha_{34} \\ 0 & 0 & 0 \end{bmatrix} [\cos\phi(t) - 1]$$

The off-diagonal matrices are

$$\mathbf{A}_{12}^c(t) = \begin{bmatrix} 0 & 0 & 0 \\ 0 & -J_x p(t) & 0 \\ 0 & 0 & 0 \end{bmatrix} \quad \text{and} \quad \mathbf{A}_{21}^c(t) = \begin{bmatrix} 0 & 0 & 0 \\ 0 & J_x p(t) & -\sin\phi(t) F_w z_{cg} \\ 0 & 0 & 0 \end{bmatrix} \tag{4.12}$$

Comparing $\mathbf{A}_{12}^c(t)$ and $\mathbf{A}_{21}^c(t)$ to $\mathbf{A}_{12}(t)$ and $\mathbf{A}_{21}(t)$ from (4.6) verifies that the number of nonzero off-diagonal coupling terms reduces when transforming the AUV pitch and yaw dynamics from the body-axis frame into the control frame. Moreover, by defining pitch rate q_c and yaw rate r_c with respect to the control frame, kinematic coupling as stated in (4.7) does not occur for model (4.10), and we find $\dot{\theta} = q_c$ and $\dot{\psi} = r_c$ in third and sixth row of (4.10).

4.4 $\mathcal{H}_\infty$ Control Design

In this section, we design an $\mathcal{H}_\infty$ controller that stabilizes the AUV's pitch and yaw motion (4.10) while providing robustness against coupling terms (4.12). We introduce a control synthesis model and motivate the use of weighting filters for control design via loop shaping. The overall feedback control structure is shown in Figure 4.2.

The reference signals for pitch and heading angle are denoted $\boldsymbol{\eta}_{\text{ref}} = \begin{bmatrix} \theta_{\text{ref}} & \psi_{\text{ref}} \end{bmatrix}^T$, while $\boldsymbol{y}_{\text{ref}} = \mathbf{G}_{\text{ref}}\, \boldsymbol{\eta}_{\text{ref}} = \begin{bmatrix} 0 & \theta_{\text{ref}} & 0 & \psi_{\text{ref}} \end{bmatrix}^T$ contains the augmented reference signals for pitch and heading. The transfer function matrix $\mathbf{G}_I(s)$ satisfies

$$\bar{\boldsymbol{e}} \;=\; \mathbf{G}_I(s)\; [\boldsymbol{y}_{\text{ref}} - \boldsymbol{y}]$$

and maps the error signal $\boldsymbol{y}_{\text{ref}} - \boldsymbol{y}$ into the augmented tracking error

$$\bar{\boldsymbol{e}} = \begin{bmatrix} -q_c & \theta_{\text{ref}} - \theta & \theta_I & -r_c & \psi_{\text{ref}} - \psi & \psi_I \end{bmatrix}^T \in \mathbb{R}^6 \tag{4.13}$$

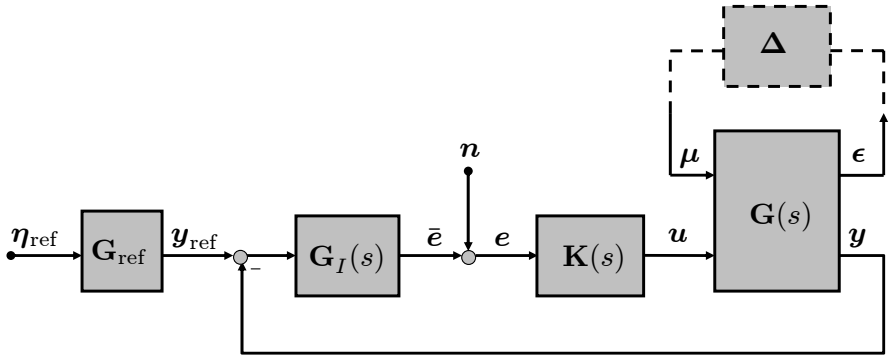

Figure 4.2: Feedback control structure for robust $\mathcal{H}_\infty$ AUV attitude control design.

The integrator states θ_I and ψ_I contained in $\mathbf{G}_I(s)$ satisfy $\dot{\theta}_I = \theta_{\text{ref}} - \theta$ and $\dot{\psi}_I = \psi_{\text{ref}} - \psi$. They are included to achieve zero steady state tracking errors for $\theta_{\text{ref}} - \theta$ and $\psi_{\text{ref}} - \psi$. The controller input signal $\boldsymbol{e} = \bar{\boldsymbol{e}} + \boldsymbol{n}$, $\boldsymbol{e} \in \mathbb{R}^6$, is a superposition of the augmented tracking error $\bar{\boldsymbol{e}}$ and anticipated sensor noise $\boldsymbol{n}$. The controller $\mathbf{K}(s)$ generates the control signal $\boldsymbol{u} = \boldsymbol{\delta}^c$.

The transfer function matrix $\mathbf{G}(s)$ represents the nominal linear model (4.4) that captures the decoupled AUV pitch and yaw motion. The exogenous signals $\boldsymbol{\epsilon}, \boldsymbol{\mu} \in \mathbb{R}^6$ connect $\mathbf{G}(s)$ to parametric uncertainties $\boldsymbol{\Delta}$ through a linear fractional transformation as presented in [47]. Recalling the results of Section 4.3, the state-space representation of

$$\mathbf{G}(s) = \begin{bmatrix} \mathbf{G}_{11}(s) & \mathbf{G}_{12}(s) \\ \mathbf{G}_{21}(s) & \mathbf{G}_{22}(s) \end{bmatrix}$$

is

$$\begin{aligned} \dot{\boldsymbol{\chi}}^c &= \bar{\mathcal{A}}\,\boldsymbol{\chi}^c + \mathbf{I}_6\,\boldsymbol{\mu} + \bar{\mathcal{B}}\,\boldsymbol{u} \\ \boldsymbol{\epsilon} &= \mathbf{I}_6\,\boldsymbol{\chi}^c \\ \boldsymbol{y} &= \bar{\mathcal{C}}\,\boldsymbol{\chi}^c \end{aligned} \tag{4.14}$$

where $\bar{\mathcal{A}} = \mathbf{E}^{-1}\mathcal{A}$ and $\bar{\mathcal{B}} = \mathbf{E}^{-1}\mathcal{B}$ describe the nominal, decoupled AUV dynam-

ics (4.4), and $\mathbf{E}$ is defined in (4.3). We capture model uncertainties, i.e. the off-diagonal terms of $\mathcal{A}^c(t)$ from (4.11), which are not included in $\bar{\mathcal{A}}$, by defining $\boldsymbol{\Delta}$ such that

$$\begin{aligned} \boldsymbol{\Delta} &= \mathbf{E}^{-1} \left[\mathcal{A}^c(t) - \mathcal{A} \right] \\ &= \begin{bmatrix} \mathbf{E}_\theta & \mathbf{0}_{3\times 3} \\ \mathbf{0}_{3\times 3} & \mathbf{E}_\psi \end{bmatrix}^{-1} \begin{bmatrix} \Delta\mathbf{A}_\theta(t) & \mathbf{A}^c_{12}(t) \\ \mathbf{A}^c_{21}(t) & \mathbf{0}_{3\times 3} \end{bmatrix} \end{aligned} \tag{4.15}$$

A quick exercise verifies that setting $\boldsymbol{\mu} = \boldsymbol{\Delta}\,\boldsymbol{\epsilon}$ in (4.14) as illustrated in Figure 4.2 recovers the coupled pitch and yaw system (4.10).

Because measuring linear velocities that define α_c and β_c is not assumed in this work, the avaiable output signals are $\boldsymbol{y} = \begin{bmatrix} q_c & \theta & r_c & \psi \end{bmatrix}^T$. Thus, the output matrix is

$$\bar{\mathcal{C}} = \begin{bmatrix} 0 & 1 & 0 & 0 & 0 & 0 \\ 0 & 0 & 1 & 0 & 0 & 0 \\ 0 & 0 & 0 & 0 & 1 & 0 \\ 0 & 0 & 0 & 0 & 0 & 1 \end{bmatrix}$$

Clearly, our approach can easily be extended to facilitate a fully instrumented AUV for which $\bar{\mathcal{C}} = \mathbf{I}_6$.

We design the controller $\mathbf{K}(s)$ for the feedback control structure in Figure 4.2 by addressing the following closed-loop transfer function matrices. First, the impact of model uncertainties $\boldsymbol{\Delta}$ is characterized by $\mathbf{T}_{\boldsymbol{\epsilon\mu}}(s)$ satisfying $\boldsymbol{\epsilon}(s) = \mathbf{T}_{\boldsymbol{\epsilon\mu}}(s)\boldsymbol{\mu}(s)$. One can derive $\mathbf{T}_{\boldsymbol{\epsilon\mu}}(s)$ from the signal diagram in Figure 4.2

$$\mathbf{T}_{\boldsymbol{\epsilon\mu}}(s) = \mathbf{G}_{11}(s) - \mathbf{G}_{12}(s)\mathbf{K}(s)\mathbf{G}_I(s)\left[\mathbf{I} + \mathbf{G}_{22}(s)\mathbf{K}(s)\mathbf{G}_I(s)\right]^{-1}\mathbf{G}_{21}(s)$$

Second, overall tracking performance is captured by the sensitivity transfer function

matrix $\mathbf{T}_{\bar{\boldsymbol{e}}\boldsymbol{\eta}_{\text{ref}}}(s)$ satisfying $\bar{\boldsymbol{e}}(s) = \mathbf{T}_{\bar{\boldsymbol{e}}\boldsymbol{\eta}_{\text{ref}}}(s)\boldsymbol{\eta}_{\text{ref}}(s)$. We find

$$\mathbf{T}_{\bar{\boldsymbol{e}}\boldsymbol{\eta}_{\text{ref}}}(s) \;=\; \left[\mathbf{I} \,+\, \mathbf{K}(s)\,\mathbf{G}_I(s)\,\mathbf{G}_{22}(s)\right]^{-1}\,\mathbf{G}_I(s)\,\mathbf{G}_{\text{ref}}$$

Third, the transfer of measurement noise from sensors to actuators is defined by $\boldsymbol{u}(s) = \mathbf{T}_{\boldsymbol{un}}(s)\,\boldsymbol{n}(s)$ where

$$\mathbf{T}_{\boldsymbol{un}}(s) \;=\; \left[\mathbf{I} \,+\, \mathbf{K}(s)\,\mathbf{G}_I(s)\,\mathbf{G}_{22}(s)\right]^{-1}\,\mathbf{K}(s)$$

For $\mathcal{H}_\infty$ control design, we define a control design input vector $\tilde{\boldsymbol{w}} \in \mathbb{R}^{14}$ and a control design output vectors $\tilde{\boldsymbol{z}} \in \mathbb{R}^{14}$ as

$$\tilde{\boldsymbol{w}} = \begin{bmatrix}\boldsymbol{\mu}^T & \boldsymbol{\eta}_{\text{ref}}^T & \boldsymbol{n}^T\end{bmatrix}^T \qquad \text{and} \qquad \tilde{\boldsymbol{z}} = \begin{bmatrix}\boldsymbol{\epsilon}^T & \bar{\boldsymbol{e}}^T & \boldsymbol{u}^T\end{bmatrix}^T \tag{4.16}$$

For $\tilde{\boldsymbol{w}}$ and $\tilde{\boldsymbol{z}}$ we derive an unweighted synthesis model $\mathbf{P}(s)$ that satisfies

$$\begin{bmatrix}\tilde{\boldsymbol{z}} \\ \boldsymbol{e}\end{bmatrix} = \begin{bmatrix}\mathbf{P}_{11}(s) & \mathbf{P}_{12}(s) \\ \mathbf{P}_{21}(s) & \mathbf{P}_{22}(s)\end{bmatrix}\begin{bmatrix}\tilde{\boldsymbol{w}} \\ \boldsymbol{u}\end{bmatrix} \tag{4.17}$$

The elements of $\mathbf{P}(s)$ can be deduced from the signal diagram in Figure 4.2. We find

$$\mathbf{P}(s) \;=\; \left[\begin{array}{c|c} \mathbf{P}_{11}(s) & \mathbf{P}_{12}(s) \\ \hline \mathbf{P}_{21}(s) & \mathbf{P}_{22}(s)\end{array}\right]$$

$$= \left[\begin{array}{ccc|c} \mathbf{G}_{11}(s) & \mathbf{0} & \mathbf{0} & \mathbf{G}_{12}(s) \\ -\mathbf{G}_I(s)\mathbf{G}_{21}(s) & \mathbf{G}_I(s)\mathbf{G}_{\boldsymbol{\eta}_{\text{ref}}} & \mathbf{0} & -\mathbf{G}_I(s)\mathbf{G}_{22}(s) \\ \mathbf{0} & \mathbf{0} & \mathbf{0} & \mathbf{I} \\ \hline -\mathbf{G}_I(s)\mathbf{G}_{21}(s) & \mathbf{G}_I(s)\mathbf{G}_{\boldsymbol{\eta}_{\text{ref}}} & \mathbf{I} & -\mathbf{G}_I(s)\mathbf{G}_{22}(s)\end{array}\right]$$

To facilitate loop shaping methods, as presented in [19], [20] and [25], we append weighting filters to each input $\boldsymbol{\mu}$, $\boldsymbol{\eta}_{\text{ref}}$, and $\boldsymbol{n}$ and each output $\boldsymbol{\epsilon}$, $\bar{\boldsymbol{e}}$, and $\boldsymbol{u}$. The

weighted output is $\boldsymbol{z}(s)$, and the output weighting matrix $\mathbf{W}_{\boldsymbol{z}}(s)$ satisfying $\boldsymbol{z}(s) = \mathbf{W}_{\boldsymbol{z}}(s)\tilde{\boldsymbol{z}}(s)$ is defined by

$$\mathbf{W}_{\boldsymbol{z}}(s) = \begin{bmatrix} \mathbf{W}_{\boldsymbol{\epsilon}}(s) & \mathbf{0}_{6\times6} & \mathbf{0}_{6\times2} \\ \mathbf{0}_{6\times6} & \mathbf{W}_{\bar{\boldsymbol{e}}}(s) & \mathbf{0}_{6\times2} \\ \mathbf{0}_{2\times6} & \mathbf{0}_{2\times6} & \mathbf{W}_{\boldsymbol{u}}(s) \end{bmatrix}$$

Similarly, input weighting $\tilde{\boldsymbol{w}}(s) = \mathbf{W}_{\boldsymbol{w}}(s)\boldsymbol{w}(s)$ is defined by

$$\mathbf{W}_{\boldsymbol{w}}(s) = \begin{bmatrix} \mathbf{W}_{\boldsymbol{\mu}}(s) & \mathbf{0}_{6\times2} & \mathbf{0}_{6\times6} \\ \mathbf{0}_{2\times6} & \mathbf{W}_{\boldsymbol{\eta}_{\text{ref}}}(s) & \mathbf{0}_{2\times6} \\ \mathbf{0}_{6\times6} & \mathbf{0}_{6\times2} & \mathbf{W}_{\boldsymbol{n}}(s) \end{bmatrix}$$

As illustrated in Figure 4.3, we append $\mathbf{W}_{\boldsymbol{w}}(s)$ and $\mathbf{W}_{\boldsymbol{z}}(s)$ to $\mathbf{P}(s)$ and obtain the transfer function matrix $\mathbf{T}_{\boldsymbol{zw}}(s)$ satisfying $\boldsymbol{z}(s) = \mathbf{T}_{\boldsymbol{zw}}(s)\boldsymbol{w}(s)$ from a linear fractional transformation

$$\mathbf{T}_{\boldsymbol{zw}}(s) = \mathbf{W}_{\boldsymbol{z}}(s)\left\{\mathbf{P}_{11}(s) + \mathbf{P}_{12}(s)\mathbf{K}(s)\left[\mathbf{I} - \mathbf{P}_{22}(s)\mathbf{K}(s)\right]^{-1}\mathbf{P}_{21}(s)\right\}\mathbf{W}_{\boldsymbol{w}}(s)$$

Utilizing the synthesis model $\mathbf{T}_{\boldsymbol{zw}}(s)$, we design $\mathbf{K}(s)$ such that $\left\|\mathbf{T}_{\boldsymbol{zw}}(s)\right\|_\infty$ is minimized. For a stable, proper transfer function matrix, the infinity-norm $\left\|.\right\|_\infty$ is defined as

$$\left\|\mathbf{T}_{\boldsymbol{zw}}(s)\right\|_\infty = \sup_{\omega\in\mathbb{R}}\left\{\sigma_{\max}\left(\mathbf{T}_{\boldsymbol{zw}}(j\omega)\right)\right\}$$

where $\sigma_{\max}(.)$ denotes the largest singular value. We derive a suboptimal controller $\mathbf{K}(s)$ such that $||\mathbf{T}_{\boldsymbol{zw}}(s)||_\infty < \gamma$ for some $\gamma > 0$. We iteratively decrease γ and refer to Theorem 16.4 in [24] in order to obtain $\mathbf{K}(s)$ for the given γ. This procedure is known as γ-iteration method, see [21] or [25], and continues until a minimum $\gamma_{\min}$ is reached.

The introduction of weighting filter $\mathbf{W}_{\boldsymbol{z}}(s)$ and $\mathbf{W}_{\boldsymbol{w}}(s)$ allows us to emphasize different control design criteria for different frequencies. For example, we choose low-pass

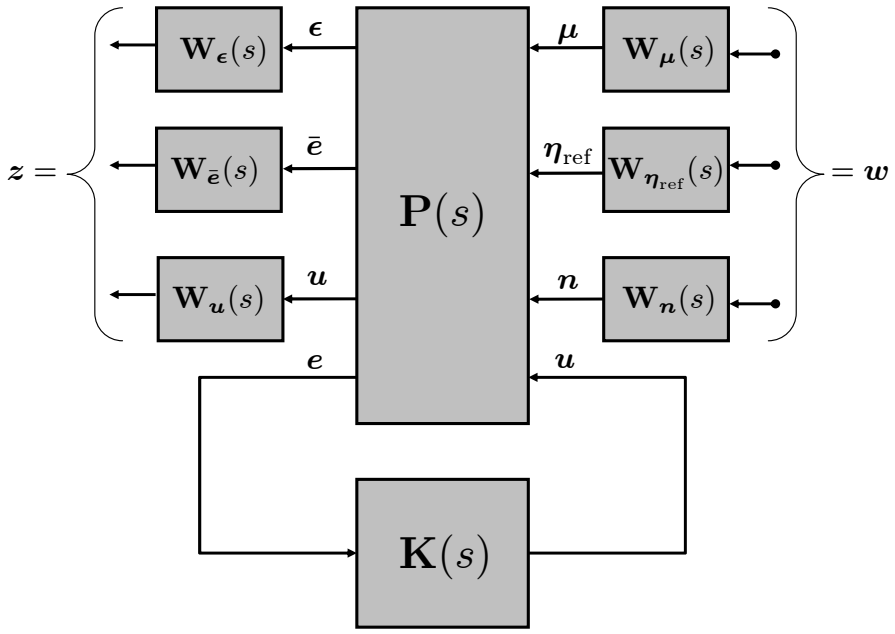

Figure 4.3: Weighted H_∞ synthesis model.

weighting filters for $\mathbf{W}_{\bar{\boldsymbol{e}}}(s)$ and $\mathbf{W}_{\boldsymbol{\eta}_{\text{ref}}}(s)$. After minimizing $\|\mathbf{T}_{\boldsymbol{zw}}(s)\|_\infty$, we obtain a smaller magnitude of the sensitivity function $\mathbf{T}_{\bar{\boldsymbol{e}}\boldsymbol{\eta}_{\text{ref}}}(s)$ and thus better tracking for low frequencies. Similarly, we select high-pass weighting filters for $\mathbf{W}_{\boldsymbol{n}}(s)$ and $\mathbf{W}_{\boldsymbol{u}}(s)$ when minimizing $\|\mathbf{T}_{\boldsymbol{zw}}(s)\|_\infty$ in order to impose low noise propagation $\mathbf{T}_{\boldsymbol{un}}(s)$ for high frequencies.

4.5 Experimental Results

In this section, we validate our control design and present experimental results using the Virginia Tech 475 AUV shown in Figure 1.1. We identify the parameters of model (4.14) by applying ad hoc system identification techniques to flight data that is obtained using separate PID-controllers for pitch and heading axes. We design

an $\mathcal{H}_\infty$ controller $\mathbf{K}(s)$ as described in Section 4.4 and evaluate the performance of the controller.

The flight performance of the Virginia Tech AUV using a separate standard PID-controller for pitch and heading control, as presented in [39], is shown in Figure 4.4. The commanded pitch angle $\theta_{\text{ref}}(t)$, plotted in gray in the upper plot, is chosen to change over time and excites unwanted coupling effects, while the commanded heading angle $\psi_{\text{ref}}(t)$, plotted in gray in the lower plot, is kept constant. The vehicle's pitch angle $\theta(t)$ and heading angle $\psi(t)$ are plotted in black. Note also that the vehicle is ballasted such that steady-state roll is nonzero. Significant oscillations at a frequency of $0.15\,Hz$ are noticeable simultaneously for the pitch and yaw motion, indicating a high level of coupling.

The reference signal $\theta_{\text{ref}}(t)$ excites the AUV's pitch motion and thus enables reliable parameter identification. Applying numerical system identification techniques from [18] or [39] to the flight data from Figure 4.4, we obtain the following parameter estimates for the nominal, linear model (4.4), see also (2.38) in Section 2.6

$$\mathbf{E}_\theta^{-1}\mathbf{A}_\theta = \begin{bmatrix} -1.39 & -0.21 & 0.03 \\ 1 & -0.91 & -0.27 \\ 0 & 1 & 0 \end{bmatrix} \quad \text{and} \quad \mathbf{E}_\theta^{-1}\mathbf{B}_\theta = \begin{bmatrix} -0.89 \\ -1.35 \\ 0 \end{bmatrix}$$

Due to the symmetry of the AUV's body, we assume the same system dynamics for the yaw motion, with the exception of the restoring pitch moment. Thus, we assume $\mathbf{E}_\theta^{-1}\mathbf{B}_\theta = \mathbf{E}_\psi^{-1}\mathbf{B}_\psi$ and

$$\mathbf{E}_\psi^{-1}\mathbf{A}_\psi = \begin{bmatrix} -1.39 & -0.21 & 0 \\ 1 & -0.91 & 0 \\ 0 & 1 & 0 \end{bmatrix}$$

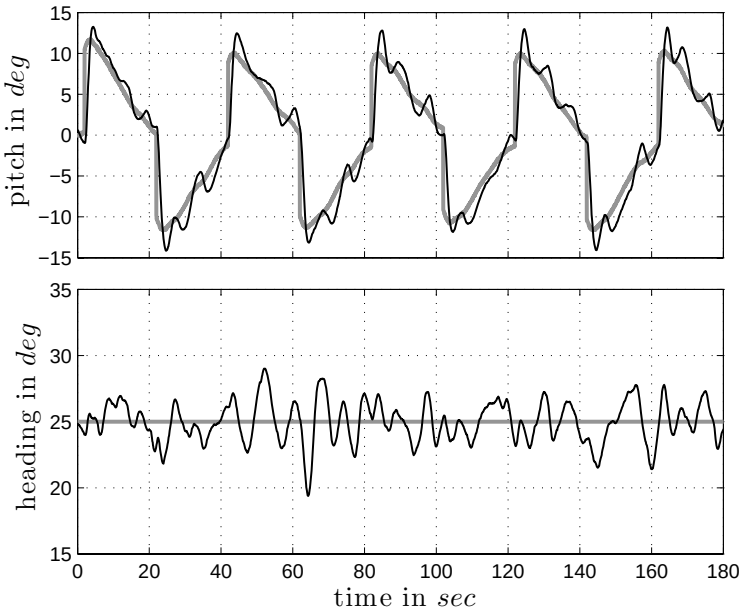

Figure 4.4: Flight performance of the Virginia Tech 475 AUV using standard PID control for pitch and heading. Commanded and actual pitch trajectory $\theta_{\text{ref}}(t), \theta(t)$ are shown in the upper plot in gray and black, respectively. The lower plot shows heading performance with commanded heading angle $\psi_{\text{ref}}(t)$ in gray and actual heading angle $\psi(t)$ in black.

For the presented field trials, we select first-order low-pass weighting filters $\mathbf{W}_{\boldsymbol{\eta}_{\text{ref}}}(s)$ and $\mathbf{W}_{\tilde{\boldsymbol{e}}}(s)$ with a cutoff frequency of $0.25\,Hz$, and first-order high-pass weighting filters $\mathbf{W}_{\boldsymbol{n}}(s)$ and $\mathbf{W}_{\boldsymbol{u}}(s)$ with a cutoff frequency of $2\,Hz$. Additionally we choose

$$\mathbf{W}_{\boldsymbol{\mu}}(s) = \mathbf{W}_{\boldsymbol{\epsilon}}(s) = \mathbf{I}_6$$

Given the parameter estimates for the AUV model (4.14) and the selection of weighting filters $\mathbf{W}_{\boldsymbol{w}}(s)$ and $\mathbf{W}_{\boldsymbol{z}}(s)$, we refer to Theorem 16.4 in [24] and numerically

minimize $\|\mathbf{T}_{\boldsymbol{zw}}(s)\|_\infty$ via γ-iteration. We find

$$\gamma_{\min} = 4.6 \qquad \text{and} \qquad \|\mathbf{T}_{\boldsymbol{zw}}(s)\|_\infty = 4.599 \approx 13.25\,\text{dB}$$

Figure 4.5 shows the singular value plot for $\mathbf{T}_{\boldsymbol{zw}}(s)$.

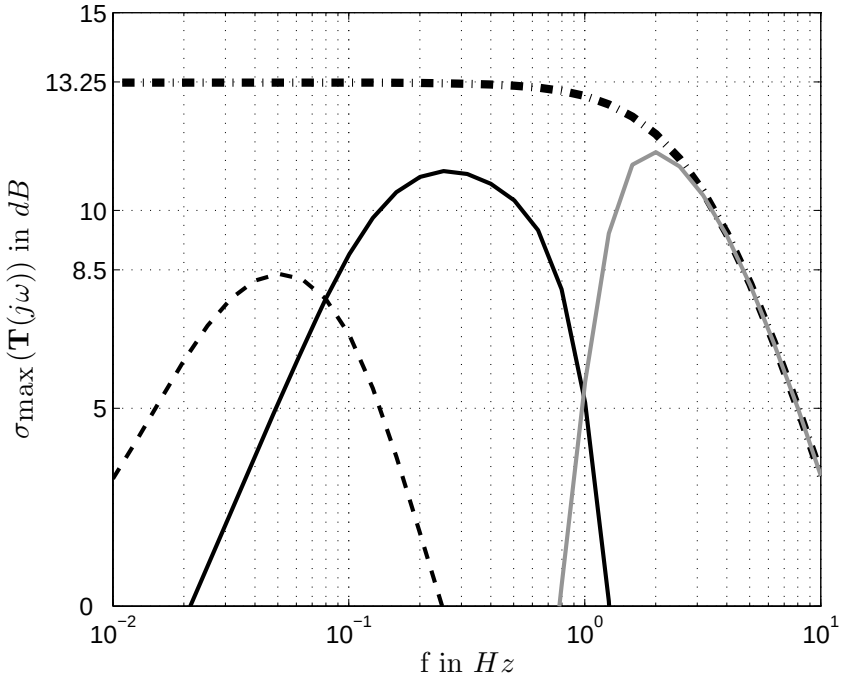

Figure 4.5: Singular value plots of weighted transfer function matrices: overall system $\mathbf{T}_{\boldsymbol{zw}}(s)$ in dashed-dotted, thick black, weighted tracking performance $\mathbf{W}_{\bar{\boldsymbol{e}}}(s)\mathbf{T}_{\bar{\boldsymbol{e}}\boldsymbol{\eta}_{\text{ref}}}(s)\mathbf{W}_{\boldsymbol{\eta}_{\text{ref}}}(s)$ in solid black, weighted robustness $\mathbf{W}_{\boldsymbol{\epsilon}}(s)\mathbf{T}_{\boldsymbol{\epsilon\mu}}(s)\mathbf{W}_{\boldsymbol{\mu}}(s)$ in dashed black, and weighted noise reduction $\mathbf{W}_{\boldsymbol{u}}(s)\mathbf{T}_{\boldsymbol{un}}(s)\mathbf{W}_{\boldsymbol{n}}(s)$ in gray.

The singular value plot for the weighted sensitivity function $\mathbf{W}_{\bar{\boldsymbol{e}}}(s)\mathbf{T}_{\bar{\boldsymbol{e}}\boldsymbol{\eta}_{\text{ref}}}(s)\mathbf{W}_{\boldsymbol{\eta}_{\text{ref}}}(s)$ is shown in solid black. We find a small magnitude for low frequencies and thus

good tracking. The small magnitude at high frequencies is due to choosing low pass weighting filters $\mathbf{W}_{\bar{e}}(s)$ and $\mathbf{W}_{\eta_{\text{ref}}}(s)$. The singular values of $\mathbf{W}_{\boldsymbol{u}}(s)\mathbf{T}_{\boldsymbol{un}}(s)\mathbf{W}_{\boldsymbol{n}}(s)$, representing the weighted transfer function from sensor noise to control inputs, is plotted in gray. It is evident that the control design emphasis shifts from tracking performance (black) dominating $\mathbf{T}_{\boldsymbol{zw}}(s)$ at lower frequencies to noise reduction (gray) dominating $\mathbf{T}_{\boldsymbol{zw}}(s)$ at higher frequencies. The separation occurs at around $1\,Hz$.

Robustness is characterized by $\mathbf{W}_{\boldsymbol{\epsilon}}(s)\mathbf{T}_{\boldsymbol{\epsilon\mu}}(s)\mathbf{W}_{\boldsymbol{\mu}}(s)$ shown in dashed black, where smaller magnitudes indicate increased robustness. In particular, the small gain theorem [54] implies that the closed-loop system remains stable for all cross-coupling matrices $\boldsymbol{\Delta}$ that satisfy

$$\|\boldsymbol{\Delta}\|_\infty < \|\mathbf{T}_{\boldsymbol{\epsilon\mu}}(s)\|_\infty^{-1} = [8.5\,\text{dB}]^{-1} \approx 0.375$$

Note, that the weighting filters $\mathbf{W}_{\boldsymbol{\mu}}(s)$ and $\mathbf{W}_{\boldsymbol{\epsilon}}(s)$ satisfy $\|\mathbf{W}_{\boldsymbol{\mu}}(s)\|_\infty = 1$ and $\|\mathbf{W}_{\boldsymbol{\epsilon}}(s)\|_\infty = 1$, and the maximum singular value of $\mathbf{T}_{\boldsymbol{\epsilon\mu}}(s)$ (dashed black), here 8.5 dB, can be read from Figure 4.5.

Figure 4.6 shows the open-loop actuator frequency responses for elevator fin deflection δ_e (dashed) and rudder fin deflection δ_r (dotted) controlling pitch and heading, respectively. For both channels, the $\mathcal{H}_\infty$ control design approach requires an actuator bandwidth of less than $0.5\,Hz$ and provides a phase margin of more than $60\,deg$.

The flight performance of the Virginia Tech 475 AUV using $\mathcal{H}_\infty$ control is shown in Figure 4.7. We notice better tracking performance as compared to Figure 4.4. Pitch and yaw motion appear to be less oscillatory and completely uncorrelated implying significant reduction of coupling. Thus, comparing the flight performances between Figure 4.7 and Figure 4.4 verifies the effectiveness of the control design and the robustness of the multi-input multi-output $\mathcal{H}_\infty$ controller.

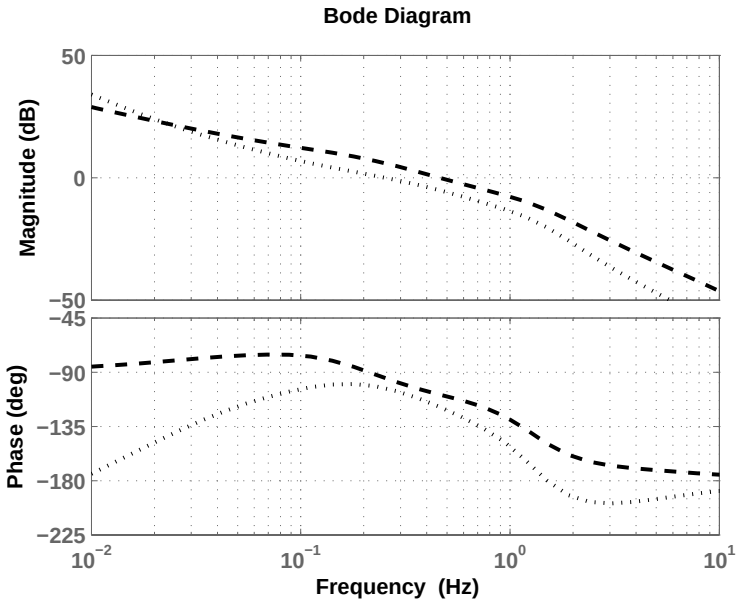

Figure 4.6: Open-loop frequency response for elevator (dashed) controlling pitch and rudder (dotted) controlling heading.

4.6 Conclusions

In this paper, we derive a novel linear time-varying model that captures the coupled pitch and yaw motion of an AUV. Our analysis shows that roll motion causes coupling between pitch and yaw dynamics, which is commonly neglected for AUV control design. We propose the use of an upright AUV body frame in which the linear model representation contains fewer nonzero off-diagonal terms. Our model facilitates the use of an $\mathcal{H}_\infty$ control design approach that specifically addresses the remaining coupling terms as structured uncertainties.

We conducted field trials using the Virginia Tech 475 AUV for which a linear model is identified in situ from flight data. Experimental field trials show that the $\mathcal{H}_\infty$ con-

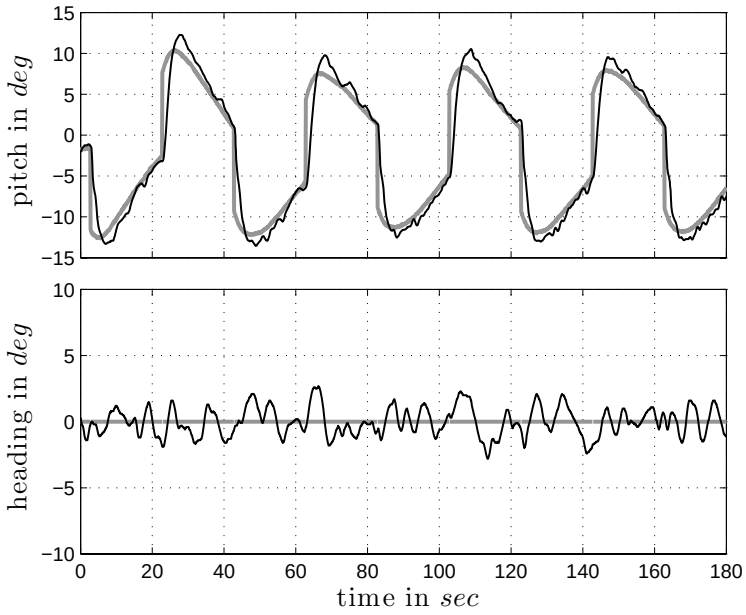

Figure 4.7: Flight performance of the Virginia Tech 475 AUV using the multi-input multi-output $\mathcal{H}_\infty$ controller $\mathbf{K}(s)$. Commanded and actual pitch trajectory $\theta_{\text{ref}}(t), \theta(t)$ are shown in the upper plot in gray and black, respectively. The lower plot shows heading performance with commanded heading angle $\psi_{\text{ref}}(t)$ in gray and actual heading angle $\psi(t)$ in black.

troller improves the tracking performance and decreases the coupling between pitch and yaw motion in comparison to single axis PID controllers implemented separately for pitch and yaw.

Chapter 5

Gyroscope Calibration

In this chapter, we propose the calibration of a tri-axis gyroscope array commonly used in the navigation system of submersibles. Under the assumption that no position reference GPS or LBL is available underwater, the AUV must rely on inertial measurements provided by gyroscope stabilized attitude sensors in order to deduce a position estimate. To increase the accuracy of inertial navigation or dead reckoning, an error model is presented containing offset and scaling parameters for each gyroscope, and identification techniques from Chapter 3 are deployed to estimate those calibration parameters. Sufficient excitation conditions for gyroscope measurements are derived so that successful parameter identification is guaranteed. Experimental results validate the identification techniques by calibrating a tri-axis microelectromechanical system (MEMS) gyroscope array of a miniature AUV.

5.1 Introduction

Improved inertial navigation can be obtained from increased accuracy of angular orientation measurements through pre-flight sensor calibration [62] or from the usage of high-precision sensors [63]. Due to weight, size and cost constraints, the integration of inertial navigation units (IMUs) into small scale AUV applications is impossible. MEMS technology provides a trade-off between accurate inertial measurements and sensor size [64], and thus allows miniature AUVs such as the ASCL's AUV [65] to perform modest-accuracy inertial navigation using three strap-down single-axis resonator gyroscopes.

Measured body-fixed angular rates are commonly used to stabilize an electronic compass and thus to improve the accuracy of heading measurements utilized for dead reckoning. Errors inherent in sensing angular velocities are caused by inaccuracies in sensor construction, temperature dependencies, and the physical size of the sensor [66]. To overcome the inherent navigation errors due to sensor drift, significant research efforts are devoted to the online calibration of inertial sensors. Calibration techniques for heading sensors, gyroscope and accelerometer configurations are discussed in [67], [28] and [68]. We adapt and extend the single-axis calibration error model from [67] to address a tri-axis gyroscope array. Moreover, we derive sufficient conditions under which successful parameter estimation is guaranteed. Suggested by experimental results in [69], we address only bias and scale factor errors for the work reported herein.

This chapter is organized as follows. An error model for the gyroscope array is introduced in Section 5.2. The angular orientation of the array is described using both Euler angles and an attitude quaternion. In Section 5.3, we show that system identification techniques presented in Chapter 3 can be employed without modifications

to estimate the calibration parameters of the gyroscope error model.Experimental results are presented in Section 5.4.

5.2 Gyroscope Model

The angular displacement of a rigid body with respect to the inertial frame is expressed using Euler angles, ϕ, θ, ψ, representing roll, pitch, and yaw, respectively. The vector of Euler angles is denoted $\boldsymbol{\eta}(t) = [\phi(t)\, \theta(t)\, \psi(t)]^T \in \mathbb{R}^3$. For most naval and aerospace applications, Euler angles are directly accessible through compass and tilt sensors. In this work, the body-fixed angular rates of a rigid body are expressed as $\boldsymbol{\omega}(t) = [p(t)\, q(t)\, r(t)]^T \in \mathbb{R}^3$. The relationship between Euler rates $\dot{\boldsymbol{\eta}}(t)$ and body fixed angular rates is

$$\dot{\boldsymbol{\eta}}(t) \;=\; \mathbf{R}_{\boldsymbol{\eta}}(\boldsymbol{\eta}(t))\, \boldsymbol{\omega}(t) \tag{5.1}$$

where

$$\mathbf{R}_{\boldsymbol{\eta}}(\boldsymbol{\eta}(t)) = \begin{bmatrix} 1 & \sin\phi(t)\tan\theta(t) & \cos\phi(t)\tan\theta(t) \\ 0 & \cos\phi(t) & -\sin\phi(t) \\ 0 & \dfrac{\sin\phi(t)}{\cos\theta(t)} & \dfrac{\cos\phi(t)}{\cos\theta(t)} \end{bmatrix}$$

The subscript $\boldsymbol{\eta}$ emphasizes the usage of Euler angles. Note that the matrix $\mathbf{R}_{\boldsymbol{\eta}}(\boldsymbol{\eta}(t))$ is non-singular

$$\begin{aligned} \det\left\{\mathbf{R}_{\boldsymbol{\eta}}(\boldsymbol{\eta}(t))\mathbf{R}^T_{\boldsymbol{\eta}}(\boldsymbol{\eta}(t))\right\} &= \left[\det\left\{\mathbf{R}_{\boldsymbol{\eta}}(\boldsymbol{\eta}(t))\right\}\right]^2 \\ &= \frac{1}{\cos^2\theta(t)} \\ &\neq 0 \end{aligned} \tag{5.2}$$

except for a pitch angle $\theta(t) = \dfrac{\pi}{2} + k\,\pi$, $k \in \mathbb{Z}$ for which $\mathbf{R}_{\boldsymbol{\eta}}(\boldsymbol{\eta}(t))$ is not defined. For this reason, we refer to [1] and alternatively utilize an attitude quaternion or Euler

parameters to describe the vehicle's angular orientation. In [70], such an attitude quaternion $\mathbf{q}$ is defined as a complex number

$$\mathbf{q} = q_0 + q_1\mathbf{i} + q_2\mathbf{j} + q_3\mathbf{k} \qquad \text{with} \qquad q_i \in \mathbb{R}, \qquad i = 1, 2, 3, 4 \tag{5.3}$$

where $\mathbf{i}$,$\mathbf{j}$, and $\mathbf{k}$ are orthogonal unit vectors. An introduction into the geometry and arithmetic of quaternions can be found in [71]. For this application, a unit quaternion $\mathbf{q}$ with

$$\begin{aligned} \mathbf{q}^T\mathbf{q} &= q_0^2 + q_1^2 + q_2^2 + q_3^2 \\ &= 1 \end{aligned} \tag{5.4}$$

is constructed as suggested in [72] utilizing Euler angles

$$\begin{aligned} q_0(t) &= \cos\frac{\psi(t)}{2}\cos\frac{\theta(t)}{2}\cos\frac{\phi(t)}{2} + \sin\frac{\psi(t)}{2}\sin\frac{\theta(t)}{2}\sin\frac{\phi(t)}{2} \\ q_1(t) &= \cos\frac{\psi(t)}{2}\cos\frac{\theta(t)}{2}\sin\frac{\phi(t)}{2} - \sin\frac{\psi(t)}{2}\sin\frac{\theta(t)}{2}\cos\frac{\phi(t)}{2} \\ q_2(t) &= \cos\frac{\psi(t)}{2}\sin\frac{\theta(t)}{2}\cos\frac{\phi(t)}{2} + \sin\frac{\psi(t)}{2}\cos\frac{\theta(t)}{2}\sin\frac{\phi(t)}{2} \\ q_3(t) &= \sin\frac{\psi(t)}{2}\cos\frac{\theta(t)}{2}\cos\frac{\phi(t)}{2} - \cos\frac{\psi(t)}{2}\sin\frac{\theta(t)}{2}\sin\frac{\phi(t)}{2} \end{aligned} \tag{5.5}$$

The inverse mapping of (5.5) is

$$\begin{aligned} \phi(t) &= \arctan\left(\frac{2\left(q_2(t)q_3(t) + q_0(t)q_1(t)\right)}{q_0^2(t) - q_1^2(t) - q_2^2(t) + q_3^2(t)}\right) \\ \theta(t) &= -\arcsin\Big(2q_1(t)q_3(t) - 2q_0(t)q_2(t)\Big) \\ \psi(t) &= \arctan\left(\frac{2\left(q_1(t)q_2(t) + q_0(t)q_3(t)\right)}{q_0^2(t) + q_1^2(t) - q_2^2(t) - q_3^2(t)}\right) \end{aligned} \tag{5.6}$$

The update equation for $\mathbf{q}(t)$, similar to (5.1), is given by

$$\dot{\mathbf{q}}(t) \;=\; \mathbf{R}_{\mathbf{q}}(\mathbf{q}(t))\,\boldsymbol{\omega}(t) \tag{5.7}$$

where

$$\mathbf{R}_{\mathbf{q}}(\mathbf{q}(t)) \;=\; \frac{1}{2}\begin{bmatrix} -q_1(t) & -q_2(t) & -q_3(t) \\ q_0(t) & -q_3(t) & q_2(t) \\ q_3(t) & q_0(t) & -q_1(t) \\ -q_2(t) & q_1(t) & q_0(t) \end{bmatrix}$$

Here, the subscript $\mathbf{q}$ emphasizes the use of an attitude quaternion. In contrast to the transformation matrix $\mathbf{R}_{\boldsymbol{\eta}}(\boldsymbol{\eta}(t))$ described by Euler angles (5.1), the matrix $\mathbf{R}_{\mathbf{q}}(\mathbf{q}(t))$ is always defined. Straightforward computation regarding the constraint (5.4) shows

$$\mathbf{R}_{\mathbf{q}}^{T}(\mathbf{q}(t))\,\mathbf{R}_{\mathbf{q}}(\mathbf{q}(t)) \;=\; \frac{1}{4}\,\mathbf{I}_{3\times 3} \tag{5.8}$$

where $\mathbf{I}$ represents the identity matrix of dimension denoted by the subscripts.

For many autonomous vehicle applications, compass and tilt-sensors directly measure Euler angles, and hence the transformation matrices $\mathbf{R}_{\boldsymbol{\eta}}(\boldsymbol{\eta}(t))$ and $\mathbf{R}_{\mathbf{q}}(\mathbf{q}(t))$ are known at all times.

Note, as discussed in [73] the discrete-time propagation of (5.7) is

$$\mathbf{q}(k+1) = \mathbf{q}(k) * \breve{\boldsymbol{\omega}}(k) \tag{5.9}$$

where $*$ denotes quaternion multiplication introduced in [71], and $\breve{\boldsymbol{\omega}}(k)$ is given by

$$\breve{\boldsymbol{\omega}}(k) = \begin{bmatrix} \cos\left(\dfrac{1}{2}\,|\boldsymbol{\omega}(k)|\,h\right) \\ \\ \dfrac{\boldsymbol{\omega}(k)}{|\boldsymbol{\omega}(k)|}\sin\left(\dfrac{1}{2}\,|\boldsymbol{\omega}(k)|\,h\right) \end{bmatrix} \qquad \in \mathbb{R}^4$$

The sample period for the system (5.9) is h. The discrete-time quaternion propagation (5.9) preserves unity length of $\mathbf{q}$, but constitutes a non-linear update law with respect to $\boldsymbol{\omega}$. Therefore, a small angle approximation $\frac{1}{2}|\boldsymbol{\omega}(k)|\,h << 1$, justifiable for this application, is applied

$$\begin{aligned} \mathbf{q}(k+1) &= \mathbf{q}(k) * \begin{bmatrix} 1 \\ \frac{1}{2}\,\boldsymbol{\omega}(k)\,h \end{bmatrix} \\ &= \mathbf{q}(k) + h\,\mathbf{R}_{\mathbf{q}}(\mathbf{q}(k))\,\boldsymbol{\omega}(k) \end{aligned} \tag{5.10}$$

In order to avoid *quaternion drift,* that is to maintain unity length (5.4), a normalization is required during each sample period.

5.3 Calibration Model

The measurement model for the tri-axial gyroscope combines scaling errors a_ϕ, a_θ, a_ψ and bias errors b_ϕ, b_θ, b_ψ

$$\begin{bmatrix} p(t) \\ q(t) \\ r(t) \end{bmatrix} = \begin{bmatrix} p_m(t) & 0 & 0 \\ 0 & q_m(t) & 0 \\ 0 & 0 & r_m(t) \end{bmatrix} \begin{bmatrix} a_\phi \\ a_\theta \\ a_\psi \end{bmatrix} + \begin{bmatrix} b_\phi \\ b_\theta \\ b_\psi \end{bmatrix} \tag{5.11}$$

The vector of gyroscope measurements is $\boldsymbol{\omega}_m(t) = [p_m(t),\, q_m(t),\, r_m(t)]^T$, and the vector of unknown calibration parameters is defined as

$$\mathbf{p}_{\boldsymbol{\eta}} = \begin{bmatrix} a_\phi & a_\theta & a_\psi & b_\phi & b_\theta & b_\psi \end{bmatrix}^T$$

The existence of a constant vector $\mathbf{p}_{\boldsymbol{\eta}}$ satisfying (5.11) is assumed. Incorporating the calibration model (5.11) containing scale and bias errors into the update equation for

the attitude quaternion (5.7) finally yields

$$\begin{aligned} \dot{\mathbf{q}}(t) &= \mathbf{R}_{\mathbf{q}}(\mathbf{q}(t))\, \boldsymbol{\omega}^T\left(\boldsymbol{\omega}_m(t)\right)\, \mathbf{p}_{\boldsymbol{\eta}} \\ \mathbf{y}_{\mathbf{q}}(t) &= \mathbf{q}(t) \end{aligned} \tag{5.12}$$

Here, the time-varying matrix $\boldsymbol{\Omega}^T\left(\boldsymbol{\omega}_m(t)\right)$ with

$$\boldsymbol{\Omega}^T\left(\boldsymbol{\omega}_m(t)\right) = \begin{bmatrix} p_m(t) & 0 & 0 & 1 & 0 & 0 \\ 0 & q_m(t) & 0 & 0 & 1 & 0 \\ 0 & 0 & r_m(t) & 0 & 0 & 1 \end{bmatrix}$$

contains the gyroscope measurements. The output equation captures the attitude measurements $\boldsymbol{\eta}(t)$ via compass and tilt sensors which determine $\mathbf{q}(t)$ uniquely, see (5.5). A representation of (5.12) based on the update equations for Euler angles (5.1) is expressed as

$$\begin{aligned} \dot{\boldsymbol{\eta}}(t) &= \mathbf{R}_{\boldsymbol{\eta}}(\boldsymbol{\eta}(t))\, \boldsymbol{\Omega}^T\left(\boldsymbol{\omega}_m(t)\right)\, \mathbf{p}_{\boldsymbol{\eta}} \\ \mathbf{y}_{\boldsymbol{\eta}}(t) &= \boldsymbol{\eta}(t) \end{aligned} \tag{5.13}$$

We utilize the error models (5.12) and (5.13) as framework to calibrate the gyroscopes by identifying the scale and bias coefficients comprised in $\mathbf{p}_{\boldsymbol{\eta}}$. The similarity between (5.12) and (5.13) is noted in the sequel and enables analytic results addressing parameter identification for one case to be nearly directly valid for the other one. Both models (5.12) and (5.13) can be parameterized in a form equivalent to those addressed in Chapter 3, see (3.3) and (3.4). Thus, system identification techniques from Chapter 3 can immediately be deployed to estimate $\mathbf{p}_{\boldsymbol{\eta}}$. In particular, for the Euler angle representation (5.13) we find

$$\begin{aligned} \dot{\mathbf{x}}_{\boldsymbol{\eta}}(t) &= \mathbf{A}_{\boldsymbol{\eta}}\mathbf{x}_{\boldsymbol{\eta}}(t) + \mathbf{W}_{\boldsymbol{\eta}}^T(t)\mathbf{p}_{\boldsymbol{\eta}} \\ \mathbf{y}_{\boldsymbol{\eta}}(t) &= \mathbf{x}_{\boldsymbol{\eta}}(t) \end{aligned} \tag{5.14}$$

where the state vector is $\mathbf{x}_{\boldsymbol{\eta}}(t) = \boldsymbol{\eta}(t) \in \mathbb{R}^3$, the system matrix is $\mathbf{A}_{\boldsymbol{\eta}} = \mathbf{0}_{3\times 3}$ and the regressor matrix is $\mathbf{W}_{\boldsymbol{\eta}}^T(t) = \mathbf{R}_{\boldsymbol{\eta}}(\boldsymbol{\eta}(t))\, \boldsymbol{\Omega}^T(\boldsymbol{\omega}_m(t)) \in \mathbb{R}^{3\times 6}$. We assume that $\mathbf{R}_{\boldsymbol{\eta}}(\boldsymbol{\eta}(t))$ is defined for all t. Similarly using an attitude quaternion (5.12), we find

$$\begin{aligned} \dot{\mathbf{x}}_q(t) &= \mathbf{A}_q \mathbf{x}_q(t) + \mathbf{W}_q^T(t)\mathbf{p}_{\boldsymbol{\eta}} \\ \mathbf{y}_q(t) &= \mathbf{x}_q(t) \end{aligned} \tag{5.15}$$

The state vector is $\mathbf{x}_q(t) = \mathbf{q}(t) \in \mathbb{R}^4$, the system matrix is $\mathbf{A}_q = \mathbf{0}_{4\times 4}$, and the regressor matrix is $\mathbf{W}_q^T(t) = \mathbf{R}_{\mathbf{q}}(\mathbf{q}(t))\, \boldsymbol{\Omega}^T(\boldsymbol{\omega}_m(t)) \in \mathbb{R}^{4\times 6}$.

Since $\mathbf{R}_{\mathbf{q}}(\mathbf{q}(t))$ and $\mathbf{R}_{\boldsymbol{\eta}}(\boldsymbol{\eta}(t))$ are full rank for all t, a persistently exciting matrix $\boldsymbol{\Omega}^T(\boldsymbol{\omega}_m(t))$ suffices to guarantee persistence of excitation for $\mathbf{W}_q^T(t)$ and $\mathbf{W}_{\boldsymbol{\eta}}^T(t)$, and thus parameter convergence using either an adaptive identifier or a Kalman filter.

Note, that persistence of excitation is only a function of measured angular rates $\boldsymbol{\omega}_m(t)$, and neither the vehicle's attitude $\mathbf{q}(t), \boldsymbol{\eta}(t)$ nor the true body-fixed angular rates $\boldsymbol{\omega}(t)$ effect the PE property.

5.4 Experimental Results

To demonstrate the gyroscope calibration, we deploy identification algorithms from Chapter 3 using a data set recorded from a tri-axis gyroscope array of a miniature autonomous underwater vehicle, the ASCL's AUV [65]. The vehicle is excited manually on the test bench in order to provide sufficiently rich gyroscope measurements in all three axes, see thick gray line in Figure 5.2 on page 114. Identification methods are applied to the data set, and the resulting steady state calibration parameters $\hat{\mathbf{p}}_{\boldsymbol{\eta}}^T = \left[\hat{\mathbf{a}}_{\boldsymbol{\eta}}^T\ \hat{\mathbf{b}}_{\boldsymbol{\eta}}^T\right]$ are shown in Table 5.1 using algorithms based on the quaternion integration (5.15) and in Table 5.2 using algorithms based on the Euler angle integration (5.14). For both cases, the adaptive identifier, Kalman filter, and least squares

solution are denoted by ai, kf, and ls, respectively.

Table 5.1: Estimated calibration parameters $\hat{\mathbf{p}}_{\boldsymbol{\eta}}$ for the three identification techniques using an attitude quaternion or Euler parameters (5.12), $\hat{\mathbf{b}}_{\boldsymbol{\eta}}$ in $deg\,s^{-1}$.

	$\hat{\mathbf{a}}_{\boldsymbol{\eta},ai}$	$\hat{\mathbf{a}}_{\boldsymbol{\eta},kf}$	$\hat{\mathbf{a}}_{\boldsymbol{\eta},ls}$	$\hat{\mathbf{b}}_{\boldsymbol{\eta},ai}$	$\hat{\mathbf{b}}_{\boldsymbol{\eta},kf}$	$\hat{\mathbf{b}}_{\boldsymbol{\eta},ls}$
ϕ	1.075	1.109	1.103	2.306	2.311	2.299
θ	1.179	1.191	1.194	12.752	12.831	12.982
ψ	1.080	1.147	1.129	−7.909	−8.539	−8.365

Table 5.2: Estimated calibration parameters $\hat{\mathbf{p}}_{\boldsymbol{\eta}}$ for the three identification techniques using Euler angles (5.13), $\hat{\mathbf{b}}_{\boldsymbol{\eta}}$ in $deg\,s^{-1}$.

	$\hat{\mathbf{a}}_{\boldsymbol{\eta},ai}$	$\hat{\mathbf{a}}_{\boldsymbol{\eta},kf}$	$\hat{\mathbf{a}}_{\boldsymbol{\eta},ls}$	$\hat{\mathbf{b}}_{\boldsymbol{\eta},ai}$	$\hat{\mathbf{b}}_{\boldsymbol{\eta},kf}$	$\hat{\mathbf{b}}_{\boldsymbol{\eta},ls}$
ϕ	1.078	1.109	1.098	2.241	2.371	2.392
θ	1.187	1.196	1.190	12.404	12.625	12.589
ψ	1.135	1.152	1.105	−8.639	−8.562	−8.120

In Figure 5.1, the transients of the parameter estimation via adaptive identifier are shown, using an attitude quaternion (black) and Euler angles (gray). As time evolves, bias parameters $\hat{\mathbf{b}}_{\boldsymbol{\eta}}(t)$ (right column) and scaling errors $\hat{\mathbf{a}}_{\boldsymbol{\eta}}(t)$ (left column) converge for both approaches. Evidently, the gyroscope measurements provide sufficient excitation for the entire data set. The final values in Table 5.1 and 5.2 are the respective averages over the last 15 seconds.

We evaluate the quality of the identified calibration parameters by estimating the

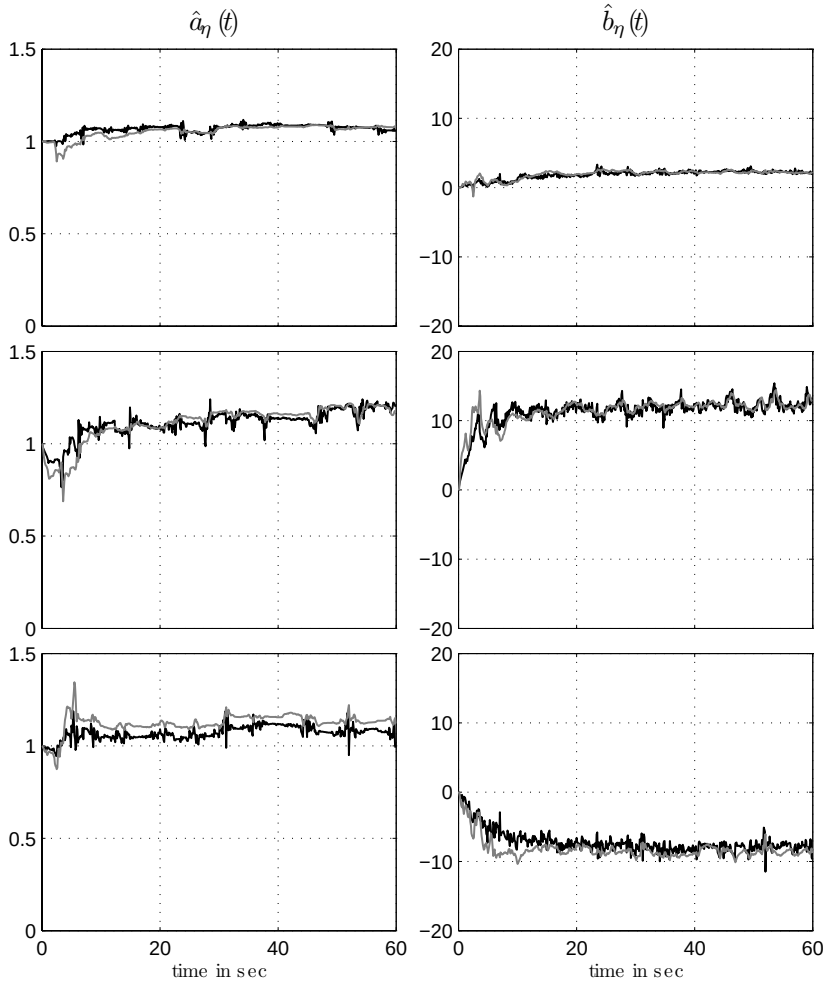

Figure 5.1: Parameter estimation utilizing the adaptive identifier applied to the gyroscope model (5.12) using an attitude quaternion $\mathbf{q}(t)$ (black) and to the gyroscope model (5.13) using Euler angles $\boldsymbol{\eta}(t)$ (gray). The left and right columns visualize the convergence of the calibration parameters $\hat{\mathbf{a}}_{\boldsymbol{\eta}}(t)$ and $\hat{\mathbf{b}}_{\boldsymbol{\eta}}(t)$, respectively, with $\hat{\mathbf{b}}_{\boldsymbol{\eta}}(t)$ in $deg\, s^{-1}$. From top to bottom, the plots show the estimated calibration parameters for roll rate $\hat{a}_\phi(t)$, $\hat{b}_\phi(t)$, pitch rate $\hat{a}_\theta(t)$, $\hat{b}_\theta(t)$, and yaw rate $\hat{a}_\psi(t)$, $\hat{b}_\psi(t)$.

vehicle's attitude using gyroscope measurements only. For reasons of practicality, Euler angles are preferred for the visualization of estimated and measured attitude of the vehicle. The raw gyroscope data is calibrated using the identified parameters summarized in Table 5.1 and Table 5.2. The calibrated angular rates are rotated into the inertial frame via estimated Euler angles (5.1), and integrated forward in time to get an estimate $\hat{\boldsymbol{\eta}}(t)$

$$\hat{\boldsymbol{\eta}}(t) = \boldsymbol{\eta}(t_0) + \int_{t_0}^{t} \mathbf{R}_{\boldsymbol{\eta}}(\hat{\boldsymbol{\eta}}(\sigma))\, \mathbf{W}^T\left(\boldsymbol{\omega}_m(\sigma)\right)\, \hat{\mathbf{p}}_{\boldsymbol{\eta}}\, d\sigma \tag{5.16}$$

Figure 5.2 and 5.3 show the estimated vehicle's attitude in Euler angles using the identified parameters of each identification technique, adaptive identifier (dashed), Kalman filter (dotted), and least squares (solid). In Figure 5.2, we propagate (5.16) using calibration parameters $\hat{\mathbf{p}}_{\boldsymbol{\eta}}$ from Table 5.1, while Figure 5.3 shows the propagation of (5.16) using calibration parameters $\hat{\mathbf{p}}_{\boldsymbol{\eta}}$ from Table 5.2.

Figure 5.2 and 5.3 illustrate that each of the identification methods provides parameter estimations that allow integrated gyroscope readings to smoothly track the measured angular orientation with minimal drift. Table 5.3 contains the root-mean-square estimation error for each algorithm over the 60 seconds of vehicle motion.

As expected, the least squares fit generates the smallest error, but its applicability is limited to off-line analysis. For this reason, it is compelling to observe that a Kalman filter and an adaptive identifier, algorithms that can both be implemented online, perform at levels approaching the least squares error minimization. Furthermore, it is interesting to note that the adaptive identifier does not require computationally intense matrix inversions as compared to the other two identification techniques and thus makes an excellent candidate for embedded real-time sensor calibration.

A well calibrated gyroscope is expected to contribute significantly to the navigation performance of AUVs. Future work will attempt to fuse calibrated gyroscope

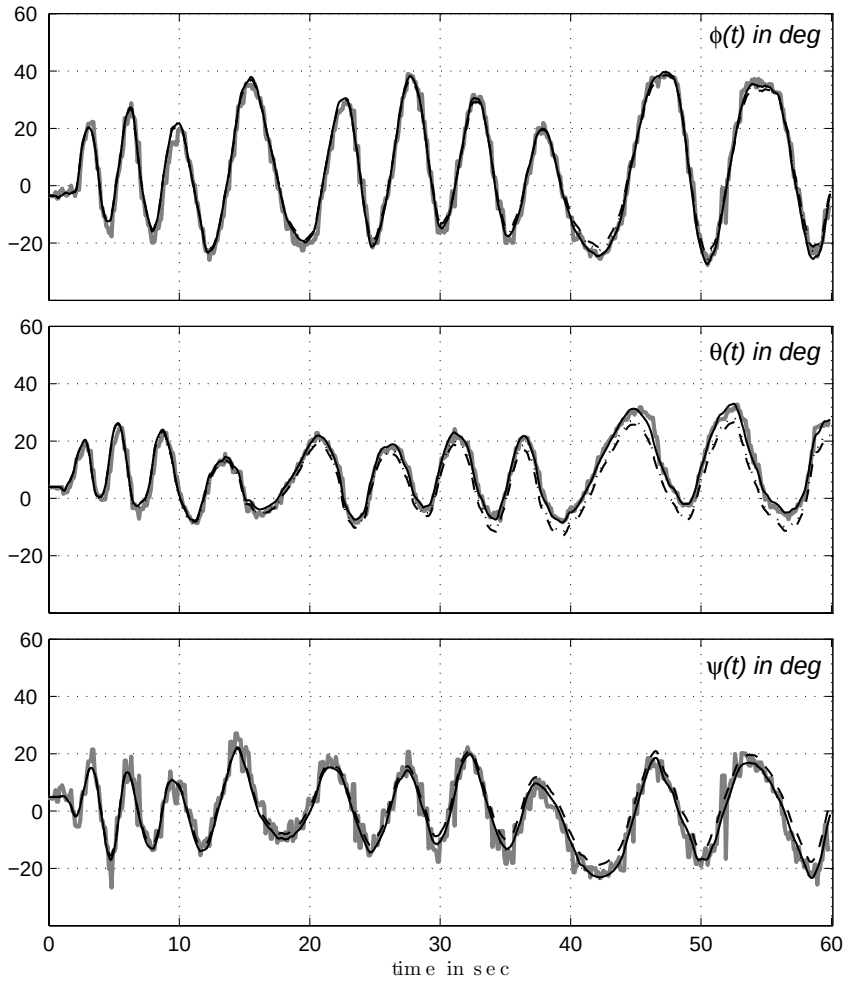

Figure 5.2: Parameter identification via attitude quaternion (5.12): Integration of calibrated gyroscope measurements vs. measured Euler angles, from top to bottom: roll $\phi(t)$, pitch $\theta(t)$ and yaw $\psi(t)$. The graphs are labeled as follows: compass/tilt sensors (reference) - thick gray, adaptive identifier - dashed, Kalman filter - dotted, least-squares - solid.

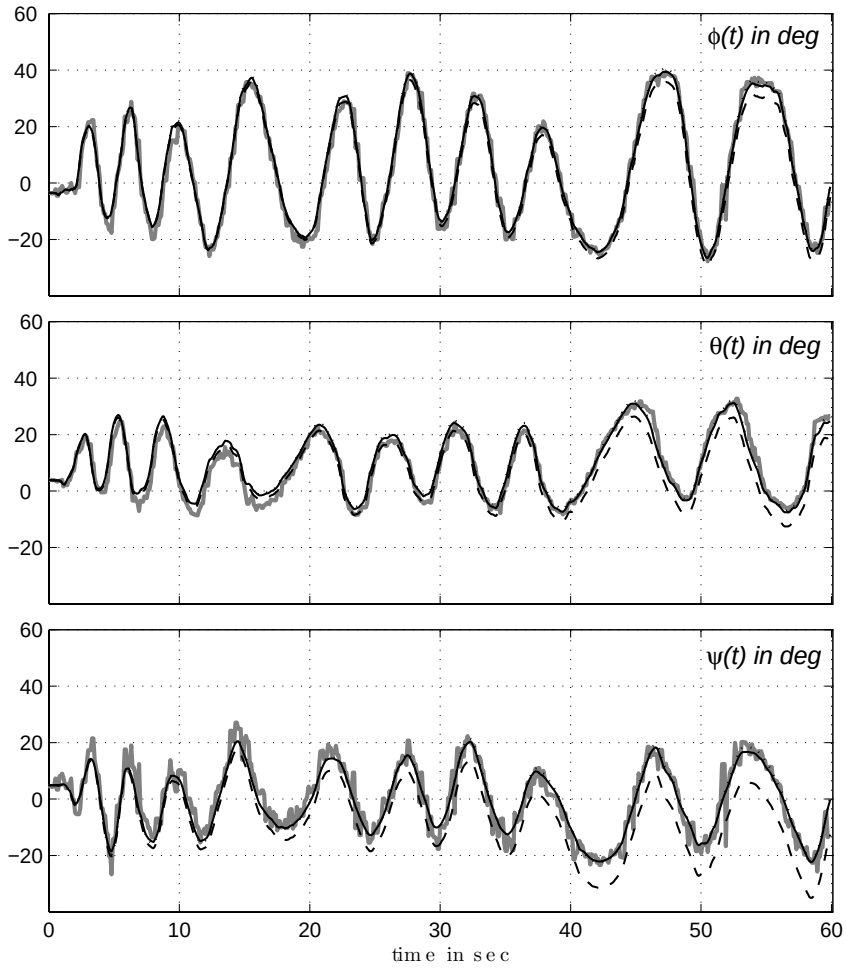

Figure 5.3: Parameter identification via Euler angles (5.13): Integration of calibrated gyroscope measurements vs. measured Euler angles, from top to bottom: roll $\phi(t)$, pitch $\theta(t)$ and yaw $\psi(t)$. The graphs are labeled as follows: compass/tilt sensors (reference) - thick gray, adaptive identifier - dashed, Kalman filter - dotted, least-squares - solid.

Table 5.3: RMS estimation error for the 60 second data set using an attitude quaternion or Euler angles, respectively, for the parameter identification (all quantities in degrees).

identification via attitude quaternion $\mathbf{q}(t)$

	$\mathbf{E}_{ai}$	$\mathbf{E}_{kf}$	$\mathbf{E}_{ls}$
ϕ	2.907	2.729	2.685
θ	4.418	3.634	1.957
ψ	4.452	3.700	3.659

identification via Euler angles $\boldsymbol{\eta}(t)$

	$\mathbf{E}_{ai}$	$\mathbf{E}_{kf}$	$\mathbf{E}_{ls}$
ϕ	3.505	2.727	2.657
θ	4.278	2.850	2.777
ψ	8.212	3.923	3.865

measurements with compass readings to enhance underwater navigation.

5.5 Conclusion

This chapter discusses the development and application of calibration methods for a tri-axis gyroscope system used for inertial navigation in an AUV. A gyroscope error model is presented containing scaling and bias parameters, and three identification techniques are deployed to estimate those parameters: an adaptive identifier, a Kalman filter, and an off-line linear least-squares algorithm. The identification is carried out using both a quaternion and Euler angles to model the vehicle's attitude. An experimental data set provides sufficient gyroscope excitation, and all methods are shown to yield parameter estimations that produce low output tracking errors over a short period of time. Although integrated gyroscope estimation will eventually drift over extended periods of time, the calibration methods proposed here allow for reducing the estimation drift and the extension of the time interval in which accurate

dead reckoning navigation can occur.

To conclude, we briefly recall the necessity of gyroscope excitation for the observability of the plant. In field experiments, there exists no un-accelerated vehicle trajectory. Due to wind, local fluid dynamics, mechanical vibrations, etc., the system of gyroscopes is guaranteed to experience non-zero excitation and thus be observable. However, in practice, system observability does not necessarily imply that accurate gyroscope calibration can occur. At a bare minimum, gyroscope excitation must exceed the zero-bias noise characteristics of the sensors used for calibration. That is, it becomes important that the level of excitation, and thus the "level" of observability can somehow be characterized.

Chapter 6

Identification of a Simplified Flow Field Model

Motivated by the desire to improve the navigation performance of small autonomous underwater vehicles, we seek simple methods for modeling the local flow that affects the vehicle's trajectory. In this chapter, published in [74], we propose a low-complexity, planar flow field model that consists of a uniform flow component and a singular flow component. Assuming this simplified flow field model, we develop identification algorithms that can be performed quickly using small, sparse data sets collected by a platoon of vehicles. The basic approach involves estimating the uniform flow component, localizing an assumed flow singularity, and identifying the parameters which characterize the singular flow. In order to identify the singular flow component, we propose a least squares and a constrained least squares approach. In the latter case, the minimization is constrained to preserve the average divergence and circulation of the measured flow. Preserving divergence and circulation predictably results in a larger overall error because it eliminates two free model parameters, but

it produces a flow model which more realistically captures the flow in the larger region of the measurement points. Numerical simulations and an initial experiment illustrate the parameter identification process as well as the benefits of incorporating a flow field model for vehicle navigation.

6.1 Introduction

In this chapter, we develop fluid flow models and associated identification algorithms in order to improve the navigation of autonomous underwater vehicles (AUVs). Driven by the stringent requirements of AUV navigation in shallow water applications (e.g, in coastal, estuarine, and riverine environments), our goal is to identify a fluid flow model using a small set of flow velocity estimates collected by a platoon of miniature AUVs. The work focuses on improving the navigational performance of AUVs which are not instrumented to measure current flow [65]. Since GPS-signals are not accessible underwater, the position of a submerged vehicle is estimated via dead reckoning, using a kinematic model for the vehicle motion. However, ambient fluid motion perturbs the vehicle's trajectory, resulting in navigation error. This navigation error can be measured when the vehicle resurfaces to obtain its current position using GPS. Given a collection of such navigation errors, from a platoon of AUVs, one may hypothesize and identify a simple flow model which can then be incorporated into the AUV's path planning routine to reduce navigation error in subsequent dives. Models and model identification techniques for fluid flow have been developed for a wide range of applications, but most are not suitable for our purposes because they rely on a dense set of flow field measurements. For this reason, we adopt a simple model and aim for a computationally efficient method that requires only a small set

of flow velocity estimates.

For oceanographic applications [30] or particle movements [31], image sequence processing [32] can quantify both large and small scale fluid motion. Analyzing the gray scale deviation of successive satellite images, for example, a two-dimensional velocity vector may be assigned to each pixel in the image. Thus, image sequence processing provides a dense set of sample vectors, at nearly the same resolution as the images. In our application, however, we can not assume that a dense set of flow measurements is available.

Lagrangian coherent structures have been proposed as a tool for modeling complex, time-varying fluid motion. Lagrangian coherent structures can be used to represent slowly varying stable and unstable manifolds of dynamical systems [75]. In terms of fluid flow, stable manifolds attract fluid particles in forward time and unstable manifolds attract fluid particles in reverse time. Lagrangian coherent structures are of interest for ocean scientists because they provide high fidelity, time-varying flow models. In this work, we focus on real-time flow field estimation to enhance short-term navigation. We therefore assume a low-complexity, time-invariant flow field. We show that a two-dimensional flow field model can improve the navigational accuracy of miniature AUVs, with relatively little communication or computational effort required.

The localization of singular or critical points represents the first step toward the identification of a singular flow pattern. Under the assumption of a dense data set, one can numerically evaluate the change in the flow direction along any closed curve within the data set. Integrating the flow field angle along such a closed curve yields the *Poincaré* index [76]. A Poincaré index of 1 indicates a full rotation of the flow field direction along the closed curve and therefore suggests the existence of a flow

singularity within the area enclosed by the curve. In [77], the author defines pie-shaped sample regions in order to numerically compute the Poincaré index for every point in the image.

Alternative approaches of extracting singular points from a dense motion field are presented in [78] and [79]. A Fourier transformation and a convolution operator are applied to a two-dimensional data set allowing the decomposition of the flow field samples into irrotational and solenoidal components. Referring to the *Helmholtz* Theorem, (see page 78 in [80]), both flow components are gradients of potential functions, and the respective extrema of those potential functions represent locations of flow singularities.

A small platoon of AUVs generates a relatively small number of flow field sample vectors, so flow identification approaches that require dense measurements are not applicable in this setting. We do adopt a least squares estimation approach, as used in [77] and [78], to estimate the parameters defining our simple flow field model, but we assume that only a sparse set of velocity measurements are available when estimating the model parameters. This chapter is an extended version of [81]. We discuss the flow field identification in more detail and provide several examples. A convergence proof for the singularity localization algorithm suggested in [81] is presented. The flow field identification allows several options for determining model parameters, as illustrated in a flow chart in Figure 6.5. A numerical example illustrates the application of the algorithm to a realistic flow data set, augmenting the experimental results first reported in [81]. We also extend our analysis of the experimental results by introducing an additional error metric that measures the accuracy of the identified flow field model over a larger region, by comparing model predictions with the true motion of a set of buoys that drifted through the test site.

In Section 6.2, we propose a two-dimensional flow field model containing a uniform flow component and a singular flow component, i.e. a source/sink or a vortex. Important flow characteristics such as divergence and rotation are introduced and their impact on the flow field pattern is illustrated. The algorithm to identify the unknown flow model parameters proceeds in four steps, which are described in Section 6.3. Estimation strategies for the uniform flow component are introduced in Section 6.3.1. Section 6.3.2 describes an approach to localize potential flow singularities. In Section 6.3.3, we transform from cartesian to polar coordinates and decompose the flow field model and measurements into solenoidal (expanding or contracting) and rotational components. Section 6.3.4 presents two schemes for identifying the singular flow portion of the flow model. Section 6.3.5 summarizes the identification process in a chart that illustrates various implementation options that are available. Initial experiments and simulation results are presented in Section 6.4. The experiments illustrate the benefits of incorporating a local flow field model when planning paths for AUVs, and simulations are used to evaluate both the performance of the flow field identification and the improved AUV navigation while providing ground truth.

6.2 Problem Statement and Flow Field Model

Similar to the approaches in [31] and [82], we assume the presence of a flow singularity which induces the regional fluid motion. We propose the following flow field model that assigns a flow velocity vector $\mathbf{V} = [V_x, V_y]^T \in \mathbb{R}^2$ to any point $\mathbf{r} = [x, y]^T \in \mathbb{R}^2$ in the horizontal plane

$$\mathbf{V}(\mathbf{r}) = \mathbf{U} + \mathbf{A}(\mathbf{r} - \mathbf{r}_s)w(\rho) \tag{6.1}$$

The constant vector $\mathbf{U} = [U_x, U_y]^T \in \mathbb{R}^2$ represents a uniform component of flow. The constant matrix

$$\mathbf{A} = \begin{bmatrix} a_{11} & a_{12} \\ a_{21} & a_{22} \end{bmatrix}$$

defines the flow pattern due to a flow singularity located at the fixed point $\mathbf{r}_s \in \mathbb{R}^2$. The function $w : \mathbb{R} \mapsto \mathbb{R}$ is introduced to weaken the singular flow component with increasing distance $\rho = \|\mathbf{r} - \mathbf{r}_s\|$. Choosing $w(\rho) = 1/\rho$, for example, will bound the flow velocity magnitude within the entire domain:

$$||\mathbf{V}(\mathbf{r})|| \leq ||\mathbf{U}|| + ||\mathbf{A}|| \qquad \forall\, \mathbf{r} \in \mathbb{R}^2$$

where $||\mathbf{A}||$ is the induced matrix norm of $\mathbf{A}$. Note that, in contrast to the Rankine vortex model presented in [78], we do not assume that the flow magnitude $||\mathbf{V}(\mathbf{r})||$ approaches zero as the distance $\rho = \|\mathbf{r} - \mathbf{r}_s\|$ goes to infinity.

To illustrate some basic properties of the singular flow component defined by the matrix $\mathbf{A}$, let $w(\rho) = 1$ in (6.1) and define

$$\mathbf{V}_s(\mathbf{r}) = \mathbf{U} + \mathbf{A}(\mathbf{r} - \mathbf{r}_s) \tag{6.2}$$

The divergence of $\mathbf{V}_s$ is given by the trace of the singularity matrix $\mathbf{A}$:

$$\text{div}\,(\mathbf{V}_s) = \frac{\partial}{\partial x} V_{s,x} + \frac{\partial}{\partial y} V_{s,y} = a_{11} + a_{22}$$

If the divergence is positive, then the singularity is a source. If it is negative, the singularity is a sink. The special case when $a_{11} = -a_{22}$ corresponds to a divergence free, purely rotational flow field.

The rotation of $\mathbf{V}_s$, or vertical vorticity [83], is

$$\text{curl}\,(\mathbf{V}_s) = \frac{\partial}{\partial x} V_{s,y} - \frac{\partial}{\partial y} V_{s,x} = a_{21} - a_{12}$$

Thus, the skew elements of **A** characterize the rotation of the flow. A positive vertical vorticity $a_{21} > a_{12}$ describes counter-clockwise rotation and vice versa. For an irrotational motion induced by a pure sink or source, the singularity matrix satisfies $a_{12} = a_{21}$.

Divergence and vorticity play an important role in characterizing fluid flow. As intrinsic flow features, they provide a physical interpretation of the elements of **A**.

To illustrate how the singularity matrix **A** affects the flow field generated by the model (6.2), assume that $\mathbf{U} = [0, 0]^T$ and that $\mathbf{r}_s = [0, 0]^T$. Consider the following special form of the singularity matrix

$$\mathbf{A} = \begin{bmatrix} \alpha & -\beta \\ \beta & \alpha \end{bmatrix}$$

Case 1: Suppose that $\beta = 0$ and $\alpha \neq 0$. Then **A** generates a solenoidal flow field (i.e., a purely expanding or contracting flow). Positive divergence ($\alpha > 0$) indicates a source, as shown in Figure 6.1. There is no rotational component of fluid motion.

Case 2: Suppose that $\alpha = 0$ and $\beta \neq 0$. Then **A** generates a rotational flow field. Positive curl ($\beta > 0$) indicates counter-clockwise rotation, as shown in Figure 6.2. In this case, the flow field is divergence free.

Additional flow features (stretching and shearing deformation) are also captured by the singularity matrix **A**, as described in [84]. By definition, the stretching and shearing deformation change under a rotation of the coordinate frame. While we attempt to preserve intrinsic flow properties, such as divergence and rotation, we do not consider stretching and shearing in identifying the model parameters.

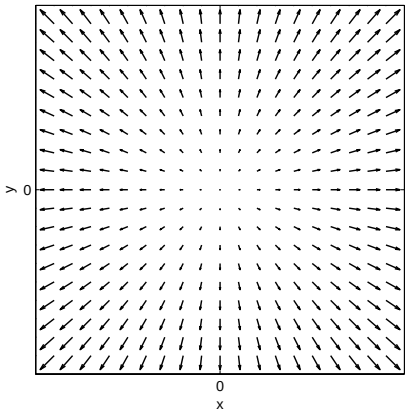

Figure 6.1: solenoidal flow field ($\alpha > 0$, $\beta = 0$).

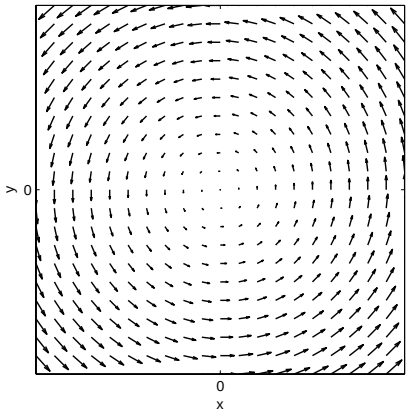

Figure 6.2: Rotational flow field ($\alpha = 0$, $\beta > 0$).

6.3 Identification

Identifying the flow field model (6.1), for a given choice of weakening function $w(\rho)$, requires one to determine eight unknown parameters

$$\{\underbrace{U_x\ U_y}_{\mathbf{U}}\ \underbrace{a_{11}\ a_{12}\ a_{21}\ a_{22}}_{\mathbf{A}}\ \underbrace{x_s\ y_s}_{\mathbf{r}_s}\}$$

A data set containing N local flow velocity measurements at specific locations is assumed to be given. These measurements might be obtained, for example, using a platoon of small AUVs. Consider the following scenario. Each vehicle begins and ends its trajectory on the surface, where GPS signals are available, but performs the remainder of its trajectory below the surface at some common, specified depth. Since GPS signals are not accessible to submerged AUVs, the submerged portion of the

trajectory $r(t) = [x(t), y(t)]^T$ is estimated using a kinematic model

$$\begin{bmatrix} \dot{x} \\ \dot{y} \end{bmatrix} = \begin{bmatrix} \sin\psi \\ \cos\psi \end{bmatrix} \hat{u}_1 + \begin{bmatrix} V_x \\ V_y \end{bmatrix} \tag{6.3}$$

where ψ is the heading angle and $\hat{u}_1$ is the water relative longitudinal speed. The x-axis points eastwards and the y-axis points northwards. We assume that the water relative vehicle motion is purely longitudinal, a reasonable assumption for steady state motion of a vehicle with good directional stability. Small AUVs typically do not carry sophisticated flow sensors, but water relative longitudinal speed may be inferred from the propeller rate.

With no *a priori* knowledge of the ambient fluid motion, V_x and V_y may be set to zero in equation (6.3) in order to obtain a best estimate of the vehicle's trajectory. Because of the ambient flow, this "dead reckoning" approach will generally result in a discrepancy between the predicted final position and the actual final position, as measured using GPS when the vehicle resurfaces. We use this discrepancy to estimate the ambient flow along a given vehicle's trajectory. Given a collection of such estimates, one from each vehicle, we may then identify the parameters of the flow field model (6.1). Although other sources of dead reckoning errors such as a compass offset or variations in magnetic declination will be present in practice, they are not addressed here.

6.3.1 Uniform Flow

We assume that N flow velocity estimates $\mathbf{V}_i$ are available, each corresponding to a measurement location $\mathbf{P}_i$, where $i \in \{1, \ldots, N\}$. The uniform flow component $\mathbf{U}$ may be treated in at least two different ways. One approach is to average over the

sample set to obtain

$$\mathbf{U} = \frac{1}{N}\sum_{i=1}^{N}\mathbf{V}_i \tag{6.4}$$

Alternatively, one may simply assume that

$$\mathbf{U} = [0,0]^T \tag{6.5}$$

and seek a flow singularity which best reproduces the measured sample vectors. Both methods for defining $\mathbf{U}$ are discussed.

6.3.2 Localization of a Flow Singularity

Having defined $\mathbf{U}$, either by (6.4) or (6.5), one may proceed to identify the remaining singular flow component of the flow model. Define

$$\begin{aligned}\tilde{\mathbf{V}}(\mathbf{r}) &:= \mathbf{V}(\mathbf{r}) - \mathbf{U} \\ &= \mathbf{A}(\mathbf{r}-\mathbf{r}_s)w(\rho)\end{aligned} \tag{6.6}$$

The first step is to determine the location $\mathbf{r}_s$ of the assumed flow singularity which induces the flow $\tilde{\mathbf{V}}(\mathbf{r})$. To determine this location, we use the residual flow velocity measurements

$$\tilde{\mathbf{V}}_i = \mathbf{V}_i - \mathbf{U} \tag{6.7}$$

Definition 6.3.1. *The* geometric center of measurements *is*

$$\mathbf{P}_{\text{cm}} = \frac{1}{N}\sum_{i=1}^{N}\mathbf{P}_i. \tag{6.8}$$

Proposition 6.3.2. *Consider a set of N velocity measurements $\mathbf{V}_i$ and suppose that the uniform flow component $\mathbf{U}$ has been computed as in (6.4) and removed as in (6.7) to produce a set of N residual velocity measurements $\tilde{\mathbf{V}}_i$. Further, suppose that these residual velocity measurements satisfy (6.6)* identically *for some nonsingular matrix $\mathbf{A}$, with $w(\rho) = 1$. Then $\mathbf{r}_s = \mathbf{P}_{\text{cm}}$.*

Proof: By assumption, each residual velocity estimate $\tilde{\mathbf{V}}_i$ satisfies

$$\tilde{\mathbf{V}}_i = \mathbf{A}\left(\mathbf{P}_i - \mathbf{r}_s\right).$$

Summing over i and dividing by N gives

$$\begin{aligned} \frac{1}{N}\sum_{i=1}^{N}\tilde{\mathbf{V}}_i &= \frac{1}{N}\sum_{i=1}^{N}\mathbf{A}\left(\mathbf{P}_i - \mathbf{r}_s\right) \\ &= \mathbf{A}\frac{1}{N}\sum_{i=1}^{N}\left(\mathbf{P}_i - \mathbf{r}_s\right) \end{aligned} \tag{6.9}$$

But (6.4) and (6.7) imply that

$$\frac{1}{N}\sum_{i=1}^{N}\tilde{\mathbf{V}}_i = \mathbf{0}.$$

Because $\mathbf{A}$ is assumed to be nonsingular, we find from (6.9) that

$$\begin{aligned} \mathbf{0} &= \frac{1}{N}\sum_{i=1}^{N}\left(\mathbf{P}_i - \mathbf{r}_s\right) \\ &= \frac{1}{N}\left(\sum_{i=1}^{N}\mathbf{P}_i\right) - \mathbf{r}_s \end{aligned}$$

It follows that

$$\mathbf{r}_s = \frac{1}{N}\sum_{i=1}^{N}\mathbf{P}_i = \mathbf{P}_{\text{cm}}$$

□

Thus, assuming that the flow model (6.2) accurately characterizes the flow measurements, the singularity location is the center of measurements $\mathbf{P}_{\text{cm}}$. A similar statement holds when one includes a weakening function $w(\rho)$. In the general case,

one finds that

$$\mathbf{r}_s = \mathbf{P}_{\text{cm}} + \frac{\displaystyle\sum_{i=1}^{N} (\mathbf{P}_i - \mathbf{r}_s)\, w(\|\mathbf{P}_i - \mathbf{r}_s\|)}{\displaystyle\sum_{i=1}^{N} w(\|\mathbf{P}_i - \mathbf{r}_s\|)}$$

Because of the weighting function $w(\cdot)$, finding the singularity location $\mathbf{r}_s$ by this approach will generally require one to solve a nonlinear algebraic equation, which must typically be done numerically. For the specific choice $w(\rho) = \dfrac{1}{\rho}$, one can show that the singularity must be located within the convex hull of the measurement locations. This observation bounds the region to be searched using a numerical root finding technique.

The approach described above for locating the singularity is somewhat dissatisfying in that it appears to take no account of the flow measurements themselves. In reality, the measurements are accounted for when one computes the uniform flow component. Still, at this early point in the flow identification process, assuming that the residual flow measurements satisfy (6.6) identically is restrictive.

Figure 6.3 illustrates a different approach for locating the assumed flow singularity. For any candidate singularity location $\mathbf{r} = [x, y]^T$, the angles $\theta_i(\mathbf{r})$ between the vectors $\mathbf{r} - \mathbf{P}_i$ and the residual flow measurements $\tilde{\mathbf{V}}_i$ can be computed. These angles, evaluated in four quadrants, correlate to the surrounding flow pattern and are defined by the geometric relations

$$\begin{aligned}
\sin\theta_i(\mathbf{r}) &= \frac{(\mathbf{r} - \mathbf{P}_i) \times \tilde{\mathbf{V}}_i}{||\tilde{\mathbf{V}}_i||\,||\mathbf{r} - \mathbf{P}_i||} \cdot \mathbf{e}_z = \frac{(x - P_{i,x})\tilde{V}_{y,i} - (y - P_{i,y})\tilde{V}_{x,i}}{||\tilde{\mathbf{V}}_i||\,||\mathbf{r} - \mathbf{P}_i||} \\
\cos\theta_i(\mathbf{r}) &= \frac{(\mathbf{r} - \mathbf{P}_i) \cdot \tilde{\mathbf{V}}_i}{||\tilde{\mathbf{V}}_i||\,||\mathbf{r} - \mathbf{P}_i||} = \frac{(x - P_{i,x})\tilde{V}_{x,i} + (y - P_{i,y})\tilde{V}_{y,i}}{||\tilde{\mathbf{V}}_i||\,||\mathbf{r} - \mathbf{P}_i||}
\end{aligned} \tag{6.10}$$

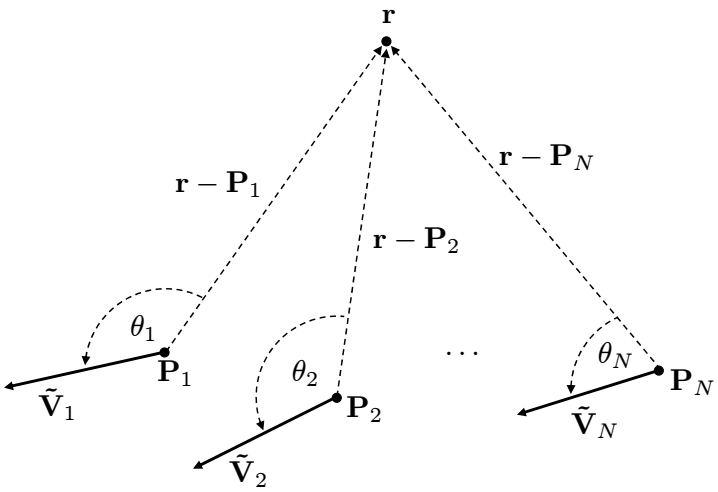

Figure 6.3: Evaluation of the singular flow pattern around $\mathbf{r}$. The residual flow field samples are $\tilde{\mathbf{V}}_i = \mathbf{V}_i - \mathbf{U}$. The measurement locations are denoted $\mathbf{P}_i$.

In [31], every location $\mathbf{r}$ that satisfies $\theta_i = 90°$ for all sample vectors is identified as a singularity location of a clockwise vortex. A similar statement holds for a counter-clockwise vortex with $\theta_i = -90°$. We expand the approach to include dilatation, as well as rotation. For a source, for example, $\theta_i = 180°$ while for a sink $\theta_i = 0°$. Associated with these four classifications are four cost functions Γ_j, with $j \in \{1, .., 4\}$, defined to evaluate how well the candidate singularity location $\mathbf{r}$ and corresponding

singularity type represent the residual flow field.

$$\begin{aligned}
&\text{sink} && \Gamma_1(\mathbf{r}) &&= \sum_{i=1}^{N} (\cos\theta_i - 1)^2 \\
&\text{source} && \Gamma_2(\mathbf{r}) &&= \sum_{i=1}^{N} (\cos\theta_i + 1)^2 \\
&\text{clockwise vortex} && \Gamma_3(\mathbf{r}) &&= \sum_{i=1}^{N} (\sin\theta_i - 1)^2 \\
&\text{counter-clockwise vortex} && \Gamma_4(\mathbf{r}) &&= \sum_{i=1}^{N} (\sin\theta_i + 1)^2
\end{aligned} \tag{6.11}$$

In the definitions (6.11), $\Gamma_j(\mathbf{r}) : \mathbb{R}^2/\mathbb{M} \mapsto \mathbb{R}$, where $\mathbb{M}$ represents the set of balls of radius $\delta > 0$ around each measurement location $\mathbf{P}_i$, i.e.

$$\mathbb{M} = \{\mathbf{r} \,|\, \|\mathbf{r} - \mathbf{P}_i\| < \delta,\ i = 1 \ldots N\}$$

We assume that the singularity is *not* located at a measurement point $\mathbf{P}_i$; otherwise, the angle θ_i would be undefined. The radius $\delta > 0$ can be chosen arbitrarily small, but should be non-zero; see proof of Proposition 6.3.3 on page 132 for details.

The best choices for singularity locations are the minima of $\Gamma_j(\mathbf{r})$. By definition, the cost functions are continuously differentiable in $\mathbb{R}^2/\mathbb{M}$. Thus, a gradient descent approach can be applied to each $\Gamma_j(\mathbf{r})$ in order to determine the respective local minima

$$\dot{\mathbf{r}}_j(t) = -\gamma_j(t)\,\mathrm{grad}\,\Gamma_j(\mathbf{r}_j) \qquad \text{with} \qquad j = 1..4 \tag{6.12}$$

The four trajectories $\mathbf{r}_j(t)$ evolve from a common initial state $\mathbf{r}_j(0) = \mathbf{P}_{\mathrm{cm}}$; see Definition 6.3.1. The adaptive step sizes $\gamma_j(t)$ with $\gamma_{max} \geq \gamma_j(t) \geq \gamma_{min} > 0$ provide a

trade-off between high accuracy of the algorithm versus computational time. They can be adjusted as $\mathbf{r}_j(t)$ evolves.

At present, convergence of (6.12) is not guaranteed for all possible sets of sample vectors and remains an open research question. For a restricted range of initial conditions, however, a gradient method (6.12) can be proven to converge to the desired local minimum.

Proposition 6.3.3. *Assume that there exists a unique minimum at* $\mathbf{r}_{s,j}$ *in a neighborhood*

$$\mathbb{B}_j = \left\{\mathbf{r} \in \mathbb{R}^2/\mathbb{M} \,|\, \|\mathbf{r} - \mathbf{r}_{s,j}\| \leq \epsilon\right\}$$

where ϵ *is sufficiently small to ensure that* $\mathbb{B}_j$ *does not contain elements of* $\mathbb{M}$. *Also assume that*

$$\operatorname{grad} \Gamma_j(\mathbf{r}_j) \neq 0 \qquad \forall \mathbf{r}_j \in \mathbb{B}_j,\ \mathbf{r}_j \neq \mathbf{r}_{s,j}.$$

Then, for any initial condition $\mathbf{r}_{0,j} \in \mathbb{B}_j$, *the gradient method (6.12) will converge to* $\mathbf{r}_{s,j}$.

A proof of Proposition 6.3.3 is given in Appendix B.2.

For experimental data, the gradient method (6.12) generally converges for more than one cost function. Thus, there is typically more than one choice of singularity location and type. The implications of such a choice are discussed in Section 6.4.1.

We illustrate the gradient algorithm with an example. For a given set of three data vectors, shown in the left-hand side of Figure 6.4, the gradient (steepest descent) methods converge for Γ_4 and Γ_2. They do not converge for Γ_1 and Γ_3. The right-hand side of Figure 6.4 displays the surfaces $\Gamma_4(x, y)$ and $\Gamma_2(x, y)$, including the paths $\Gamma_4(\mathbf{r}_4(t))$ and $\Gamma_2(\mathbf{r}_2(t))$ (in white) corresponding to the trajectories $\mathbf{r}_4(t)$ and $\mathbf{r}_2(t)$ of (6.12) that end at the local minima $\mathbf{r}_{s,4}$ and $\mathbf{r}_{s,2}$, respectively.

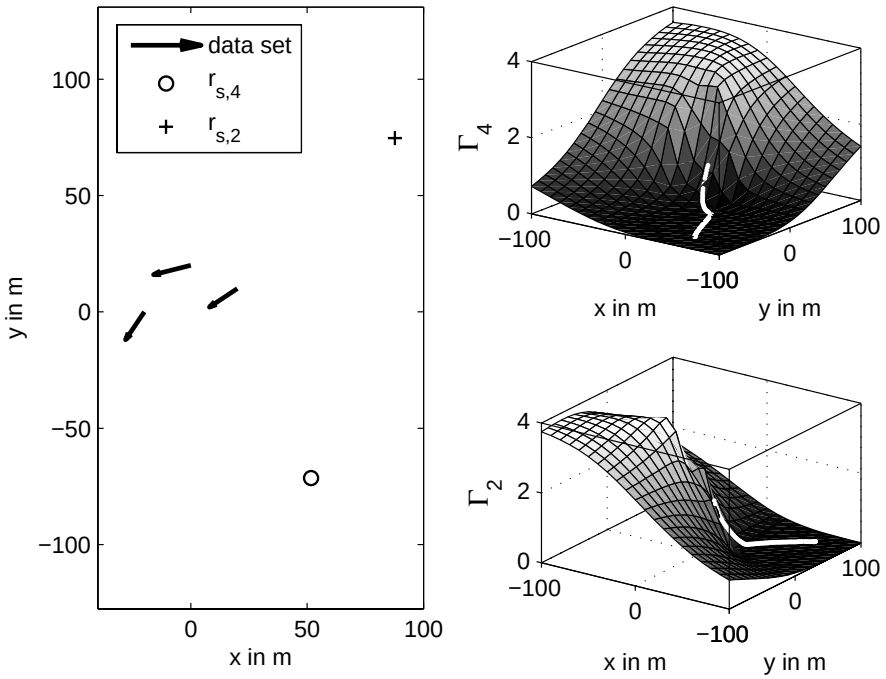

Figure 6.4: Singularity detection based on three measured data vectors.

By definition, the minima of Γ_4 and Γ_2 represent locations of a counter-clockwise rotational vortex and a source, respectively. Rather than restrict the form of $\mathbf{A}$ to represent a pure singularity, however, we take the identified location $\mathbf{r}_{s,j}$ to be the center of a more general flow singularity. For example, having selected the candidate singularity location $\mathbf{r}_{s,4}$, we do not continue to assume that the flow is purely rotational. We do expect, however, that the matrix $\mathbf{A}$ which we ultimately identify assuming the singularity *location* $\mathbf{r}_{s,4}$ will correspond to a predominantly rotational flow.

6.3.3 Polar Representation of the Flow Field Model

To identify the singularity matrix $\mathbf{A}$, the flow field model (6.6) is transformed into polar coordinates. Given that the singularity location $\mathbf{r}_s$ has been determined, as described in Section 6.3.2, a polar coordinate system with the origin at $\mathbf{r}_s = [x_s, y_s]^T$ provides a more concise mathematical representation of the singular flow, one which naturally decomposes the flow field model and measurement vectors into rotational and solenoidal components. For any point $\mathbf{r} = [x, y]^T$, define the angle φ by the expression

$$\tan\varphi = \frac{y - y_s}{x - x_s}$$

where the four-quadrant arctangent is used, i.e., $\varphi \in [0, 2\pi)$. Recalling that $\rho = \|\mathbf{r} - \mathbf{r}_s\|$, one finds the polar coordinate representation of the singular flow (6.6) is

$$\tilde{\mathbf{V}}(\rho, \varphi) = \tilde{V}_\rho(\rho, \varphi)\mathbf{e}_\rho + \tilde{V}_\varphi(\rho, \varphi)\mathbf{e}_\varphi \tag{6.13}$$

where $\mathbf{e}_\rho$ and $\mathbf{e}_\varphi$ are the unit vectors corresponding to the radial and azimuthal directions, respectively. Explicitly, we have

$$\begin{aligned} \tilde{V}_\rho(\rho, \varphi) &= w(\rho)\rho\left[a_{11}\cos^2\varphi + a_{22}\sin^2\varphi + (a_{12} + a_{21})\sin\varphi\cos\varphi\right] \\ \tilde{V}_\varphi(\rho, \varphi) &= w(\rho)\rho\left[a_{21}\cos^2\varphi - a_{12}\sin^2\varphi + (a_{22} - a_{11})\sin\varphi\cos\varphi\right] \end{aligned} \tag{6.14}$$

Notice in (6.14) that choosing $w(\rho) = \dfrac{1}{\rho}$ cancels the dependency of $\tilde{\mathbf{V}}(\rho, \varphi)$ on ρ. Thus, in this case, the singular flow field model (6.13) is invariant with distance from the origin. While fixing the form of $w(\rho)$ limits the versatility of the flow field model somewhat, the choice $w(\rho) = \dfrac{1}{\rho}$ bounds the magnitude of the flow vectors in $\mathbb{R}^2$, as explained earlier. The result is a more physically intuitive flow model that may even be useful outside the immediate vicinity of the flow measurements. Moreover, sufficient freedom remains in the model to capture intrinsic flow characteristics, such as

divergence and circulation, in the region where measurements are made. We therefore choose $w(\rho) = \frac{1}{\rho}$ and we omit the argument ρ from the components of the flow field model:

$$\begin{aligned} \tilde{V}_\rho(\varphi) &= \left[a_{11}\cos^2\varphi + a_{22}\sin^2\varphi + (a_{12}+a_{21})\sin\varphi\cos\varphi\right] \\ \tilde{V}_\varphi(\varphi) &= \left[a_{21}\cos^2\varphi - a_{12}\sin^2\varphi + (a_{22}-a_{11})\sin\varphi\cos\varphi\right] \end{aligned} \tag{6.15}$$

To rewrite (6.15) in a form more amenable to parameter identification, we use the trigonometric relations

$$\cos^2\varphi = \frac{1}{2}(1+\cos 2\varphi), \quad \sin^2\varphi = \frac{1}{2}(1-\cos 2\varphi), \quad \text{and} \quad \sin\varphi\cos\varphi = \frac{1}{2}\sin 2\varphi$$

With these identities, we may rewrite the components of the residual flow as

$$\begin{bmatrix} \tilde{V}_\rho(\varphi) \\ \tilde{V}_\varphi(\varphi) \end{bmatrix} = \begin{bmatrix} \mathbf{b}_\rho^T(\varphi) \\ \mathbf{b}_\varphi^T(\varphi) \end{bmatrix} \mathbf{p} \tag{6.16}$$

where

$$\mathbf{b}_\rho^T(\varphi) = \begin{bmatrix} \cos 2\varphi & \sin 2\varphi & 1 & 0 \end{bmatrix}, \qquad \mathbf{b}_\varphi^T(\varphi) = \begin{bmatrix} -\sin 2\varphi & \cos 2\varphi & 0 & 1 \end{bmatrix}$$

and

$$\mathbf{p} = \begin{bmatrix} p_1 \\ p_2 \\ p_3 \\ p_4 \end{bmatrix} = \frac{1}{2}\begin{bmatrix} 1 & 0 & 0 & -1 \\ 0 & 1 & 1 & 0 \\ 1 & 0 & 0 & 1 \\ 0 & -1 & 1 & 0 \end{bmatrix}\begin{bmatrix} a_{11} \\ a_{12} \\ a_{21} \\ a_{22} \end{bmatrix}. \tag{6.17}$$

Note that identifying the new parameter vector $\mathbf{p}$ is equivalent to identifying the components of $\mathbf{A}$.

6.3.4 Singular Flow Identification

A technique that determines the parameters $\mathbf{p}$ and thus the singularity matrix $\mathbf{A}$ is presented in this section. The goal is to approximate the measured flow field vectors

using the proposed model by minimizing the root-mean-squared error

$$\eta(\mathbf{V}_i, \mathbf{V}) = \sqrt{\frac{1}{N}\sum_{i=1}^{N} ||\mathbf{V}_i - \mathbf{V}(\mathbf{P}_i)||^2}. \tag{6.18}$$

(Note: $\mathbf{V}_i$ is the flow measured at $\mathbf{P}_i$ whereas $\mathbf{V}(\mathbf{P}_i)$ is the flow model (6.1) evaluated at $\mathbf{P}_i$.) After the uniform flow $\mathbf{U}$ and the singularity location $\mathbf{r}_s$ are determined, minimizing η^2 becomes a linear least squares problem. Thus, one can directly obtain $\mathbf{A}$ by minimizing

$$\begin{aligned} \eta^2(\mathbf{V}_i, \mathbf{V}) &= \frac{1}{N}\sum_{i=1}^{N} \left\| \mathbf{V}_i - \left(\mathbf{U} + \frac{1}{\rho_i}\mathbf{A}(\mathbf{r}_s - \mathbf{P}_i) \right) \right\|^2 \\ &= \frac{1}{N}\sum_{i=1}^{N} \left\| \tilde{\mathbf{V}}_i - \frac{1}{\rho_i}\mathbf{A}(\mathbf{r}_s - \mathbf{P}_i) \right\|^2 . \end{aligned} \tag{6.19}$$

More generally, one may use (6.16) instead and minimize

$$\begin{aligned} J &= \sum_{i=1}^{N} \left[q_{i,\rho} \left(\tilde{V}_\rho(\varphi_i) - \tilde{V}_{i,\rho} \right)^2 + q_{i,\varphi} \left(\tilde{V}_\varphi(\varphi_i) - \tilde{V}_{i,\varphi} \right)^2 \right] \\ &= \sum_{i=1}^{N} \left[q_{i,\rho} \left(\mathbf{b}_\rho^T(\varphi_i)\, \mathbf{p} - \tilde{V}_{i,\rho} \right)^2 + q_{i,\varphi} \left(\mathbf{b}_\varphi^T(\varphi_i)\, \mathbf{p} - \tilde{V}_{i,\varphi} \right)^2 \right] \end{aligned} \tag{6.20}$$

where the weight coefficients $q_{i,\rho}$ and $q_{i,\varphi}$ may be adjusted to emphasize solenoidal or rotational flow, whichever is suggested by the data. Note in (6.20) that the residual data vectors $\tilde{\mathbf{V}}_i$ are decomposed into solenoidal $\tilde{V}_{i,\rho}$ and rotational $\tilde{V}_{i,\varphi}$ components.

Suppose we stack the measurement vectors and parameter coefficients $\mathbf{b}_\rho$ and $\mathbf{b}_\varphi$

as follows

$$\mathbf{W} = \begin{bmatrix} \tilde{V}_{i,\rho}(\varphi_i) \\ \vdots \\ \tilde{V}_{i,\rho}(\varphi_N) \\ \tilde{V}_{i,\varphi}(\varphi_i) \\ \vdots \\ \tilde{V}_{i,\varphi}(\varphi_N) \end{bmatrix} \quad \text{and} \quad \mathbf{B} = \begin{bmatrix} \mathbf{b}_\rho^T(\varphi_i) \\ \vdots \\ \mathbf{b}_\rho^T(\varphi_N) \\ \mathbf{b}_\varphi^T(\varphi_i) \\ \vdots \\ \mathbf{b}_\varphi^T(\varphi_N) \end{bmatrix}.$$

Define the diagonal weighting matrix

$$\mathbf{Q} = \operatorname{diag}\left(\begin{bmatrix} q_{1,\rho} & \cdots & q_{N,\rho} & q_{1,\varphi} & \cdots & q_{N,\varphi} \end{bmatrix} \right).$$

The solution $\mathbf{p}$ of the linear algebraic equation

$$\mathbf{Q}\,(\mathbf{B}\mathbf{p} - \mathbf{W}) = \mathbf{0} \tag{6.21}$$

which minimizes J is

$$\mathbf{p} \;=\; \mathbf{B}_Q^\dagger\,\mathbf{W} \tag{6.22}$$

where $\mathbf{B}_Q^\dagger$ is the weighted Moore-Penrose matrix pseudo-inverse:

$$\mathbf{B}_Q^\dagger = \left(\mathbf{B}^T\,\mathbf{Q}\,\mathbf{B}\right)^{-1}\mathbf{Q}\,\mathbf{B}^T$$

The singularity matrix is then obtained by solving (6.17) for the components of $\mathbf{A}$.

Experimental results discussed in Section 6.4.1 (with $\mathbf{Q}$ chosen as the identity matrix) show that minimizing η yields a suitable flow field representation in the immediate region of the measurements. The larger regional flow may not be as accurately characterized, however. Depending on the application, capturing the regional flow characteristics may have a higher priority than minimizing the identification error η. In AUV applications, for example, it is often necessary to navigate beyond the

region of existing flow measurements. A flow field model which accurately reproduces intrinsic features of the flow, such as divergence and rotation, may provide a better representation of the actual flow over a larger region. In the following, we discuss a trade-off between these two objectives: higher flow model accuracy locally versus better qualitative agreement over a larger region.

Natural flow phenomena, such as upwellings and swirling flow described in [83], justify using average divergence and vertical vorticity to partially describe a planar flow. In the proposed method, estimates of these quantities are obtained directly from the flow field samples. The average divergence and vertical vorticity are then reproduced by the flow field model discussed in Section 6.2.

In polar coordinates, the divergence of the flow field model (6.13) is [85]

$$\begin{aligned} \operatorname{div}\left(\tilde{\mathbf{V}}\right) &= \frac{1}{\rho}\frac{\partial}{\partial\rho}(\rho\tilde{V}_\rho) + \frac{1}{\rho}\frac{\partial}{\partial\varphi}\tilde{V}_\varphi \\ &= \frac{1}{\rho}\begin{bmatrix} -\cos 2\varphi & -\sin 2\varphi & 1 & 0 \end{bmatrix}\mathbf{p} \end{aligned} \tag{6.23}$$

For the proposed flow field model, we consider the average divergence per unit area. Define a horizontal disc $\mathbb{A} = \{(\rho,\varphi) \mid \rho \le \rho_{\mathbb{A}},\, \varphi \in [0, 2\pi)\}$ with the radius $\rho_{\mathbb{A}}$ centered at the singularity. The area is $A_{\mathbb{A}} = \pi\rho_{\mathbb{A}}^2$ and a differential area element is $d\mathbb{A} = \rho\, d\rho\, d\varphi$. The radius $\rho_{\mathbb{A}}$ is chosen sufficiently large that $\mathbb{A}$ contains all flow velocity measurements. The average divergence per unit area is

$$\begin{aligned} \overline{\operatorname{div}\left(\tilde{\mathbf{V}}\right)} &= \frac{1}{A_{\mathbb{A}}}\int_{\mathbb{A}} \operatorname{div}\left(\tilde{\mathbf{V}}\right) d\mathbb{A} \\ &= \frac{1}{\pi\rho_{\mathbb{A}}^2}\int_0^{\rho_{\mathbb{A}}}\int_0^{2\pi} \operatorname{div}\left(\tilde{\mathbf{V}}\right)\, \rho\, d\varphi\, d\rho \\ &= \frac{2}{\rho_{\mathbb{A}}}\, p_3 \end{aligned} \tag{6.24}$$

Thus, $\overline{\operatorname{div}\left(\tilde{\mathbf{V}}\right)}$ is directly proportional to the parameter $p_3 = \frac{1}{2}(a_{11} + a_{22})$.

Evaluating partial derivatives (6.23) in order to compute $\overline{\text{div}\left(\tilde{\mathbf{V}}\right)}$ and to estimate p_3 in (6.24) is not feasible for a small, sparse set of measurement vectors. This issue is circumvented by using Gauss' integral theorem of divergence:

$$\int_{\mathbb{A}} \text{div}\left(\tilde{\mathbf{V}}\right)\, d\mathbb{A} = \oint_{\mathbf{S}} \tilde{\mathbf{V}} \cdot d\mathbf{S}_{\perp} \tag{6.25}$$

where $d\mathbf{S}_{\perp}$ is the unit normal to the closed curve $\mathbf{S} = \{(\rho, \varphi) \,|\, \rho = \rho_{\mathbb{A}},\ \varphi \in [0, 2\pi)\}$ at a given angle φ. Applying Gauss' integral theorem to (6.24) yields

$$\begin{aligned}
\overline{\text{div}\left(\tilde{\mathbf{V}}\right)} &= \frac{1}{A_{\mathbb{A}}} \oint_{\mathbf{S}} \tilde{\mathbf{V}} \cdot d\mathbf{S}_{\perp} \\
&= \frac{1}{\pi \rho_{\mathbb{A}}^2} \int_0^{2\pi} \left[\tilde{V}_{\rho}\mathbf{e}_{\rho} + \tilde{V}_{\varphi}\mathbf{e}_{\varphi}\right] \cdot (\rho_{\mathbb{A}}\, d\varphi\, \mathbf{e}_{\rho}) \\
&= \frac{2}{\rho_{\mathbb{A}}} \frac{1}{2\pi} \int_0^{2\pi} \tilde{V}_{\rho}\, d\varphi
\end{aligned} \tag{6.26}$$

Assuming that the residual measured flow velocities are induced by the proposed singular flow model (6.6), equation (6.26) may be used to approximate the average divergence $\overline{\text{div}\left(\tilde{\mathbf{V}}\right)}$ using the solenoidal parts of $\tilde{\mathbf{V}}_i$. Comparing coefficients in (6.24) and (6.26) gives

$$\overline{\text{div}\left(\tilde{\mathbf{V}}\right)} = \frac{2}{\rho_{\mathbb{A}}}\, p_3 = \frac{2}{\rho_{\mathbb{A}}} \frac{1}{2\pi} \int_0^{2\pi} \tilde{V}_{\rho}\, d\varphi$$

from which

$$p_3 = \frac{1}{2\pi} \int_0^{2\pi} \tilde{V}_{\rho}\, d\varphi$$

Sample vectors will not generally be available along the entire circle $\mathbf{S}$; in fact, none of the sample points may lie on the unit circle. Recall, however, that $\tilde{\mathbf{V}}$ given by (6.13) and (6.14) depends only on the angle φ, assuming that $w(\rho) = \dfrac{1}{\rho}$. Thus, the value of $\tilde{\mathbf{V}}$ at a point on the unit circle is the same as its value anywhere on the ray passing through that point. This observation suggests the following approximation:

$$p_3 \approx \bar{V}_{\rho} := \frac{1}{N} \sum_{i=1}^{N} \tilde{V}_{i,\rho} \tag{6.27}$$

where $\tilde{V}_{i,\rho}$ is the radial component of the residual data vector $\tilde{\mathbf{V}}_i$. This approximation is well-justified if the divergence remains nearly constant within the sample set.

Next, consider the rotation of (6.13)

$$\begin{aligned}\text{curl}\left(\tilde{\mathbf{V}}\right) &= \frac{1}{\rho}\frac{\partial}{\partial\rho}(\rho\tilde{V}_\varphi) - \frac{1}{\rho}\frac{\partial}{\partial\varphi}\tilde{V}_\rho \\ &= \frac{1}{\rho}\begin{bmatrix} \sin 2\varphi & -\cos 2\varphi & 0 & 1 \end{bmatrix}\mathbf{p}\end{aligned}$$

The average rotation per unit area is

$$\begin{aligned}\overline{\text{curl}\left(\tilde{\mathbf{V}}\right)} &= \frac{1}{A_{\mathbb{A}}}\int_{\mathbb{A}} \text{curl}\left(\tilde{\mathbf{V}}\right)\cdot\mathbf{e}_z\, d\mathbb{A} \\ &= \frac{1}{\pi\rho_{\mathbb{A}}^2}\int_0^{\rho_{\mathbb{A}}}\int_0^{2\pi} \text{curl}\left(\tilde{\mathbf{V}}\right)\cdot\mathbf{e}_z\,\rho\, d\rho\, d\varphi \\ &= \frac{2}{\rho_{\mathbb{A}}}\, p_4 \end{aligned} \tag{6.28}$$

Invoking Stoke's integral theorem

$$\int_{\mathbb{A}} \text{curl}\left(\tilde{\mathbf{V}}\right)\cdot\mathbf{e}_z\, d\mathbb{A} = \oint_{\mathbb{S}} \tilde{\mathbf{V}}\cdot d\mathbf{S}$$

yields

$$\begin{aligned}\overline{\text{curl}\left(\tilde{\mathbf{V}}\right)} &= \frac{1}{A_{\mathbb{A}}}\oint_{\mathbb{S}} \tilde{\mathbf{V}}\cdot d\mathbf{S} \\ &= \frac{1}{\pi\rho_{\mathbb{A}}^2}\int_0^{2\pi}\left[\tilde{V}_\rho\mathbf{e}_\rho + \tilde{V}_\varphi\mathbf{e}_\varphi\right]\cdot(\rho_{\mathbb{A}}\, d\varphi\,\mathbf{e}_\varphi) \\ &= \frac{2}{\rho_{\mathbb{A}}}\frac{1}{2\pi}\int_0^{2\pi}\tilde{V}_\varphi\, d\varphi \end{aligned} \tag{6.29}$$

From (6.28) and (6.29), we conclude that

$$\overline{\text{curl}\left(\tilde{\mathbf{V}}\right)} = \frac{2}{\rho_{\mathbb{A}}}\, p_4 = \frac{2}{\rho_{\mathbb{A}}}\frac{1}{2\pi}\int_0^{2\pi}\tilde{V}_\varphi\, d\varphi$$

from which

$$p_4 = \frac{1}{2\pi}\int_0^{2\pi}\tilde{V}_\varphi\, d\varphi$$

Thus, approximating p_4 as

$$p_4 \approx \bar{V}_\varphi := \frac{1}{N}\sum_{i=1}^{N} \tilde{V}_{i,\varphi} \tag{6.30}$$

captures the regional rotation of the flow.

Choosing $p_3 = \bar{V}_\rho$ and $p_4 = \bar{V}_\varphi$ reduces the number of parameters that remain to be identified to two. The cost function (6.20), with the pre-determined parameters $\bar{V}_\rho$ and $\bar{V}_\varphi$, becomes

$$\tilde{J} = \sum_{i=1}^{N} \left[q_{i,\rho} \left(\mathbf{b}_\rho^T(\varphi_i) \begin{bmatrix} p_1 \\ p_2 \\ 0 \\ 0 \end{bmatrix} + \bar{V}_\rho - \tilde{V}_{i,\rho} \right)^2 + q_{i,\varphi} \left(\mathbf{b}_\varphi^T(\varphi_i) \begin{bmatrix} p_1 \\ p_2 \\ 0 \\ 0 \end{bmatrix} + \bar{V}_\varphi - \tilde{V}_{i,\varphi} \right)^2 \right] \tag{6.31}$$

which can be solved similarly to (6.21). Of course, removing the free parameters p_3 and p_4 will generally result in a larger minimum value of $\tilde{J}$ than of J. Minimizing $\tilde{J}$, however, is inspired by physical considerations and produces flow models that appear to better capture the regional flow pattern in examples.

The two strategies for identifying the singular flow, either by using a least squares approach for all four parameters $p_1, .., p_4$ or by constraining p_3 and p_4 to match intrinsic flow characteristics, are compared in Section 6.4 using experimental data.

6.3.5 Summary of Identification Algorithm

The flow chart in Figure 6.5 summarizes the flow identification process. The key steps in the algorithm involve

1. approximating the uniform flow $\mathbf{U}$,

2. selecting the singularity location $\mathbf{r}_s$, and

3. identifying the singular flow matrix $\mathbf{A}$.

The optional approaches for the first and third step are indicated in Figure 6.5. Experimental results in Section 6.4 illustrate the impact of these choices on the identified flow model.

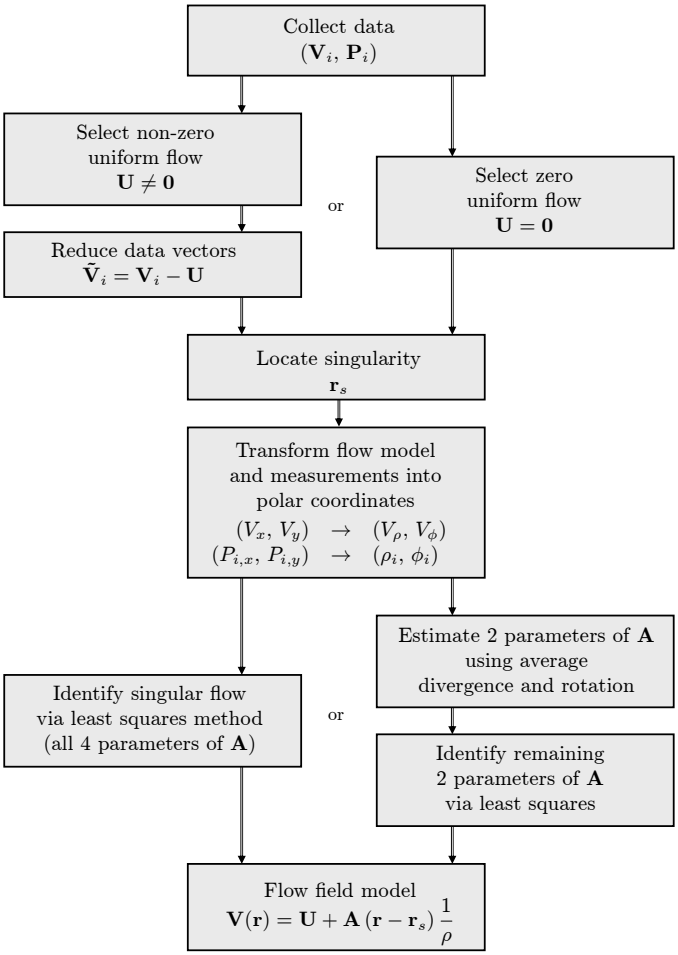

Figure 6.5: Flow chart of the flow field identification process.

We note that the identification process illustrated in Figure 6.5 can be used to incorporate multiple flow singularities. One may iteratively superimpose singularities in order to capture the residual flow field error vectors from the flow model generated by previous iterations. With P flow singularities at the locations $\mathbf{r}_{s,i},\ i = 1...P$, the flow field model becomes

$$\mathbf{V}(\mathbf{r}) = \mathbf{U} + \sum_{i=1}^{P} \mathbf{A}_i (\mathbf{r} - \mathbf{r}_{s,i})\, w(\rho_i) \qquad \text{where} \qquad \rho_i = \|\mathbf{r} - \mathbf{r}_{s,i}\| \tag{6.32}$$

The relative advantages of such an iterative modeling method are not investigated here.

6.4 Experimental Results and Numerical Simulations

In this section, we perform field experiments and numerical simulations that show the performance of the flow field identification algorithm. Moreover, we illustrate the benefit of incorporating a flow field model for underwater navigation. In Section 6.4.1, we use real data collected by a single AUV to identify the parameters of the ambient flow field. We recompute the AUV's trajectory under the effect of the modeled flow in Section 6.4.2 showing an improvement in navigational accuracy. In Section 6.4.3, we conduct numerical simulations in which we send a platoon of AUVs through a known flow environment. Thus, we provide ground truth to evaluate both the flow field identification and the improvements in underwater navigation.

6.4.1 Flow Field Identification

In this section, the flow field identification algorithm is applied to a set of data that was collected during field experiments in the Lafayette River near Norfolk, Virginia [86]. In the field experiment, a single vehicle was commanded to operate on the surface, so that GPS position updates could be obtained along the entire trajectory. While AUVs are normally submerged, the experiment was conducted in this manner to provide ground truth for the AUV trajectory. In executing the flow model identification algorithm, position updates were collected every 30 seconds. Between each two successive position measurements, the kinematic model (6.3) was used to estimate the trajectory. The error between the true and predicted final position was used to estimate the fluid flow velocity $\mathbf{V}_i$ along that segment. (The flow velocity was assumed to be uniform along each segment.) Figure 6.6 shows the GPS data and the extracted flow velocity measurements. GPS-tracked surface drifters were deployed simultaneously [87]. Assuming that the drifters followed the true flow, their GPS tracks provide at least a qualitative measure of a given flow model's accuracy. The performance of the flow field model (6.1) is examined for several proposed variations of the algorithm described in Section 6.3.

Assuming that the drifters follow streamlines of the flow, estimated flow field vectors $\mathbf{W}_i$ can be extracted at locations $\mathbf{D}_j$, $j = 1..M$; see the right plot of Figure 6.8. These sample vectors may then be compared to the modeled flow field $\mathbf{V}(\mathbf{D}_j)$ at the same locations. In addition to the performance measures η used in [81], we define an identification error ζ along the drifters' tracks:

$$\zeta(\mathbf{W}_j, \mathbf{V}) = \sqrt{\frac{1}{M}\sum_{j=1}^{M} \|\mathbf{W}_j - \mathbf{V}(\mathbf{D}_j)\|^2}. \tag{6.33}$$

This measure is analogous to the error measure η, given in (6.18), that accounts

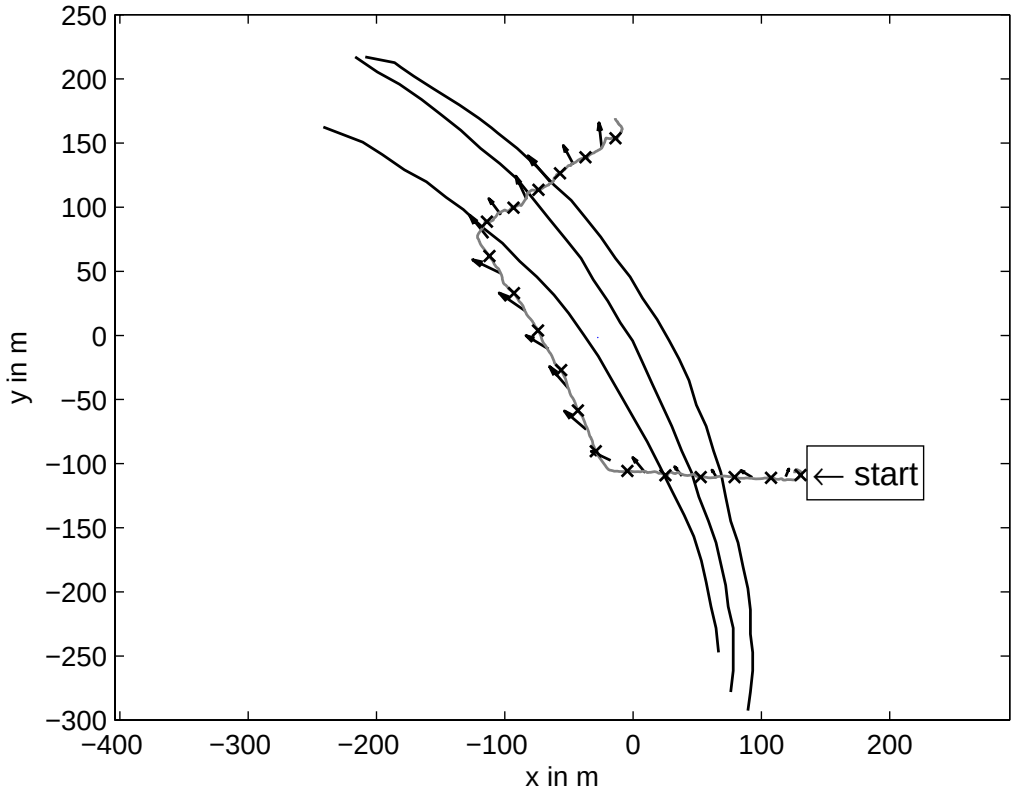

Figure 6.6: GPS way points $'\times'$ along the vehicle's trajectory (solid gray lines) are used to extract the local flow measurements (black arrows). The drifter tracks (solid black lines) provide independent data for evaluating the performance of the identification algorithm.

for the identification error along the vehicle's trajectory. Because the drifters are tracked over a large region, relative to the AUV's path, ζ measures the validity of the flow field model in a larger neighborhood of the vehicle's trajectory.

Four different estimated flow fields are computed. The assumptions used in com-

puting the flow fields and the resulting estimation errors are summarized in Table 6.1.

Table 6.1: Several identification options and their impact on the modeled flow.

Flow identification	Assumption	Singular flow pattern	Identification error
Case 1 Figure 6.8	$\mathbf{U} \neq \mathbf{0}$	$\Gamma_2(\mathbf{r}_{s,2}) = 0.2027$ source	$\eta = 0.0882$ ms^{-1} $\zeta = 0.1299$ ms^{-1}
Case 2 Figure 6.9	$\mathbf{U} = \mathbf{0}$	$\Gamma_4^*(\mathbf{r}_{s,4}^*) = 0.0130$ vortex	$\eta = 0.1133$ ms^{-1} $\zeta = 0.1531$ ms^{-1}
Case 3 Figure 6.10	$\mathbf{U} = \mathbf{0}$	$\Gamma_2^*(\mathbf{r}_{s,2}^*) = 0.0027$ source	$\eta = 0.1173$ ms^{-1} $\zeta = 0.2026$ ms^{-1}
Case 4 Figure 6.11	$\mathbf{U} = \mathbf{0}$	$\Gamma_4^*(\mathbf{r}_{s,4}^*) = 0.0130$ vortex	$\eta = 0.1424$ ms^{-1} $\zeta = 0.0772$ ms^{-1}

Case 1 ($\mathbf{U} \neq \mathbf{0}$): The uniform flow $\mathbf{U}$ is identified as the average over all flow velocity estimates (6.4). The computed uniform flow is shown in the left-hand side of Figure 6.7. The residual flow velocity measurements $\tilde{\mathbf{V}}_i = \mathbf{V}_i - \mathbf{U}$, shown in right-hand side of Figure 6.7, are used to identify the singular flow. In minimizing the four cost functions $\Gamma_j(\mathbf{r})$ defined in (6.11), a singularity is detected at $\mathbf{r}_{s,2}$. The singularity matrix $\mathbf{A}$ corresponding to this location is identified using the least squares approach applied to the cost function (6.20). Figure 6.8 shows the identified singular flow component (6.6) and the full flow field model (6.1). Of the various approaches suggested, this approach yields the smallest RMS error η as defined in (6.18).

Cases 2 and 3 ($\mathbf{U} = \mathbf{0}$): The flow is assumed to be purely singular. In minimizing the four cost functions $\Gamma_j(\mathbf{r})$ defined in (6.11), two singularities are detected:

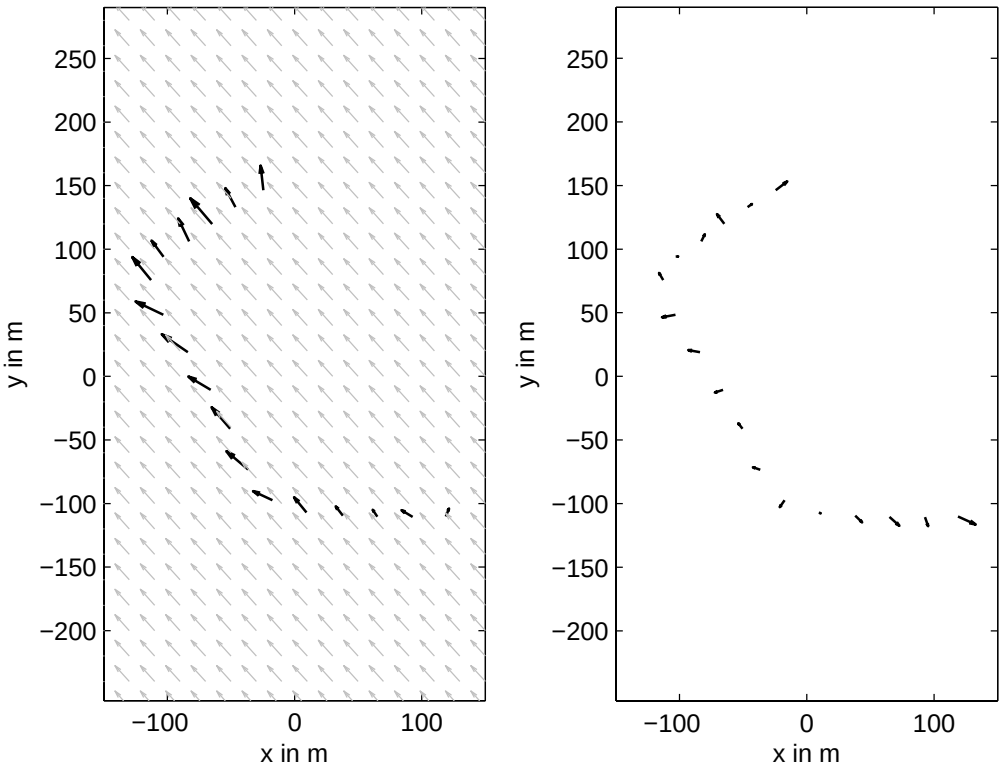

Figure 6.7: Left plot: The uniform flow $\mathbf{U}$ (gray) is identified as the average over all flow velocity estimates (black). Right plot: The residual data vectors are obtained by subtracting the uniform flow from the flow velocity measurements $\tilde{\mathbf{V}}_i = \mathbf{V}_i - \mathbf{U}$.

a counter-clockwise vortex at $\mathbf{r}^*_{s,4}$ and a source at $\mathbf{r}^*_{s,2}$. (The superscript asterisk distinguishes the case $\mathbf{U} = \mathbf{0}$ from $\mathbf{U} \neq \mathbf{0}$, for which the residual data set is different.) In both cases, the singularity matrix $\mathbf{A}$ is identified using the least squares approach applied to the cost function (6.20). The resulting flow field corresponding to $\mathbf{r}^*_{s,4}$ is shown in Figure 6.9, and the flow field corresponding to $\mathbf{r}^*_{s,2}$ is shown in Figure 6.10.

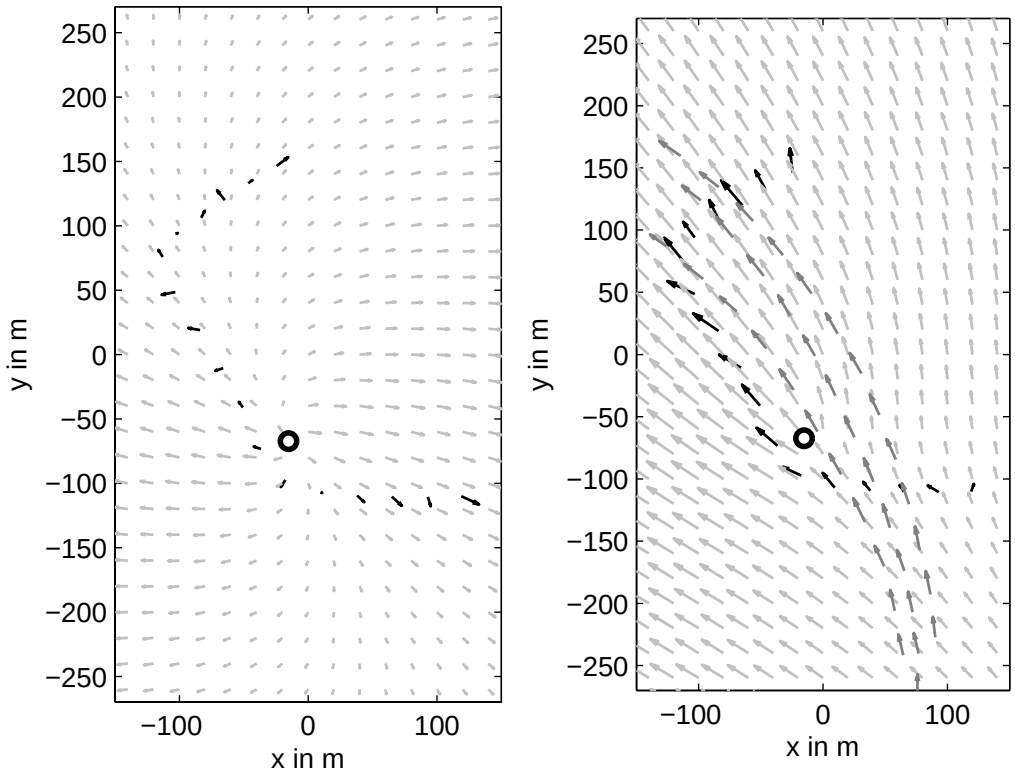

Figure 6.8: Left plot: The singular flow $\tilde{\mathbf{V}}(\mathbf{r})$ (gray) is identified using the residual sample vectors $\tilde{\mathbf{V}}_i(\mathbf{P}_i)$ (black). A source (represented by a $'\circ'$) is detected at $\mathbf{r}_{s,2}$. Right plot: The set of sample vectors $\mathbf{V}_i(\mathbf{P}_i)$ (black) is used to parameterize the combined uniform and singular flow components of $\mathbf{V}(\mathbf{r}) = \mathbf{U} + \tilde{\mathbf{V}}(\mathbf{r})$ (light gray). For reasons of comparison, a set of flow field sample vectors $\mathbf{W}_j$ (dark gray) is extracted along the drifters' tracks $\mathbf{D}_j$.

Note that the singularity $\mathbf{r}^*_{s,4}$ is located far outside the region in which the measurements are taken. Recall that if one computes the average flow velocity $\mathbf{U}$ and

removes it from the flow measurements, there are guaranteed bounds on the candidate singularity locations. In contrast, for the present case where $\mathbf{U}$ is assumed to be zero, there are no such bounds. Also note, in Figure 6.9, that the flow characteristics change dramatically outside the immediate neighborhood of the measurements, with the flow reversing direction near the start of the drifter tracks. The identification errors η in Table 6.1 are slightly larger for this case; this is to be expected, since setting $\mathbf{U} = \mathbf{0}$ eliminates two free parameters from the flow model. Comparing Figure 6.9 and Figure 6.10, one can see that the selection of the singularity location has a significant impact on the modeled flow pattern, even though there is little difference in the identification errors η given in Table 6.1.

Case 4 ($\mathbf{U} = \mathbf{0}$): Again, the flow is assumed to be purely singular. The counterclockwise vortex at $\mathbf{r}^*_{s,4}$ identified in Case 2 is assumed. Now, the singular flow model is constrained to preserve the average divergence and vertical vorticity given by the flow velocity measurements, as proposed in Section 6.3.4. Using this identification strategy, only the two parameters p_1 and p_2 remain to be determined by minimizing the modified cost function (6.31). The resulting flow field model is shown in Figure 6.11. As indicated in Table 6.1, this approach results in a slightly larger identification error η compared to the approach used in Figure 6.9 that presumes the same singularity location. Perhaps surprisingly, though, the model yields the smallest error ζ with respect to the drifters. This approach provides a better flow field model in the larger neighborhood of the vehicle's path.

Summary of Experimental Results: Of the four approaches shown, there are potentially many factors that contribute to a selection of one solution over another. Based on the limited experimental work reported here, we may offer the following guidelines: If regional flow characteristics of the flow are desired and should be pre-

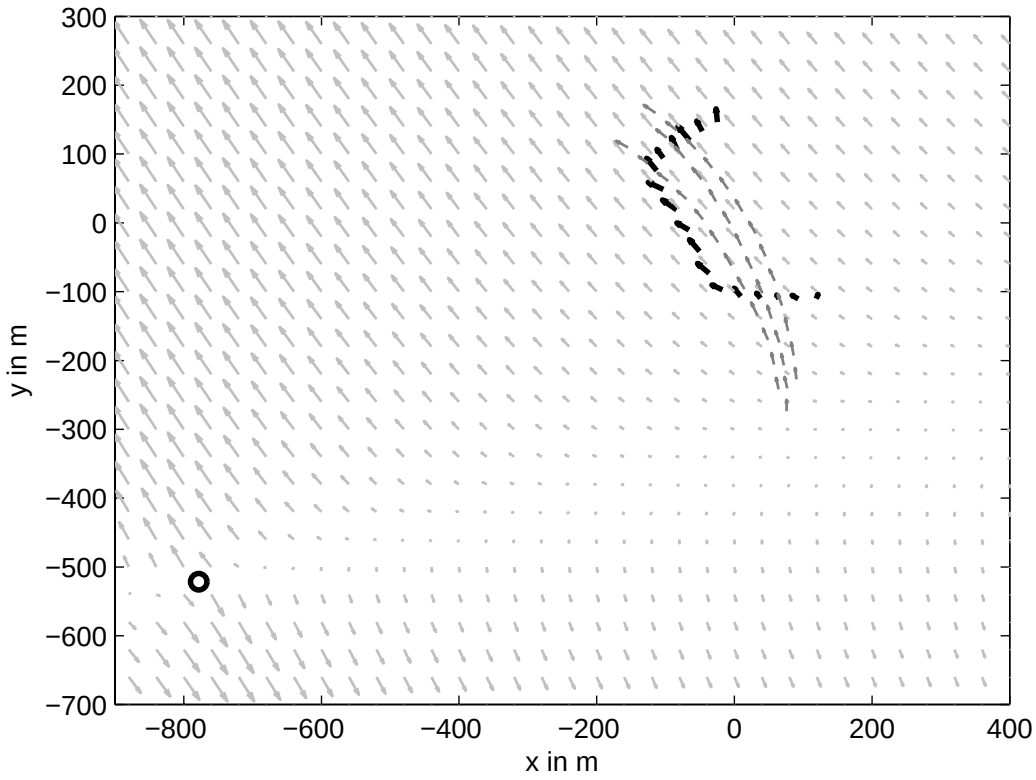

Figure 6.9: The flow field is identified assuming a zero uniform flow. A counter-clockwise vortex (represented by a $'\circ'$) is detected at $\mathbf{r}^*_{s,4}$. The sets of flow field sample vectors along the drifters' tracks and along the AUV trajectory are shown in dark gray and black, respectively.

served, then assume that $\mathbf{U} = \mathbf{0}$ and proceed with the constrained two-parameter estimation, which attempts to preserve the average vorticity and divergence. For our example, this approach generates a reliable flow field model even in regions where no flow measurements were taken. Alternatively, for improved AUV navigation in

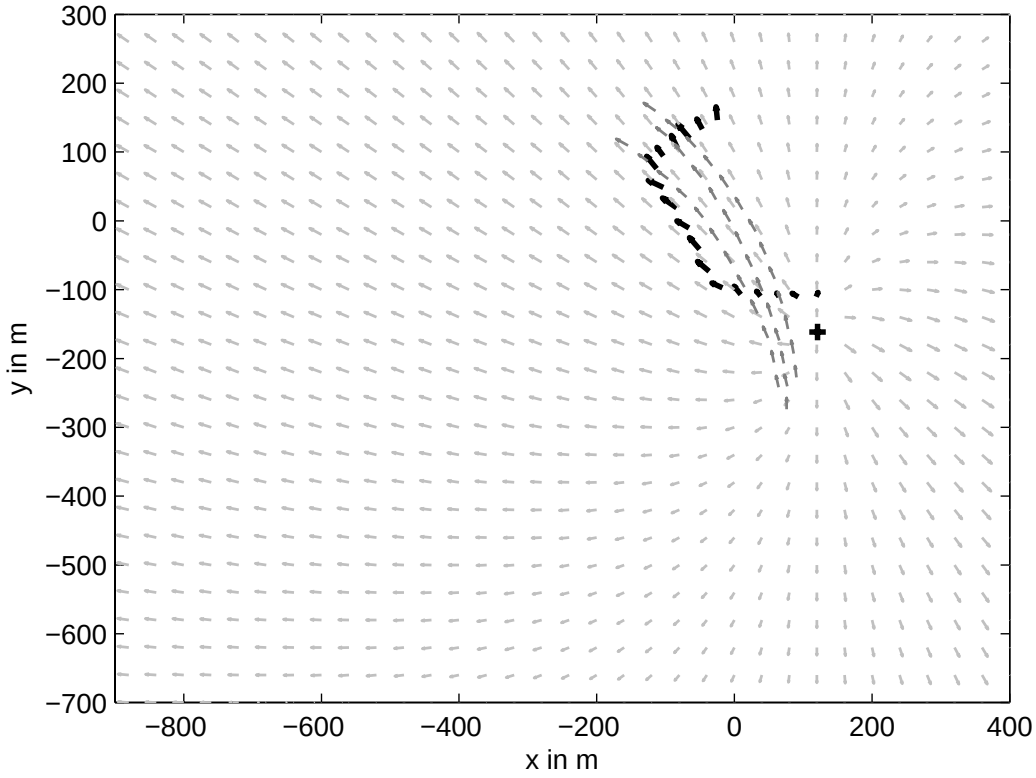

Figure 6.10: The flow field is identified assuming a zero uniform flow. An alternative flow singularity, a source (represented by a $'+'$) is detected at $\mathbf{r}^*_{s,2}$. The sets of flow field sample vectors along the drifters' tracks and along the AUV trajectory are shown in dark gray and black, respectively.

settings where the vehicles remain in one region, one might choose an approach that results in the lowest identification error η. For our example, the approach that yielded the smallest identification error η involved first computing the average flow velocity, treating it as a uniform flow component ($\mathbf{U} \neq \mathbf{0}$) and then locating and identifying a

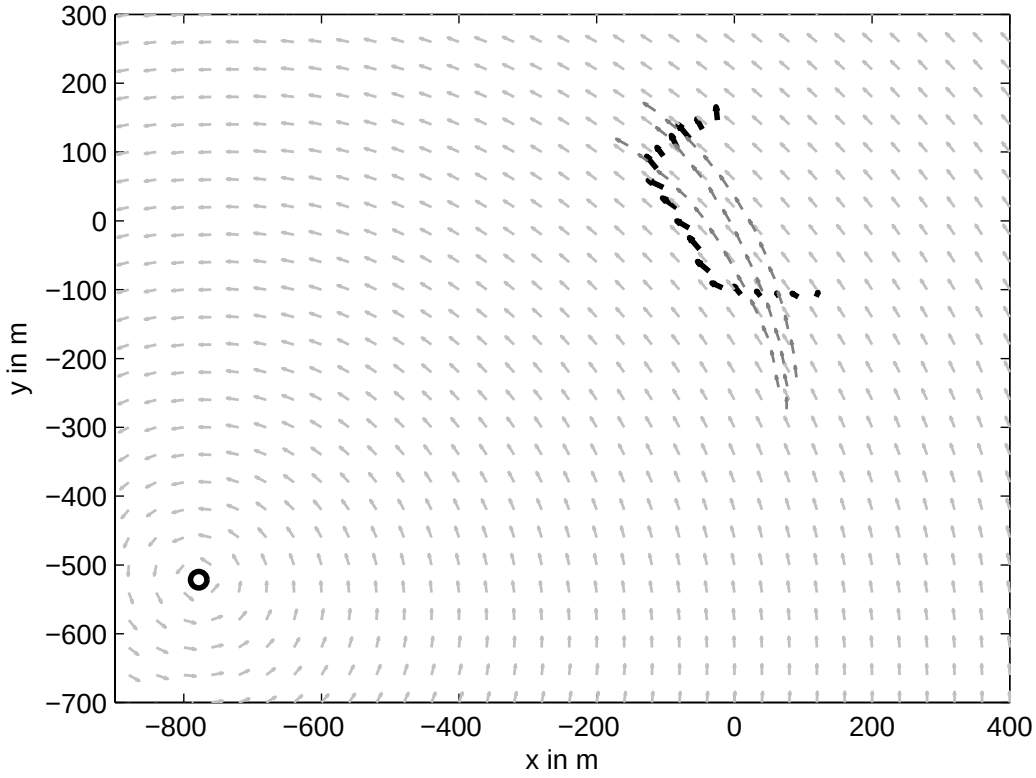

Figure 6.11: The flow field is identified assuming a zero uniform flow. A counter-clockwise rotational singularity (represented by a $'\circ'$) is detected at $\mathbf{r}^*_{s,4}$. The average divergence and vorticity are estimated from data and the resulting model is constrained to preserve these characteristics. The sets of flow field sample vectors along the drifters' tracks and along the AUV trajectory are shown in dark gray and black, respectively.

superimposed flow singularity.

6.4.2 Application in AUV Navigation

Figure 6.12 illustrates the advantage of assessing the ambient fluid motion for AUV navigation. Based on the vehicle's estimated water relative velocity and the compass heading angle, the AUV's trajectory is recalculated using the kinematic model (6.3) with and without the modeled environmental flow field presented in Figure 6.11. The error of the predicted destination decreases from 34.1 percent of distance traveled (%DT) to 5.6 %DT. This illustration of improved performance is an ideal case. The flow field was computed using flow samples generated by the AUV, and then the resulting flow field was used to improve knowledge of the *same* AUV path. However, the example demonstrates the potential utility of simple flow models for improved AUV navigation.

6.4.3 Numerical Simulation

In this Section, we present numerical simulations to evaluate the performance of the flow field identification algorithm. Moreover, we intend to validate improvements in underwater navigation when assessing an ambient flow field model. We provide ground truth by sending a platoon of AUVs through a *known* flow field environment. Using only 24 flow field sample vectors, we conduct the flow field identification and re-navigate the AUVs through the same region.

For the simulations in this section, we use the data file *wind.mat* provided within MATLAB [88]. The data file represents air currents over a region of North America. For our purpose, we select the 8th altitude layer of the three-dimensional data set to model planar fluid flow. We also stretch the physical dimension in x and y direction by a factor of 10 and assume a unit length of one meter. In addition, we reduce

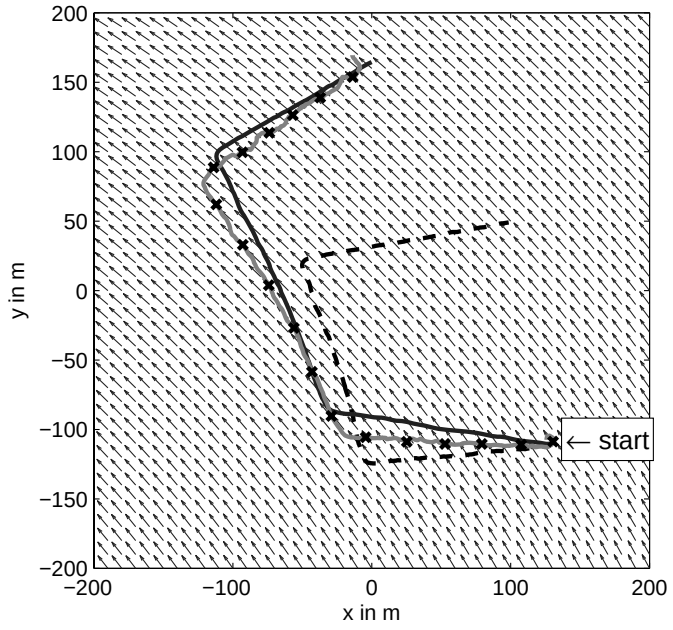

Figure 6.12: Dead reckoning: The AUV trajectory is recalculated using the kinematic model (6.3) with (solid black line) and without (dashed black line) an ambient flow model. During the field experiment, GPS way points $'\times'$ were collected every 30 seconds along the AUV's trajectory (gray).

the magnitude of the entire vector field to 0.4 % yielding a maximum flow magnitude of 0.25 ms^{-1}, which is more consistent with typical ocean currents. The flow field data set is denoted $\mathbf{V}_0(\mathbf{r})$ and is shown in gray in Figure 6.13.

We simulate the kinematics (6.3) of three AUVs, each traveling at a water relative speed of $\hat{u}_1 = 1.5$ ms^{-1}. After 60 seconds of travel time, the vehicles surface to obtain a GPS fix and continue to dive starting with a 90 degree right turn. Thus, their intended trajectories are square-shaped shown as dotted lines in Figure 6.13. The

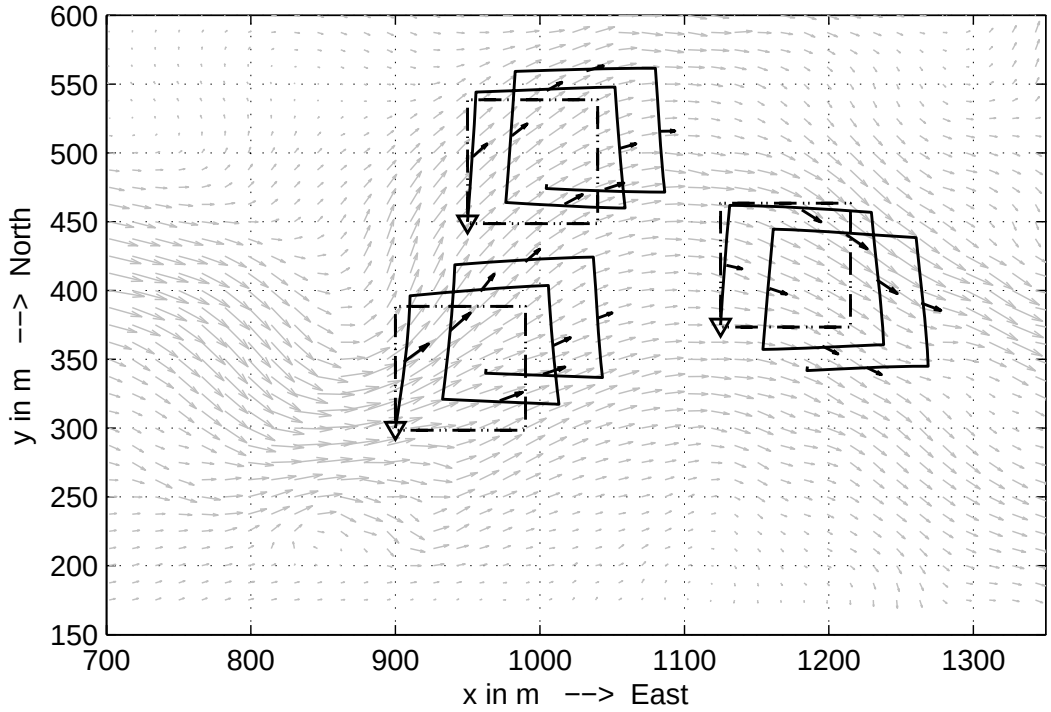

Figure 6.13: The real, known flow field $\mathbf{V}_0(\mathbf{r})$ is shown in gray. The trajectories of three AUVs are superimposed, intended trajectories (dash dotted) and actual trajectories (solid). The AUV trajectories start at ∇. Flow field samples $\mathbf{V}_i$, $i = 1..24$ (black arrows) are collected along the AUV trajectories at locations $\mathbf{P}_i$.

mission lasts 8 minutes. Each AUV conducts 8 right turns, and their quadrangular trajectories are shown as solid lines in Figure 6.13. As one can see, the actual vehicle trajectories are affected significantly by the ambient fluid flow.

Start and end points of each 60 second trajectory segment are known through GPS. By evaluating the dead reckoning error for each segment, the AUVs assign flow field sample vectors $\mathbf{V}_i$ at locations $\mathbf{P}_i$ along their trajectories. Again, we assume uniform

flow along each trajectory segment when extracting flow field sample vectors. Black arrows in Figure 6.13 represent the set of flow field sample vectors obtained during the simulation.

We parameterize a flow field model $\mathbf{V}(\mathbf{r})$ defined in (6.1) using the set of flow field samples $\mathbf{V}_i(\mathbf{P}_i)$. For this experiment, we assume zero uniform flow $\mathbf{U} = \mathbf{0}$ and identify the singular flow using the constrained least squares approach which preserves average divergence and rotation. The identification approach is identical to Case 4 in Section 6.4.1. The algorithm detects a singularity at $\mathbf{r}_s = \begin{bmatrix} 1111\,\mathrm{m} & 173\,\mathrm{m} \end{bmatrix}^T$ and identifies a clockwise rotation pattern of the singular flow. Figure 6.14 shows the flow field model $\mathbf{V}(\mathbf{r})$ in gray and the sample set $\mathbf{V}_i(\mathbf{P}_i)$ in black. The identification error (6.18) is $\eta = 0.04$ ms^{-1}.

Both flow fields: the data set $\mathbf{V}_0(\mathbf{r})$ and the identified model $\mathbf{V}(\mathbf{r})$ are plotted in Figure 6.15 in gray and black, respectively. It is evident that the flow field model captures the fluid motion well, especially in the area where measurements are taken. However, moderate differences can be seen on the left hand side of Figure 6.15 where both flow fields are almost perpendicular to one another.

In addition, we compute the relative flow field error $\mathbf{V}_E(\mathbf{r})$ defined by

$$\mathbf{V}_E(\mathbf{r}) = \frac{\mathbf{V}_0(\mathbf{r}) - \mathbf{V}(\mathbf{r})}{V_{0,\max}} \qquad \text{where} \qquad V_{0,\max} = \max_{\mathbf{r}} \|\mathbf{V}_0(\mathbf{r})\| \tag{6.34}$$

Here $V_{0,\max} = 0.25$ ms^{-1} is the maximum flow velocity within the given data set. The magnitude of the relative flow field error $\|\mathbf{V}_E(\mathbf{r})\|$ is shown in Figure 6.16. Again, as indicated by the small magnitude of $\mathbf{V}_E(\mathbf{r})$, the identified flow field model approximates the fluid flow very well in regions where measurements are taken.

In order to illustrate the benefit of incorporating a flow field model into AUV navigation, we re-navigate the AUVs through the flow field $\mathbf{V}_0(\mathbf{r})$. Now the vehicles compensate for the disturbing flow field using the flow field model $\mathbf{V}(\mathbf{r})$. Figure 6.17

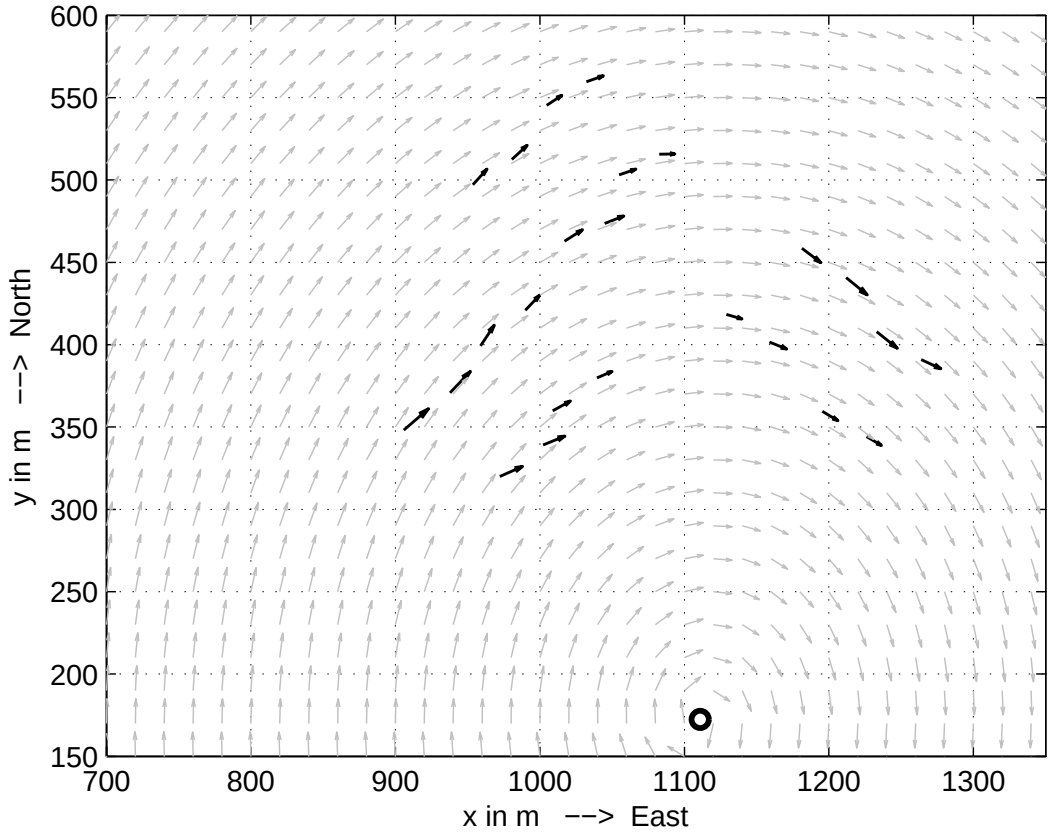

Figure 6.14: Using the flow field sample vectors $\mathbf{V}_i(\mathbf{P}_i)$ (black), a flow singularity ($'\circ'$) is detected. The flow field model $\mathbf{V}(\mathbf{r})$ (gray) is identified assuming a zero uniform flow, and the parameters of the singular flow are obtained via constrained least squares preserving average divergence and rotation.

shows the compensated AUV trajectories (solid black) in direct comparison with the uncompensated trajectories (solid gray) from Figure 6.13. Clearly, the navigation error reduces significantly when incorporating the flow field model $\mathbf{V}(\mathbf{r})$. One can

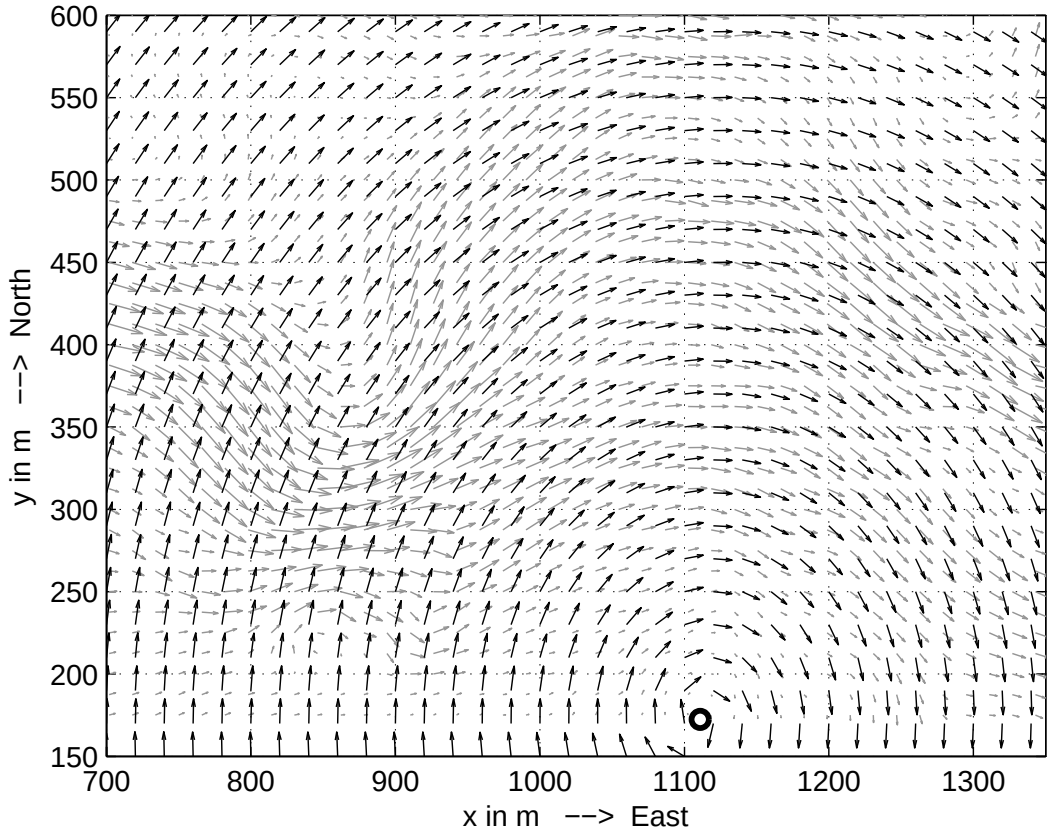

Figure 6.15: The data set $\mathbf{V}_0(\mathbf{r})$ is shown in gray, and the identified flow field model $\mathbf{V}(\mathbf{r})$ is shown in black.

show that the average navigation error decreases from 10 percent of distance traveled (%DT) to 2.5 %DT.

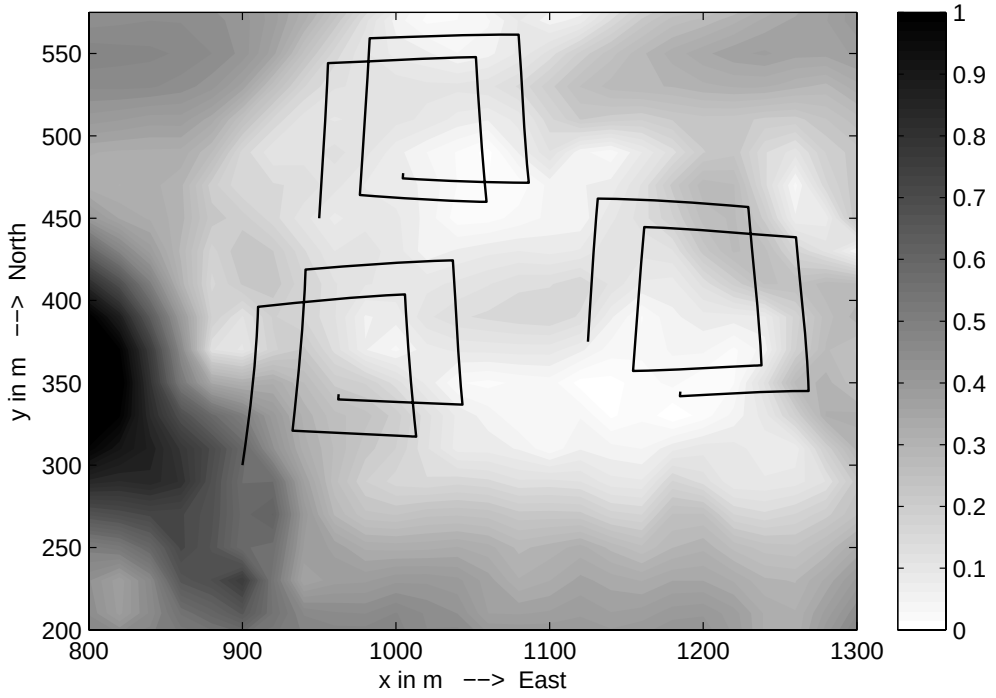

Figure 6.16: Magnitude of relative flow field error $\|\mathbf{V}_E(\mathbf{r})\|$ that is normalized with respect to the maximum flow velocity $V_{0,\max} = 0.25$ ms^{-1}, see (6.34). Lower values (white) indicate a good match between the real data $\mathbf{V}_0(\mathbf{r})$ and the flow field model $\mathbf{V}(\mathbf{r})$. The AUV trajectories are superimposed in black.

6.5 Conclusions

In this chapter, we develop a technique to identify a proposed planar flow field model using a small, sparse set of flow velocity measurements that might be collected by a platoon of AUVs. The flow model includes a uniform flow component and a singular flow component (a source/sink or point vortex). The approach proceeds in three

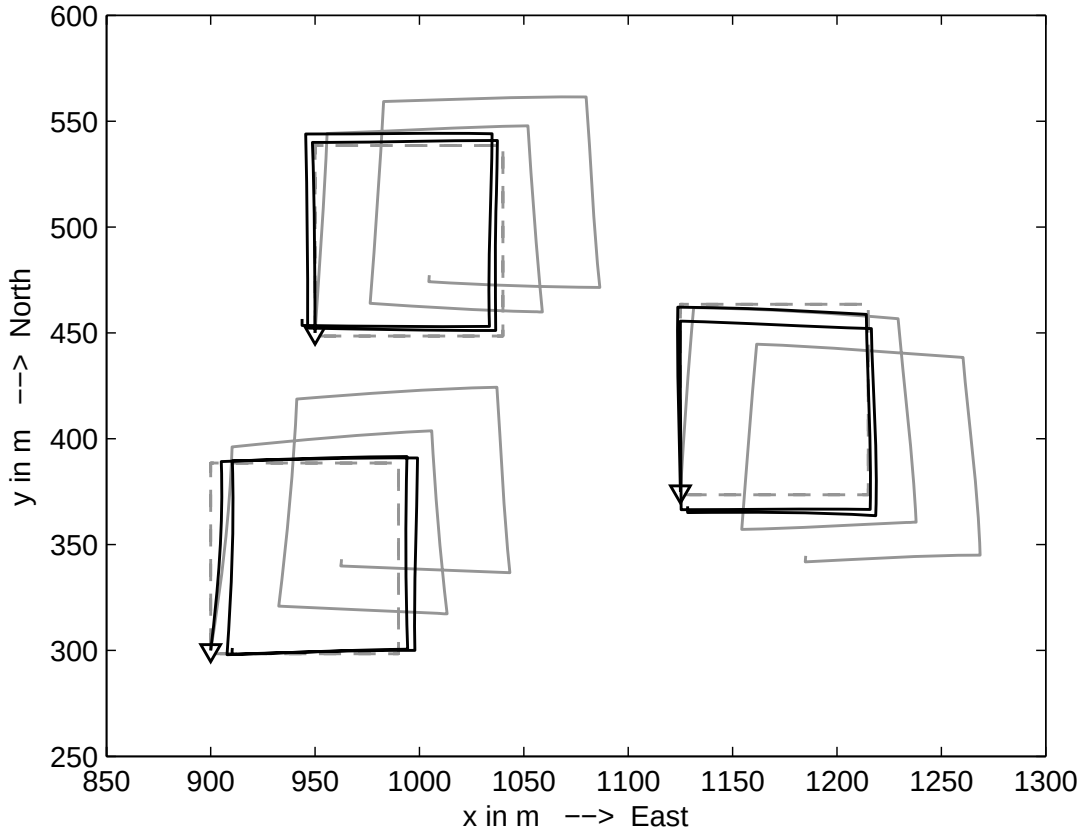

Figure 6.17: Uncompensated (solid gray) and compensated (solid black) AUV trajectories using the flow field model $\mathbf{V}(\mathbf{r})$. The intended AUV trajectories are plotted in dashed gray.

steps: identifying the uniform flow component, determining the location of the flow singularity, and identifying the parameters that define the singular flow. A gradient method is used to detect candidate locations for flow singularities which appear to match the flow pattern of the data vectors, a process which results in multiple flow

model possibilities. The best model is selected using an error metric.

Two concepts to identify the singular flow are examined. First, a least squares approach is used to identify four parameters which characterize the singular flow. This approach yields the minimum identification error and generates a fluid flow model that is valid in the domain where measurements were taken. A second approach preserves intrinsic regional flow characteristics, such as average divergence and vorticity. In numerical and experimental applications, a flow model is obtained that adequately represents the local flow and also provides a reasonable flow model in a larger region surrounding the existing measurements.

The variety of approaches allows us to adapt the algorithm depending on the identification priority. For example, a bend in a river might suggest a largely rotational singularity while an upwelling event might suggest a largely solenoidal singularity. The apparent trade-off between a low identification error and good qualitative agreement with the regional flow pattern is a topic for further study.

It is expected that the proposed method for flow field identification may improve navigational accuracy for AUVs that operate by dead reckoning, with periodic GPS updates. Included in this category are underwater gliders, which surface periodically in order to transmit data and receive new instructions. Because they move at low speeds, underwater gliders are more susceptible to currents. Small improvements in the estimate of the ambient current could dramatically improve glider navigational accuracy and efficiency. Although an underwater glider's depth varies continuously throughout its flight, the proposed strategy is appropriate in cases where the subsurface flow does not vary significantly with depth.

Chapter 7

Conclusions

This dissertation addresses attitude control and inertial navigation of AUVs. We present theoretical justification for using simplified models, derive system identification algorithms, and verify our results through extensive field trials.

We establish theoretical and practical justification for using linear second-order AUV pitch-axis models for system identification and attitude control design. We prove that vehicle parameters such as hydrodynamic coefficients or added mass terms cannot be obtained from data collected onboard the AUV without instrumenting linear velocities. Given the limited instrumentation of small AUV systems, a third-order model does not provide any advantages over a second-order approximation for the purpose of parameter identification. We rigorously analyze truncating the third-order dynamics and assess the utility and limitations of a controller that is based on a second-order approximation. Our analysis and field trials show that second-order models are often adequate for model-based control design for streamlined AUVs.

We present online system identification algorithms that estimate the parameters of a linear second-order AUV pitch-axis model. For the given system, formal ob-

servability analysis shows equivalence between persistence of excitation and uniform observability. Our theoretical results are validated through field experiments using multiple AUV configurations. For each AUV configuration, we obtain a linear second-order model and present model-based control redesign.

For robust attitude control, we derive a novel linear time-varying model that captures pitch and yaw motion of an AUV. Our analysis shows that roll motion causes coupling between pitch and yaw dynamics, which is commonly neglected for AUV control design. We propose the use of an upright AUV body frame in which the linear model representation contains fewer nonzero off-diagonal terms. Our model facilitates the use of an $\mathcal{H}_\infty$ control design approach that specifically addresses the remaining coupling terms as structured uncertainties. Field trials show that the $\mathcal{H}_\infty$ controller decreases the coupling between pitch and yaw motion in comparison to single axis PID controllers implemented separately for pitch and yaw.

For the purpose of improving inertial navigation, we develop an online calibration method for a triaxial gyroscope system. We propose a gyroscope error model containing scaling and bias parameters, which are subject to parameter identification. We investigate excitation condition which guarantee the convergence of parameter estimates and verify our results during bench tests. The gyroscope calibration allows for low output tracking errors when integrating the calibrated gyroscope measurements over a short period of time.

In addition, we present a technique to identify the parameters of a simplified flow field model that captures an ambient planar flow field effecting the AUV trajectory. Our algorithm requires only a sparse set of flow velocity measurements that might be collected by a platoon of AUVs. In numerical and experimental applications, a flow model is obtained that adequately represents the local flow.

Appendix A

AUV Model

In this section, we recall the equations of motion of a rigid body in ideal fluid. Modeling approaches for self-propelled and tail-controlled submersibles can be found throughout the literature [1], [34], [89] and [90]. For example, a non-linear model of a streamlined, tail-controlled AUV is proposed in [35], in which kinematic and dynamic equations are derived using Kirchhoff's equations of motion [91]. However, the large number of vehicle specific parameters and hydrodynamic coefficients, that are usually obtained through complex and costly tow tank experiments or time consuming computational fluid dynamics (CFD) simulations, disqualifies these models for real-time system identification. For example in [92], the author claims that 150 parameters are necessary in order to describe the full nonlinear dynamics of today's underwater vehicles. Starting from the equations of motion presented in [35], our goal is to derive lower-order linear AUV models suitable for parameter estimation and control design.

Due to the symmetrical mass distribution and the streamlined shape of AUVs, the equations of motion can be simplified. Under the assumption of zero-roll motion, we derive a pitch-axis or longitudinal model that describes the motion in the xz-plane

often referred to as dive plane. A linearization around a steady state flight condition at constant depth and zero angle of attack suggests that the vehicle's forward speed decouples from the vehicle's pitch motion. Thus, assuming constant speed reduced the pitch model to third order.

A.1 Rigid Body Kinematics

Let the position of a rigid body in the inertial frame be given by $\boldsymbol{r} = [X,\, Y,\, Z]^T$. The body's linear velocity vector $\boldsymbol{v} = [u,\, v,\, w]^T$ denotes surge, sway and heave relative to the body-axis frame. For submarines, the body axes are usually chosen to coincide with the principal axes of inertia with the origin at the center of buoyancy CB, which is assumed to be located at the geometric center, as illustrated in Figure A.1. The center of gravity CG is located at $\boldsymbol{r}_{cg} = [x_{cg}, y_{cg}, z_{cg}]^T$. For the AUV model derived in this dissertation, we assume no lateral separation between the center of buoyancy and the center of gravity, that is $y_{cg} = 0$, which can be accomplished by proper ballasting.

The angular displacement of a rigid body with respect to the inertial frame is commonly expressed using Euler angles, ϕ, θ, and ψ representing roll, pitch, and yaw, respectively. The vector of Euler angles is $\boldsymbol{\eta} = [\phi,\, \theta,\, \psi]^T$. Conventionally, Euler angles define a zyx-sequence (also 321) of rotations relating the inertial frame to the body-axis frame, see [1]. Using the transformation matrix $\mathbf{R}_{\boldsymbol{r}}(\boldsymbol{\eta})$, the flight path in the inertial frame is given by

$$\dot{\boldsymbol{r}} = \mathbf{R}_{\boldsymbol{r}}(\boldsymbol{\eta})\, \boldsymbol{v} \tag{A.1}$$

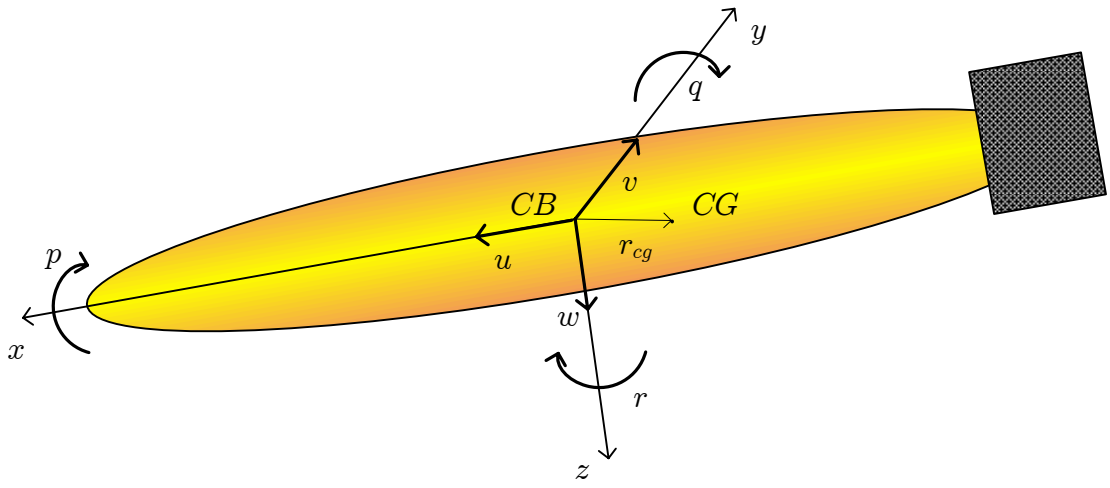

Figure A.1: Rigid Body Motion of an AUV described by linear velocity $\boldsymbol{v} = [u,\, v,\, w]^T$ and angular velocity $\boldsymbol{\omega} = [p,\, q,\, r]^T$. The principal axes of inertia (body-axes) are denoted x, y and z.

where

$$\mathbf{R}_{\boldsymbol{r}}(\boldsymbol{\eta}) = \begin{bmatrix} \cos\psi\cos\theta & -\sin\psi\cos\phi + \cos\psi\sin\theta\sin\phi & \sin\psi\sin\phi + \cos\psi\sin\theta\cos\phi \\ \sin\psi\cos\theta & \cos\psi\cos\phi + \sin\psi\sin\theta\sin\phi & -\cos\psi\sin\phi + \sin\psi\sin\theta\cos\phi \\ -\sin\theta & \cos\theta\sin\phi & \cos\theta\cos\phi \end{bmatrix}$$

The angular motion of a rigid body is defined by body-fixed angular rates $\boldsymbol{\omega} = [p,\, q,\, r]^T$. The relationship between Euler rates $\dot{\boldsymbol{\eta}}$ and body fixed angular rates is

$$\dot{\boldsymbol{\eta}} = \mathbf{R}_{\boldsymbol{\eta}}(\boldsymbol{\eta})\, \boldsymbol{\omega} \tag{A.2}$$

where

$$\mathbf{R}_{\boldsymbol{\eta}}(\boldsymbol{\eta}) = \begin{bmatrix} 1 & \sin\phi\tan\theta & \cos\phi\tan\theta \\ 0 & \cos\phi & -\sin\phi \\ 0 & \dfrac{\sin\phi}{\cos\theta} & \dfrac{\cos\phi}{\cos\theta} \end{bmatrix}$$

For conventional flight regimes assumed in this work with $|\theta| < \frac{\pi}{2}$, three Euler angles suffice to describe the vehicle's attitude. However, some maneuvers might include $\theta = \frac{\pi}{2} + n\,\pi$, $n \in \mathbb{Z}$, for which the vehicle's nose is straight up or down and $\mathbf{R}_{\boldsymbol{\eta}}(\boldsymbol{\eta})$ is not defined. For this situation, one would represent the vehicle attitude using a four-dimensional attitude quaternion [1] for which there is no kinematic singularity. Although the AUV model is derived using Euler angles, we use an attitude quaternion for attitude representation in Chapter 5.

The equations (A.1) and (A.2) describe the changes of the body's position and angular orientation over time. Thus, they are referred to as *kinematic* equations.

A.2 Equations of Motion

To derive the equations of motion for a body in ideal fluid, it is common to evaluate the body's linear and angular momentum as defined in [91] or [93]. In particular, one examines their respective rates of change caused by external forces and moments.

Derived in [35], the complete non-linear, six degree of freedom AUV model is

$$\begin{bmatrix} m_x\dot{u} + m\left(z_{cg}\dot{q} - y_{cg}\dot{r}\right) \\ m_y\dot{v} + \left(mx_{cg} + Z_{\dot{q}}\right)\dot{r} - mz_{cg}\dot{p} \\ m_z\dot{w} + my_{cg}\dot{p} - \left(mx_{cg} + Z_{\dot{q}}\right)\dot{q} \end{bmatrix} =$$

$$\begin{bmatrix} m_x u + m\left(z_{cg}q - y_{cg}r\right) \\ m_y v + \left(x_{cg} + Z_{\dot{q}}\right)r - mz_{cg}p \\ m_z w + my_{cg}p - \left(mx_{cg} + Z_{\dot{q}}\right)q \end{bmatrix} \times \begin{bmatrix} p \\ q \\ r \end{bmatrix} + \begin{bmatrix} F_x \\ F_y \\ F_z \end{bmatrix}$$

$$\begin{bmatrix} J_x\dot{p} + m\left(y_{cg}\dot{w} - z_{cg}\dot{v}\right) \\ J_y\dot{q} + mz_{cg}\dot{u} - \left(mx_{cg} + Z_{\dot{q}}\right)\dot{w} \\ J_z\dot{r} + \left(mx_{cg} + Z_{\dot{q}}\right)\dot{v} - my_{cg}\dot{u} \end{bmatrix} = \begin{bmatrix} J_x p + m\left(y_{cg}w - z_{cg}v\right) \\ J_y q + mz_{cg}u - \left(mx_{cg} + Z_{\dot{q}}\right)w \\ J_z r + \left(mx_{cg} + Z_{\dot{q}}\right)v - my_{cg}u \end{bmatrix} \times \begin{bmatrix} p \\ q \\ r \end{bmatrix}$$

$$+ \begin{bmatrix} m_x u + m\left(z_{cg}q - y_{cg}r\right) \\ m_y v + \left(mx_{cg} + Z_{\dot{q}}\right)r - mz_{cg}p \\ m_z w + my_{cg}p - \left(mx_{cg} + Z_{\dot{q}}\right)q \end{bmatrix} \times \begin{bmatrix} u \\ v \\ w \end{bmatrix} + \begin{bmatrix} M_x \\ M_y \\ M_z \end{bmatrix} \tag{A.3}$$

Here m_x, m_y and m_z represent the vehicle's mass including added mass along the respective body axis. Added mass terms account for the acceleration of fluid across the moving body, see [91] or [94]. The dry mass is m. The body's moments of inertia including added inertia along the x, y and z axes are J_x, J_y and J_z. For a streamlined AUV with two planes of symmetry, we find $m_y = m_z$ and $J_y = J_z$. External forces and moments along the body axes are denoted F_x, F_y, F_z, M_x, M_y and M_z. External forces and moments include hydrodynamic forces and moments such as lift and drag, hydrostatic forces and moments due to the separation between center of gravity and center of buoyancy, and control forces and moments induced by elevator and rudder fin

deflections. The cross added mass term $Z_{\dot{q}}$ is non-zero if the vehicle is not symmetric about the yz-plane. For an AUV with two planes of symmetry, one may similarly use $M_{\dot{w}}$, $N_{\dot{v}}$, or $Y_{\dot{r}}$, see [4] or [34], with

$$Z_{\dot{q}} = M_{\dot{w}} = -N_{\dot{v}} = -Y_{\dot{r}}$$

A.3 Coordinate Transformation

In general, hydrodynamic forces and moments F_x, F_y, F_z, M_x, M_y, and M_z are more conveniently expressed in terms of vehicle speed V and angles of incident such as sideslip angle β and angle of attack α, see [91] or [94]. Due to the simplification that result in the equations of motion, we transform the system (A.3) from the body-axis frame b using the state vector $\boldsymbol{\chi}_b$

$$\boldsymbol{\chi}_b = \begin{bmatrix} u & v & w & p & q & r \end{bmatrix}^T$$

into the stability-axis frame with the state vector $\boldsymbol{\chi}_w$

$$\boldsymbol{\chi}_w = \begin{bmatrix} V & \beta & \alpha & p & q & r \end{bmatrix}^T$$

For aircraft application, the stability-axis frame is often referenced as *zero-lift* or *wind-axis* frame w, see [95]. Both representation of the vehicle's velocity vector are illustrated in Figure A.2. The transformation is given by

$$V = \sqrt{u^2 + v^2 + w^2} \qquad \beta = \arctan \frac{v}{\sqrt{u^2 + w^2}} \qquad \text{and} \qquad \alpha = \arctan \frac{w}{u}$$

and its inverse is

$$u = V \cos\beta \cos\alpha \qquad v = V \sin\beta \qquad \text{and} \qquad w = V \cos\beta \sin\alpha \tag{A.4}$$

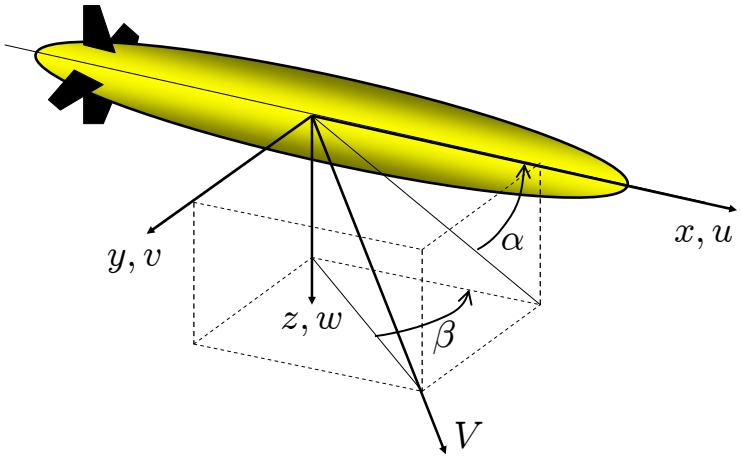

Figure A.2: In the body-axis frame, the vehicle's velocity is expressed by the three components u, v and w. In the wind-axis or stability-axis frame, the velocity is expressed by speed V, sideslip angle β and angle of attack α.

The time derivative of (A.4) is

$$\begin{aligned}\begin{bmatrix}\dot{u}\\ \dot{v}\\ \dot{w}\end{bmatrix} &= \begin{bmatrix}\cos\beta\cos\alpha & -V\sin\beta\cos\alpha & -V\cos\beta\sin\alpha\\ \sin\beta & V\cos\beta & 0\\ \cos\beta\sin\alpha & -V\sin\beta\sin\alpha & V\cos\beta\cos\alpha\end{bmatrix}\begin{bmatrix}\dot{V}\\ \dot{\beta}\\ \dot{\alpha}\end{bmatrix}\\ &= \hat{\mathcal{T}}\left(V,\beta,\alpha\right)\begin{bmatrix}\dot{V}\\ \dot{\beta}\\ \dot{\alpha}\end{bmatrix}\end{aligned} \tag{A.5}$$

The transformation matrix satisfying $\dot{\boldsymbol{\chi}}_b = \mathcal{T}\left(\boldsymbol{\chi}_w\right)\dot{\boldsymbol{\chi}}_w$ is given by

$$\mathcal{T}\left(\boldsymbol{\chi}_w\right) = \begin{bmatrix}\hat{\mathcal{T}}\left(\boldsymbol{\chi}_w\right) & \mathbf{0}_{3\times3}\\ \mathbf{0}_{3\times3} & \mathbf{I}_3\end{bmatrix}$$

Expressed in the stability-axis frame, the AUV model combining dynamics (A.3) and kinematics (A.2) is

$$\begin{aligned} \mathcal{E}\,\mathcal{T}\,(\boldsymbol{\chi}_w)\;\dot{\boldsymbol{\chi}}_w &= \mathcal{R}(\boldsymbol{\chi}_w) + \mathcal{F}(\boldsymbol{\chi}_w, \boldsymbol{\eta}, \boldsymbol{\delta}) \\ \dot{\boldsymbol{\eta}} &= \mathbf{R}_{\boldsymbol{\eta}}(\boldsymbol{\eta})\boldsymbol{\omega} \end{aligned} \tag{A.6}$$

The inertia matrix $\mathcal{E}$ in (A.6) is

$$\mathcal{E} = \begin{bmatrix} m_x & 0 & 0 & 0 & mz_{cg} & 0 \\ 0 & m_z & 0 & -mz_{cg} & 0 & mx_{cg} + Z_{\dot{q}} \\ 0 & 0 & m_z & 0 & -mx_{cg} - Z_{\dot{q}} & 0 \\ 0 & -mz_{cg} & 0 & J_x & 0 & 0 \\ mz_{cg} & 0 & -mx_{cg} - Z_{\dot{q}} & 0 & J_y & 0 \\ 0 & mx_{cg} + Z_{\dot{q}} & 0 & 0 & 0 & J_y \end{bmatrix} \tag{A.7}$$

The right hand side terms of (A.6) are

$$\mathcal{R}(\boldsymbol{\chi}_w) = \begin{bmatrix} -p\,r\,mz_{cg} + V\,(\sin\beta\,r\,m_y - \cos\beta\,\sin\alpha\,q\,m_z) + (r^2 + q^2)\,(m\,x_{cg} + Z_{\dot{q}}) \\ -q\,r\,m\,z_{cg} + V\,(\cos\beta\,\sin\alpha\,p\,m_z - \cos\beta\,\cos\alpha\,r\,m_x) - p\,q\,(m\,x_{cg} + Z_{\dot{q}}) \\ V\,(\cos\alpha\,\cos\beta\,q\,m_x - \sin\beta\,p\,m_y) + (p^2 + q^2)\,m\,z_{cg} - p\,r\,(m\,x_{cg} + Z_{\dot{q}}) \\ V\,\cos\beta\,m\,z_{cg}\,(r\,\cos\alpha - p\,\sin\alpha) \\ V\,(p\,\sin\beta - q\,\cos\alpha\,\cos\beta)\,(m\,x_{cg} + Z_{\dot{q}})\ldots \\ \quad +V^2\,\cos\alpha\,\sin\alpha\,\cos^2\beta\,(m_z - m_x)\ldots \\ \quad\quad +V\,(r\,\sin\beta - q\,\cos\beta\,\sin\alpha)\,m\,z_{cg} + p\,r\,(J_y - J_x) \\ V\cos\beta\,(p\,\sin\alpha - r\,\cos\alpha)\,(mx_{cg} + Z_{\dot{q}})\ldots \\ \quad +V^2\cos\beta\sin\beta\cos\alpha\,(m_x - m_z) + p\,q\,(J_x - J_y) \end{bmatrix}$$

and

$$\mathcal{F}(\boldsymbol{\chi}_w, \boldsymbol{\eta}, \boldsymbol{\delta}) = \begin{bmatrix} F_x(.) & F_y(.) & F_z(.) & M_x(.) & M_y(.) & M_z(.) \end{bmatrix}^T$$

The matrix $\mathbf{R}_{\boldsymbol{\eta}}(\boldsymbol{\eta})$ is given in (A.2). A detailed discussion of $\mathcal{F}(\boldsymbol{\chi}_w, \boldsymbol{\eta}, \boldsymbol{\delta})$ is presented in the next section.

A.4 External Forces and Moments

External forces and moments $\mathcal{F}(\boldsymbol{\chi}_w, \boldsymbol{\eta}, \boldsymbol{\delta})$ influencing the AUV's motion (A.6) include hydrodynamic lift and drag forces of body and fins, hydrostatic forces such as weight, buoyancy and thrust, and centripetal forces inherent to rigid body motion. The control vector $\boldsymbol{\delta} = \begin{bmatrix} \delta_e & \delta_r \end{bmatrix}^T$ contains elevator δ_e and rudder δ_r fin deflection. In (A.6) external forces and moments along the body axes are

$$\begin{aligned}
F_x(.) &= \cos\beta\cos\alpha F_D(.) - \cos\alpha\sin\beta F_S(.) - \sin\alpha\cos\beta F_L(.) + F_{x,HS}(\boldsymbol{\eta}) + F_t \\
F_y(.) &= \sin\beta F_D(.) + \cos\beta F_S(.) + F_{y,HS}(\boldsymbol{\eta}) \\
F_z(.) &= \sin\alpha\cos\beta F_D(.) - \sin\alpha\sin\beta F_S(.) + \cos\alpha\cos\beta F_L(.) + F_{z,HS}(\boldsymbol{\eta}) \\
M_x(.) &= K_p + M_{x,HS}(\boldsymbol{\eta}) \\
M_y(.) &= M_q(.) + M_{y,HS}(\boldsymbol{\eta}) \\
M_z(.) &= N_r(.) + M_{z,HS}(\boldsymbol{\eta})
\end{aligned} \tag{A.8}$$

Using the body's weight and buoyancy forces F_w and F_b, the hydrostatic forces and moments along all three body axes are

$$\begin{aligned}
F_{x,HS}(\boldsymbol{\eta}) &= -(F_w - F_b)\sin\theta, & M_{x,HS}(\boldsymbol{\eta}) &= -F_w z_{cg}\cos\theta\sin\phi \\
F_{y,HS}(\boldsymbol{\eta}) &= (F_w - F_b)\cos\theta\sin\phi, & M_{y,HS}(\boldsymbol{\eta}) &= -F_w\left(x_{cg}\cos\theta\cos\phi + z_{cg}\sin\theta\right) \\
F_{z,HS}(\boldsymbol{\eta}) &= (F_w - F_b)\cos\theta\cos\phi, & M_{z,HS}(\boldsymbol{\eta}) &= F_w x_{cg}\cos\theta\sin\phi
\end{aligned} \tag{A.9}$$

The thrust force is F_t and the propeller torque is K_p. Hydrodynamic moments are denoted by $M_q(V, \alpha, q, \delta_e)$ and $N_r(V, \beta, r, \delta_r)$. Hydrodynamic drag, side and lift forces F_D, F_S, F_L generated by the body and fins are

$$\begin{aligned}
F_D(V, \alpha, \beta, \boldsymbol{\delta}) &= F_{Db}(V, \alpha, \beta) + F_{Df}(V, \boldsymbol{\delta}) \\
F_S(V, \beta, \delta_r) &= F_{Sb}(V, \beta) + F_{Sf}(V, \delta_r) \\
F_L(V, \alpha, \delta_e) &= F_{Lb}(V, \alpha) + F_{Lf}(V, \delta_e)
\end{aligned} \tag{A.10}$$

with the subscripts b and f denoting body and fins, respectively. For some known geometric shapes, drag and lift forces (A.10) can be modeled as presented in [96] and [97]. However, for the remainder of this work, we assume that both the body and fins operate in a linear regime and do not stall. Hydrodynamic surfaces stall beyond a critical angle of attack as the flow separates behind the surface, see [97]. By keeping α, β and $\boldsymbol{\delta}$ small in magnitude, we are able to employ simplifying approximations and model hydrodynamic lift and drag forces of body and fins. We find

$$\begin{aligned} F_{Db}(V,\alpha,\beta) &= P_{\text{dyn}}\, A_b\, [C_{Db_0} + C_{Db_2}\,(\alpha^2+\beta^2)] \\ F_{Df}(V,\boldsymbol{\delta}) &= P_{\text{dyn}}\, A_f\, [C_{Df_0} + C_{Df_2}\,(\delta_e^2+\delta_r^2)] \\ F_{Sb}(V,\beta) &= P_{\text{dyn}}\, A_b\, C_{L_\alpha}\,\beta \\ F_{Sf}(V,\delta_r) &= -P_{\text{dyn}}\, A_f\, C_{L_\delta}\,\delta_r \\ F_{Lb}(V,\alpha) &= P_{\text{dyn}}\, A_b\, C_{L_\alpha}\,\alpha \\ F_{Lf}(V,\delta_e) &= P_{\text{dyn}}\, A_f\, C_{L_\delta}\,\delta_e \end{aligned} \tag{A.11}$$

Here, the reference surface areas of body and fins are A_b and A_f. The quantity P_{dyn} represents the dynamic pressure with $P_{\text{dyn}} = \frac{1}{2}\rho V^2$, and the density of water is ρ. The respective drag and lift coefficients for body and fins are C_{Db_0}, C_{Db_2}, C_{Df_0}, C_{Df_2}, C_{L_α} and C_{L_δ}. To simplify (A.11), we set $C_{Df_0} = 0$ as fin drag forces are negligible for zero fin deflection.

Drag forces counteract the AUV motion, and C_{Db_0}, C_{Db_2}, and C_{Df_2} are negative by definition. Consistent with standard conventions, we note that $C_{L_\delta} < 0$ and $C_{L_\alpha} < 0$ because elevator fins and the body generate negative lift forces (up) for a positive elevator fin deflection $\delta_e > 0$ (trailing edge down) and a positive angle of attack $\alpha > 0$.

Assuming two planes of symmetry of the vehicle's body, the lift coefficients C_{L_α} and C_{L_δ} apply for sway and heave motion. By definition, a positive rudder deflection $\delta_r > 0$ (trailing edge port) generates a positive side force $F_{Sf}(V,\delta_r) > 0$, whereas

a positive elevator deflection $\delta_e > 0$ (trailing edge down) generates a negative lift force $F_{Lf}(V, \delta_e) < 0$. Thus, we find a negative sign for $F_{Sf}(V, \delta_r)$ in (A.11).

The equation for the hydrodynamic pitch moment $M_q(V, \alpha, q, \delta_e)$ and the hydrodynamic yaw moment $N_r(V, \beta, q, \delta_r)$ are taken from [98]. Assuming a small magnitude in fin deflection $\boldsymbol{\delta}$, we find

$$\begin{aligned} M_q\,(V, \alpha, q, \delta_e) &= P_{\text{dyn}}\, A_b\, L\, \left(C_{m_\alpha}\alpha + C_{m_q} q\right) + P_{\text{dyn}}\, A_f\, x_f\, C_{L_\delta}\, \delta_e \\ N_r\,(V, \beta, r, \delta_r) &= P_{\text{dyn}}\, A_b\, L\, \left(C_{n_\beta}\beta + C_{n_r} r\right) + P_{\text{dyn}}\, A_f\, x_f\, C_{L_\delta}\, \delta_r \end{aligned}$$

using the reference length of the vehicle L and the fin location x_f along the x-axis with respect to the center of buoyancy. The hydrodynamic coefficients C_{m_α} and C_{n_β} account for the body's restoring pitch and yaw moments. Note, that by definition of α and β, the vehicle's body generates a negative restoring moment around the pitch-axis for $\alpha > 0$, and a positive restoring moment about the yaw-axis for $\beta > 0$. Thus, we find $-C_{n_\beta} = C_{m_\alpha} < 0$. The coefficients C_{n_r} and C_{m_q} model linear, viscous damping and satisfy $C_{n_r} = C_{m_q} < 0$.

A.5 Pitch-axis Model

In this section, we use (A.1) and (A.6) to derive an AUV pitch-axis model. We assume zero roll motion and describe the AUV's kinematics and dynamics in the xz-plane, ofter referred to as *dive*-plane.

A kinematic pitch-axis model falls from restricting the rigid body kinematics (A.1) to the xz-plane. In other words, we constrain the motion by $\beta = 0$, that is $v = 0$, $\phi = 0$ and $\psi = 0$ allowing only for surge and heave motion. Under these assumptions,

equation (A.1) simplifies to

$$\begin{bmatrix} \dot{X} \\ \dot{Z} \end{bmatrix} = \begin{bmatrix} \cos\theta & \sin\theta \\ -\sin\theta & \cos\theta \end{bmatrix} \begin{bmatrix} u \\ w \end{bmatrix}$$

Setting $u = \cos\alpha\, V$ and $w = \sin\alpha\, V$ as stated in (A.4) for $\beta = 0$, we find the kinematic *heave* model

$$\begin{bmatrix} \dot{X} \\ \dot{Z} \end{bmatrix} = \begin{bmatrix} \cos\theta\cos\alpha & \sin\theta\sin\alpha \\ -\sin\theta\cos\alpha & \cos\theta\sin\alpha \end{bmatrix} V \tag{A.12}$$

Similarly, we derive a dynamic pitch-axis model from (A.6) by restricting the motion to $\phi = 0$, $\psi = 0$, $p = 0$, $r = 0$ and $v = 0$, and by assuming $\delta_r = 0$. The remaining state vector is

$$\hat{\boldsymbol{\chi}}_\theta = \begin{bmatrix} V & \alpha & q & \theta \end{bmatrix}^T \tag{A.13}$$

In the stability-axis frame, the pitch model becomes

$$\hat{\mathbf{E}}\,\hat{\mathbf{T}}(\hat{\boldsymbol{\chi}}_\theta)\,\dot{\hat{\boldsymbol{\chi}}}_\theta = \hat{\mathbf{R}}(\hat{\boldsymbol{\chi}}_\theta) + \hat{\mathbf{F}}(\hat{\boldsymbol{\chi}}_\theta, \delta_e) \tag{A.14}$$

The transformation matrix $\hat{\mathbf{T}}(\hat{\boldsymbol{\chi}}_\theta)$ is

$$\hat{\mathbf{T}}(\hat{\boldsymbol{\chi}}_\theta) = \begin{bmatrix} \cos\alpha & -V\sin\alpha & 0 & 0 \\ \sin\alpha & V\cos\alpha & 0 & 0 \\ 0 & 0 & 1 & 0 \\ 0 & 0 & 0 & 1 \end{bmatrix} \tag{A.15}$$

and the inertia matrix $\hat{\mathbf{E}}$ is

$$\hat{\mathbf{E}} = \begin{bmatrix} m_x & 0 & mz_{cg} & 0 \\ 0 & m_z & -(mx_{cg} + Z_{\dot{q}}) & 0 \\ mz_{cg} & -(mx_{cg} + Z_{\dot{q}}) & J_y & 0 \\ 0 & 0 & 0 & 1 \end{bmatrix} \tag{A.16}$$

The right hand side terms of (A.14) are

$$\hat{\mathbf{R}}(\hat{\boldsymbol{\chi}}_\theta) = \begin{bmatrix} -m_z \sin\alpha \, qV - m x_{cg} q^2 \\ m_x \cos\alpha \, qV + m z_{cg} q^2 \\ (m_z - m_x) \cos\alpha \sin\alpha V^2 - m \left(\cos\alpha \, x_{cg} + \sin\alpha \, z_{cg}\right) qV \\ q \end{bmatrix}$$

and

$$\hat{\mathbf{F}}(\hat{\boldsymbol{\chi}}_\theta, \delta_e) = \begin{bmatrix} F_x(\hat{\boldsymbol{\chi}}_\theta, \delta_e) \\ F_z(\hat{\boldsymbol{\chi}}_\theta, \delta_e) \\ M_y(\hat{\boldsymbol{\chi}}_\theta, \delta_e) \\ 0 \end{bmatrix}$$

Under the given assumptions, in particular from $\phi = 0$, we find $\dot{\theta} = q$ as fourth state equation in (A.14). External forces and moments $\hat{\mathbf{F}}(\hat{\boldsymbol{\chi}}_\theta, \delta_e)$ are given in (A.8). For the pitch-axis model, these forces and moments simplify by setting $\beta = 0$ and $\delta_r = 0$.

Figure A.3 illustrates the modeling approach for the hydrodynamic and hydrostatic forces and moments for a streamlined, tail-controlled AUV in the dive plane.

A.5.1 Steady State Conditions around Pitch-axis

From the heave kinematics in (A.12), it follows that the vehicle is in level flight whenever steady state pitch angle θ_0 and steady state angle of attack α_0 coincide. For $\theta_0 = \alpha_0$, we find $\dot{Z} = 0$ and $\dot{X} = V$.

The equilibrium point of the pitch model (A.14) is found by setting by $\dot{\hat{\boldsymbol{\chi}}}_\theta = \mathbf{0}$. Assuming $\det(\hat{\mathbf{E}}) \neq 0$, the matrix $\hat{\mathbf{E}}\,\hat{\mathbf{T}}(\hat{\boldsymbol{\chi}}_\theta)$ is non-singular for $V > 0$. Hence, the point $\left(\hat{\boldsymbol{\chi}}_{\theta,0}, \delta_{e,0}\right)$ with $\hat{\boldsymbol{\chi}}_{\theta,0} = [V_0,\, \alpha_0,\, q_0,\, \theta_0]^T$ is an equilibrium point of (A.14) if

$$\hat{\mathbf{R}}(\hat{\boldsymbol{\chi}}_{\theta,0}) + \hat{\mathbf{F}}(\hat{\boldsymbol{\chi}}_{\theta,0}, \delta_{e,0}) = \mathbf{0}$$

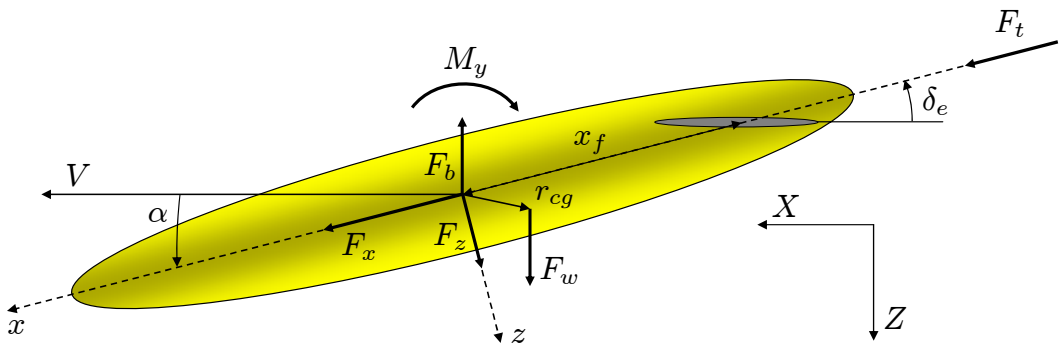

Figure A.3: Pitch-axis model for a streamlined AUV traveling at a speed V, a negative angle of attack α, and with a positive elevator fin deflection δ_e.

The subscript 0 indicates the steady state value of the respective system state or input. Again, for level flight, we also require $\alpha_0 = \theta_0$. From $\dot{\theta}_0 = 0$, it follows immediately that $q_0 = 0$. The steady state flight conditions become

$$\begin{aligned} F_x(\hat{\boldsymbol{\chi}}_{\theta,0}, \delta_{e,0}) &= 0 \\ F_z(\hat{\boldsymbol{\chi}}_{\theta,0}, \delta_{e,0}) &= 0 \\ M_y(\hat{\boldsymbol{\chi}}_{\theta,0}, \delta_{e,0}) &= -(m_z - m_x)\cos\alpha_0 \sin\alpha_0 V_0^2 \end{aligned} \tag{A.17}$$

where the forces $F_x(\hat{\boldsymbol{\chi}}_{\theta,0}, \delta_{e,0})$, $F_z(\hat{\boldsymbol{\chi}}_{\theta,0}, \delta_{e,0})$, and the moment $M_y(\hat{\boldsymbol{\chi}}_{\theta,0}, \delta_{e,0})$ can be derived from (A.8) assuming $\beta = 0$ and $\delta_r = 0$. The first and second equation characterize the equilibrium between thrust and drag forces along the body's x-axis and the equilibrium between lift, weight and buoyancy forces along the body's z-axis, respectively. The equilibrium of moments around the pitch axis is

$$\begin{aligned} 0 \;=\; & P_{\text{dyn}}\ (A_b L C_{m_\alpha}\alpha_0 + A_f x_f C_{L_\delta}\delta_{e,0}) \\ & -\ (x_{cg}\cos\theta_0 + z_{cg}\sin\theta_0)\ F_w\ +\ (m_z - m_x)\ \cos\alpha_0\ \sin\alpha_0\ V_0^2 \end{aligned} \tag{A.18}$$

The first term in (A.18) combines hydrodynamic moments generated by the body and elevator fins, and the second term represents the hydrostatic moment due to the

displaced center of gravity. The third term resembles the *centripetal* or *munk* moment induced by differences in the body's added mass along the x and z-axes.

The equilibria (A.17) determine speed V_0, angle of attack $\alpha_0 = \theta_0$ and elevator fin deflection $\delta_{e,0}$ during steady state flight. They are referred to as *trim conditions.* For underwater vehicles, the location of the center of gravity is an important design variable. Placing the center of gravity x_{cg},z_{cg} appropriately is desired in order to avoid a large magnitudes in elevator fin deflection $\delta_{e,0}$ during steady state flight and thus to reduce drag. As fin deflection is commonly limited to avoid stall, a small $\delta_{e,0}$ is especially important to provide enough margin for attitude control. A vehicle is said to be well trimmed or well ballasted if $\delta_{e,0}$ is small.

A.5.2 Derivation of a Linear Heave and Pitch Model

Linearizing the heave model (A.12) around a constant speed V_0 and any steady state angle of attack and pitch angle $\alpha_0 = \theta_0$ yields

$$\begin{bmatrix} \Delta\dot{X} \\ \dot{Z} \end{bmatrix} = \begin{bmatrix} 1 & 0 & 0 \\ 0 & V_0 & -V_0 \end{bmatrix} \begin{bmatrix} \Delta V \\ \Delta\alpha \\ \Delta\theta \end{bmatrix} \tag{A.19}$$

where Δ indicates the deviation from the respective operating point. The vehicle's nominal trajectory is given by $X_0 = V_0\, t$. For convenience, we choose $Z_0 = 0$.

In Chapter 2, we investigate the dynamics of the system mode associated with $\Delta\alpha$. For now, we assume that the state $\Delta\alpha$ is inherently stable and sufficiently fast, which implies a quasi-steady angle of attack $\Delta\alpha = \alpha - \alpha_0 \approx 0$. By truncating ΔX and assuming $\Delta\alpha \approx 0$, the linear model (A.19) simplifies to

$$\dot{Z} = -V_0\,(\theta - \alpha_0) \tag{A.20}$$

In Chapter 3, we refer to (A.20) as linear *heave* model and utilize it for the purpose of system identification.

To linearize the pitch model (A.14), we adopt a simplification commonly made regarding the mass distribution of streamlined, neutrally buoyant AUVs with three planes of symmetry, see [18] or [42].

Assumption A.5.1. *The displacement $\boldsymbol{r}_{cg}$ between center of gravity and center of buoyancy is small. Moreover, the vehicle has three planes of symmetry implying $Z_{\dot{q}} = 0$. Thus, the inertia matrix $\hat{\mathbf{E}}$ from (A.16) is dominated by its diagonal terms and can be approximated by truncating all off-diagonal elements. Thus*

$$\hat{\mathbf{E}} = \begin{bmatrix} m_x & 0 & 0 & 0 \\ 0 & m_z & 0 & 0 \\ 0 & 0 & J_y & 0 \\ 0 & 0 & 0 & 1 \end{bmatrix}$$

Assumption A.5.2. *The AUV is nearly neutrally buoyant with $F_w \approx F_b$, and the lift force induced by the elevator fins during steady state flight is negligible compared to the body's lift, weight and buoyancy force. Thus, we find*

$$\alpha_0 = \theta_0 = 0$$

and the transformation matrix $\hat{\mathbf{T}}(\hat{\boldsymbol{\chi}}_\theta)$ from (A.15) simplifies to

$$\hat{\mathbf{T}}(\hat{\boldsymbol{\chi}}_\theta) = \begin{bmatrix} 1 & 0 & 0 & 0 \\ 0 & V & 0 & 0 \\ 0 & 0 & 1 & 0 \\ 0 & 0 & 0 & 1 \end{bmatrix}$$

Using Assumptions A.5.1 and A.5.2, linearizing (A.14) around the operating point, given by $\hat{\boldsymbol{\chi}}_{\theta,0} = \begin{bmatrix} V_0 & 0 & 0 & 0 \end{bmatrix}^T$ and $\delta_{e,0} = 0$, yields

$$\begin{bmatrix} \Delta\dot{V} \\ \dot{\alpha} \\ \dot{q} \\ \dot{\theta} \end{bmatrix} = \begin{bmatrix} a_{11} & 0 & 0 & 0 \\ 0 & a_{22} & a_{23} & 0 \\ 0 & a_{32} & a_{33} & a_{34} \\ 0 & 0 & 1 & 0 \end{bmatrix} \begin{bmatrix} \Delta V \\ \alpha \\ q \\ \theta \end{bmatrix} + \begin{bmatrix} 0 \\ b_{21} \\ b_{31} \\ 0 \end{bmatrix} \delta_e \tag{A.21}$$

with the system parameters

$$\begin{aligned} a_{11} &= \frac{1}{m_x}\rho V_0 A_b C_{D_0} \\ a_{32} &= \frac{1}{J_y}\left\{ (m_z - m_x) V_0^2 + \frac{1}{2}\rho V_0^2 A_b L C_{m_\alpha} \right\} \\ a_{22} &= \frac{1}{2m_z}\rho V_0 A_b \left(C_{D_0} + C_{L_\alpha} \right) \\ a_{33} &= \frac{1}{J_y}\left\{ \frac{1}{2}\rho V_0^2 A_b L C_{m_q} - m V_0 x_{cg} \right\} \\ a_{23} &= \frac{m_x}{m_z} \\ a_{34} &= -\frac{1}{J_y} z_{cg} F_w \\ b_{21} &= \frac{1}{2m_z}\rho V_0 A_f C_{L_\delta} \\ b_{31} &= \frac{1}{2J_y}\rho V_0^2 A_f x_f C_{L_\delta} \end{aligned} \tag{A.22}$$

For zero angle of attack flight with small steady state elevator fin deflection $\delta_{e,0}$, the state ΔV decouples completely from the remaining three states.

It is important to note that for aircraft steady-state and level flight, see [95] or [99], the speed V does not decouple from the remaining states of the linear system. Aircraft weight forces are not compensated for by buoyancy forces, as in the case of a neutrally buoyant AUV, and a negative (positive) pitch angle accelerates (decelerates) the aircraft.

As suggested in [90] and [100], a linear AUV pitch-axis model reduces to third order

$$\begin{bmatrix} \dot{\alpha} \\ \dot{q} \\ \dot{\theta} \end{bmatrix} = \begin{bmatrix} a_{22} & a_{23} & 0 \\ a_{32} & a_{33} & a_{34} \\ 0 & 1 & 0 \end{bmatrix} \begin{bmatrix} \alpha \\ q \\ \theta \end{bmatrix} + \begin{bmatrix} b_{21} \\ b_{31} \\ 0 \end{bmatrix} \delta_e \tag{A.23}$$

Note that $C_{D_0} = C_{Db_0} + C_{Df_0} < 0$ assures stability of the truncated state ΔV. In Chapter 2, we use (A.23) to investigate inherent stability of the AUV pitch-axis motion, study identifiability of system parameters (A.22) and propose further model simplifications.

Appendix B

B.1 Parameter Convergence, Proof of Proposition 3.1.2

Given the convergence of the state estimation error (3.9), we can evaluate the limit of (3.8) for $t \to \infty$ and rewrite the remaining term

$$\mathbf{0} = \lim_{t\to\infty} \mathbf{W}_\theta^T(t)\tilde{\mathbf{p}}_\theta(t)$$

Using scalar notation, we may instead write

$$0 = \lim_{t\to\infty} \left\|\mathbf{W}_\theta^T(t)\tilde{\mathbf{p}}_\theta(t)\right\|^2$$

or equivalently

$$0 = \lim_{t\to\infty} \tilde{\mathbf{p}}_\theta^T(t)\mathbf{W}_\theta(t)\mathbf{W}_\theta^T(t)\tilde{\mathbf{p}}_\theta(t) \tag{B.1}$$

Let T be the finite time interval for which $\mathbf{W}_\theta^T(t)$ satiesfies the PE condition (3.17). From (B.1) follows

$$0 = \lim_{t\to\infty} \int_t^{t+T} \tilde{\mathbf{p}}_\theta^T(\sigma)\mathbf{W}_\theta(\sigma)\mathbf{W}_\theta^T(\sigma)\tilde{\mathbf{p}}_\theta(\sigma)d\sigma \tag{B.2}$$

To integrate (B.2) by parts, we introduce the following substitution

$$\boldsymbol{\Theta}(\sigma,t)=\int_t^{\sigma}\mathbf{W}_\theta(\tau)\mathbf{W}_\theta^T(\tau)d\tau \tag{B.3}$$

Note, that

$$\boldsymbol{\Theta}(\sigma,t)'=\mathbf{W}_\theta(\sigma)\mathbf{W}_\theta^T(\sigma)$$

where $'$ denotes the derivative with respect to σ. Using the proposed substitutions, the condition (B.2) becomes

$$0=\lim_{t\to\infty}\int_t^{t+T}\tilde{\mathbf{p}}^T(\sigma)\boldsymbol{\Theta}(\sigma,t)'\tilde{\mathbf{p}}(\sigma)d\sigma \tag{B.4}$$

From the chain rule

$$\left[\tilde{\mathbf{p}}_\theta^T(\sigma)\boldsymbol{\Theta}(\sigma,t)\tilde{\mathbf{p}}_\theta(\sigma)\right]'=\tilde{\mathbf{p}}_\theta^T(\sigma)\boldsymbol{\Theta}(\sigma,t)'\tilde{\mathbf{p}}_\theta(\sigma)+\tilde{\mathbf{p}}_\theta^T(\sigma)'\boldsymbol{\Theta}(\sigma,t)\tilde{\mathbf{p}}_\theta(\sigma)+\tilde{\mathbf{p}}_\theta^T(\sigma)\boldsymbol{\Theta}(\sigma,t)\tilde{\mathbf{p}}_\theta(\sigma)'$$

follows by integration

$$\begin{aligned}\left[\tilde{\mathbf{p}}_\theta^T(\sigma)\boldsymbol{\Theta}(\sigma,t)\tilde{\mathbf{p}}_\theta(\sigma)\right]_t^{t+T} &= \int_t^{t+T}\tilde{\mathbf{p}}_\theta^T(\sigma)\boldsymbol{\Theta}(\sigma,t)'\tilde{\mathbf{p}}_\theta(\sigma)d\sigma\\ &+\int_t^{t+T}\tilde{\mathbf{p}}_\theta^T(\sigma)'\boldsymbol{\Theta}(\sigma,t)\tilde{\mathbf{p}}_\theta(\sigma)d\sigma\\ &+\int_t^{t+T}\tilde{\mathbf{p}}_\theta^T(\sigma)\boldsymbol{\Theta}(\sigma,t)\tilde{\mathbf{p}}_\theta(\sigma)'d\sigma\end{aligned}$$

We can now rearrange terms in the previous equation to evaluate the right hand side of (B.4)

$$\begin{aligned}\lim_{t\to\infty}\int_t^{t+T}\tilde{\mathbf{p}}_\theta^T(\sigma)\boldsymbol{\Theta}(\sigma,t)'\tilde{\mathbf{p}}_\theta(\sigma)d\sigma &= \lim_{t\to\infty}\left[\tilde{\mathbf{p}}_\theta^T(\sigma)\boldsymbol{\Theta}(\sigma,t)\tilde{\mathbf{p}}_\theta(\sigma)\right]_t^{t+T}\\ &-\lim_{t\to\infty}\int_t^{t+T}\tilde{\mathbf{p}}_\theta^T(\sigma)'\boldsymbol{\Theta}(\sigma,t)\tilde{\mathbf{p}}_\theta(\sigma)d\sigma\\ &-\lim_{t\to\infty}\int_t^{t+T}\tilde{\mathbf{p}}_\theta^T(\sigma)\boldsymbol{\Theta}(\sigma,t)\tilde{\mathbf{p}}_\theta(\sigma)'d\sigma\end{aligned} \tag{B.5}$$

From the Lyapunov analysis in Section 3.1, in particular from (3.16), it follows that

$$\lim_{\sigma\to\infty} \tilde{\mathbf{p}}_\theta(\sigma)' = \mathbf{0}$$

Thus, the last two terms on the right hand side of (B.5) containing $\mathbf{p}_\theta(\sigma)'$ and $\mathbf{p}_\theta^T(\sigma)'$ vanish. The remaining term evaluated at t and $t+T$ yields

$$\begin{aligned}\lim_{t\to\infty}\int_t^{t+T} \tilde{\mathbf{p}}_\theta^T(\sigma)\boldsymbol{\Theta}(\sigma,t)'\tilde{\mathbf{p}}_\theta(\sigma)d\sigma &= \lim_{t\to\infty}\left[\tilde{\mathbf{p}}_\theta^T(\sigma)\boldsymbol{\Theta}(\sigma,t)\tilde{\mathbf{p}}_\theta(\sigma)\right]_t^{t+T} \\ &= \lim_{t\to\infty}\left[\tilde{\mathbf{p}}_\theta^T(t+T)\boldsymbol{\Theta}(t+T,t)\tilde{\mathbf{p}}_\theta(t+T)\right] \\ &\quad - \lim_{t\to\infty}\left[\tilde{\mathbf{p}}_\theta^T(t)\boldsymbol{\Theta}(t,t)\tilde{\mathbf{p}}_\theta(t)\right]\end{aligned}$$

By definition (B.3), we find

$$\boldsymbol{\Theta}(t,t) = \mathbf{0}_{4\times 4}$$

Thus, (B.4) can be expressed as

$$\begin{aligned}0 &= \lim_{t\to\infty}\int_t^{t+T} \tilde{\mathbf{p}}_\theta^T(\sigma)\boldsymbol{\Theta}(\sigma,t)'\tilde{\mathbf{p}}_\theta(\sigma)d\sigma \\ &= \lim_{t\to\infty} \tilde{\mathbf{p}}_\theta^T(t+T)\boldsymbol{\Theta}(t+T,t)\tilde{\mathbf{p}}_\theta(t+T)\end{aligned} \tag{B.6}$$

By assumption, the matrix $\mathbf{W}_\theta^T(t)$ is persistently exciting over any time interval of length T, thus the matrix $\boldsymbol{\Theta}(t+T,t)$ is full rank for all t. Therefore, we only find the trivial solution for (B.6)

$$\lim_{t\to\infty} \tilde{\mathbf{p}}_\theta(t+T) = \lim_{t\to\infty} \tilde{\mathbf{p}}_\theta(t) = \mathbf{0}$$

indicating convergence of the parameter estimation error as stated in (3.18).

□

B.2 Convergence for Gradient method, Proof of Proposition 6.3.3

For this proof, we consider a generalized cost function $\Gamma(\mathbf{r})$ and omit the index j. Suppose the non-autonomous system, page 132 in [54]

$$\dot{\mathbf{r}}(t) = f(\mathbf{r}, t) = -\gamma(t)\,\mathrm{grad}\,\Gamma(\mathbf{r}) \tag{B.7}$$

with the equilibrium at $\mathbf{r}_s$

$$\mathrm{grad}\,\Gamma(\mathbf{r}_s) = 0$$

where $f : [0, \infty) \times \mathbb{B} \mapsto \mathbb{R}^2$ is piecewise continuous in t and locally Lipschitz in $\mathbf{r}$ on $[0, \infty) \times \mathbb{B}$. The bounds for the time-varying step size are

$$0 < \gamma_{min} \leq \gamma(t) \leq \gamma_{max} \qquad \forall t$$

For a vector-valued function the Lipschitz condition, page 71 in [54], is expressed as

$$\|f(\mathbf{r}_1) - f(\mathbf{r}_2)\| \leq L\|\mathbf{r}_1 - \mathbf{r}_2\| \;\; \Rightarrow \;\; \left\|\frac{\partial f}{\partial \mathbf{r}}(\mathbf{r}, t)\right\| \leq L$$

with

$$\frac{\partial f}{\partial \mathbf{r}}(\mathbf{r}, t) = -\gamma(t) \begin{bmatrix} \frac{\partial^2}{\partial x^2}\Gamma & \frac{\partial^2}{\partial x \partial y}\Gamma \\ \frac{\partial^2}{\partial x \partial y}\Gamma & \frac{\partial^2}{\partial y^2}\Gamma \end{bmatrix} = \underbrace{\begin{bmatrix} H_{11} & H_{12} \\ H_{21} & H_{22} \end{bmatrix}}_{\mathbf{H}}$$

Referring to the definitions of the cost functions $\Gamma_j(x, y)$, $j = 1, .., 4$, and with the aid of Mathematica, one can find bounds for the respective second derivatives that

represent the elements of the Hessian matrix $\mathbf{H}$

$$|H_{kk}| \leq \sum_{i=1}^{N} \gamma(t) \frac{78}{\|\mathbf{r}-\mathbf{P}_i\|^2} \leq \gamma_{max} \frac{78N}{\min_i \|\mathbf{r}-\mathbf{P}_i\|^2} \qquad k=1,2$$

$$|H_{12}| = |H_{21}| \leq \sum_{i=1}^{N} \gamma(t) \frac{66}{\|\mathbf{r}-\mathbf{P}_i\|^2} \leq \gamma_{max} \frac{66N}{\min_i \|\mathbf{r}-\mathbf{P}_i\|^2}$$

Hence

$$\|\mathbf{H}\|_2 \leq \gamma_{max} \frac{144N}{\min_i \|\mathbf{r}-\mathbf{P}_i\|^2}$$

We introduce a domain $\mathbb{M}$ as the union of N discs with the radii $\delta > 0$ around the measuring points $\mathbf{P}_i$

$$\mathbb{M} = \{\mathbf{r} \,|\, \|\mathbf{r}-\mathbf{P}_i\| < \delta,\ i = 1 \ldots N\}$$

and find f to be Lipschitz in $\mathbb{B} = \mathbb{R}^2/\mathbb{M}$

$$L = \gamma_{max} \frac{144N}{\delta^2} \geq \left\| \frac{\partial f}{\partial \mathbf{r}}(\mathbf{r},t) \right\| \qquad \forall \mathbf{r} \in \mathbb{B}$$

From Theorem 3.8, page 138 in [54] (Lyapunov's direct method for non-autonomous systems), we consider a time-invariant Lyapunov function candidate

$$\Psi(\mathbf{r},t) = \Psi(\mathbf{r}) = \Gamma(\mathbf{r}) > 0 \qquad \forall \mathbf{r} \neq \mathbf{r}_s$$

Computing the time derivative yields

$$\dot{\Psi}(\mathbf{r},t) = \underbrace{\frac{\partial \Psi}{\partial t}}_{=0} + \tfrac{\partial \Psi}{\partial \mathbf{r}} f(\mathbf{r},t) = -\gamma(t) \,\|\mathrm{grad}\,\Gamma(\mathbf{r})\|^2$$

$$\leq -\gamma_{min} \,\|\mathrm{grad}\,\Gamma(\mathbf{r})\|^2$$

where $-W_3(\mathbf{r}) = -\gamma_{min} \|\text{grad}\,\Gamma(\mathbf{r})\|^2 < 0$ is a time-invariant, negative definite upper bound of $\dot{\Psi}(\mathbf{r}, t)$.

Therefore, under the assumptions that there exists a local minimum $\mathbf{r}_s$ such that $\text{grad}\,\Gamma(\mathbf{r}_s) = 0$ and that the initial condition $\mathbf{P}_{\text{cm}}$ is chosen sufficiently close to $\mathbf{r}_s$, the non-autonomous system (B.7) converges to $\mathbf{r}_s$.

Bibliography

[1] T. I. Fossen, *Guidance and Control of Ocean Vehicles*. England: John Wiley & Sons, 1994.

[2] C. Silvestre and A. Pascoal, "Control of an auv in the vertical and horizontal planes: system design and test at sea," *Transactions of the Institute of Measurement and Control*, vol. 19, no. 3, pp. 126–138, 1997.

[3] C. Vuilmet, "High order sliding mode control applied to a heavyweight torpedo," in *Proceedings of the 2005 IEEE Conference on Control Applications*, Toronto, ON, Canada, 2005, pp. 61–66.

[4] T. Prestero, *Verification of a six-degree of freedom simulation model for the REMUS AUV*. Massachusetts Institute of Technology, MA: Woods Hole Oceanographic Institution, Departments of Ocean and Mechanical Engineering, 2001.

[5] R. Cristi and A. Healey, "Adaptive identification and control of an autonomous underwater vehicle," in *Unmanned Untethered Submersible Technology, 1989. Proceedings of the 6th International Symposium on*, Monterey, CA, 1989, pp. 563–572.

[6] J. H. Li, P. M. Lee, and B. H. Jun, "Application of a robust adaptive controller to autonomous diving control of an auv," in *The 30th Annual Conference of the IEEE Industrial Electronics Society*, Busan, Korea, November 2-6, 2004.

[7] J. Kim, K. Kim, H. Choi, W. Seong, and K.-Y. Lee, "Depth and heading control for autonomous underwater vehicle using estimated hydrodynamic coefficients," in *OCEANS, 2001. MTS/IEEE Conference and Exhibition*, Honolulu, Hawaii, Nov. 5-8, 2001, pp. 429 – 435.

[8] R. Cristi, O. Papoulias, and A. Healey, "Adaptive sliding mode control of autonomous underwater vehicles in the dive plane," *IEEE Journal of Oceanic Engineering*, vol. 15, 1990.

[9] D. G. Mitchell and R. H. Hoh, "Low-order approaches to high-order systems: Problems and promises," *Journal of Guidance, Control and Dynamics,*, vol. 5(5), p. 482–489, Sep.-Oct. 1982.

[10] J. Hodgkinson, "Equivalent systems criteria for handling qualities of military aircraft," in *In AGARD Conference Proceedings No.333, Criteria for Handling Qualities of Military Aircraft*, Ft. Worth, Texas, April 1982.

[11] Y. Hwang, "Hydrodynamic modeling of lmrs unmanned underwater vehicle and tow tank test validation," in *Proceedings of MTS/IEEE Oceans 2003*, vol. 3, San Diego, CA, September 22-26 2003, pp. 1425– 1430.

[12] E. Barros, J. Dantas, A. Pascoal, and E. de Sa, "Investigation of normal force and moment coefficients for an auv at nonlinear angle of attack and sideslip range," *IEEE Journal of Oceanic Engineering*, vol. 33, no. 4, pp. pages 538–549, October 2008.

[13] C. Williams, T. Curtis, J. Doucet, and F. Issac, M.T. Azarsina, "Effects of hull length on the hydrodynamic loads on a slender underwater vehicle during manoeuvres," in *OCEANS 2006, Proceedings of MTS/IEEE*, Boston, MA, 2006, pp. 1–6.

[14] D. Humphreys, "Correlation and validation of a cfd based hydrodynamic and dynamic model for a towed undersea vehicle," in *Proceedings of OCEANS, 2001. MTS/IEEE Conference and Exhibition*, vol. 3, Honolulu, Hawaii, 5-8 Nov. 2001, pp. 1755 – 1760.

[15] S. A. Jenkins, D. E. Humphreys, J. Sherman, J. Osse, C. Jones, N. E. Leonard, R. Bachmayer, J. Graver, E. Clem, P. Carrolla, P. Davis, J. Berry, P. Worley, and J. Wasyl, *Underwater glider system study.* Office of Naval Research: Technical report, 2003.

[16] I. Sahin, J. Crane, and K. Watson, "Application of a panel method to hydrodynamics of underwater vehicles," *Ocean Engineering*, vol. 24, no. 6, pp. 501–512, 1997.

[17] J. S. Geisbert, *Hydrodynamic Modeling for Autonomous Underwater Vehicles Using Computational and Semi-Empirical Methods.* Blacksburg, VA: Master Thesis, Virginia Tech Department of Aerospace and Ocean Engineering, 2007.

[18] M. E. Rentschler, F. S. Hover, and C. Chryssostomidis, "System identification of open-loop maneuvers leads to improved auv flight performance," *IEEE Journal of Oceanic Engineering*, vol. 31, no. 1, pp. 200 – 208, 2006.

[19] Z. Feng and R. Allen, "Reduced order h_∞ control of an autonomous underwater vehicle," *Control Engineering Practice*, vol. 12, pp. 1511–1520, 2004.

[20] C. L. Logan, "A comparison between h-infinity/mu-synthesis control and sliding-mode control for robust control of a small autonomous underwater vehicle," in *Proceedings of the 1994 Symposium on Autonomous Underwater Vehicle Technology, AUV '94*, 19-20 July 1994, pp. 399 – 416.

[21] D. Desanj, M. Grimble, and M.R.Katebi, "State-space adaptive h_∞ controller with application to a ship control system," *Transactions of the Institute of Measurement and Control*, vol. 19, no. 3, pp. 139–153, 1997.

[22] M. J. Ruth and D. E. Humphreys, "A robust depth and speed control system for a low-speed undersea vehicle," in *Proceedings of the Autonomous Underwater Vehicle Technology, AUV '90*, Washington, DC, USA, 1990, pp. 51–58.

[23] M. J. Ruth, "Robust control of a coupled undersea vehicle using μ-synthesis," in *Proceedings of the 1990 American Control Conference*, vol. 3, 1990, pp. 2374–2379.

[24] K. Zhou, J. Doyle, and K. Glover, *Robust and Optimal Control*. New Jersey: Prentice Hall, 1996.

[25] I. Kaminer, A. M. Pascoal, C. J. Silvestre, and P. P. Khargonekar, "Control of an underwater vehicle using $\mathcal{H}_\infty$ synthesis," in *Proceedings of the 30th Conference on Decision and Control*, Brighton, England, December 1991, pp. 2350–2355.

[26] P. Garnell, *Guided Weapon Control Systems*, 2nd ed. Oxford, Great Britain: Pergamon Press, 1980.

[27] G. Siouris, *Missile Guidance and Control Systems*. New York: Springer-Verlag, 2004.

[28] A. J. Healy, P. E. An, and D. B. Marco, "Online compensation of heading sensor bias for low cost auvs," *Proceedings of the 1998 Workshop on Autonomous Underwater Vehicles*, pp. 35–42, August 1998.

[29] A. Gadre, *Observability Analysis in Navigation Systems with an Underwater Vehicle Application*. Blacksburg, VA: PhD Dissertation, The Bradley Department of Electrical and Computer Engineering, Virginia Tech, 2007.

[30] E. Memin and P. Perez, "Fluid motion recovery by coupling dense and parametric vector fields," in *Proceedings of the Seventh IEEE International Conference on Computer Vision*, vol. 1, Los Alamitos, CA, 1999, pp. 620–625.

[31] L. Graftieux, M. Michard, and N. Grosjean, "Combining piv, pod and vortex identification algorithms for the study of unsteady turbulent swirling flows," *IOP Publishing, Measurement Science & Technology*, vol. 12, no. 9, pp. 1422–1429, September 2001.

[32] T. Kohlberger, C. Schnorr, and E. Memin, "Variational dense motion estimation using a div-curl high-order regularization," in *Proceedings of The Seventh International Symposium on Signal Processing and Its Applications*, vol. 1, Paris, France, 2003, pp. 641–644.

[33] I. Cohen and I. Herlin, "Optical flow and phase portrait methods for environmental satellite image sequences," in *Proceedings of the 4th European Conference on Computer Visiont*, vol. 2, Springer-Verlag London, UK, 1996, pp. 140–150.

[34] M. Gertler and G. Hagen, *Standard Equations of Motion for Submarine Simulation*. Bethesda, MD: Naval ship research and development center, 1967.

[35] H. Arafat, D. Stilwell, and W. Neu, "Development of a dynamic model of a small high-speed autonomous underwater vehicle," in *OCEANS 2006, Proceedings of MTS/IEEE*, Boston, MA, 2006, pp. 1–6.

[36] S. Smith, S. Dunn, T. Hopkins, K. Heeb, and T. Pantelakis, "The application of a modular auv to coastal oceanography: case study on the ocean explorer," in *Proceedings of OCEANS '95. MTS/IEEE. Challenges of Our Changing Global Environment*, vol. 3, San Diego, CA, USA, October 1995, pp. 1423–1432.

[37] N. Cruz and A. Matos, "The mares auv, a modular autonomous robot for environment sampling," in *Proceedings of the MTS-IEEE Conference Oceans'2008*, Quebec, Canada, September 2008.

[38] M. Moline and S. Blackwell, "Remote environmental monitoring units: An autonomous vehicle for characterizing coastal environments*," *Journal of Atmospheric & Oceanic Technology*, vol. 22, pp. 1797–1808, 2005.

[39] J. Petrich, W. Neu, and D. J. Stilwell, "Identification of a simplified auv pitch axis model for control design: Theory and experiments," *Proceedings of MTS/IEEE Oceans Conference 2007*, pp. 1–7, 2007.

[40] J. H. Blakelock, *Automatic Control of Aircrafts and Missiles*, 2nd ed. Yellow Springs, Ohio: John Wiley & Sons, Inc., 1991.

[41] D. McRuer, I. Ashkenas, and D. Graham, *Aircraft Dynamics and Automatic Control*. Princeton, New Jersey: Princeton University Press, 1973.

[42] D. A. Smallwood and L. L. Whitcomb, "Preliminary experiments in the adaptive identification of dynamically positioned underwater robotic vehicles," *Pro-*

ceedings of the 2001 IEEE/RSJ International Conference on Intelligent Robots and Systems, 2001.

[43] D. Fryxell, P. Oliveira, A. Pascoal, and C. Silvestre, "An integrated approach to the design and analysis of navigation, guidance and control systems for auvs," *Proceedings of the 1994 Symposium on Autonomous Underwater Vehicle Technology*, pp. 208 – 217, 1994.

[44] L. Ljung, *System Identification : Theory for the User*. Englewood Cliffs, NJ: Prentice-Hall, 1987.

[45] P. Eykhoff, *System Identification : Parameter and State Estimation*. London, England: John Wiley & Sons, 1974.

[46] A. C. Antoulas, *Approximation of Large-Scale Dynamical Systems*. Philadelphia, PA: SIAM, 2005.

[47] M. Grewal and K. Glover, "Identifiability of linear and nonlinear dynamical systems," *Transactions on Automatic Control*, vol. AC-21, no. 6, pp. 833–837, 1976.

[48] M. Narasimhan and S. N. Singh, "Adaptive optimal control of an autonomous underwater vehicle in the dive plane using dorsal fins," *Ocean Engineering*, vol. 33, p. 404–416, 2006.

[49] M. Narasimhan, R. Mittal, S. N. Singh, and H. Dong, "Optimal yaw regulation and trajectory control of biorobotic auv using mechanical fins based on cfd parametrization," *Journal of Fluids Engineering*, vol. 128, p. 687 –698, July 2006.

[50] E. J. Routh, *Dynamics of a System of Rigid Bodies, Part I.* London: MacMillan and Co, 1930.

[51] J. Lagarias, J. Reeds, M. Wright, and P. Wright, "Convergence properties of the nelder–mead simplex method in low dimensions," *SIAM Journal on Optimization*, vol. 9 no.1, pp. pages 112–147, 1998.

[52] S. Sastry and M. Bodson, *Adaptive Control: Stability, Convergence, and Robustness.* New Jersey: Prentice Hall, 1989.

[53] W. J. Rugh, *Linear System Theory.* New Jersey: Prentice Hall, 1996.

[54] H. K. Khalil, *Nonlinear Systems*, 3rd ed. New Jersey: Prentice Hall, 2002.

[55] J. Masen, E. Bai, L.C.Fu, M.Bodson, and S. Sastry, "Analysis of adaptive identifiers in the presence of unmodeled dynamics: Averaging and tuned parameters," *Automatic Control, IEEE Transactions on*, vol. 33, pp. 969 – 976, October 1988.

[56] J. O'Reilly, *Observers for Linear Systems.* Academic Press, Inc., 1983.

[57] D. Catlin, *Estimation, control, and the discrete Kalman filter.* New York: Springer-Verlag, 1988.

[58] R. Kalman, "A new approach to linear filtering and prediction problems," *Transactions of the ASME Journal of Basic Engineering*, pp. 35–45, 1960.

[59] K. Astrom and B. Wittenmark, *Adaptive Control.* Addison-Wesley Publishing Company, 1998.

[60] O. E. Fjellstad and T. I. Fossen, "Cascaded adaptive control of marine vehicles with significant actuator dynamics," *Journal of Modeling, Identification, and Control*, vol. 15, 1994.

[61] D. B. Ridgely, Y. Lee, and T. Fanciullo, "Dual aero/propulsive missile control — optimal control and control allocation," in *Proceedings of the AIAA Guidance, Navigation, and Control Conference and Exhibit*, Keystone, Colorado, 21 - 24 August 2006.

[62] E. Nebot and H. Durrant-Whyte, "Initial calibration and alignment of low-cost inertial navigation units for land vehicle appplications," *Journal of Robotic Systems*, pp. 81–92, 1999.

[63] J. C. Kinsey and L. L. Whitcomb, "Towards in-situ calibration of gyro and doppler navigation sensors for precision underwater vehicle navigation," *IEEE International Conference on Robotics and Automation*, pp. 4016 – 4023, 2002.

[64] A. Devices, $\pm 150^o/s$ *Single Chip Yaw Rate Gyro with Signal Conditioning.*

[65] A. Gadre, J. Mach, D. Stilwell, and C. Wick, "A prototype miniature autonomous underwater vehicle," in *Proceedings of IEEE/RSJ International Conference on Intelligent Robots and Systems*, Las Vegas, NV, 2003.

[66] A. Lawrence, *Modern Inertial Technology - Navigation, Guidance, and Control*, 2nd ed. New York: Springer-Verlag, 1998.

[67] D. J. Stilwell, C. E. Wick, and B. E. Bishop, "Small inertial sensors for a miniature autonomous underwater vehicle," *Proceedings of IEEE Conference on Control Applications*, pp. 842–847, 2001.

[68] L. Wenger and D. Gebre-Egziabher, "System concepts and performance analysis of multi-sensor navigation systems for uav applications," in *2nd AIAA 'Unmanned Unlimited' Systems, Technology, and Operations*, San Diego, California, 2003.

[69] J. Thienel and R. M. Sanner, "Nonlinear observers for gyro calibration coupled with a nonlinear control algorithm," in *Proceedings of the 27th Annual AAS Rocky Mountain Guidance and Control Conference*, San Diego, California, 2004, pp. 197–216.

[70] J. Chou, "Quaternion kinematic and dynamic differential equations," *Robotics and Automation, IEEE Transactions on*, pp. 53–64, Feb. 1992.

[71] J. Conway and D. Smith, *On Quaternions and Octonions, their Geometry, Arithmetic and Symmetry*. Natick, MA: A K Peters Ltd., 2003.

[72] J. Junkins and J. Turner, "Optional continuous torque attitude maneuvers," in *AIAA-AAS Astrodynamics Conference*, Palo Alto, California, 1978.

[73] R. M. Murray, Z. Li, and S. S. Sastry, *A mathematical introduction to robotic manipulation*. Boca Raton, Fl: CRC Press, 1994.

[74] J. Petrich, C. Woolsey, and D. Stilwell, "Planar flow model identification for improved navigation of small auvs," *Ocean Engineering*, vol. 36, pp. 119–131, 2009.

[75] G. Haller, "Finding finite-time invariant manifolds in two-dimensional velocity fields," *Chaos*, vol. 10, 2000.

[76] J. Barron, D. Fleet, and S. Beauchemin, "Performance of optical flow techniques," in *International Journal on Computer Vision*, vol. 12, no.1, 1994, pp. 641–644.

[77] R. A. Ford, "Critical point detection in fluid flow images using dynamical system properties," in *Pattern Recognition*, vol. 30, no.12, 1997, pp. 1991–2000.

[78] T. Corpetti and E. Memin, "Extraction of singular points from dense motion fields: An analytic approach," in *Journal of Mathematical Imaging and Vision*, vol. 19, 2003, pp. 175–198.

[79] A. Cuzol, P. Hellier, and E. Memin, "A low dimensional fluid motion estimator," in *International Journal of Computer Vision*, vol. 75, no.3, 2007, pp. 329–349.

[80] G. Arfken, *Mathematical Methods for Physicists*, 3rd ed. Orlando, FL: Academic Press, 1985.

[81] J. Petrich, C. Woolsey, and D. Stilwell, "Identification of a low-complexity flow field model for auv applications underwater vehicles," in *OCEANS, 2005. Proceedings of MTS/IEEE*, vol. 2, Washington, DC, 2005, pp. 1595 – 1602.

[82] K. Polthier and E. Preuss, "Variational approach to vector field decomposition," in *Proceedings of the Joint EUROGRAPHICS and IEEE TCVG Symposium on Visualization*, Wien, Austria, 2000, pp. 147–155.

[83] J. Knauss, *Introduction to Physical Oceanography.* Prentice-Hall, 1978.

[84] A. Okubo, "Horizontal dispersion of floatable trajectories in the vicinity of velocity singularities such as convergences," *Deep-Sea Res.*, vol. 17, pp. 445–454, 1970.

[85] K. Karamcheti, *Principles of Ideal-Fluid Aerodynamics.* Melbourne, Fl: Krieger Publishing Company, Reprint Edition, 1980.

[86] A. S. Gadre and D. J. Stilwell, "Underwater navigation in the presence of unknown currents based on range measurements from a single source," *Proceedings of the American Control Conference*, 2005.

[87] J. Austin and S. Atkinson, "The design and testing of small, low-cost gps-tracked surface drifters," *Estuarine*, 2004.

[88] MathWorks, *MATLAB Version R2006b, www.mathworks.com.* Natick, Massachusetts, USA: The MathWorks Inc., 2006.

[89] M. Abkowitz, *Stability and Motion Control of Ocean Vehicles.* Massachusetts Institute of Technology, MA: MIT Press, 1972.

[90] K. Rawson and E. Tucker, *Basic Ship Theory*, 4th ed. Essex, England: Longman Scientific & Technical, 1994, vol. 2.

[91] H. Lamb, *Hydrodynamics*, 6th ed. Cambridge, United Kingdom: University of Cambridge Press, 1932.

[92] D. Humphreys, "Dynamics and hydrodynamics of ocean vehicles," in *OCEANS*, vol. 13, Boston, MA, September 1981, pp. 88–91.

[93] B. W. McCormick, *Aerodynamics, Aeronautics, and Flight Mechanics.* New York City, NY: John Wiley & Sons, Inc., 1979.

[94] J. Newman, *Marine Hydrodynamics.* Cambridge, MA: The MIT Press, 1977.

[95] B. Etkin, *Dynamics of Flight, Stability and Control*. New York: John Wiley & Sons, 1959.

[96] S. Hoerner, *Fluid-dynamic drag: practical information on aerodynamic drag and hydrodynamic resistance*, Midland Park, N.J., 1965.

[97] ——, *Fluid-dynamic lift: practical information on aerodynamic and hydrodynamic lift*. Brick Town, N.J.: L.A. Hoerner, 1975.

[98] V. Stepanyan, N. Hovakimyan, and C. Woolsey, "Adaptive output feedback control of a spheroidal underactuated underwater vehicle," in *OCEANS 2005, Proceedings of MTS/IEEE*, vol. 1, Washington, DC, 2005, pp. 278–284.

[99] B. Stevens and F. Lewis, *Aircraft Control and Simulations*, 2nd ed. Hoboken, New Jersey: John Wiley & Sons, 2003.

[100] A. Babister, *Aircraft Stability and Control*. London, England: Pergamon Press, 1961, vol. 1.